

Electronic Thesis and Dissertation Repository

9-3-2014 12:00 AM

Conversion Of Dimethyl-Ether to Olefins Over HZSM-5: Reactivity and Kinetic Modeling

Abdullah Saad Dughaiter
The University of Western Ontario

Supervisor
Hugo de Lasa
The University of Western Ontario

Graduate Program in Chemical and Biochemical Engineering
A thesis submitted in partial fulfillment of the requirements for the degree in Doctor of Philosophy
© Abdullah Saad Dughaiter 2014

Follow this and additional works at: <https://ir.lib.uwo.ca/etd>

Recommended Citation

Dughaiter, Abdullah Saad, "Conversion Of Dimethyl-Ether to Olefins Over HZSM-5: Reactivity and Kinetic Modeling" (2014). *Electronic Thesis and Dissertation Repository*. 2437.
<https://ir.lib.uwo.ca/etd/2437>

This Dissertation/Thesis is brought to you for free and open access by Scholarship@Western. It has been accepted for inclusion in Electronic Thesis and Dissertation Repository by an authorized administrator of Scholarship@Western. For more information, please contact wlsadmin@uwo.ca.

CONVERSION OF DIMETHYL ETHER TO OLEFINS OVER HZSM-5: REACTIVITY AND KINETIC MODELING

(Thesis format: Monograph)

by

Abdullah Saad Al-Dughauther

Graduate Program in Engineering Science
Department of Chemical and Biochemical Engineering

A thesis submitted in partial fulfillment
of the requirements for the degree of
Doctor of Philosophy

The School of Graduate and Postdoctoral Studies
Western University
London, Ontario, Canada

© Abdullah Saad Al-Dughauther 2014

ABSTRACT

The conversion of natural gas to light olefins, having dimethyl ether (DME) as a key intermediate, is a promising route for olefin manufacturing. Syngas can be used to produce DME. DME, can, in turn, be used as a feedstock to produce light olefins catalytically (dimethyl ether to olefin, or DTO process). Thus, selecting a proper catalyst and suitable operating conditions is the key for the implementation of the DTO conversion process.

The aim of the present research is to investigate HZSM-5 as a potential selective catalyst for light olefin production from DME. The detailed objectives of this PhD dissertation include: a) catalyst preparation, b) characterization, c) testing under reaction conditions, and d) kinetic modeling. The catalyst characterization addresses the influence of the $\text{SiO}_2/\text{Al}_2\text{O}_3$ ratio (30, 80, and 280) on HZSM-5 physicochemical properties. The reactivity runs, on the hand, are intended to achieve the maximum catalyst performance and light olefin selectivity by varying the $\text{SiO}_2/\text{Al}_2\text{O}_3$ ratio in the HZSM-5 catalyst. The kinetic study involves a reaction scheme and the development of a model suitable to describe the reaction network.

X-ray diffraction (XRD) and N_2 isotherms show that $\text{SiO}_2/\text{Al}_2\text{O}_3$ has no noticeable influence on HZSM-5 morphology or porosity characteristics. On the other hand, TPD (temperature programmed desorption) and FTIR (Fourier transform infrared spectroscopy) data along with the NH_3 -desorption kinetics all display weak and strong acid sites on HZSM-5 with both their ratio and total acidity being reduced by increasing the $\text{SiO}_2/\text{Al}_2\text{O}_3$ ratio. The NH_3 -desorption kinetics show that the activation energies augmented with the raise of the $\text{SiO}_2/\text{Al}_2\text{O}_3$ ratio.

DME conversion and coke formation both rose with HZSM-5 acidity along with the reactor temperature. In the case of ZSM5-280, coke was limited and this led to negligible catalyst deactivation and higher light olefins selectivity. Furthermore, when the DME conversion on ZSM5-280 was increased, C_5^+ olefins, paraffins, and aromatics selectivities were consistently augmented and this happened at the expense of light olefins (C_4^-).

A DTO reaction network was developed having methoxy species as the key methylating species. In this respect, it is proposed that ethylene is formed through DME dehydration.

Following this, light olefins experience methylation up to octene. In addition, hexene is partially dehydrogenated to benzene, with benzene experiencing further methyl group insertion forming heavier aromatics.

The DTO kinetic study shows that the pre-exponential constant for methylating olefins and aromatics was decreased consistently with the carbon number increase of the methylated species. On the other hand, the activation energy for methylating light olefins was found to be slightly higher when compared to that for the heavy olefins. Aromatic methylation reactions displayed higher activation energy as the number of methyl groups in the aromatic ring increased.

Thus, the present research demonstrates that HZSM-5 with $\text{SiO}_2/\text{Al}_2\text{O}_3 = 280$ can be used as a potential catalyst for the dimethyl ether (DME) transformation into light olefins (DTO). Furthermore, it is also proven that a proposed reaction scheme and kinetic model can be established using rigorous statistical methods for parameter estimation.

Keywords: HZSM-5, micro zeolite, $\text{SiO}_2/\text{Al}_2\text{O}_3$ ratio, NH_3 -TPD kinetics, dimethyl ether, light olefins, Berty Reactor, DTO reaction network, solid-state kinetics, DTO kinetic modeling.

DEDICATION

This dissertation is dedicated with all my heart:

To my lovely wife,

whose love, endurance, inspiration and endless support made this dissertation possible.

To my mother,

whose sincere prayers, sacrifice, and support made this dissertation a success.

To my parents-in-law,

for their sincere prayers and support in several ways.

To my daughter and son (Areen, and Saad),

for their encouraging smiles every morning.

ACKNOWLEDGMENTS

Praise and gratitude be to ALLAH Almighty, with whose gracious help it was possible to accomplish this work.

I wish to express my deepest gratitude and sincere appreciation to my supervisor Dr. Hugo de Lasa for his generous support, encouragement, suggestions, patience and assistance throughout the work of this thesis.

I wish also to gratefully acknowledge the Saudi Basic Industries Corporation (SABIC) for the scholarship awarded for granting and sponsoring my PhD study.

Special thanks are extended to Dr. Rezwatul Quddus for his constructive comments, helpful suggestions, and excellent support in many aspects of this research.

I would like also to thank Eng. Jose Munoz and Dr. Pastor Solano for their extensive assistance and cooperation during my experimental work.

My thanks go to my colleagues and friends at CREC. Special thanks go to Dr. Sameer Al-Ghamdi and Dr. Saad Al-Bogami for fruitful technical discussions.

Acknowledgement and thanks are due to Chemical and Biochemical Engineering Department at Western University for providing all facilities and utilities.

Lastly, but by no means the least, I am obliged to offer my indebtedness and sincere appreciation to my mother, brothers, parents-in-law, brothers- and sister-in-law, wife and sons, for their love, moral support, sincere prayers and encouragement that made this work a success. May Allah bless them all.

TABLE OF CONTENTS

ABSTRACT	II
DEDICATION	IV
ACKNOWLEDGMENTS	V
TABLE OF CONTENTS	VI
LIST OF TABLES	X
LIST OF FIGURES	XII
LIST OF APPENDICES	XVIII
CHAPTER 1 INTRODUCTION	1
CHAPTER 2 LITERATURE REVIEW	3
2.1 INTRODUCTION	3
2.2 LIGHT OLEFINS APPLICATIONS	3
2.3 LIGHT OLEFINS PRODUCTION	7
2.3.1 <i>Paraffins Thermal Cracking</i>	7
2.3.2 <i>Paraffins Catalytic Cracking</i>	10
2.3.3 <i>Methanol to Olefins Process (MTO)</i>	12
2.3.4 <i>Dimethyl Ether to Olefins (DTO)</i>	16
2.4 DIMETHYL ETHER TO OLEFINS (DTO). A LITERATURE REVIEW	19
2.4.1 <i>Introduction</i>	19
2.4.2 <i>DTO Catalysts</i>	20
2.4.3 <i>DTO Catalyst Performance</i>	22
2.4.4 <i>Conversion of DME to Light Olefins over HZSM-5</i>	24
2.4.5 <i>Kinetic Modeling of DME Conversion to Olefins over HZSM-5</i>	33
2.4.6 <i>Outlooks on DME Conversion to Olefins over HZSM-5</i>	41
CHAPTER 3 SCOPE OF RESEARCH	44
CHAPTER 4 EXPERIMENTAL METHODS	46
4.1 INTRODUCTION	46

4.2	PREPARATION OF THE H-ZSM5 SAMPLES.....	46
4.3	STRUCTURAL CHARACTERIZATION METHODS.....	47
4.3.1	<i>XRD analysis</i>	47
4.3.2	<i>Particle size distribution</i>	48
4.3.3	<i>N₂ isotherm</i>	48
4.4	SURFACE ACIDITY CHARACTERIZATION METHODS.....	49
4.4.1	<i>NH₃-TPD</i>	49
4.4.2	<i>Pyridine-FTIR</i>	49
4.5	REACTIVITY TESTS IN THE BERTY REACTOR UNIT.....	50
4.5.1	<i>Berty reactor</i>	50
4.5.2	<i>Experimental Apparatus</i>	51
4.5.3	<i>Experimental Procedure</i>	52
4.5.4	<i>Reactor outlet and coke analysis</i>	55
4.5.5	<i>Reactivity tests evaluation</i>	56
4.6	CONCLUDING REMARKS.....	57
CHAPTER 5 CHARACTERIZATION OF HZSM-5 AND NH₃ DESORPTION		
KINETICS..... 58		
5.1	INTRODUCTION.....	58
5.2	PHYSICAL CHARACTERIZATION.....	59
5.2.1	<i>XRD Crystallinity</i>	59
5.2.2	<i>N₂ Isotherm</i>	62
5.3	SURFACE ACIDITY CHARACTERIZATION.....	80
5.3.1	<i>Total Acidity and Acidity Distribution</i>	80
5.3.2	<i>Nature of HZSM-5 Acid Sites</i>	84
5.4	NH ₃ -DESORPTION KINETICS FOR HZSM-5.....	88
5.5	CONCLUSIONS.....	97
CHAPTER 6 CONVERSION OF DIMETHYL-ETHER TO OLEFINS OVER		
HZSM-5: REACTIVITY AND REACTION MECHANISM..... 99		
6.1	INTRODUCTION.....	99
6.2	DME REACTIVITY RUNS.....	99
6.2.1	<i>Thermal Conversion of DME</i>	99

6.2.2	<i>Conversion of DME to Olefins (DTO) over HZSM-5 with Different SiO₂/Al₂O₃: Catalyst Screening</i>	100
6.2.3	<i>Conversion of DME to Olefins (DTO) over HZSM-5 with SiO₂/Al₂O₃ = 280.</i>	105
6.3	DTO REACTION NETWORK.....	114
6.3.1	<i>Surface Methoxy Formation</i>	116
6.3.2	<i>Formation of Primary Hydrocarbons Products</i>	119
6.3.3	<i>Methylation of C₃⁺ Olefins</i>	121
6.3.4	<i>Hexene Aromatization</i>	121
6.3.5	<i>Methylation of C₆+ Aromatics</i>	122
6.4	CONCLUSIONS.....	122
CHAPTER 7 KINETIC MODELING OF DIMETHYL ETHER CONVERSION TO OLEFINS OVER HZSM-5		125
7.1	INTRODUCTION	125
7.2	MODEL ASSUMPTIONS	125
7.3	KINETIC MODEL DEVELOPMENT.....	127
7.4	SPECIES MOLE BALANCE IN BERTY REACTOR.....	131
7.5	MODEL SIMPLIFICATION AND REPARAMETERIZATION	134
7.6	REGRESSION ANALYSIS AND PARAMETER ESTIMATION.....	139
7.6.1	<i>DME Reaction Rate</i>	140
7.6.2	<i>Light Olefins Methylation Reactions</i>	142
7.6.3	<i>Heavy Olefins Methylation Reactions</i>	146
7.6.4	<i>Hexene Aromatization to Toluene</i>	148
7.6.5	<i>Aromatics Methylation Reactions</i>	149
7.6.6	<i>Discussions</i>	151
7.7	CONCLUSIONS.....	154
CHAPTER 8 CONCLUSIONS AND RECOMMENDATIONS.....		157
8.1	CONCLUSIONS.....	157
8.2	RECOMMENDATIONS.....	160
REFERENCES.....		162
APPENDICES.....		183

CURRICULUM VITAE..... 187

LIST OF TABLES

Table 2.1: Selectivity of light olefins (wt%) from a cracking unit using various feedstocks .	9
Table 2.2: Comparison between DCC and FCC processes	12
Table 2.3: Catalyst performance for DTO reaction.	23
Table 2.4: Effect of promoters on HZSM-5 acidity and performance in DTO reaction	27
Table 5.1: HZSM-5 crystallinity and particle diameter.	62
Table 5.2: NLDFT ^a standard deviation (STD) of isotherm fit.	68
Table 5.3: Statistical parameters for N ₂ isotherm linear methods.	69
Table 5.4: HZSM-5 and pellets pore size (Å).	74
Table 5.5: Pore surface area (m ² /g) and pore volume (ml/g).	78
Table 5.6: Theoretical and measured acidities for HZSM-5 samples ($\times 10^{-5}$ mol _{NH₃} /g _{HZSM-5}).	82
Table 5.7: NH ₃ -TPD data.	84
Table 5.8: Relative hydrogen-bonded, Lewis, and Brønsted acid sites concentrations obtained from the areas of the FTIR bands (au/cm ⁻¹) using a nitrogen gas purge flow at 100°C.	87
Table 5.9: Optimized kinetic constants for NH ₃ desorption in HZSM-5	93
Table 5.10: Cross-correlation coefficient matrix for the desorption kinetic constants.	94
Table 5.11: Measured and estimated ratio of weak to strong acidity.	96
Table 7.1: Elementary steps of the DTO reaction network with the related reaction rates and equilibrium parameters.	129
Table 7.2: Lumped reaction rate and equilibrium constants.	136

Table 7.3: Experimental and model components reaction rates after simplification and reparameterization.....	137
Table 7.4: Optimized intrinsic kinetic constants for DME reaction rate (Table 7.3-a).	141
Table 7.5: Optimized intrinsic kinetic constants for DME reaction rate (Equation 7.29)....	141
Table 7.6: Optimized intrinsic kinetic constants for C ₂ to C ₄ olefins reactions.	144
Table 7.7: Optimized intrinsic kinetic constants for C ₂ to C ₄ olefin methylation reactions with single activation energy.	144
Table 7.8: Optimized intrinsic kinetic constants for C ₅ to C ₇ olefin methylation reactions with a single activation energy.....	146
Table 7.9: Optimized intrinsic kinetic constants for toluene formation (<i>r</i> ₈ , Equation 7.40)	148
Table 7.10: Optimized intrinsic kinetic constants for aromatics methylation reactions.	149
Table 7.11: Intrinsic kinetic and statistical parameters for the proposed DTO kinetic model.	151
Table 7.12: Reported activation energies for the methylation reactions of light olefins and aromatics using HZSM-5 catalyst.....	153

LIST OF FIGURES

Figure 2.1: Global Olefins Consumption in 2007	4
Figure 2.2: United States ethylene consumption in 2008	5
Figure 2.3: Global propylene demand pattern, 1970–2004.....	6
Figure 2.4: United States propylene consumption in 2007.....	6
Figure 2.5: Regional propylene/ethylene demand ratio growth, 1992–2004.....	7
Figure 2.6: Global propylene production methods, 2007.....	8
Figure 2.7: Global feedstocks used in steam cracking.....	9
Figure 2.8: Fluid-bed MTG and MTO demonstration plant.....	14
Figure 2.9: UOP/HYDRO MTO Simplified Process Flow Diagram.....	15
Figure 2.10: Lurgi MTP Simplified Process Flow Diagram	16
Figure 2.11: JGC/ Mitsubishi DTP Simplified Process Flow Diagram [41,43].....	19
Figure 2.12: ZSM structural diagram (a) face (100) (b) Channel system.....	21
Figure 2.13 SAPO-34: structural diagram (a) Cage interconnections (b) One cage dimensions [65].....	21
Figure 2.14: Proposed reversible conversion of Brønsted acid to Lewis acid.....	25
Figure 4.1: Sectional view of the Bertly reactor: (a) Detailed assembly; (b) Gas circulation pattern	51
Figure 4.2: Schematic diagram of the reactivity test setup.....	52
Figure 4.3: GC-FID chromatogram for quantification of all species. Note: identified and quantified products are assigned numbers from 1 to 19.	56

Figure 4.4: GC-FID temperature profile of the oven calibration program.	56
Figure 5.1: Particle size distribution for: (a) Pure HZSM-5 (b) HZSM-5 pellets.....	60
Figure 5.2: XRD spectra for the following zeolites: (a) ZSM5-30, (b) ZSM5-80, (c) ZSM5-280, (d) ZMPL-30, (e) ZMPL-80, (f) ZMPL-280, (g) ZMPL-BL.....	61
Figure 5.3: N ₂ adsorption/desorption isotherm for ZSM5-30 and ZMPL-30: (a) Normal scale, (b) Semi-log scale.	65
Figure 5.4: N ₂ adsorption/desorption isotherm for ZSM5-80 and ZMPL-80: (a) Normal scale, (b) Semi-log scale.	66
Figure 5.5: N ₂ adsorption/desorption isotherm for ZSM5-280 and ZMPL-280: (a) Normal scale, (b) Semi-log scale.	66
Figure 5.6: N ₂ adsorption/desorption isotherm for Versal 950 and Fused Al : (a) Normal scale, (b) Semi-log scale.	66
Figure 5.7: NLDFT N ₂ isotherm goodness of fit using cylindrical geometry for ZSM5-30 (a) Normal scale, (b) Semi-log scale.....	68
Figure 5.8: NLDFT N ₂ isotherm goodness of fit using slit-like geometry for ZSM5-30 (a) Normal scale, (b) Semi-log scale.....	68
Figure 5.9: NLDFT pore size distribution of HZSM-5 (cylindrical geometry model).....	73
Figure 5.10: NLDFT pore size distribution of HZSM-5 (slit-like geometry model).....	73
Figure 5.11: Pore Size Distribution (NLDFT cylindrical model): (a) Micropores, (b) Mesopores.	75
Figure 5.12: NH ₃ -TPD thermograms at $\beta = 15^\circ\text{C}/\text{min}$ for: (a) pure HZSM-5 (b) HZSM-5 pellets.	80

Figure 5.13: Pyridine-FTIR spectra of HZSM-5 measured in the 1400-1600 cm^{-1} region when using different purge temperatures. (a) ZSM5-30, (b) ZSM5-80, (c) ZSM5-280, and (d) Plain ZSM5-30.	85
Figure 5.14: Pyridine-FTIR Spectra of HZSM-5 Measured in the Region 3550-3800 cm^{-1} After Different Purge Temperatures. (a) ZSM5-30, (b) ZSM5-80, (c) and ZSM5-280.	87
Figure 5.15: Cumulative volume of desorbed ammonia over a ZSM5-80 at different Ramping temperatures.	90
Figure 5.16: Illustration of the deconvolution of the weak and strong acidity data for NH_3 desorption kinetics (ZSM5-80 at $\beta = 20^\circ\text{C}/\text{min}$). T_1 shows the temperature where the sole influence of weak sites ends and T_2 represents the temperature where the sole influence of strong sites begins.	93
Figure 5.17: Comparison of experimental ammonia volume desorbed versus model ammonia volume desorbed for ZSM5-30 (Equation (5.11)).	94
Figure 5.18: Comparison of experimental ammonia volume desorbed versus model ammonia volume desorbed for ZSM5-80 (Equation (5.11)).	94
Figure 5.19. Comparison of experimental ammonia volume desorbed versus model ammonia volume desorbed for ZSM5-280 (Equation (5.11)).	95
Figure 6.1: Changes of HC Conversion of DME with time on stream (TOS) at different temperatures using different HZSM-5 catalysts.	100
Figure 6.2: Coke Concentration in Different Spent HZSM-5 Catalysts as a Function of Temperature. TOS=300min.	101
Figure 6.3: Lumped product selectivity versus total acidity of HZSM-5 at different reaction temperatures. (a) Light olefins (ethylene- butene), (b) Heavy olefin lump (pentene-octene), (c) Paraffins (butane-octane), (d) Aromatics (C7-C12 methylbenzene). Note: Acidity at 106 $\mu\text{mol}_{\text{NH}_3}/\text{g}_{\text{HZSM-5}}$ is for ZSM5-280, acidity at 332 $\mu\text{mol}_{\text{NH}_3}/\text{g}_{\text{HZSM-5}}$ is for ZSM5-80, and acidity at 640 $\mu\text{mol}_{\text{NH}_3}/\text{g}_{\text{HZSM-5}}$ is for ZSM5-30.	102

Figure 6.4: Individual light olefin selectivity vs total acidity of HZSM-5 at Different Reaction Temperatures.	104
Figure 6.5: Changes of light olefin selectivity with DME conversion for various SiO ₂ /Al ₂ O ₃ ratios. Note: For each catalyst, the increase in the DME conversion is the result of higher reaction temperatures in the 330-450°C range.	105
Figure 6.6: Coke concentration in spent ZMPL-280 as a function of temperature. TOS = 10 h.	106
Figure 6.7: ZMPL-280 total surface area at different coke yields. Note: 0% coke content refers to a fresh catalyst.	107
Figure 6.8: DME conversion vs contact time (τ) at different reaction temperatures.	108
Figure 6.9: Lumped product selectivity vs DME conversion.	108
Figure 6.10: Individual light olefin selectivity vs DME conversion.	109
Figure 6.11: Individual heavy olefins selectivity vs DME conversion: (a) Pentene and octene, (b) Hexene and octene.	110
Figure 6.12: Individual paraffin selectivity vs DME conversion: (a) Butane and pentane, (b) Hexane, (c) Heptane, (d) Octane.	112
Figure 6.13: Individual aromatic selectivity vs DME conversion: (a) Toluene, (b) Xylene and mesitylene, (c) Durene, (d) Pentamethylbenzene (PMB) and Hexamethylbenzene (HMB).	113
Figure 6.14: Butane/(Butane+Butene) Ratio versus DME conversion.	116
Figure 6.15: Reaction scheme for the surface methoxy species formation by DME dehydration over HZSM-5.	119
Figure 6.16: Proposed DTO elementary reaction network over HZSM-5.	120
Figure 7.1: Ratio of C ₂ -C ₅ olefins to the total hydrocarbon products reaction rates.	135

Figure 7.2: Variation of DME rate equation (Table 7.3-a) adsorption term with reaction temperature.	141
Figure 7.3: Comparison of experimental DME reaction rates versus model calculations: a) individual conditions (Note: Full lines represent calculated values using estimated rate parameters), b) overall parity plot.....	142
Figure 7.4: Hydrocarbon product pressure ratio versus reaction temperature.....	143
Figure 7.5: Comparison of experimental ethylene reaction rates versus model calculations: a) individual conditions (Note: curves with lines are calculated using the estimated rate parameters), b) overall parity plot.....	145
Figure 7.6: Comparison of experimental propene reaction rates versus model calculations: a) individual conditions (Note: curves with lines are calculated using the estimated rate parameters), b) overall parity plot.....	145
Figure 7.7: Comparison of experimental butene reaction rates versus model calculations: a) individual conditions (Note: curves with lines are calculated using the estimated rate parameters), b) overall parity plot.....	145
Figure 7.8: Comparison of experimental pentene reaction rates versus model calculations: a) individual conditions (Note: curves with lines are calculated using the estimated rate parameters), b) overall parity plot.....	147
Figure 7.9: Comparison of experimental heptene reaction rates versus model calculations: a) individual conditions (Note: curves with lines are calculated using the estimated rate parameters), b) overall parity plot.....	147
Figure 7.10: Comparison of experimental octene reaction rates versus model calculations: a) individual conditions (Note: curves with lines are calculated using the estimated rate parameters), b) overall parity plot.....	147
Figure 7.11: Comparison of experimental toluene formation rates r_8 versus model calculations: a) individual conditions (Note: curves with lines are calculated using the estimated rate parameters), b) overall parity plot.	148

Figure 7.12: Comparison of experimental xylene reaction rates versus model calculations: a) individual conditions (Note: curves with lines are calculated using the estimated rate parameters), b) overall parity plot..... 150

Figure 7.13: Comparison of experimental mesitylene reaction rates versus model calculations: a) individual conditions (Note: curves with lines are calculated using the estimated rate parameters), b) overall parity plot. 150

Figure 7.14: Comparison of experimental durene reaction rates versus model calculations: a) individual conditions (Note: curves with lines are calculated using the estimated rate parameters), b) overall parity plot..... 150

LIST OF APPENDICES

Appendix A. Reactivity tests data collection sheet	184
Appendix B. Atomic Balance Calculation	185

CHAPTER 1 INTRODUCTION

Lower C₂-C₄ olefins are key intermediates in petrochemical industries. Among these olefins, the two most commonly used ones are ethylene and propylene. Ethylene and propylene are the backbone of petrochemical processes given their high double bond reactivity, making light olefin ideal molecules for being converted into many useful end products [1–6]. As a measure of the significance of these light olefins based processes, in recent years, ethylene production, the largest volume organic chemical has become a barometer of economical activity in developed countries [7].

Light olefins are mainly produced via steam cracking of hydrocarbon feedstocks. Additional light olefin production is also achieved in oil upgrading processes and by catalytic dehydrogenation of paraffins. One can note that the higher prices for conventional petrochemical feedstocks along with the wide usage of olefins have been major stimulating factors to further exploit alternative non-petroleum feedstocks such as coal and natural gas for light olefin production [5,8].

The conversion of natural gas into light olefins is a promising route for light olefin production. This process has attracted researchers' attention since the discovery of the HZSM-5 catalyst back in 1970s. If one considers the overall natural gas conversion into the olefin process, DME is a key intermediate in light olefins manufacturing. Syngas can be produced in a first step process from natural gas. Then, DME can be synthesized either in two steps from methanol or directly from syngas. The latter route implies that DME can be converted into olefins in one single step. This process step is designated as DTO (Dimethyl-ether to Olefins).

It has been found that DTO appears to be a more viable alternative for olefin production versus the conversion of methanol into olefins, or the MTO (Methanol to Olefins) process. DTO advantages potentially include: a) higher hydrocarbon selectivity, b) higher catalyst durability and selectivity to olefins, c) lower equipment costs, d) reduced thermodynamic constraints, e) lower reaction exothermicity, and f) lower H₂/CO ratio requirements for DME Synthesis.

Despite the economic attractiveness of producing light olefins from DME, research work in this area is still in the early stages. According to the published literature, zeolite-type materials are considered as potential catalysts for both of MTO and DTO reactions. Two types of zeolites have been examined for DTO: HZSM-5 and HSAPO-34. Employing HSAPO-34 has shown to have serious limitations, while HZSM-5 provides more flexibility in terms of catalyst formulation and reactor designs [9–16].

In the DTO process over HZSM-5, the DME is first converted to light olefins. These formed olefins may continue reacting, forming heavier hydrocarbons such as C_4^+ [17]. It was found, however, that when using pure or highly concentrated DME, DME secondary reactions are enhanced [10,11,17–19]. Thus, DME partial pressure reduction is advisable to decrease undesirable olefin transformations. [9,18]. However and to comply with process economic constraints, selecting proper diluents species at appropriate levels is still a challenging task. In this context, the development of a DME conversion selective catalyst, which operates at DME partial pressures close to atmospheric, with light olefin selectivity, is critical.

To address these important matters, the present study considers, in Chapter 4, the preparation methods of an HZSM-5 catalyst and its pellets. Three different SiO_2/Al_2O_3 ratios (30, 80, and 280) are used. In Chapter 4 also, the various techniques for HZSM-5 zeolite physicochemical characterization are reported as well as the experimental setup used for the reactivity tests. Following this, Chapter 5 describes the influence of the SiO_2/Al_2O_3 ratio on HZSM-5 zeolite physicochemical characteristics and on ammonia desorption kinetics. After that, Chapter 6 displays the effect of the SiO_2/Al_2O_3 ratio on the reactivity properties of the HZSM-5. This is done with the aim of choosing a selective and durable catalyst for the DTO process. Chapter 6 also reports a proposed DTO reaction network, based on the reactivity runs using neat DME over HZSM-5. With this end in mind, reactivity runs with an HZSM-5 catalyst and having a SiO_2/Al_2O_3 ratio of 280, at different thermal and contact time levels, are considered. Chapter 7 reports kinetic modeling together with the estimation of kinetic parameters using various statistical indicators. Finally, Chapter 8 provides concluding remarks and recommendations for the present PhD dissertation.

CHAPTER 2 LITERATURE REVIEW

2.1 Introduction

This literature covers first the most important applications of light olefins in petrochemical industries (section 2.2). Following this, section 2.3 reports the major technologies used for the production of the light olefins using various hydrocarbon feedstocks (from thermal and catalytic cracking) and oxygenates such as methanol and di-methyl-ether (from methanol-to-olefins and DME-to-olefins).

Furthermore, Section 2.4, specifically reports the conversion processes of dimethyl-ether to olefins (DTO). It is in this section, where the selection and performance of zeolites used nowadays in DTO conversion processes are reviewed (Sections 2.4.2 and 2.4.3). Following this, Section 2.4.4 describes the key parameters that have been found to influence the olefin synthesis in the DTO. Furthermore, the development of the DTO kinetic lumped models is reviewed in section 2.4.5. Finally, section 2.4.6 summarizes the outlook and the insights into the now available know-how for the DTO process and the potential areas of research needed to bring being this technology to full commercial scale and application.

2.2 Light olefins applications

Olefins are the class of hydrocarbons having a single double bond and the C_nH_{2n} generic chemical formula. Light olefins are one of the building blocks in the petrochemical industry for the manufacturing of many products, including the aromatic hydrocarbons such as benzene, toluene and xylenes (BTX).

In this respect, one can identify polyolefin manufacturing as one of the largest sectors of olefin demand, with a 57% of total olefin consumption, as reported in Figure 2.1. One can also note that polyolefin manufacturing will continue to be for the sector of future growth of olefin demand.

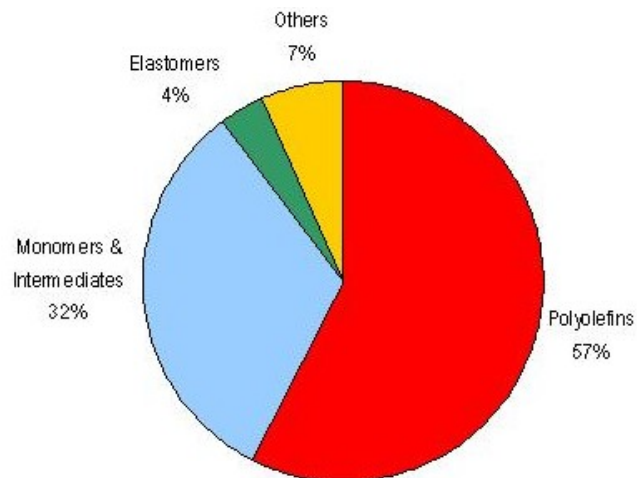


Figure 2.1: Global Olefins Consumption in 2007 [20].

Monomers and intermediate species are the second largest group of chemicals for both of ethylene and propylene [20]. Some examples of major intermediate chemicals and polymers produced from ethylene include among others: a) linear low and high density polyethylene (LDPE, LLDPE and HDPE), b) ethylene dichloride (EDC), c) vinyl chloride monomer (VCM), d) polyvinyl chloride (PVC) and its copolymers, e) alpha-olefins (AO), f) ethylene oxide (EO) used primarily to make mono ethylene glycol (MEG) for polyester and antifreeze production, g) vinyl acetate (VAM), h) ethyl alcohol (ethanol), i) ethylene propylene diene monomer (EPDM), j) as a co-monomer for polypropylene, k) ethylbenzene (EB), l) styrene monomer (SM), m) polystyrene (PS) and its copolymers [2].

Figure 2.2 illustrates the U.S. ethylene consumption percentages of the major chemicals and polymers in 2008 [1]. It is apparent from these data that polyethylene represents the major end use commodity for ethylene. Its consumption represents 58% of total ethylene produced.

The end use markets for ethylene products involve a wide spectrum of possible applications. These applications include: wire and cable insulation; consumer, industrial and agricultural packaging; woven fabrics and assorted coverings; pipes, conduits and assorted construction materials; drums, jars, containers, bottles and the racks in which to hold them; antifreeze; solvents and coatings [3].

Propylene demand is approximately one-half of the ethylene demand. Propylene is the second most important olefin manufactured at the industrial scale. Similar to ethylene, propylene is a primary petrochemical feedstock [4,21]. Figure 2.3 illustrates the global demand breakdown for propylene from 1970 to 2004. One can notice that in 1970, polypropylene consumption was shared at 11-18% of total propylene demand for a number of products. Nowadays, however, this situation has changed significantly. Today, polypropylene consumes up to 64% of the world's propylene production (not including fuel use). Therefore, polypropylene is the main driver for propylene demand [5]. Figure 2.4 also reports major end-uses for propylene in the United States in 2007. It is reported that polypropylene manufacturing accounts nowadays for 59% of the total of propylene produced [4].

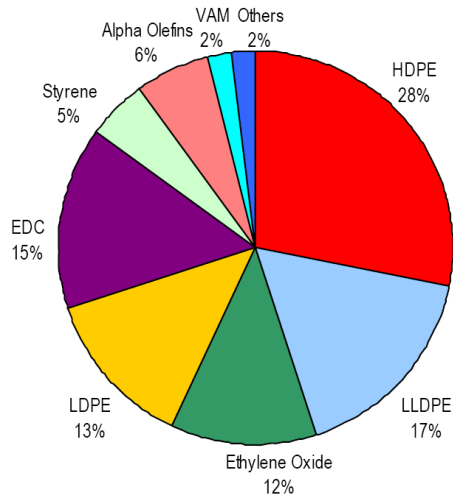


Figure 2.2: United States ethylene consumption in 2008 [1].

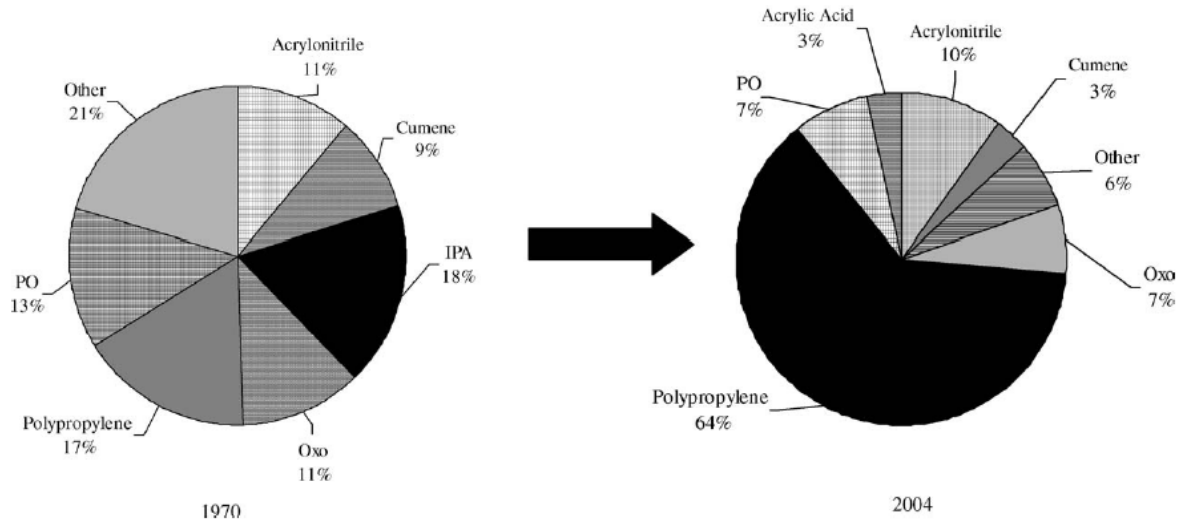


Figure 2.3: Global propylene demand pattern, 1970–2004 [5].

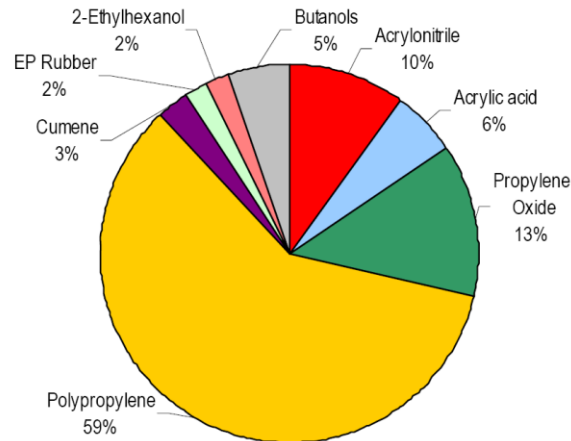


Figure 2.4: United States propylene consumption in 2007 [4].

Since polypropylene growth continues to be strong, this is forcing a structural change in the supply pattern for propylene manufacturers. Figure 2.5 compares the regional demand ratio between ethylene and propylene over the 1992–2004 periods. While the overall demand for ethylene is greater than that for propylene over this timeframe, the demand growth rate for propylene has outpaced the one for ethylene. For instance, in the U.S., the propylene/ethylene demand ratio has increased from 0.43 in 1992 to 0.54 in 2004. The same phenomenon has been observed in Western Europe and in the Asia-Pacific region. Moreover, in these cases, this trend has also been seen to occur to an even greater degree. In the Asia-Pacific region, the propylene/ethylene demand ratio is as high as 0.77. One should note, however, that the

Middle East, still remains a heavily ethylene-centered area, given the low cost of ethane with propylene/ethylene ratios staying relatively low and unchanged since 1996 [5].

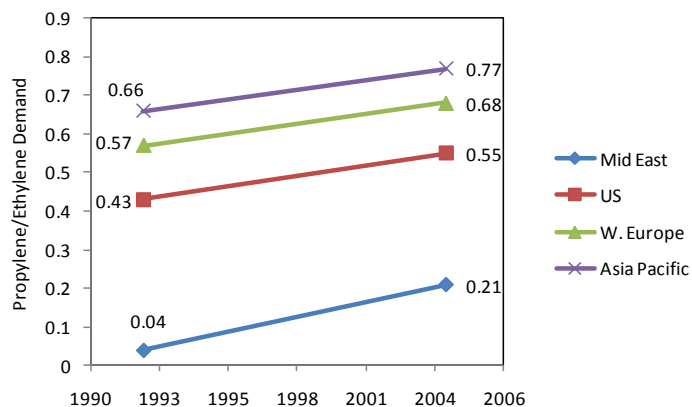


Figure 2.5: Regional propylene/ethylene demand ratio growth, 1992–2004 [5].

2.3 Light Olefins Production

Currently, there are three main technologies for producing olefins: a) thermal cracking of hydrocarbons (naphtha, ethane, gas oil and LPG), b) catalytic cracking of vacuum gas oil and c) paraffin dehydrogenation [22]. In addition to these commercial processes, there are some economically non-proven technologies still under development such as: a) methane oxidative coupling (MOC), b) partial oxidation of paraffins, c) olefin recovery from refinery streams, d) methanol-to-olefins (MTO) and e) di-methyl-ether to olefins (DTO). In the following subsections of this chapter, some of the already demonstrated technologies will be reviewed.

2.3.1 Paraffins Thermal Cracking

Thermal cracking, sometimes called “steam cracking” (also known as pyrolysis), is a non-catalytic thermal reaction in which saturated hydrocarbons (paraffins) are broken down into smaller chemical species. These product chemical species are often unsaturated hydrocarbons (olefins). In the thermal cracking process, the reaction occurs in a pyrolysis furnace at high temperatures and in the presence of steam. The selectivity of the steam cracking towards olefins can be controlled through a careful adjustment of temperatures and residence time in the pyrolysis furnace [7].

Nowadays, most of the ethylene and propylene produced are synthesized in steam crackers. In contrast to the fluid catalytic cracking used by the petroleum industry to obtain large amounts of gasoline, thermal cracking is still used since it yields larger percentages of C₂, C₃, and C₄ olefins [22].

Figure 2.6 shows Nexant ChemSystems' estimation of global propylene production methods in 2007. This figure illustrates that 63% of the global propylene is generated by steam crackers, 28% by refinery FCC/DCC units, 4% by refinery splitters, 2.6% by propane dehydrogenation and 2% by metathesis.

The endothermic dehydrogenation reaction of both ethane and propane can be described by the following stoichiometric equations:

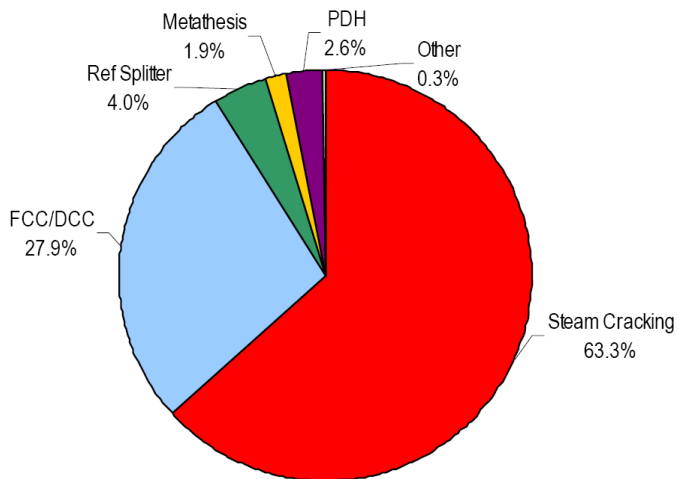
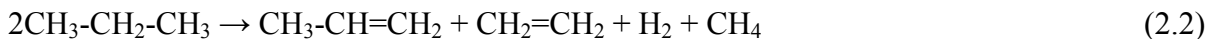


Figure 2.6: Global propylene production methods, 2007 [4].

The reactor (furnace) in which the thermal cracking takes place consists of tube bundles operating at 815-870°C and 500 psig. Steam is used as a solvent to reduce coking in the tubes and to increase the ethylene selectivity. The required amount of steam increases as the feedstock gets heavier and varies from 0.3 kg steam/kg ethane to 0.9 kg steam/kg gas oil [7]. Originally the feedstock for this process was mostly composed of ethane and propane from

natural gas. But naphtha and gas oil fractions from petroleum can also be used. Recently their use has increased dramatically with the high price and the short supply of natural gas. The percentages of different steam cracking feedstocks used worldwide are shown in Figure 2.7 where Naphtha is dominant in the feedstock, accounting for about 55% [6].

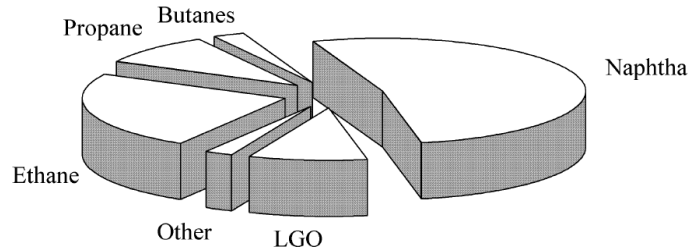


Figure 2.7: Global feedstocks used in steam cracking [6]

A typical ethylene plant achieves an ethane conversion of about 60% [23]. The olefins produced in the crackers are associated with the feedstock molecular weight. In this respect, a high percentage of ethylene can be produced by using lighter feedstocks such as ethane and propane. On the other hand, heavier feedstocks, such as naphtha and gas oil, are used if more propylene is preferred. The following table summarizes the typical selectivity of olefins obtained from various feeds.

Table 2.1: Selectivity of light olefins (wt%) from a cracking unit using various feedstocks [7]

Product	Ethane	Propane	Naphtha	Gas Oil
Ethylene	76	42	31	23
Propylene	3	16	16	14
Butene	2	5	9	9

The steam cracking processes for ethylene and propylene production are highly endothermic reactions and take place at a substantially high pressure. They consume, as a result, a large amount of energy. Additionally, steam cracking involves the significant formation of coke on the inner reactor tube surface, with this requiring frequent plant shutdowns for tube cleaning. Moreover, coke deposits on the inner walls of the reactor tubes reduce heat transfer. This requires higher wall temperatures as high as 1100°C, to maintain operating temperatures of 870°C. This results in a reduction of the life time of the tubes [24]. Moreover, higher temperatures of operation lead to the formation of NO_x, and consequently NO_x emissions to

the atmosphere. These NO_x emissions may create issues in complying with increasingly strict environmental regulations.

Other problems associated with the current steam cracking processes for ethylene production are related to thermodynamic limitations. Dehydrogenation reactions taking place in the steam cracking of hydrocarbons are of reversible character, resulting in thermodynamic restrictions on paraffins conversion.

2.3.2 Paraffins Catalytic Cracking

Fluid catalytic cracking (FCC) is one of the most important chemical processes used in petroleum refineries. Catalytic cracking converts vacuum gasoil into gasoline range hydrocarbons with ethylene and propylene being gas by-products [4,22,25].

Thus, there is a need of an alternative process to steam cracking to produce propylene. This becomes essential as the propylene/ethylene demand ratio is steadily increasing as reported in Figure 2.5.

Until now, FCC has made up for this shortfall and currently accounts for 28% of the worldwide propylene production (refer to Figure 2.6) [4]. In the FCC fluidized bed unit, the catalyst particles are suspended by an upward gaseous flow in a riser reactor. In the riser, there is a rapid catalyst deactivation. As a result, catalyst particles have to be regenerated continuously in another unit called the “regenerator”. With this end, the superficial gas velocity in the riser is kept high enough in order to entrain the catalyst along with the hydrocarbon vapors.

As previously mentioned, the cracking reactions of the crude oil involve coke formation. In the FCC process, coke deposits on the catalyst surface and very quickly reduces the catalyst activity. Therefore, the FCC unit requires a proper selection of conditions for catalyst regeneration with an essentially complete combustion of deposited coke (e.g. 670-700°C). The integrated FCC unit also allows the efficient utilization of heat released from coke combustion in the regenerator. This heat is transferred to the regenerated catalyst, to supply

the energy required for vaporizing the feedstock and for the endothermic cracking reactions in the riser [25].

Due to the formerly mentioned drawbacks of thermal cracking, major efforts in the last few decades have addressed the development of a feasible catalytic process to produce light olefins. A variety of very promising processes have been considered and some have already been commercialized.

The Deep Catalytic Cracking (DCC) process was developed by the Research Institute of Petroleum Processing (RIPP) of SINOPEC. This was done to catalytically crack heavy oil such as atmospheric residue (AR) and vacuum gas oil (VGO) in order to produce light olefins in the range of C_3 – C_5 [5,6,22,25]. The first commercial plant was built in 1997 in Thailand, and as of now nine commercial plants are in operation. This process is considered one of the most efficient processes to deal with the increasing demand of propylene. The DCC process is similar to conventional FCC. It is, however, operated with a different zeolite (HZSM-5) and at milder operating conditions as described in Table 2.2. A specially designed catalyst, named ZRP and having an HZSM-5 zeolite instead of a Y zeolite, is used in this process to increase the light olefin yield [25]. Similarly to the data reported in Table 2.1 for thermal cracking, the light olefin yields are greatly dependent on the selected feedstock.

Furthermore, a Catalytic Pyrolysis Process (CPP) was also considered by RIPP of SINOPEC. The CPP is an extension of DCC. This process keeps the propylene production at a reasonable rate along with increasing the ethylene yield. The important key feature of this process is given by the new ZSM-5 catalyst which allows the catalytic reaction to be carried out at a significantly lower temperature in comparison to steam cracking. This process also favors the production of light olefins. A specially designed stripper located between the regenerator and reactor removes the flue gas carried over from the regenerator. Commercial trial runs were successfully completed in early 2001 in China using operating conditions favoring various product distributions. One should mention that the total yield of C_2 – C_4 olefins stays close to 46 wt% [6].

Finally, a process of oxidative dehydrogenation of paraffinic hydrocarbons to olefins has been developed by Dow Chemical. In this partial oxidation catalytic process, paraffinic

hydrocarbons are contacted with surface bound oxygen in the presence of hydrogen. This is a partial oxidation reaction where oxidative dehydrogenation leads to olefin formation, and where complete oxidation combustion products (water and carbon oxides) are minimized. This is an “autothermal” process where the partially combusted feed provides the heat required by the endothermic overall reaction. The implementation of this process on a large scale has to be envisioned as a fluidized bed operating slightly above minimal fluidization. Under these conditions, less methane and carbon oxides are formed and the production of ethylene is maximized. Selectivity to olefins has been, however, low while compared to thermal cracking due to substantial amounts of carbon oxides formed. Conversion of 70% with an ethylene selectivity of about 82% were reported [23].

Table 2.2: Comparison between DCC and FCC processes [6].

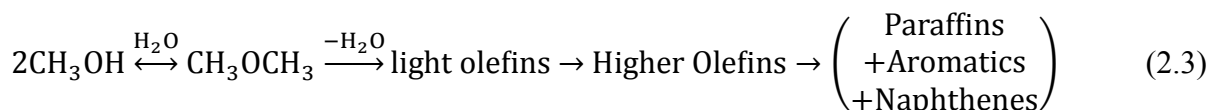
Process	FCC	DCC
Feedstock	A wide range of heavy oils	A wide range of heavy oils preferably paraffinics
Catalyst	Various types of Y zeolite	A modified pentasil structure zeolite
<u>Hardware:</u>		
Reactor	Riser	Riser and bed
Regenerator	Base	Similar
Main fractionator	Base	Higher vapor/liquid ratio
Stabilizer/absorber	Base	Bigger
Compressor	Base	Larger capacity
<u>Operating conditions:</u>		
Reaction temp.	Base	+30~50°C
Regeneration temp.	Base	Similar
Catalyst/oil ratio	Base	1.5~2 times
Residence time	Base	More
Oil partial pressure	Base	Lower
Dilution steam	Base	More

2.3.3 Methanol to Olefins Process (MTO)

The production of gasoline from coal or natural gas was the original target for developing the “methanol to hydrocarbons” technology over zeolites [26]. The advantages of light olefin production in the methanol to gasoline conversion process were established, as soon as the MTBE demand as a gasoline additive was reduced due to the new environmental regulations in the US. This motivated chemical companies to explore alternate and feasible utilization of their existing methanol plants. One interesting possibility which was identified was the conversion of methanol into gasoline (MTG) or into olefins (MTO) [22]. Regarding MTO, extensive studies were triggered by the discovery of the ZSM-5 catalyst (Zeolite Socony

Mobil)-5 by Mobil's research group (Chang and Silvestri) back in 1977 [10,22]. As a follow up to this discovery, a number of attempts were made to selectively form light olefins from methanol [27,28].

In the MTG process, which uses the HZSM-5 as a catalyst, methanol is first dehydrated to dimethyl ether (DME). The equilibrium mixture formed, consisting of methanol, dimethyl ether and water, is then converted to light olefins. In the last step of this process, the light olefins can react to form paraffins, aromatics, naphthenes and higher olefins via hydrogen transfer, alkylation and polycondensation [17,22,25,27,29,30]. Thus, the following overall scheme can be used to describe the conversion of methanol to hydrocarbons:



The industrial MTO process over a ZSM-5 zeolite catalyst, is based on synthesis gas being converted to methanol and di-methyl ether, was demonstrated by Mobil and Lurgi [27,31]. One could mention in this respect, a new Norsk Hydro process which converts methanol-to-propylene over SAPO-34 zeolite [2,27,28].

2.3.3.1 MOBIL MTG and MTO Process

The Mobil MTG and MTO processes have been demonstrated in a pilot plant of 4000 ton/year capacity in Wesseling (Germany) using a HZSM-5 catalyst [27,28]. A simplified scheme of the entire plant is reported in Figure 2.8. Crude methanol is vaporized and fed to the reactor that is operated at a pressure between 2.2 and 3.5 barg and a temperature of about 500°C. The catalyst is continuously withdrawn and regenerated by partially burning off the coke to achieve steady state operation. The rate of catalyst circulation through the regenerator determines the average activity of the catalyst in the reactor. A bank of different cyclones returns the entrained catalyst powder from the reactor overhead back to the reactor bed achieving olefins yield of nearly 60% [27].

2.3.3.2 UOP/HYDRO MTO Process

The UOP/HYDRO Methanol-to-Olefins (MTO) process represents advancement over the MOBIL's MTO technology. This process uses a new zeolite based on SAPO-34. In the 1980s, scientists at Union Carbide discovered SAPO-34, silicon, aluminum and phosphorous based molecular sieve. SAPO-34 was found to be an excellent catalyst for conversion of methanol to ethylene (48%) and propylene (33%) producing high yields of both. This catalytic process had the flexibility of varying the ethylene/propylene ratio by tuning reaction conditions [27,28,32-34]. Figure 2.9 reports a simplified flow scheme of the UOP/HYRO MTO process. In this diagram, evaporated methanol is being fed directly to the fluidized bed reactor, which is operated in the temperature range of 350-525°C and pressure of about 1-3 barg.

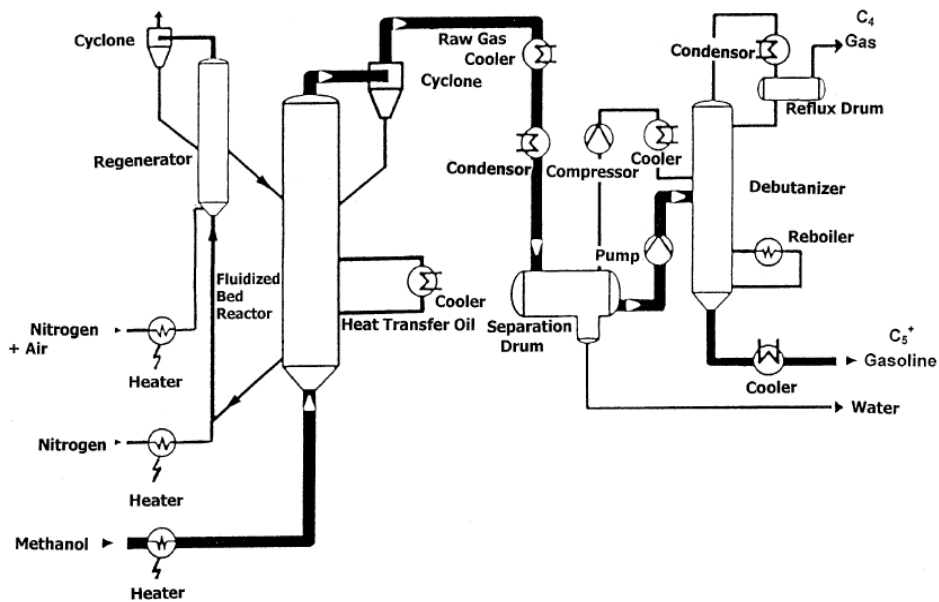


Figure 2.8: Fluid-bed MTG and MTO demonstration plant [27].

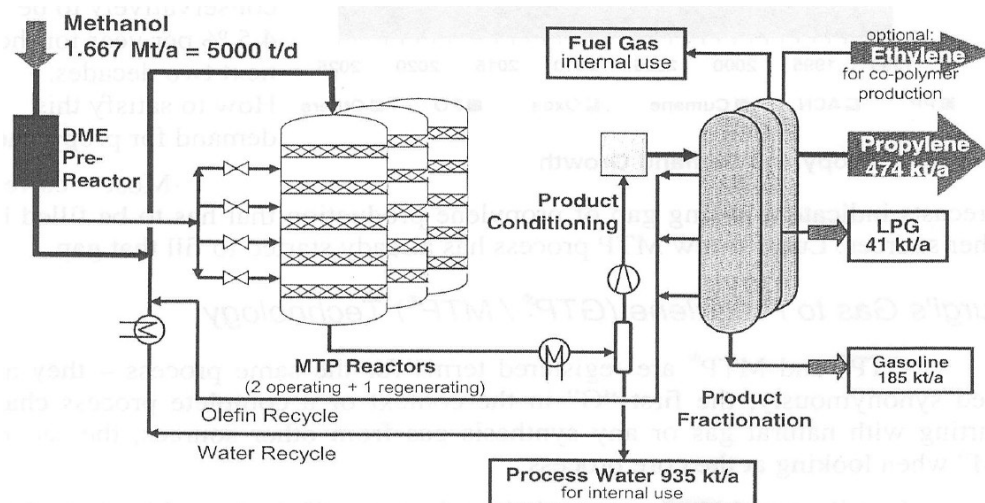


Figure 2.10: Lurgi MTP Simplified Process Flow Diagram [31].

This catalytic process is based on using an HZSM-5 zeolite, a 0.5-1 barg total pressure and a 350-500°C temperature [17]. Methanol/DME are both fully converted [31], with propylene hydrocarbon yields of 65% [26].

Figure 2.10 reports a schematic flow diagram of the Lurgi's MTP process. Vaporized methanol is first directed to an adiabatic DME pre-reactor where some of the methanol is converted to dimethyl ether (DME) and water. The methanol/water/DME mixture along with the recycled olefins and water are fed to three MTP reactors. Typically, two of these reactors are in an "active" cycle (on line) producing olefins, paraffins and gas oil while the third is in a "passive" cycle (stand by) with the catalyst being regenerated.

2.3.4 Dimethyl Ether to Olefins (DTO)

DME is proving to be a valuable chemical for petrochemical processes [8]. DME is a useful intermediate for the preparation of many specialty chemicals, including methyl sulphate from which dimethyl sulphate (DMS), oxygenates ethers, acetaldehyde, methyl acetate, acetic acid, ethylene glycol, etc are produced [35]. As already mentioned in section 2.3.3, DME is also an essential intermediate in the synthesis of light olefins from methanol. Hence, the synthesis of light olefins from DME is one of the potential routes to olefins to be considered in the near future.

In this respect, the successful manufacture of light olefins ($C_2^- - C_4^-$) by selective dehydration of methanol has attracted researcher attention in recent years [13]. Two possible routes for the synthesis of light olefins from syngas can be considered. The first one includes DME synthesis from syngas via a methanol dehydration step according to the following equation:



Thus, methanol can be considered as a reactant species leading to olefin production. In this respect, many studies have been developed using the well-known “methanol to olefin (MTO)” process. In this process, methanol is first dehydrated to dimethyl ether (DME). Once the equilibrium mixture is formed, consisting of methanol, dimethyl ether and water, these chemical species are then converted into light olefins.

A second alternative is the direct production of DME from synthesis gas in a single step:



Using this route, DME is available as a feedstock for olefin synthesis, or what is designated as the “DME to olefins” or DTO process. Using DME as a feedstock, instead of methanol for olefin production, has a number of advantages that can be summarized as follow:

1. *Higher Hydrocarbon Selectivity for DME Conversion.* Methanol can be converted almost completely into hydrocarbons following the stoichiometric $CH_3OH = [CH_2] + H_2O$ with 14 g-atoms of hydrocarbons and 18 g-atoms of water being formed. This means that at best, one can get 44 wt.% hydrocarbon selectivity with the rest being water. Using a similar analysis, in the case of DME conversion into hydrocarbons ($CH_3OCH_3 = [CH_2 \cdot CH_2] + H_2O$), 28 g-atoms of hydrocarbons and 18 g-atoms of water can be formed. As a result, the hydrocarbon selectivity can rise up to 61 wt% with the rest being water. Thus, at identical conditions, the selectivity towards hydrocarbons is 38% higher when using DME instead of methanol [18].
2. *Lower Equipment Costs.* The DME route to olefin production circumvents the need of a separate dehydration reactor [8,11,36,37], making possible substantial capital operating and maintenance cost savings.

3. *Reduced Thermodynamic Constraints.* In the case of methanol conversion, the water produced (Equation 1) promotes the forward water-gas shift reaction [8,11,18]. On the other hand, in the case of the DME production from syngas, the thermodynamic constraints for methanol conversion are removed, with this leading to a process requiring lower operating pressures and yielding 90 % CO conversions. This ends up reducing capital cost by 5-8 % and operating costs by 5 % [13,35,36,38,39].
4. *Lower Exothermicity.* Since DME eliminates an exothermic dehydration step, the DTO reaction releases only 77.5% of the heat of reaction of methanol conversion. Kolesnichenko et al. [16] compared the light olefin production from DME using a modified HZSM-5 catalyst with the data of a commercial MTO process over a ZSM-5 catalyst at 450°C. It is shown that higher olefin selectivity (90 wt%) with a stable catalyst activity (700 hrs) can be achieved at a lower temperature (340°C). Thus, heat control in the DME conversion process is better.
5. *Lower H₂/CO Ratio for DME Synthesis.* Synthesis gas contains CO, CO₂ and H₂. DME can be produced with an H₂/CO = 1 (Equation (2)) instead of an H₂/CO = 2 (Equation (1)), in the case of methanol synthesis. As result, a lower total pressure is adequate for DME synthesis. This lower H₂/CO entails significant equipment and energy savings and increases the use of a syngas feedstock. All this can be accomplished if one keeps CO₂ concentration as low as possible. This is given the water-gas shift influence on the DME synthesis process [40].

Despite the economic attractiveness of light olefin synthesis from DME, research work in this area is still in its early stages [41]. Currently, JGC/ Mitsubishi DTP market the only technology available to manufacture high yield of propylene via one step DME synthesis from syngas. The development of the JGC/ Mitsubishi DTP process is ongoing since 2007. This research is being made by JGC jointly with Mitsubishi Chemicals [42].

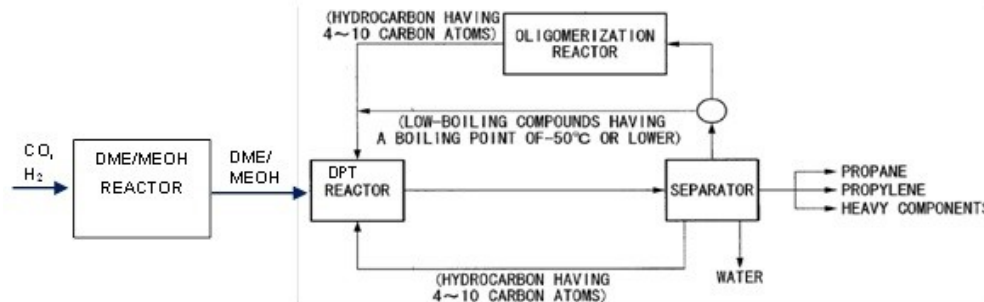


Figure 2.11: JGC/ Mitsubishi DTP Simplified Process Flow Diagram [41,43].

Figure 2.11 highlights the flow diagram for the JGC/ Mitsubishi DTP process. DME and/or methanol are synthesized from $\text{CO} + \text{H}_2$ in the oxygen-containing compound synthesis reactor [41]. Then, the produced DME and methanol are mixed with the recycled $\text{C}_4\text{-C}_{10}$ hydrocarbons. Following this, they are fed to the DPT reactor over Ca promoted HZSM-5 at 350-600 °C, 1-10 bargs, and WHSV of 0.025-50 $\text{g}_{\text{DME}}/\text{g}_{\text{Cat}}/\text{hr}$. The DPT reactor can be a fixed bed, a fluidized bed, or a moving bed type. Regarding this step, one should mention that the lower the reaction pressure, the higher the propylene selectivity. Different examples have been described in the JGC patent [43], where DME is equimolarly diluted using different amounts of steam, methane, ethylene, or nitrogen. The examples provided show a DME conversion of almost 100% with propylene yields of 40%. Late in 2009, JGC announced the completion of this research and the construction of a pilot plant to validate their process [42].

2.4 Dimethyl ether to Olefins (DTO). A Literature Review

2.4.1 Introduction

Research concerning light olefin yields from DME is a relatively recent area of study. It only started to be considered in the last 15 years. Examples can be found in a number of citations [8,11–16,26,29,35,44–48]. However, in reviewing the open literature, one cannot find any article regarding the state-of-the-art DTO. Some highlights of the DTO process are reviewed as going to be detailed in the upcoming subsections.

2.4.2 DTO Catalysts

According to the published literature, zeolite-type materials are generally considered as favorable catalysts for the DTO reaction as it is closely related to the MTO reaction. This is the case given the fast equilibrium reaction between methanol, DME, and water. Despite the differences between MTO and DTO systems, ZSM-5 and SAPO-34 catalysts that were previously considered for MTO were found to be promising for DTO reaction [9,10] as well. Reported efficiencies were, however, different.

The ZSM-5 zeolite is an aluminosilicate material with an inverted mordenite structure (MFI). The ZSM-5 zeolite provides a two-dimensional channel network of intersecting microchannels with a 5-6 Å size [49–52]. The ZSM-5 precursor zeolites can be represented by the $\text{Na}_n\text{Al}_n\text{Si}_{96-n}\text{O}_{192}\cdot\text{H}_2\text{O}$. The “n” parameter is consistently smaller than 27 being typically close to 3. The Na^+ cations in the precursor zeolite can be removed from the ZSM-5 via ion-exchange and replaced by H^+ . This yields zeolites in their protonic form, i.e. HZSM-5 [51]. Regarding the $\text{SiO}_2/\text{Al}_2\text{O}_3$ ratio, it plays a major role in both the HZSM-5 physicochemical and reactivity properties [49,51,53–58]. The structure of ZSM-5 is a crystalline phase. It contains two perpendicularly intersecting channel systems formed by 10-ring oxygen: a straight channel of slightly elliptical shape running parallel to plane (010) with openings of 0.51×0.55 nm, and other zigzag sinusoidal channels parallel to plane (100) with circular windows of 0.54×0.56 nm [30,51]. It is believed that the active sites are located in the free space at the intersections that have square opening of 0.9 nm [51]. A simplified diagram of face (100) and channel systems of ZSM-5 is shown in Figure 2.12.

The HZSM-5 can be used for molecular sieving [59,60]. Thus, only reactant molecules with a kinetic diameter smaller than the HZSM-5 channel openings can access the zeolite pore network. Admitted molecules can be adsorbed and eventually be converted on the zeolite acid sites [30,52,53,59–62]. An alternative selectivity effect is the so-called product selectivity. Bulkier product molecules that cannot diffuse out of the pore network are being either converted to smaller molecules or accumulated as coke causing eventual pore blockage [30,60,61].

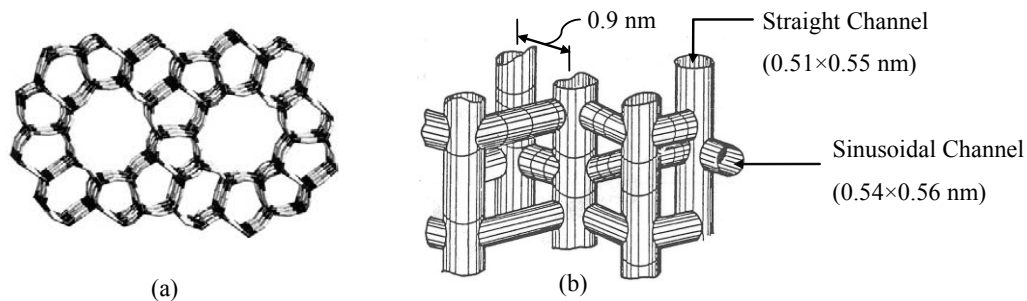


Figure 2.12: ZSM structural diagram (a) face (100) [63] (b) Channel system [30].

SAPO-34 is a silicoaluminophosphate microporous zeolite with the chabazite (CHA) type framework and a small pore size of 0.43 nm [51,64]. The SAPO-34 composition encompasses a range of $0-0.3R \cdot (\text{Si}_x\text{Al}_y\text{P}_z)\text{O}_2$, where R represents tetra-ethyl-ammonium ion template and x, y, and z parameters ranging from 0.01 to 0.98, 0.01 to 0.60, and 0.01 to 0.52, respectively, with $x + y + z = 1$ [64]. The chabazite structure is built on the basis of six double rings arranged in layers and forming one cavity per unit cell. Each cage has six octagonal, twelve quadrilateral, and two hexagonal windows [22,51,65]. Figure 2.13 shows a simplified illustration of the SAPO-34 structure. Figure 2.13-a shows the interconnection of cages where each cage is connected to six others through octagonal openings of 0.44×0.31 nm. Figure 2.13-b expands the view of one cage that has dimensions of 1×0.7 nm [22,65].

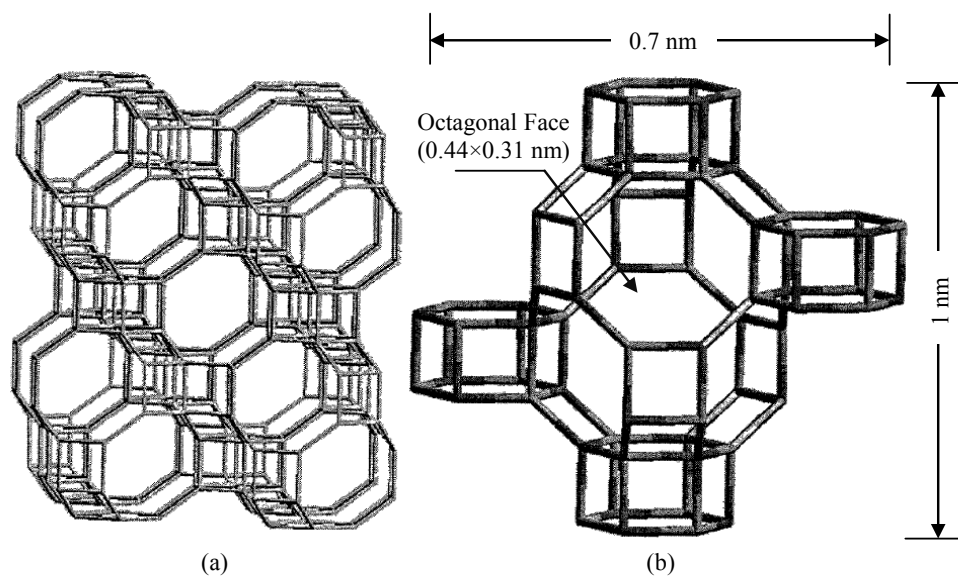


Figure 2.13 SAPO-34: structural diagram (a) Cage interconnections (b) One cage dimensions [65].

2.4.3 DTO Catalyst Performance

In the DME conversion to light olefins (DTO), the catalyst performance is assisted by DME conversion, selectivity to light olefins (C_2^- - C_4^-), and durability (life time). The performance of a DTO catalyst over prolonged operating times is one of the key indicators for selecting the DTO catalyst for industrial applications. The catalyst life time is an essential factor for designing the reaction area in the DTO process ensuring stable plant operation. As a result, if the DTO catalyst can continue to be active up until the plant annual turnaround then a tubular type reactor would be the first choice for reactor selection. Furthermore, if the catalyst has a long enough life time to allow complete regeneration, without frequent plant disturbances, then selecting two tubular reactors running interchangeably is feasible. However, if the catalyst deactivates quickly, continuous regeneration is necessary and the circulating fluidized bed reactor is the best option. In this respect, it is valuable to establish catalyst durability as a parameter related to the catalyst activity decay. This parameter is defined as the period from initiation of catalyst utilization until the time the feedstock conversion starts declining.

The DTO reaction system development has benefited from the knowledge and experience on MTO reaction studies. As a result, one can notice early demonstrations with excellent catalyst performance.

Best performances are reported for different DTO reaction systems in Table 2.3. The operating conditions include DME dilution level, gas hourly space velocity (GHSV), reaction temperature and pressure. The DME was diluted with an inert gas (mainly N_2) from a level of 6.4 to 100 vol% (neat DME). Feed gas hourly space velocity (GHSV) changed with the unit used. It varied from 3.5 to 27.6 $g_{gas}/(g_{cat} h)$ and from 1000 to 2000 $liter_{gas}/(liter_{cat} h)$. The reaction temperatures considered, varied from 340 – 530°C while the reaction pressure was maintained at 1 barg in all the cases. One can notice that DME conversion was almost complete in all the studies reported. However, light olefin selectivity changed for different catalytic systems in the 64 to 93 wt% range. One can notice a 63 C-mole % [14] and 64 C-mole % [9] reported for light olefins selectivity. A C-mole % selectivity is calculated by relating the number of moles for the carbon atoms in the product to total number of the

carbon moles of the species being produced. Catalyst life and selected reactor type were directly related to the catalyst selected with this either being an HZSM-5 or an HSAPO-34. One can notice that from the 11 references cited, three studies used an HSAPO-34 catalyst while the eight others used an HZSM-5 catalyst.

Table 2.3: Catalyst performance for DTO reaction.

Catalyst components	Rxr type	Feed (vol %)	T (°C)	P (barg)	GHSV (h ⁻¹)	Life time (h)	DME Conv. (%)	Sel ^a C ₂ ⁼ (wt%)	Sel ^a C ₃ ⁼ (wt%)	Sel ^a C ₂ ⁼ -C ₄ ⁼ (wt%)	Ref.
Hierarchical nanostructured SAPO-34 (polyethylene glycol/triethylamine =0.1)	Fixed bed	100% DME	450	1.2	DME/cat = 0.8 (mol/mol)	-	99	46	35	93	[66]
SAPO34/11% ZrO ₂ (binder)	Fixed bed	DME(25%) + N ₂	400	1	3.5 (g _{gas} /g _{Cat} /h)	6	100	23	36	81	[67]
La-Zr modified HTsVM (HZSM-5 analog)/ Al ₂ O ₃ (18wt%)	Fixed bed	DME (20%) + N ₂	360	1	2000 (l _{gas} /l _{Cat} /h)	-	98	29	49	89 ^b	[13]
Supported SAPO-34 (14 wt% SAPO-34/a-Al ₂ O ₃ (filler), silica (binder) composite)	Fluid bed	DME(14%) + N ₂	450	1	4.2 (g _{gas} /g _{Cat} /h)	1	100	35	35	-	[44]
Zn- modified HTsVM (HZSM-5 analog) / Al ₂ O ₃ (binder)	Fixed bed	DME (20%) + N ₂ +water (trace)	400	1	1250 (l _{gas} /l _{Cat} /h)	19	93	48	30	83	[26]
CeO ₂ (35 wt%) - Ca modified HZSM-5 (SiO ₂ /Al ₂ O ₃ = 200, CaO/SiO ₂ = 0.025)	Fixed bed	DME (50%) + N ₂	530	1	19.04 (g _{gas} /g _{Cat} /h)	200	100	-	45	-	[46]
H ₃ PO ₄ /ZrO ₂ (12.5 wt%)/H-ZSM-5	Fixed bed	DME(17%) + N ₂	450	1	27.6 (g _{gas} /g _{Cat} /h)	30	100	3 ^c	45 ^c	63 ^c	[14]
Ca-B-P-modified HZSM-5 (Si/Al=250, Si/Ca=20, Si/P=400, Si/B=200)	Fixed bed	DME(90%) + N ₂	530	1	1000 (l _{gas} /l _{Cat} /h)	146	100	-	-	64 ^c	[9]
La-Zr-Rh modified HTsVM (HZSM-5 analog)/ Al ₂ O ₃ (18wt%)	Fixed bed	DME(10%) + CO (30%) + H ₂	340	1	2000 (l _{gas} /l _{Cat} /h)	700	96	32	48	90	[16]
Ca modified HZSM-5 (Si/Al=100, Si/Al=3.7)	Fixed bed	DME (50%) + N ₂	530	1	4.8 (g _{DME} /g _{cat} /h)	254	100	-	-	79	[12]
Ca modified HZSM-5/ Boehmite binder (10:3 wt ratio)	Fixed bed	DME(17%) + N ₂	400	1	1440 (l _{gas} /l _{Cat} /h)	36	100	10	26	64	[15]

^a HC selectivity, ^b C₂⁼-C₅⁼ olefins selectivity, ^c C-mole%.

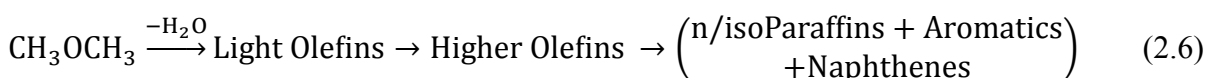
Note: (-) means no information.

Regarding the HZSM-5 catalyst reported as having a long time-on-stream (up to 29 days), one can observe that it is a good catalyst to be used in the pellet form in fixed bed reactors. Conversely, the HSAPO-34 exhibits quick deactivation, making frequent regeneration a necessary step. This limits its application to circulating fluidized bed reactors. However, a recent report claimed 6 h of durability for a SAPO-34 catalyst with a ZrO₂ binder. It appears that a 6 h cycle is still short to justify a two fixed-bed reactor system, with one reactor being in operation and the other regenerating the catalyst.

One should also mention that even though the HSAPO-34 has been established for olefin synthesis from methanol, some difficulties have arisen when it is used in DTO applications. Chen et al. [48] studied the DTO reaction over hydrothermally treated HSAPO-34 using both fixed bed and fluidized bed reactors. These authors reported a quick drop in DME conversion in both reactors. The same findings were reported also by Zhou et al. [44] and Chen et al. [68] when investigating DTO using SAPO-34. The reason for the fast deactivation of HSAPO-34 was attributed to its cage dimensions being of 0.43 nm pore size. This size is smaller than the kinetic diameter of branched paraffins, olefins and aromatic molecules, but large enough to allow the access of linear paraffins and olefins molecules [22,48,51,63]. However, when these larger size species are trapped inside the HSAPO-34 pores, they may cause diffusional hindrances with species being prevented to leave the HSAPO-34 pore network. As a result, HSAPO-34 deactivation by coke has been found to be more severe in DTO than in MTO [9,68]. On the other hand, utilizing HZSM-5 would benefit from its larger cage sizes making it a more suitable zeolite.

2.4.4 Conversion of DME to Light Olefins over HZSM-5

The synthesis of hydrocarbons from DME is a combination of consecutive reactions where the first reaction helps in converting DME into light olefins. Light olefins may continue to react to form heavy olefins, normal-/iso-paraffins, naphthenes and aromatics [8,11,14,17,26,48]. Thus, the DTO overall reaction scheme can be represented by [17]:



It is a primary objective during the design of the DTO catalytic process to select the optimum parameters that lead the light olefins to desorb from the active catalyst surface before they are further transformed. These parameters are either related to catalyst properties or to the reaction conditions.

While, in our view, it is difficult to establish operational strategies that can be applied to every DTO reaction system; it is our intent to review the technical literature to identify key parameters that have been found to influence the olefin selectivity in the DTO reaction.

2.4.4.1 Catalyst acidity

The acidity of the HZSM-5 catalyst is a main catalyst property with significant influence on the reaction pathways and product distribution. Thus, controlling the acid properties is among the key techniques to inhibit the olefins conversion.

Acid properties of the HZSM-5 catalyst include total acidity (density) and acid strength. There are two types of acid sites contributing to total acidity: Brønsted (proton donor) and Lewis (electron-pair acceptor) acidities. The former is related to the protons belonging to the structural OH-groups of the zeolite associated with the Al-O-Si binding oxygen. If this structure is heated, Brønsted acid sites can be dehydroxylated reversibly forming Lewis acid sites. Lewis acid sites are incomplete coordinated Al-species as shown in Figure 2.14 [30,51]. One should mention that the contribution of Lewis acidity in the conversion of hydrocarbons from methanol was found to be minor in comparison to Brønsted acidity [51].

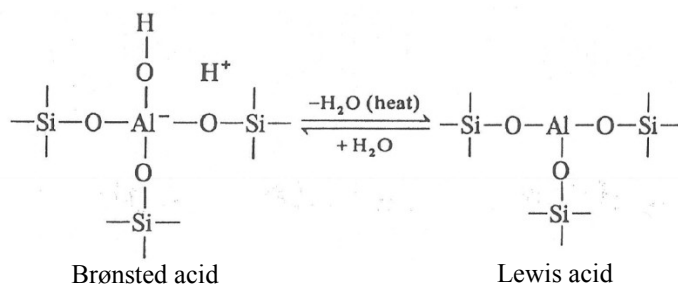


Figure 2.14: Proposed reversible conversion of Brønsted acid to Lewis acid [30].

The role of HZSM-5 acidity on light olefins formation in the DTO process has been the subject of several investigations. In this respect, there is agreement, that the decrease in total

acidity limits the olefin consumption, in which weak/strong acid ratio are assigned a major role [13,14,17,35,47]. As a result, the reduction of HZSM-5 acid sites is critical. In order to achieve this, the following approaches are reported as follows:

- **HZSM-5 modification:** HZSM-5 can be modified by inclusion of metallic and/or non-metallic elements. Table 2.3 reports DTO catalyst performance using metallic promoters like La, Zr, Zn, Ce, Ca, and Rh and/or non-metallic promoters such as B and P. One should mention that the studies reported in Table 2.4 show favorable effect of included promoters on HZSM-5 acidity. In fact, weakening acid site strength reduces acid density leading to a better performance of the promoted HZSM-5 compared with the HZSM-5 free of promoter.
- **SiO₂/Al₂O₃ ratio:** There is a linear correlation between the Al-content of the ZSM-5 and its acidity. In addition, varying the Si/Al-ratio can influence the methanol/DME reaction path [51]. Benito et al. [54] measured the change in acidity spectrum at different Si/Al molar ratios of HZSM-5. These authors reported that HZSM-5 total acidity is reduced and weakened with increasing Si/Al ratios. Additionally, the rise in the Si/Al yields an increased Brønsted/Lewis acid site ratio [54]. Furthermore, the influence of the SiO₂/Al₂O₃ ratio on the extent of olefin conversion in the DTO reaction may vary. This is based on the selected SiO₂/Al₂O₃ ratio range. Sardesai et al. [8,11,18,45] investigated the influence of changing SiO₂/Al₂O₃ within a molar ratio range of 30 to 150 for DTO. This author reported that the sample of SiO₂/Al₂O₃ = 30 yielded after 10 h of TOS, 7.41 wt% coke with a reduction in C₂⁼ - C₄⁼ selectivity down to 13 wt%. Moreover the sample with a SiO₂/Al₂O₃ = 150 molar ratio gave lower coke (3.4 wt%) with a stable conversion over 60 h TOS and a 61wt% C₂⁼-C₄⁼ selectivity. To further consider this matter, Omata et al. [9] extended the range of the SiO₂/Al₂O₃ ratio to cover the 100 to 1600 range in their DTO reaction study using Ca-HZSM-5. These authors reported that initial C₂⁼-C₄⁼ selectivity was 54 C% for a SiO₂/Al₂O₃ =100. The initial conversion was, however, 63 C% for a SiO₂/Al₂O₃ =200 during the first 25 h of time-on-stream. It was reduced, however, to a 53 C% during the first 5 h of time-on-stream for the SiO₂/Al₂O₃ = 1600 catalyst sample. As a result one can conclude that the higher the SiO₂/Al₂O₃ ratio, the higher light-olefin selectivity and catalyst life time. This trend is true until acid sites are drastically reduced and there is not, as a result, adequate DME transformation.

Table 2.4: Effect of promoters on HZSM-5 acidity and performance in DTO reaction

Catalyst	HZSM-5 before modification					HZSM-5 After modification					Ref
	Total acidity ($\mu\text{mol}_{\text{NH}_3}/\text{g}_{\text{cat}}$)	$\frac{W^a}{s}$	TOS (h)	DME Conv. (%)	Sel $\text{C}_2^=-\text{C}_4^=-$ (wt%)	Total acidity ($\mu\text{mol}_{\text{NH}_3}/\text{g}_{\text{cat}}$)	$\frac{W^a}{s}$	TOS (h)	DME Conv. (%)	Sel $\text{C}_2^=-\text{C}_4^=-$ (wt%)	
HTsVM (HZSM-5 analog)/ Al_2O_3 binder (18 wt%)	757	0.6 7	-	75.3	$\text{C}_2^=-\text{C}_5^=-$ 45.4	611	0.83	-	97.8	$\text{C}_2^=-\text{C}_5^=-$ 88.6	[13]
HZSM-5 / Al_2O_3 binder (23 wt%)	757	0.6	3	67.4	44.7	585	0.8	3	77	65.4	[35]
Ca modified HZSM-5 ($\text{SiO}_2/\text{Al}_2\text{O}_3 = 200$, $\text{CaO}/\text{SiO}_2 = 0.025$)	117	-	40	100	$\text{C}_3^=-$ = 40	24	-	200	100	$\text{C}_3^=-$ = 45	[46]

Note: (-) means no information.

^a weak/strong acidity ratio.

2.4.4.2 Catalyst porous structure

One of the most important features of the zeolite framework is its ability to act as a molecular sieve. Three types of shape selectivity can occur: reactant shape selectivity, product shape selectivity, and transition state shape selectivity. These three types of shape selectivity are determined by whether reactants can enter, products can leave, or intermediates can be formed in the zeolite catalyst. ZSM-5 zeolites have been shown to have excellent transition state shape selectivity, given the existence of two types of intersecting channels with the following occurring: a) reactant molecules preferentially diffusing in through a first class of channels, b) products diffusing out through a second class of perpendicular channel, so that counter-diffusion limitations are avoided [51].

In the case of the DTO catalyst, designing a porous structure that allows the diffusion of DME and cause the formed light olefins to desorb and diffuse out to the reaction bulk, is of critical value [17]. The precursor HZSM-5, as such, has a certain topology that cannot serve this purpose completely. Thus, the addition of a promoter which would serve the goal of selectively producing light olefins is required. For example, in the work by Zhao et al. [14,47], the incorporation of certain amounts of P and Zr to the HZSM-5 resulted in an increase in $\text{C}_2^=-\text{C}_4^=-$ selectivity from 40.1 C-mol% after 2 hrs to 63.1 C-mol% after 30 hrs operating time. When the authors measured the pore size distribution of the HZSM-5 before

and after modification, they found that the pore size of the P-Zr-HZSM-5 was reduced slightly from 5.5 to 5.3 Å while the pore volume shrank considerably from 0.047 to 0.025 ml/Å/g. According to Zhao et al. [14,47], the reduction in the modified HZSM-5 pore volume was due to a uniform distribution of the promoter molecules along the inner surfaces that impaired larger hydrocarbons formation.

2.4.4.3 DME residence time

The influence of the DME residence time shall include both the outside catalyst (interparticle) and the inside catalyst (intraparticle) phenomena. Given that the DME conversion follows an “in series” reaction network; one can expect high DME conversion with high selectivity at specific residence times.

The interparticle space residence time, or what is more commonly designated as space time (τ), represents the time that the reactants are in contact with the outer pellet catalyst surfaces. The space time is determined by dividing the catalyst interparticle bed volume (catalyst weight/bed apparent density and the bed porosity) by the volumetric flow rate of the feed gas. Therefore, either increasing the incoming feed flow (or space velocity at a fixed amount of catalyst) or reducing the catalyst amount would lower the interparticle space time. In addition, space velocities can be defined by using the inverse of space time.

In the MTO conversion on the HZSM-5 [51] catalyst, the $C_2^- - C_4^-$ yield was almost nil (0.16 wt%) at a high feed space velocity (14.3 mol_{gas}/(g_{cat} h)). This was also true for catalytic DME conversions close to zero. However, by reducing space velocity, olefins yields increased, up to a maximum of 15.9 wt% and 90.5 % DME conversion at 0.45 mol_{gas}/g_{cat}/h. Thereafter, DME conversion continued increasing to 100% with the olefin yield declining down to 1.2 wt% for a 0.014 mol_{gas}/g_{cat}/h contact time. Chang and Silvestri [69] studied the methanol to hydrocarbon conversion rates as a function of the space time from 6×10^{-4} h to 2 h. These authors reported complete conversion of oxygenates (methanol and DME) at 0.04 h contact times with $C_2^- - C_4^-$ selectivity attaining a maximum at 0.05 h. After this space time was reached, $C_2^- - C_4^-$ selectivity diminished at a higher space time. These authors also studied DME conversion to hydrocarbons using DME with no water addition. Interestingly, similar hydrocarbon trends (including light olefins) were observed as in the case of methanol

conversion. Omata et al. [9] selected a wider range of contact times from 550 to 8800 $\text{lit}_{\text{gas}}/\text{lit}_{\text{cat}}/\text{h}$ for the DTO reaction (10 vol% N_2) over a Ca-HZSM-5. These authors reported a $\text{C}_2^- - \text{C}_4^-$ yield of 56 C% at 550 and 1100 $\text{lit}_{\text{gas}}/\text{lit}_{\text{cat}}/\text{h}$, with a 100 C% DME conversion. The $\text{C}_2^- - \text{C}_4^-$ yield and DME conversion declined, however, at space times larger than 8800 $\text{lit}_{\text{gas}}/\text{lit}_{\text{cat}}/\text{h}$.

The intraparticle residence time is the time that the reacting molecules are in contact with the active sites inside the catalyst pores. The intraparticle contact time involves species diffusional distance and accounts for possible diffusion limitations. One can expect that at higher residence times, the diffusion of formed light olefins from active acid sites to the bulk phase, is hindered, thereby promoting their further conversion. Thus, one can conclude that a way to reduce the intraparticle residence time is to reduce the HZSM-5 crystallite size. In this respect, the dependence of DME conversion and $\text{C}_2^- - \text{C}_5^-$ selectivity on particle size was investigated by Birykova et al. [35] using a La-Zr-HZSM-5. These authors reported stable DME conversion and olefin selectivity over a range of 1.3 – 6 mm particle sizes. They, therefore, concluded that the DME conversion occurs in the reaction control regime with no internal diffusional transport affecting the DME reaction rate.

Another possible approach to reduce the residence time effect is to increase the feed flow (or space velocity at a fixed catalyst mass). This facilitates the transport of the formed olefins away from the catalyst and thus prevents their transformation into hydrocarbons with a higher carbon number.

2.4.4.4 Reaction temperature

Reaction rate constants dependence with the temperature, and thereby, the rate of a chemical reaction can be described using the Arrhenius equation. As DTO is an exothermic reaction not controlled by chemical equilibrium, DTO provides thermal energy for higher temperatures and increased DME conversion.

However, if one targets the maximum catalyst performance for DTO, temperature increases have to be limited to control coke formation. Coke reduces olefin selectivity and catalyst time-on-stream. In this respect, studies related have considered the temperature effect on

DTO while using an HZSM-5 catalyst. Authors agreed, in this respect, that DME conversion augments with increasing thermal levels. However, the extent of the secondary reactions varied with the temperature range and the DTO catalyst used. Zhao et al. [14,47] investigated the DTO reaction over a Zr-P-HZSM-5 catalyst. These authors pointed out that lowering the temperature from 450 to 250°C reduced DME conversion from 100 to 8.6% while C₂[≡]-C₄[≡] selectivity was improved from 64.6 to 75.2 C-mole%. Birykova et al. [35] investigated the influence of changing the temperature, on the performance of a La-Zr-HZSM-5 catalyst in the 320–360°C range. Their data agreed with Zhao's results, in which DME conversion increased to 100%. At higher temperatures with selectivity for C₂[≡]-C₅[≡], on the other hand, decreasing from 75.7 to 44.1 wt%. This was also accompanied with an increase in the production of the alkanes. Thus, these authors concluded that the rate of the secondary reactions increases at higher temperatures. Abramova et al. [17,26] described two different potential effects of temperature. These authors examined DME conversion and C₂[≡]-C₄[≡] selectivity from 350 to 450°C using both the parent and the Zn-, Fe-, and Co-HZSM-5 modified catalyst. While DME conversion was completed in the entire temperature range studied, the yield of light olefins increased slightly and peaked at 400°C. Thereafter, C₂[≡]-C₄[≡] selectivity decreased for all catalysts except for the Zn-containing catalyst. These authors attributed these findings to the reduced intensity of the cracking of the formed light olefins at temperatures above 400°C. Similar observations were reported by Kolesnichenko et al. [16], in which light olefin selectivity peaked at 75% from 23% when temperature was augmented from 240 to 320 °C. Olefin selectivity was, however, reduced back to 50% at 340 °C. DME conversion, on the other hand, showed a steady and proportional increase with temperature.

2.4.4.5 Reaction time-on-stream (TOS)

The extent of the DTO secondary reactions differs within TOS (time-on-stream) depending on the catalytic system used as follows:

- In DTO catalytic systems, a significant amount of coke may be formed during the initial stages of catalyst time-on-stream. One can expect, under such conditions, significant catalyst activity decay. This activity decay by coke, was not, however, observed when using HZSM-5, but seen when using HSAPO-34 as described in section 2.4.3.

- In DTO, design and operation parameters have to be selected carefully to suppress undesirable olefin conversion. For example, Zhao et al. [14,47] compared C₂=-C₄= selectivity after 2 and 30 hrs TOS for DME conversion on a Zr-P-HZSM-5 catalyst. These authors found that 30 hrs of continuous reactor operation affected neither the DME conversion (100%) nor C₂=-C₄= selectivity (64.6 mole% with 2 hrs TOS, 63.1% with 30 hrs TOS).
- In DTO, enhancements in the structural features of the zeolite framework can be used to improve olefin selectivity. An example is the study of Abramova et al. [26]. These authors modified HZSM-5 with Zn, added traces of water (H₂O/N₂=2×10⁻³) to the feed keeping a DME/N₂ of 1/4 at 400°C, 1 barg of total pressure at 1250 lit_{gas}/lit_{cat}/h contact time. Under these conditions, these authors reported a continuous increase of C₂= - C₄= selectivity from 52.6 to 82.47 wt% during 1- 19 h of operation. These authors argued that the observed effect was due to the change in the structural characteristics of Zn-HZSM-5.

2.4.4.6 DME partial pressure

As indicated earlier in section 2.4.3, DTO conversion under diluted DME leads to good catalyst performance. However, using pure or highly concentrated DME was found to enhance some DME secondary reactions [10,11,17–19]. For instance, reducing the DME partial pressure has a positive effect on depressing the olefin transformation. This was attributed to the lesser DME availability for further olefin conversion [18]. Thus, it appears that selecting the proper diluent species at appropriate dilution levels is vital to making the process economical. In view of this, the following suggestions are given while selecting the diluent species and its concentration:

1. The diluent should not impact the overall catalyst performance.
2. The price, abundance, and continuous availability of the diluent gas should be such, that there is no negative influence in the process economics.
3. The boiling temperature of the diluents should be different from that of the DME and its products. This will make the recovery of the diluent easy to be implemented. In addition, the diluent recycling system should be designed carefully to recover the diluent without compromising the product purity.

4. The selected diluents should be environmentally friendly.

In this respect, many single and mixed gases with different compositions have been examined for DME dilution. All the considered diluents have been proven to reduce the DME partial pressure. Furthermore, authors have explored side effects on the catalyst performance. In the following section, the influence of different DME diluents is reviewed as follows:

- **N₂ diluent:** In most of the DTO studies, DME partial pressure is reduced using N₂. It can be noticed that out of the eleven DTO systems listed in Table 2.3, nine of them have used N₂ as diluent. N₂ usage fulfills the criteria mentioned above, being an inert gas for DTO reaction, economically viable, easy to separate, and environmentally friendly. However, as the DME reaction is strongly affected by DME partial pressure, the dilution has to be optimized to achieve feasible light olefin yields. In this respect, the expected improvement in light olefin yields with the reduction of DME partial pressure was confirmed by Sardesai et al. [8,11,18] and Omata et al. [9]. Furthermore, in certain studies [11,13,15,17,35], N₂ has been used as a benchmark to assess side effects of other diluents.
- **CO₂ diluent:** Different effects have been reported for CO₂ as a diluent and this depends on the DTO catalytic system used. Jian-ming et al. [15] examined the Ca-HZSM-5 efficiency in the DTO reaction using various DME diluents. These authors reported a positive enhancement by CO₂ dilution in term of olefin yields and catalyst stability. These improvements were explained, assigned them to the possible removal of deposited coke, via $C+CO_2 \rightarrow 2CO$. These authors supported their assumption about the CO₂ influence by tracking the CO composition in the tail gas (H₂, CO, CO₂, CH₄) at the reactor outlet using N₂ and CO₂ as diluents. In another study by Sardesai et al. [11], it was found that a CO₂ diluent has no side effects when compared with a N₂ diluent, within the 30-75 vol% dilution range over HZSM-5 (SiO₂/Al₂O₃ = 280) at 400°C and 1 barg. In contrast, experiments performed by Kolesnichenko et al. [13], showed a slightly negative effect when CO₂ replaced N₂. DME conversion was reduced from 97.8 to 89.4 %. Similarly, C₂⁼ - C₅⁼ selectivity was decreased from 88.6 to 80.7 wt%.

- **H₂O diluent:** Water vapor can be used as an alternative for reducing DME partial pressure. In this respect, Jian-ming et al. [15] reported that HZSM-5 showed an activity decline under a steam atmosphere of 94 to 80% within 8 h of operating time. One possible explanation is that DME is being used additionally as a reactant to produce methanol at high water concentrations. Therefore, the equilibrium of DME hydrolysis to methanol is shifted in the direction of methanol formation.
- **Syngas (CO+H₂) diluent:** Jiang-ming et al. [15] reported similar dilution effect of DME with CO as with N₂. However, when CO and H₂ are used as a syngas, the authors observed an increase in ethane and propane selectivity. This was at the expense of the ethylene and propene, with the DME conversion remaining stable. In addition, these findings showed that the presence of hydrogen may promote hydrogenation of light olefins to light alkanes. Furthermore, Kolesnichenko et al. results [13] agreed with Jian-ming's findings in which DME concentration was lowered to 20 vol% syngas and N₂ using La-Zr- HZSM-5, 360°C, 1 barg, 2000 liter_{gas}/liter_{cat}/h feed space velocity, and complete DME conversion. This was accompanied with C₂⁼ - C₅⁼ selectivity being reduced from 88.6 to 46.7 wt% and C₂- C₅ alkanes selectivity increased from 8.7 to 52.6 %. Kolesnichenko et al. [16] attained, however, different results when comparing the 90 vol% dilution of DME by He and syngas over La-Zr-Rh-HZSM-5 at 340°C, 1 barg, and 2000 lit_{gas}/lit_{cat}/h feed velocity. When He was replaced by syngas (30% CO, 60 % H₂), light olefin selectivity was comparable at 87 - 90 % with DME conversion being increased from 73 to 96 % with 700 h durability. While these observations were valuable, these authors did not provide an explanation of this enhanced catalyst performance. A possible justification for this was Rh doping of the HZSM-5 [70].

2.4.5 Kinetic Modeling of DME Conversion to Olefins over HZSM-5

DTO is a complex reaction system that involves the production of a wide range of hydrocarbons from C₁ to C₁₂⁺. Each species may undergo some of the following reactions: methylation, hydrogenation, dehydrogenation, cracking, oligomerization, and condensation. Due to the high number of product species involved in the DTO process, it is a challenge to identify the way each component is produced and/or reacted. One possible approach is to apply a lumped reaction scheme that depends purely on empirical observations at which the

components that are kinetically similar are grouped into one family of chemical species or pseudo-species such as olefins, paraffins, naphthenes and aromatics. Following this approach, all reaction steps consider lumped chemical species.

Thus, the formulation of a detailed DTO reaction mechanism involves the specification of lump balances including either simple or complex set of consecutive reactions. One should notice that the lumped model is more common in reactor design since it is easier to develop than the detailed models involving individual chemical species. One should mention as well, that in a complex process such as MTO, involving elementary steps, while more rigorous in principle, may lead to kinetic model overparameterization [27,71,72]. Thus, one has to strike the delicate balance between rigorous and practical.

Regarding DTO reaction modeling studies over HZSM-5 one can consider them in the early stages. In this respect, most studies are still attempting to optimize the catalytic process. To our knowledge, there is no study in the technical literature addressing this topic and this is in spite of its great significance for DTO reactor scale-up. A good point to start is to propose a reaction scheme analogous to MTO over HZSM-5, for DTO. One should notice, however, that in the MTO reaction mechanisms, methanol is contributing to the production of the olefins and their condensation [22,27,51,73,74]. There are, however, some relevant aspects that could be retained such as the lumped species treatment, well validated for MTO and with the potential of being extended for DTO products.

Concerning the MTO conversion over HZSM-5, many reaction steps have been considered since its introduction by Mobil researchers in late 1970's. Kail [27] summarized the development stages of the MTO lumped models. This process was started with the studies made by Chen and Reagan [75], who assumed that the equilibrium oxygenates mixture (methanol, DME and water) could be grouped (lumped together) in a single pseudospecies with a fast reaction rate. These authors showed in this respect, the autocatalytic nature of the oxygenates with its rate of disappearance being enhanced by the oxygenate reaction with olefins. Accordingly, these authors proposed the following hydrocarbons (HC) model (water not involved) neglecting the effect of deactivation:



where A \equiv oxygenates, B \equiv olefins, G \equiv gasoline range hydrocarbons (aromatics + paraffins + naphthenes). Accordingly, the rate of oxygenates consumption are represented by:

$$\frac{dX_A}{d\tau} = r_A = -k_1X_A - k_2X_AX_B \tag{2.8}$$

where τ is the space time obtained, by dividing the catalyst weight by the methanol inlet mass flow ($\text{g}_{\text{cat}} \text{ h g}_{\text{MeOH}}^{-1}$). X_A and X_B are the water free hydrocarbons mass fractions (i.e with excluding the produced water) of oxygenates and olefins.

Chang [76] modified the scheme of Chen and Reagan by adding a step accounting for the carbene ($:\text{CH}_2$) insertion into the olefins:



where C \equiv CH₂ group.

By assuming all reactions to be first order and C formation to be in a steady state, Chang [76] formulate the following kinetic equations after incorporating the the correction by Anthony [77]:

$$\begin{aligned}
\frac{dX_A}{d\tau} = r_A &= -k_1X_A - k_2X_AX_C \\
\frac{dX_B}{d\tau} = r_B &= k_2X_AX_C - k_4X_B \\
\frac{dX_C}{d\tau} = r_C &= k_1X_A - k_2X_AX_C - k_3X_BX_C = 0
\end{aligned} \tag{2.10}$$

Sedran et al. [78] successfully validated the corrected model by Chang at a temperature range of 302-370°C using a gradientless Berty Reactor running in CSTR operation. Moreover, Schipper and Krambeck [79] considered the deactivation effect by introducing a catalyst activity parameter (a) in their simplified reaction kinetics. This parameter accounts both for the irreversible activity loss (a_{ir}) and the reversible loss by coking (a_r). Then, the rate of total activity loss is defined as:

$$\frac{da}{d\tau} = \frac{d(a_{ir}a_r)}{d\tau} = a_{ir} \left(-k_{dr}(a_{ir}a_r)^b - k_{dir}a_{ir}^{c-2}(a_{ir}a_r) \right); \quad b, c > 1 \quad (2.11)$$

Their proposed water free (i. e. considering hydrocarbons species only) reaction kinetics is:



Thus, the product lump rate (r_i) for the feed oxygenates and light olefins involves the fresh catalyst rate (r_{i0}) and the remaining catalyst activity (a) becomes:

$$\begin{aligned} \frac{dA}{d\tau} = r_A = ar_{A0} &= a(-k_1A - k_3AG) \\ \frac{dB}{d\tau} = r_B = ar_{B0} &= a(k_1A - k_2B^2 - k_4BG) \end{aligned} \quad (2.13)$$

Schipper's model was used in Mobil's MTG process simulation that employs an adiabatic fixed bed reactor working under a reaction-regeneration cycle.

Sedran et al. [80] proposed three water free kinetic models with a special focus on the individual light olefins (C_2^- - C_4^-) in a MTG reaction over an HZSM-5 catalyst at a 302-370°C range using Berty Reactor. The catalyst reversible deactivation was expressed by an exponential activity decay function that relates the decrease of the reaction rate constants to the total amount of hydrocarbons produced per catalyst weight ($\overline{Hc/W}$):

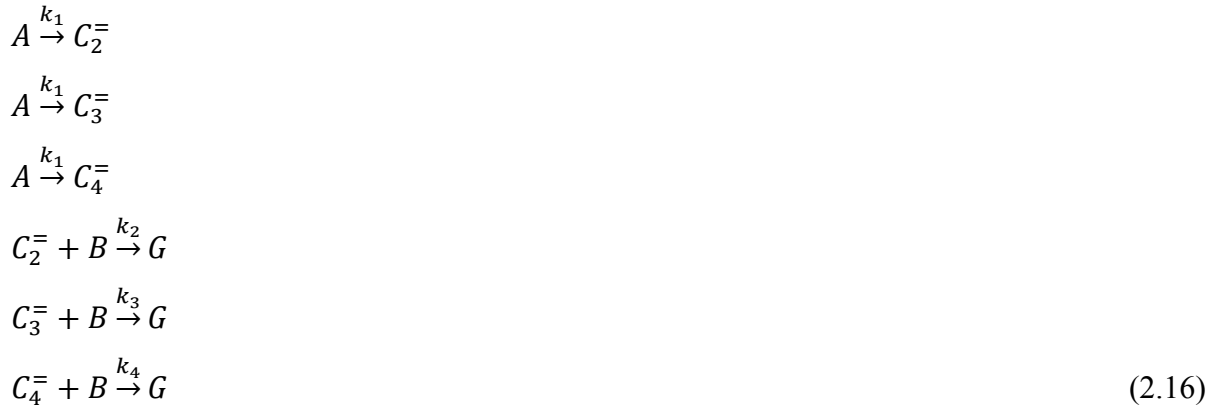
$$k_i = k_{i0} \exp \left(-\lambda_i \frac{\overline{Hc}}{W} \right) \quad (2.14)$$

where λ is the deactivation coefficient. Therefore, the average amount of hydrocarbons formed has a direct impact on the coke formation. These authors found that two out of three reaction schemes were adequate to treat their experimental data. It was also observed that regressed kinetic parameters were in agreement with the Arrhenius law. Those proposed reaction schemes are as follows:

Scheme I:



Scheme II:



where $C_2^= \equiv$ ethylene, $C_3^= \equiv$ propylene, $C_4^= \equiv$ butane, and $B = \text{sum}(C_2^= + C_3^= + C_4^=)$.

Gayubo's research group [73,81–84] reported results on modelling MTO/MTG reaction over an HZSM-5 catalyst with including and excluding deactivation effect. In the first case of excluding deactivation, Gayubo et al. [83] validated a four rate equation model (Equations 2.7, 2.9, 2.12, and 2.15) over HZSM-5 using in an isothermal fixed bed reactor at 300-375°C

and 0-0.1 h⁻¹ space times. Additionally, these authors proposed two alternative models. The first one is a modification of Chen's model (Equation 2.7) as follows:



where $B_1 \equiv$ light olefins (C₂⁻-C₃⁻) and $B_2 \equiv$ rest of olefins.

In a second alternative model, oxygenates are adsorbed on active sites (L) first, then they react with a non-adsorbed oxygenate species forming light olefins:



The kinetic parameters for the proposed models were calculated by solving the continuity equations in the reactor, in conjunction with the rate equations for the various lumps. Among the six models selected, the one proposed by Schipper and Krambeck (Equation 2.9) was observed to provide the best fitting to the data. As an extension to the former study, Gayubo et al. [81] and Benito et al. [84] both adopted Schipper and Krambeck's model to validate a reversible deactivation model considering the effect of individual lump concentrations on coke formation:

$$\frac{da}{\tau} = -(\sum k_{di} X_i) a^d \tag{2.19}$$

where $a \equiv$ the remaining catalyst activity, $k_{di} \equiv$ deactivation kinetic constant for lump i , $X_i \equiv$ lump " i " weight fraction, and $d \equiv$ deactivation order. The remaining catalyst activity was considered to be the same for each individual lump:

$$a = \frac{r_i}{r_{i0}} = \frac{\left(\frac{dX_i}{d\tau}\right)_{TOS}}{\left(\frac{dX_i}{d\tau}\right)_{TOS=0}} \quad (2.20)$$

However, the assumption included in Equation 2.20, was adjusted in a later study by Gayubo et al. [82], using modifications to the Schipper and Krambeck model as follow: (a) methanol and DME are accounted as separate species. It was proven that these species display different reactivities with methanol dehydration being a required step; (b) the oxygenate reaction with gasoline is portrayed as consecutive steps involving olefin condensation with methanol and DME; (3) the contribution of the light olefin formation by cracking of the gasoline lump is required in the kinetic model. Thus, a modified scheme can be advanced as:



where M \equiv methanol, D \equiv DME , and W \equiv water. In their kinetic experiments, water was co-fed with methanol for dilution purpose.

Regarding kinetic modeling, one can notice that separation of oxygenates along with diluting methanol and water have several implications. First, the reaction rates of DME and methanol are defined with separate rate equations. Second, the dilution effect of water is accounted via a term in the denominator both in the initial reaction rate and deactivation rate equations. Third, the deactivation due to methanol dehydration is considered a slower step than the ones from the kinetic network. Accordingly, the activity decay due to methanol dehydration (a_D) is

accounted for differently from the other steps (a) and is defined as: $a_D = a^\alpha$ where $\alpha < 1$. The kinetic equations of this modified reaction network are, thus, given by the following expressions:

$$\begin{aligned}
\frac{dM}{d\tau} = r_M &= \frac{a^\alpha(-k_1X_M^2+k_1'X_DX_W)-a(k_2X_M+k_5X_MX_B)}{1+k_{w0}X_W} \\
\frac{dD}{d\tau} = r_D &= \frac{a^\alpha(k_1X_M^2-k_1'X_DX_W)-a(k_3X_D+k_6X_DX_B)}{1+k_{w0}X_W} \\
\frac{dB}{d\tau} = r_C &= a \left(\frac{k_2X_M+k_3X_D-k_4X_B^2-k_5X_MX_B-k_6X_DX_B-k_7X_GX_B+k_8X_G}{1+k_{w0}X_W} \right) \\
\frac{da}{d\tau} &= - \left(\frac{k_{dA}X_A+k_{dB}X_B+k_{dG}X_G}{1+k_wX_W} \right) a
\end{aligned} \tag{2.22}$$

where X_A = water free mass fraction of oxygenates (X_M+X_D), X_W = mass ratio of total water (fed and formed) to organic products in the reaction media, k_{di} =reversible deactivation rate constant for coke formation from lump i , X_w = water mass fraction in the reactor outlet. k_{w0} and k_w are parameters that account for the water dilution effect in the lump reaction rate and deactivation rate, respectively.

Gayubo et al., in a recent study [73], expanded the temperature range (400-525°C) of (word missing) to cover the irreversible deactivation due to dealumination of zeolites by water. These authors found that when running at $T \leq 400^\circ\text{C}$, coke deposition was the only form of deactivation. However once temperature exceeded 400°C , an irreversible deactivation was observed, with this irreversible deactivation becoming more severe as temperature increased. As a result, the activity remaining in the catalyst (a) was proposed to be quantified as a product of reversible activity (a_r) and irreversible activity (a_{ir}): $a = a_r a_{ir}$. Thus, the reversible activity reduction rate ($da_r/d\tau$) was considered a function of the total activity remaining (a) as defined in Equation 2.22 while the irreversible activity was expressed given by the following empirical power law model:

$$\frac{da_{ir}}{d\tau} = -k_{dir}X_W^\delta a_{ir}^\sigma \tag{2.23}$$

where k_{dir} is the rate constant for irreversible deactivation; δ and σ are exponents for the irreversible deactivation kinetics.

Schoenfelder et al. [74] developed an MTO lumped kinetics combined with data from a circulating fluidized bed reactor model. Their model is described as follow:



Where W \equiv water, G \equiv gasoline range hydrocarbons (aromatics + paraffins + naphthenes), and F \equiv tail gas (CH₄+CO+H₂+H₂O). These authors included water production from olefins and oxygenates. Additionally, individual light olefins (C₂⁻-C₄⁻) and production of tail gas (F) from oxygenate oligomerization were also accounted for. The kinetic data was obtained at initial reaction conditions over an HZSM-5 catalyst in a Berty reactor at 400 - 500°C. The regressed kinetic parameters were in agreement with the Arrhenius law. The model was able to predict the product distribution fairly well at initial time-on-stream (fresh catalyst). However, this model does not have the capability to predict reactor performance within the expected time-on-stream since deactivation was excluded.

Regarding the lumped models, it is possible to argue that these may not reflect the surface chemistry of the adsorbed species. Additionally, the estimated kinetic parameters including rate constants, equilibrium coefficients and activation energies may strongly be affected by reaction conditions and reactor scale. As a result, and as attempted in the present study in Chapter 7, kinetic modeling based on detailed reaction kinetics is a worthwhile approach for the reaction engineering of DTO.

2.4.6 Outlooks on DME Conversion to Olefins over HZSM-5

Although the application of the HZSM-5 catalyst to MTO dates of 30 years only, its application to the DME conversion to light olefins (DTO) is even more recent. In particular,

the promoted HZSM-5, offers a unique promise for DTO. One can also notice that considerable knowledge concerning the design of the catalyst and operating parameters was gained and led to 96% DME conversion, 90% light olefins selectivity with 700 h time-on-stream [16]. In spite of this, there is still a lack of understanding of reaction mechanisms on the basis of kinetically significant chemical species. This leads to the following identified challenges for the DTO process:

1. To establish the value of highly concentrated DME feed to the DTO process. This is envisioned as a means of improving and reaching high olefin performance.
2. To consider the effect of the textural and surface chemistry properties of HZSM-5 by varying Al content (i.e. $\text{SiO}_2/\text{Al}_2\text{O}_3$). This is proposed as a way of linking catalytic performance to the DTO process with major catalyst structural properties.
3. To develop reaction pathways with the aim of identifying relevant reaction steps and the required kinetic parameters.
4. To establish phenomenologically based kinetic models based on physicochemical phenomena such as intrinsic reactions and chemical species adsorption. These kinetic models are considered will provide reaction engineering tools for the design and operation of future commercial reactors.

Given the above cited technical challenges, it can be concluded that research is required in DTO reaction over HZSM-5 in the following areas:

1. An enhanced understanding of DME dilution in terms of its effects on reactor capacity and equipment sizing. Therefore, in this respect, the use of neat DME could be considered for industrial applications.
2. A more detailed understanding of the role of HZSM-5 physicochemical characteristics for improved catalyst performance.
3. A detailed reaction scheme defining the olefin role in DME conversion over HZSM-5 catalysts. This would allow optimization in both catalyst design and reactor operating parameters.

4. A kinetic model based on a detailed reaction scheme that accounts for physicochemical phenomena such as chemical species adsorption and intrinsic chemical reactions.

CHAPTER 3 SCOPE OF RESEARCH

This PhD dissertation is aimed at investigating an HZSM-5 zeolite as a potential catalyst for olefins production from DME. The detailed objectives of this PhD dissertation are the following:

1. The preparation of HZSM5 pellets with three different $\text{SiO}_2/\text{Al}_2\text{O}_3$ ratios (30, 80, and 280).
2. The investigation of the influence of the $\text{SiO}_2/\text{Al}_2\text{O}_3$ ratio on HZSM-5 zeolite structural and acidity properties using various catalyst characterization methods in terms of:
 - a. Crystallinity and morphological properties of the HZSM-5 framework.
 - b. Surface acidity distribution of the HZSM-5, including strength and type.
3. The establishment of the NH_3 desorption kinetics based on NH_3 -TPD data. It was envisioned that this would encompass the calculation of activation energies and desorption rate constants for both strong and weak acid sites. It was also anticipated that the changes of these parameters with the aluminum content of the HZSM-5 could be quantified.
4. The development of catalytic runs in a Berty reactor unit aiming to achieve maximum catalyst performance by considering the following:
 - a. By examining the acidity effect on the DME conversion and selectivity using different HZSM-5 samples with various $\text{SiO}_2/\text{Al}_2\text{O}_3$ ratios.
 - b. By evaluating the effect of changing operating conditions on DME conversion and light olefins selectivity using various HZSM-5 catalysts. This includes the effect of space time and reaction temperature.
5. The establishment of a kinetic model based on elementary reaction steps. It is expected that the main assumptions of this kinetic model could be supported with product distribution data from DME selective conversion into light olefins.

6. The development of phenomenologically based heterogeneous reaction kinetics for DME selective conversion into olefins using the allowed kinetic model simplification and non-linear regression analysis.
7. The calculation of kinetic model parameters and the demonstration of model applicability using statistical indicators such as parameters spans for the 95% confidence interval and matrix of cross correlation coefficients.

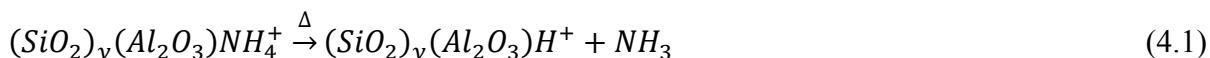
CHAPTER 4 EXPERIMENTAL METHODS

4.1 Introduction

This chapter describes the various experimental activities developed in the present PhD dissertation. Section 4.2 addresses the formulation of the HZSM-5 pellets with different SiO₂/Al₂O₃ ratios. Following this, sections 4.3 and 4.4 summarize the steps of the various characterization techniques used to evaluate the physicochemical characteristics of the prepared HZSM-5 and its formulated pellets. The experimental apparatus and procedures used to perform the reactivity tests are detailed in section 4.5 including the outlet analysis techniques. The evaluation of the reactivity runs is described in this section as well.

4.2 Preparation of the H-ZSM5 Samples

This study was carried out using three commercial NH₄⁺ZSM-5 (ZSM-5 zeolite in the ammonium form) supplied by Zeolyst International (USA) with SiO₂/Al₂O₃ ratios of 30, 80 and 280 and are denoted herein as ZSM5-30, ZSM5-80 and ZSM5-280. The bulk Na₂O content was negligible, as confirmed by the vendor to be ≤ 0.01 wt%. The calcination of the samples was performed by heating the NH₄⁺ZSM-5 precursor zeolite in a quartz tube reactor under N₂ flow at 550°C for 6 h. This allowed NH₃ to be formed, leaving the ZSM-5 in the protonic form (H⁺ZSM-5) according to the following reaction:



where y is the SiO₂/Al₂O₃ ratio. Then, the catalyst extrudates were prepared using the following steps:

1. Mixing 25% of the active HZSM-5 with 5% binder (Versal 950, α -alumina monohydrate (Al(OH)O), Kaiser Chemicals) and 70% filler (Fused Alumina, 100% Al₂O₃, Sigma-Aldrich: CAS# 1344-28-1). Fused alumina was used as cementing agent. Fused alumina means nonporous Al₂O₃ and as a result negligible internal surface area and acidity were expected. This made the thermal conductivity of the fused alumina high enough to absorb the heat released from the DTO reaction along with increasing the true density of the

- catalyst pellets. Alumina monohydrate was selected as a binder so that after thermal treatment, the formed pellets became mechanically strong enough to resist attrition.
2. The mixture was stirred well in a ceramic crisol. Following this, distilled water was added gradually until it reached 50% of the total weight of the mixture. The solution was further mixed until a consistent paste was obtained.
 3. Following this, using an extruder, pellets were fabricated from the paste with dimensions of 3 mm in diameter and 10 mm average length.
 4. Finally, the pellets were heat treated at room temperature for 2 hrs, at 120°C for 10 hrs, and then calcined at 550 °C for 3 hr. The first two drying steps were for water removal and the third step (firing) was to bake the alumina monohydrate in order to achieve the required mechanical strength for the pellets. The ZSM5-30, ZSM5-80 and ZSM5-280 were designated as ZMPL-30, ZMPL-80 and ZMPL-280 once the pellets were formed. A blank pellet (5% versal 950 and 95% Fused Alumina) was also prepared and named ZMPL-BL.

The above method of HZSM-5 pelletization with the selected combination of binder and filler materials was demonstrated to work well in the MTO/MTG studies by Hagey [72] and Sedran et al. [78,80], Benito et al. [84], Gayubo et al. [73,81–83], and Schoenfelder et al. [85].

4.3 Structural Characterization Methods

4.3.1 XRD analysis

X-ray Diffraction (XRD) was performed to identify the product phase and calculate the HZSM-5 crystallinity with various SiO₂/Al₂O₃ ratios. XRD patterns were recorded on an Ultima IV Miniflex Diffractometer (from Rigaku, USA) using Ni filtered Cu K α radiation (λ = 0.15406 nm). This instrument is equipped with: a) a copper tube with a 40 kV voltage and a 40 mA current, b) a graphite receiving monochromator, c) a scintillation counter equipped with pulse height discriminator, and d) a sample holder. XRD analysis was performed in the 5-50° 2 θ range. Step width and scanning speed were set to 0.02° and 2°/min, respectively.

4.3.2 Particle size distribution

The Particle Size Distribution (PSD) analysis was carried out in a Mastersizer 2000E (from Malvern, UK), which uses a laser diffraction technique. The wet dispersion unit (Hydro 2000 MU) attached to the Mastersizer 2000E was utilized to capture the individual particles suspended in water. PSD analysis was initiated by considering the zeolite refractive index (1.50) and water as a dispersant. Following this, a small amount of the sample was added gradually to the circulated water in the dispersion unit. This was done while observing that its concentration fell into an adequate measuring range. Since the sample tested contained fine particles, ultrasound was applied to the well dispersed particles. As a result, a homogenous slurry of suspended particles was continuously fed to the measuring zone and the scattered laser light intensity was quantified. This data was then analyzed to calculate the particle size distribution resulting from the particle scattering pattern.

4.3.3 N₂ isotherm

The structural properties of different HZSM-5 samples were determined by measuring N₂ adsorption-desorption isotherms at 77 K using an ASAP 2010 Automatic Adsorption Analyzer from Micrometrics[®], USA. For the purpose of removing the possible physisorbed moisture and organics as per IUPAC recommendation [86], each sample was initially degassed at 300 °C under a high vacuum (5 mmHg) for 3 h. The measurements were initiated at a low relative pressure taken down to 10⁻⁶ so as to be able to access the micropore zeolite channels and derive information regarding their size distribution [87–89]. The ASAP 2010 analyzer is equipped with the DFT plus™ data reduction software which operates in conjunction with a DFT plus™ model library. Porosity was analyzed with this software in conjunction to the Non-Local Density Functional Theory (NLDFT) algorithm with two possible pore geometries: the slit-like and the cylindrical pores. In addition, the DTF plus™ software allows one to apply a certain degree of smoothing to prevent over-fitting in the case of noisy data or ill-fitting models.

4.4 Surface Acidity Characterization Methods

4.4.1 NH₃-TPD

Ammonia temperature programmed desorption (NH₃-TPD) tests were conducted *in situ* using a Micrometrics AutoChem II 2920 Analyzer, to evaluate the strength and the density of the active sites. For each test, a “ball” of quartz wool approximately 8 mm in diameter was placed in the wide opening side of a fused quartz U-tube microreactor. The microreactor had a dimension of 20 cm in length and 0.9 cm diameter on the wide opening side. Following this step, the sample weighing about 0.12 to 0.15 g, was placed on top of the quartz wool in the microreactor and was then degassed at a 30 ml/min flow rate of He purge gas at 500°C for 1 h. Next, the sample was cooled down to 100°C. It was then flushed with a 4.55% NH₃/95.55% He mixture at a rate of 50 ml/min for 1 h to obtain the sample saturation with ammonia. Then, the ammonia flow was replaced by a helium flow at the same conditions for 1 h to remove the physisorbed ammonia. Subsequently, the temperature was raised gradually. As a result, ammonia was desorbed as it gained enough energy to overcome the activation energy barrier of the acid sites. The amount of desorbed ammonia was recorded every 10 sec while the temperature was increased at a specified heating rate (10-30 °C/min) and ended at 650°C for ZSM5-30, 600°C for ZSM5-80, and 500°C for ZSM5-280. With the aim of establishing the NH₃ desorption kinetics, NH₃-TPD chromatograms at different heating rates were collected (10, 15, 20, 25, and 30 °C/min).

4.4.2 Pyridine-FTIR

The pyridine adsorption process was performed, *in situ*, in a fused-quartz-tube reactor. Each sample was first, heat treated in an N₂ flow at 550 °C for 1h. The samples were then cooled down to 100°C. Then, the pyridine vapor contained in an N₂ flow was introduced for 1 h to ensure its adsorption on the zeolite sample. The zeolite sample was then flushed with N₂, at different temperatures (100, 150 and 200°C) for 1 h.

Subsequently, the pyridine rich sample was diluted with potassium bromide, a non-absorbing matrix. This was done to ensure a deeper penetration of the incident beam into the sample, reducing specular-reflection and increasing the scattered contribution [90]. Then, the sample

was collected in a stainless steel dish and placed in an Equinox 55 FTIR Spectrometer from Bruker, USA. This instrument operates at 4 cm^{-1} resolution, producing 100 scans per sample. The infrared spectra of all samples were recorded at room temperature using the Diffuse Reflectance Infrared Fourier Transform Spectroscopy (DRIFTS) technique.

4.5 Reactivity Tests in the Berty Reactor Unit

4.5.1 Berty reactor

The reactivity runs were performed using a 1" inner diameter Berty Reactor fabricated by Autoclave Engineers (Figure 4.1-a). This reactor is a continuous flow unit designed for catalyst evaluation and kinetic studies under CSTR conditions. It is an internal recycle reactor that is designed to hold a fixed catalyst bed in a basket. At the bottom of the unit, there is a vane type blower. Gas circulation is attained using a motor sealed magnetic impeller running at 1600 rpm. The gas flow is directed upward along the outer channel and downwards inside the central catalyst bed (Figure 4.1-b). This design offers a high degree of mixing with an essentially gradientless operation which enables the reactor to be modeled as CSTR. Additionally, the Berty reactor allows operation at close to industrial unit conditions or even enhanced heat and mass pellet interface transport. Therefore, the performance of the catalyst can be evaluated independently of reactor performance [91,92]. On the other hand, Mahay et al. [93], demonstrated the exclusion of the external mass transfer limitation when running this Berty reactor at impeller speed ≥ 1500 rpm. The reactor is equipped with three zone electrical heated jackets (one 0.8 and two 1.1 kW) and two thermocouples. One thermocouple is located inside the reactor to measure the reaction temperature while the other one that is hooked up between the reactor wall and the heated jacket is used for temperature control. Except for the reactor total pressure set at 1.36 barg, the other operating conditions (temperature, space time), they were varied to represent an ample range of reaction conditions.

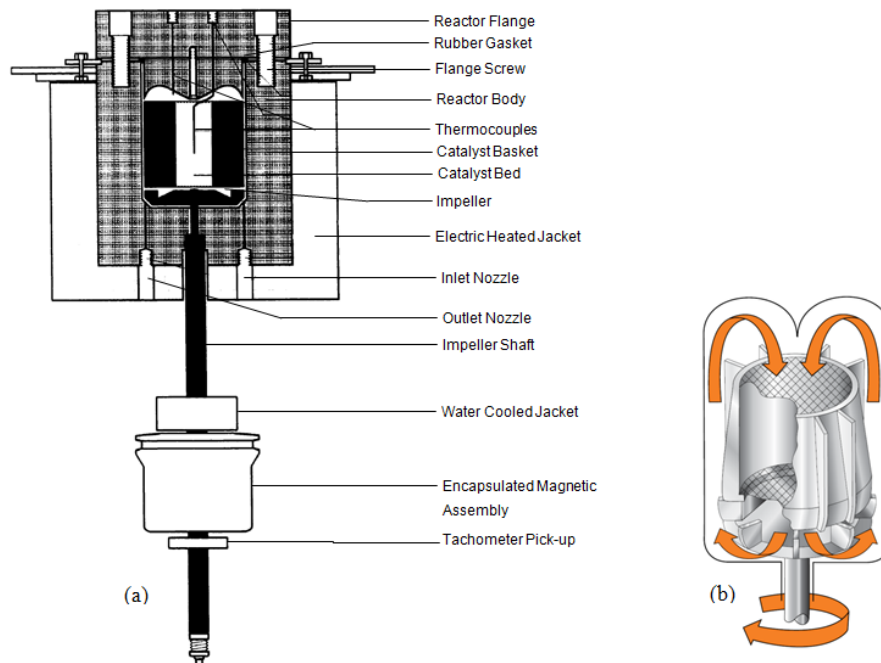


Figure 4.1: Sectional view of the Berty reactor: (a) Detailed assembly; (b) Gas circulation pattern [94].

4.5.2 Experimental Apparatus

A schematic diagram of the experimental set-up is reported in Figure 4.2. The experimental apparatus consists of the following components:

1. Two pressurized cylinders for DME and He, where each is equipped with a pressure regulator.
2. Two Brooks 5850 mass flow control valves connected to two position indicators and a controller to check the inlet flow for the He and DME.
3. A set of seven three ways valves.
4. An insulated Berty Reactor.
5. An electric heated and insulated box that covers the reactor outlet to the sample box
6. An electric heated six port valve placed in an insulated box. This six port valve allows a 1 ml product sample injection into a GC.

7. A pressure safety valve for the DME cylinder as a protection against overpressure. A pressure regulator in the reactor outlet to adjust the reactor pressure according to the pressure indicator in the reactor inlet.
8. Two ice water coolers in the reactor outlet to reduce the temperature.
9. A bubble flow meter to measure the non-condensed part of reactor outlet.
10. Two vent lines in the fumed hood.
11. The entire reactor set-up is housed in a properly vented area.

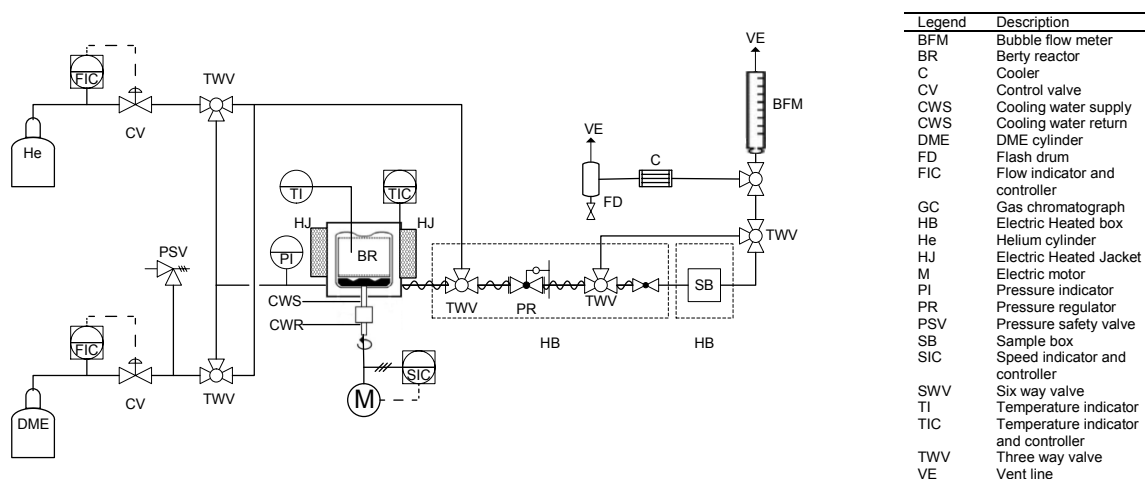


Figure 4.2: Schematic diagram of the reactivity test setup.

4.5.3 Experimental Procedure

The experimental run operation is organized in three stages: a) pre start up, b) start up, and c) shutdown. The operating procedure for each stage is detailed as follow:

4.5.3.1 Reactor pre start up procedure

The following methodological steps were involved prior to reactor start up:

1. Regenerate the used pellets by air at 480°C for 10 h to burn off the deposited coke.
2. Measure the required amount of catalyst to be used (normally 10 g).
3. Open the reactor flange, clean the reactor well, load it with the catalyst, and then box it up again.

4. Connect the cooling water to the reactor stirrer motor shaft.
5. Ensure that the reactor pressure regulator is fully closed and then connect the helium flow to the reactor vent.
6. Open the He cylinder valve and then pressurize the reactor until 40 psig is reached.
7. Perform a leak test for the reactor and all connections.
8. Once the reactor leak-free test completed, set again the reactor insulation to its former position.
9. Adjust the reactor pressure to 20 psig using the pressure regulator.
10. Start the heater and set it according to the following correlation:

$$T_{SP} = 234.72 \exp(0.0018 T_{reactor}) \quad (4.2)$$

with T measured in °C

11. Set the reactor outlet to 180°C and the sample box temperature to 330°C and then switch on the heat tracing.
12. Once the temperatures are stabilized, turn on the FIC and set it to position 2 (He) at low flow (e.g. 2).
13. Check the bubble-flow meter and continue the He purging for 1 h in order to precondition the catalyst and to remove any hydrocarbon species inside the reactor.

4.5.3.2 Reactor startup procedure

After completing the various preparation steps, the following reactor operation protocol was developed

14. Start the motor at 1600 rpm speed.
15. Once the reactor and outlet box temperature are both set at the required values, change the He flow by the DME flow.
16. Change the FIC to position 1 (DME) and then set the digital display to the required flow according to the following correlation:

$$\text{Digital display} = 2.2852F_{DME}(\text{ml/s}) + 2.1361 \quad (4.3)$$

17. Adjust the reactor pressure regulator to reach the desired pressure.
18. Record the experimental readings as outlined in the run log sheets.
19. After a 1 h reaction, ensure that all variables are at steady conditions (reactor pressure and temperature, DME flow, motor speed, and gas product bubble meter flow). Record all previous parameters in the data collection sheet detailed in Appendix A.
20. In order to have similar measurement points as in the analysis and to facilitate the material balance, the following steps were considered:
 - a. Isolate the cooler.
 - b. Connect the outlet line to the bubble flow meter. Measure four consecutive times for 90 ml gas displacement volume in the flow meter.
 - c. Connect the outlet line back to the cooler.
21. Connect the sample box with the six port valve in the “loop fill” position for 5 minutes. Following this reconnect the bypass line; bring the sample box for GC analysis.
22. Continue sampling and recording readings every 1 hr.

4.5.3.3 Reactor shutdown

Finally, once the reactivity run is completed, the following steps must be implemented:

23. Turn off the heaters (reactor, sample box, and outlet line) and the stirrer motor.
24. Change the FIC position back to 2 and then gradually swap the DME with the He. After this, continue purging the reactor at low flow for ½ hr until all hydrocarbons have been purged out from the reactor.
25. Once the reactor is completely purged, stop the helium flow.
26. Once the temperature has been reduced below 100 °C, turn off the cooler.
27. Once the reactor is cooled down to ambient temperature, open the reactor flange and then unload the catalyst.

4.5.4 Reactor outlet and coke analysis

The reactor unit, as described in Figure 4.2, is equipped with an outlet sampling valve. This valve allows one to collect 1 ml of product sample at preset times. Samples were analyzed offline using an electrically heated sample box. The heated box was hooked up to an Agilent 6890N gas chromatograph (GC) with a flame ionization detector (FID). This unit was also equipped with a capillary column, model Agilent 19091Z (HP-1 Methyl Siloxane, 50 m×200 µm×0.5 µm). Thus, the capillary column-FID results allow one to quantify various product hydrocarbon species as weight fractions equivalent to GC area fractions. The analytical system was also equipped with an Agilent 5973N mass selective detector (MSD). This permitted the identification of product species as described in Figure 4.3. Furthermore, the gas phase chemical species at the outlet of the condenser, were analyzed using an on-line GC (Shimadzu 2014) equipped with an 80/100 Poropak Q packed column, (2 m×2 mm×2 µm) with FID, and TCD connected in series. Quantification of light hydrocarbons using combined FID and TCD specially helped on detecting species such as methanol, and methane. In both of the aforementioned GCs, a GC oven temperature program was developed as shown in Figure 4.4 and employed during the experiments to achieve good separation of the detected species at the reactor outlet.

Furthermore, at the end of each run, the coked catalyst was unloaded from the reactor to measure the coke content in wt% carbon. This was achieved by loading one pellet (about 180 mg) to the Shimadzu TOC-VCPH Total Carbon Analyzer. This analyzer was equipped with a solid sample module (SSM-5000) where coke was combusted at 900°C forming CO₂. The resulting CO₂ peak was stoichiometrically related to the carbon weight fraction according to an established calibration curve.

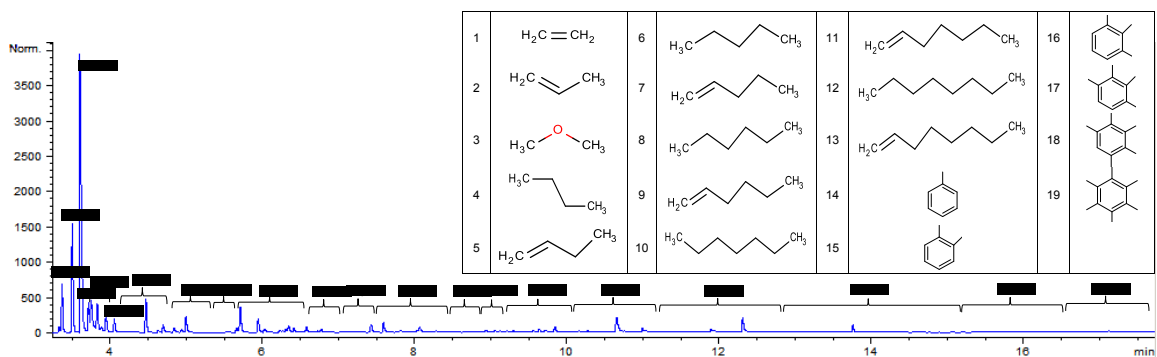


Figure 4.3: GC-FID chromatogram for quantification of all species. Note: identified and quantified products are assigned numbers from 1 to 19.

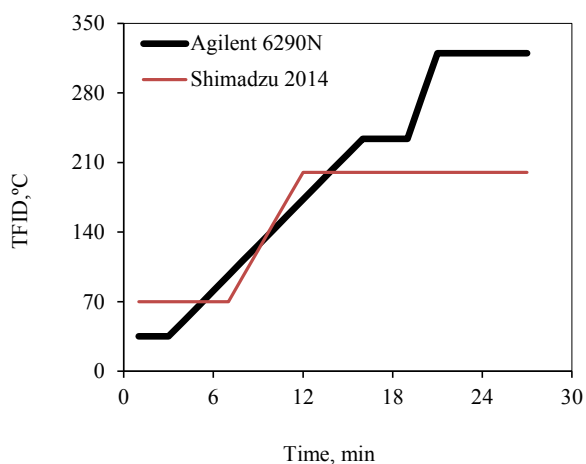


Figure 4.4: GC-FID temperature profile of the oven calibration program.

4.5.5 Reactivity tests evaluation

As described in section 4.5.3, the experimental data were directly recorded from the set-up instruments. The contact time was obtained as the ratio of the catalyst weight per molar DME feed flow ($\tau = W/F_{\text{DME}0}$). In order to analyze the product species at the reactor outlet, samples were collected in gas phase and then injected to the GC equipped with an FID. The FID results give peak areas for every hydrocarbon compound as a retention time. On this basis, the component weight fraction was estimated as a fraction of its peak area to the summation of peak areas.

The closure for the atomics balance (C, H, and O) for each run was established for each run. The detailed procedure of calculating the species balance is shown in Appendix B.

In order to evaluate the catalyst performance, the conversion and hydrocarbons selectivity (i.e. with excluding the formed water) were estimated as follows:

$$DME \text{ mass conversion} = \frac{wt \ DME \ in - wt \ DME \ out}{wt \ DME \ in} \quad (4.4)$$

$$HC_i \text{ mass selectivity} \left(\frac{g \ HC_i \ formed}{g \ total \ HC \ formed} \right) = \frac{x_{HC_i}}{1 - x_{DME,HC \ out}} \quad (4.5)$$

4.6 Concluding Remarks

This chapter describes the experimental methods used for: a) the preparation of the HZSM-5 pellets, b) the establishment of the physicochemical properties of the high SiO₂/Al₂O₃ ratio zeolites, c) the reactivity evaluation and kinetic modeling of the HZSM-5 prepared pellets.

CHAPTER 5 CHARACTERIZATION OF HZSM-5 AND NH₃ DESORPTION KINETICS

5.1 Introduction

Protonic zeolite-type materials are the catalysts of choice for a wide range of industrial processes. The HZSM-5 type, in particular, is used in a number of catalytic processes such as: a) the conversion of oxygenates (methanol and dimethyl ether) into olefins, b) fluid catalytic cracking (FCC), c) alkylation of aromatics, d) ethyl-benzene production and e) xylene isomerization [30,60,62,95,96].

The quantitative characterization of acidity on heterogeneous catalysts is very important for many catalytic processes. In this respect, the acidity introduced by aluminum in the silicate-alumina framework is a major contributor to the HZSM-5 reactivity. Thus, changes in acidity may affect both reaction pathways and product distribution [62]. One should note that the low density HZSM-5 acid sites are the result of the high SiO₂/Al₂O₃ ratio (>20) [49,59]. Moreover, controlling acid properties is among the key factors for achieving selective DME transformation to olefins using HZSM-5 zeolites [30,52,97,98].

Acid site strength, density and desorption kinetics can be measured using ammonia Temperature Programmed Desorption (TPD) as a probe molecule. This is due to ammonia's strong basicity and its small kinetic diameter [99,100]. Acidity characterization can also be complemented using Fourier Transform Infrared (FTIR). FTIR using pyridine as a probe molecule allows the identification of the adsorbent site types, i.e. Brønsted, Lewis, hydrogen-bonded, and silanols [101]. Pyridine is a basic heterocyclic organic species with a C₅H₅N chemical formula. Its lone-pair electrons of the nitrogen atom are involved in sorption interactions with surface acid sites [102].

The effect of the SiO₂/Al₂O₃ ratio on HZSM-5 acidity has already been investigated in the technical literature. This has been accomplished using both NH₃-TPD and pyridine-FTIR. However, little attention has been given to the influence of the SiO₂/Al₂O₃ ratio on the NH₃-TPD desorption kinetics. Therefore, the studies in this chapter attempt to establish ammonia

desorption kinetics, ammonia desorption parameters and their changes with HZSM-5 aluminum content. This represents a significant step towards an in-depth understanding of HZSM-5 as a potential catalyst for DTO process. Furthermore, the effect of the $\text{SiO}_2/\text{Al}_2\text{O}_3$ ratio and the pelletization of HZSM-5 on its acidity have been investigated as well using NH_3 -TPD and Pyridine-FTIR techniques. Moreover, HZSM-5 textural properties including porosity and crystallinity were studied using N_2 isotherm and XRD methods, respectively. Universal ASTM standards and IUPAC recommendations along with the statistical measures were employed to add a level of validity and applicability to the obtained results.

5.2 Physical Characterization

5.2.1 XRD Crystallinity

HZSM-5 zeolites are highly crystalline materials. Their purity can be assessed using their degree of crystallinity. Degree of crystallinity is an important variable given that there is the possibility of an amorphous phase, which provides an indication of impurities that may impair the HZSM-5 catalytic properties [103]. Among several methods that have been utilized for monitoring the degree of HZSM-5 crystallinity, XRD is the most commonly used technique.

There are some factors that may affect XRD peak patterns apart from the HZSM-5 composition such as the counter-ion type, the adsorbate presence [103], and the crystal dimensions [56,104–108]. Differences in HZSM-5 preparation procedures such as synthesis temperature, crystallization time [109], and calcination procedure [105,110] are all factors reported to affect XRD crystallinity as well.

In the present study, each of the aforementioned factors was expected to remain unchanged for all samples. This was required to have a good correlation between crystallinity and the HZSM-5 compositions. Samples were also carefully selected in order to ensure that $\text{SiO}_2/\text{Al}_2\text{O}_3$ ratios could vary widely. In this respect, the commercial zeolite samples in the ammonium form were provided by Zeolyst with a certified composition. Zeolite samples were calcined as described in section 4.2. As a result, a consistent HZSM-5 form was available in all cases. Additionally, it was found that particle sizes were approximately the

same in all HZSM-5 samples as reported in Table 5.1. Given that the particle size distribution for all HZSM-5 samples was within the same range as displayed in the semi-log plot of Figure 5.1-a, there were no expected particle size effects on the crystallinity.

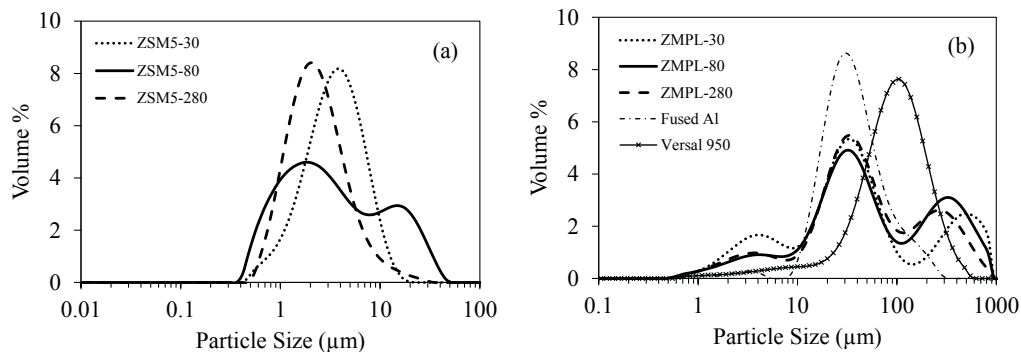


Figure 5.1: Particle size distribution for: (a) Pure HZSM-5 (b) HZSM-5 pellets.

The XRD spectra provide the fingerprint of a zeolite structure. Figure 5.2 (a-c) reports the XRD patterns for the HZSM-5 zeolites studied. These XRD peaks correspond to those of the reference standard for a highly pure calcined HZSM-5 [111]. Two of the strongest peaks at low 2θ reflections (i.e. 7.94 and 8.9°) were used to identify the HZSM-5 zeolites. These peaks correspond to (h,k,l) values of (011) and (200) lattice planes, respectively [111]. For the samples used in the present study, the 7.92 and 8.8° characteristic angles with a small shift from the reference peaks were observed. This difference was attributed to the different X-rays sources used. Figure 5.2 reports a slight reduction of the (011) and (200) peaks with the increase of the aluminum while having less pronounced effects on the (051), (033) and (313) peaks. A similar influence of the $\text{SiO}_2/\text{Al}_2\text{O}_3$ ratio was observed by others [53,57,110]. However, when this is combined with a low intensity background, it is an indicator of excellent crystallinity [112].

The slight difference in the heights of XRD intensities could be attributed to the unique unit-cell-volume parameters of each HZSM-5 sample. It is known that the unit-cell-volume becomes larger when small silicon atoms (2.22 \AA) are replaced by larger aluminum atoms (2.86 \AA). Awate et al. [113] demonstrated a linear expansion of HZSM-5 unit-cell-volume with a decreasing $\text{SiO}_2/\text{Al}_2\text{O}_3$ ratio.

Figure 5.2 (d-g) displays the XRD intensities for the HZSM-5 pellets. One can observe a significant pellet matrix effect on XRD intensities (Versal 950 and Fused Al) on the HZSM-5 with lines at 25.5, 35.1, 37.8, and 43.3° 2θ angles being new and with an attenuation at (011), (200), (051), (033) and (313) peaks. Such effect could be assigned to the dilution by the matrix materials. The other possible influence on XRD results can be assigned to the particle size increase after pelletization. As shown in Figure 5.1-b and Table 5.1, the mean particle size for HZSM-5 was increased from (2-2.9) to (12.8-14.7) μm following pelletization.

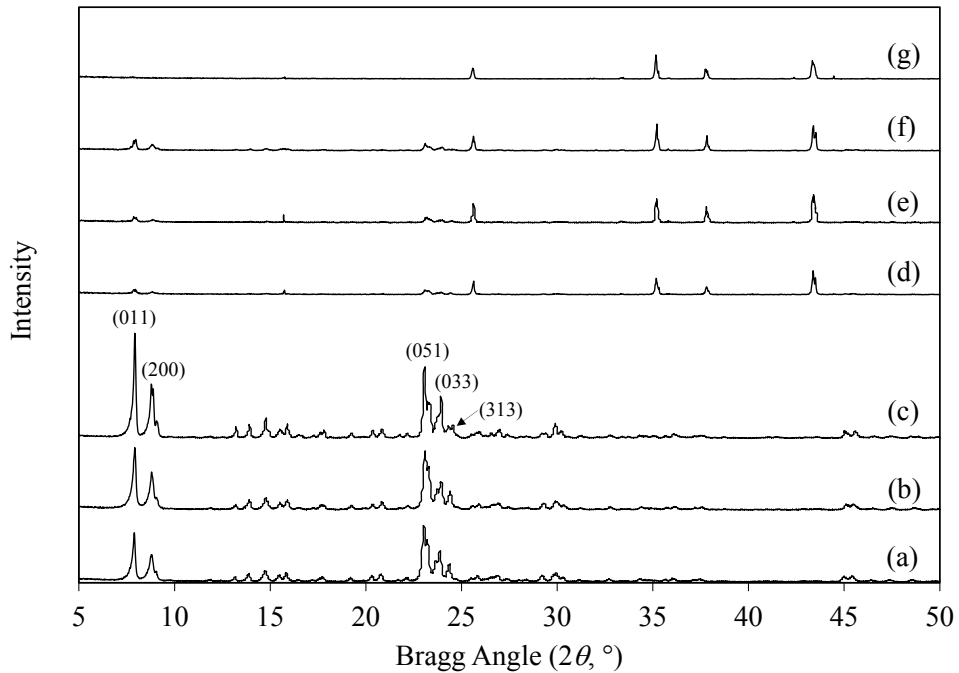


Figure 5.2: XRD spectra for the following zeolites: (a) ZSM5-30, (b) ZSM5-80, (c) ZSM5-280, (d) ZMPL-30, (e) ZMPL-80, (f) ZMPL-280, (g) ZMPL-BL.

In order to analyze the effect of the $\text{SiO}_2/\text{Al}_2\text{O}_3$ ratio on the degree of HZSM-5 relative crystallinity, calculations were developed according to ASTM standard D5758-01 [96]. Using this approach, one has two possible alternatives: a) The use of the integrated peaks displayed within 22.5 to 25° 2θ angle range, b) The consideration of the single peak height at 24.3° 2θ angle.

In the present study, XRD crystallinity of the HZSM-5 samples were determined according to the first method, where XRD peaks are accounted for as the sum of several peaks rather than just a single peak. Once these areas are obtained, a relative crystallinity parameter can

be considered using the ratio of the area of the sample being studied over the highly crystalline reference sample. This method was also employed by others [103,114,115] to estimate the HZSM-5 crystallinity.

ZSM5-280 was considered as the reference sample, as it is the one that displays the highest intensities at (051), (033) and (313) reference positions. Table 5.1 reports results confirming that crystallinities were comparable for all samples studied with a minor enhancement noticed when the aluminum content was reduced. Since differences in crystallinity were not found to be pronounced, it is hypothesized that the aluminum content does not have a significant effect on crystallinity.

Table 5.1: HZSM-5 crystallinity and particle diameter.

Sample	Crystallinity (%)	d_{32}^* (μm)
ZSM5-30	94.3	2.85
ZSM5-80	96.4	2.14
ZSM5-280	100.0	2.04
ZMPL-30	N/A	12.82
ZMPL-80	N/A	14.37
ZMPL-280	N/A	14.23
Fused Al	N/A	21.98
Versal 950	N/A	36.1

* Surface weighted mean particle diameter.

5.2.2 N₂ Isotherm

The effect of the HZSM-5 composition on its micro- and meso-structural properties was investigated by analyzing the data from the N₂ adsorption/desorption isotherms considering the IUPAC recommended *check list* [86].

5.2.2.1 N₂ Isotherm plot

Figure 5.3-a to Figure 5.5-a report adsorption/desorption isotherms for the HZSM-5 and its fabricated pellet. One can observe that there was a considerable influence of intercrystalline mesopores in the adsorption/desorption isotherms. Thus, adsorption/desorption cannot be presumably described using one N₂ filling stage. It appears that a two steps pore filling process for low and high pressures is more adequate. One can notice from the low pressure

branch of the isotherm at $P/P_0 = 0.01$, a steep increase in the adsorbed volume up to 90, 99, and 96 ml/g for ZSM5-30, -80, and -280, respectively. It is in this initial low P/P_0 region where a very strong type I adsorption (Langmuir isotherms) [86] can be considered. This low pressure isotherm branch is the result of micropore filling, and can be better appreciated in semi-log plots as in Figure 5.3-b to Figure 5.5-b. The high pressure filling, which continues between 0.01 and 1 P/P_0 , can be related to filling mesopore spacing between the zeolite aggregates.

In the case of the HZSM-5 pellets, the filling capacity of microspores was considerably reduced by about 76% (down to about 25 ml/g volume adsorbed) as one can see from Figure 5.3 to Figure 5.5. This was assigned to the fused alumina that occupies 70 wt% of the pellets with a negligible adsorption capacity of about 1 ml/g as reported in Figure 5.6 (a,b). Concerning Versal 950 (Figure 5.6-a), one can observe an isotherm of Type IV that can be associated with capillary condensation in mesopores [86]. The semi-log plots in Figure 5.6-b validate such an assumption in which 73% of the filling capacity was accomplished in the mesopores span. However, the influence of the Versal 950 on the HZSM-5 pellets isotherms was not noticeable due to its small fraction (5 wt%).

Furthermore, Figure 5.5-a displays double hysteresis for the ZSM5-280 isotherm wherein filling the micropores at $P/P_0 \leq 0.25$, encompasses two substeps designated as “A” and “B”. The presence of these dual substeps was also reported for HZSM-5 with high $\text{SiO}_2/\text{Al}_2\text{O}_3$ ratios [49,50,55,56,87,105,116–118]. Llewellyn et al. [55,56] and Müller et al. [50,116] attempted to explain the origin of such dual substeps by correlating the N_2 isotherms curves with the results from the microcalorimetric and the XRD measurements. In this case, at each isotherm substep, there was a noticeable XRD peak along with an increase in the net differential enthalpy of adsorption. These authors argued that at each substep, the augmentation in the adsorption exothermicity and the XRD intensities were due to the densification of the adsorbate phase. This, therefore, allowed a steep increase in the N_2 uptake probably creating such a substep. Müller et al. [50] supported the idea of liquid-solid phase transition. They did so by: a) demonstrating the similarity between the N_2 uptake ratio before and after the second substep (24/30.5) and b) showing the resemblance of the N_2

liquid/solid density ratio (0.808/1.027) in the N₂ isotherm of the HZSM-5 with a high Si/Al ratio (> 1000)

Considering the above explanations regarding the first substep 'A', at a coverage of about 96 ml/g STP as depicted in Figure 5.5-a, one can postulate that the adsorbate N₂ undergoes a phase transition from a 'disorder fluid like' to a 'dense fluid like' phase that leads to an increase in the adsorbate loading. Further adsorption on the ZSM5-280, in the region between 96 and 120 ml/g STP leads to the formation of the second larger substep 'B' at a P/P₀ = 0.1. This substep is suggested to be a result of the adsorbate solidification from the 'dense fluid like' phase [49,50,55,56,87,116,118].

The presence of dual substeps for ZSM5-280 generates a hysteresis loop at the second substep span. Such a low pressure hysteresis effect has been reported experimentally for an HZSM-5 of very low aluminum content [49,56,87,107,116,117]. This was also theoretically explained using the simulations of Lennard-Jones fluid adsorption on narrow cylindrical pores by employing local and non-local density function theories [119].

The isotherms for ZSM5-30 and ZSM5-80, on the other hand, show only one substep (B) with no hysteresis loop in the low pressure area (P/P₀ ≤ 0.05). Knowing that the energy capacity for HZSM-5 is proportional to its aluminum content from the microcalorimetric measurements, Llewellyn et al. [55,56] suggested that the aluminum in the HZSM-5 framework creates more acid sites. These acid sites strongly interact with nitrogen, adsorbing and thus affecting the early start of the adsorption isotherm with a 'dense fluid like' behavior. These authors hypothesized that the change from a 'dense fluid like' phase to a 'solid like' phase is expected to take place in the vicinities around the aluminum centers. However, this transition process may take place at a lower pressure than those for the HZSM-5 which possess low aluminum content due to the increased adsorbate-adsorbent interactions. This may broaden the curve around substep B which would result in the disappearance of the low pressure hysteresis for HZSM-5 with a low SiO₂/Al₂O₃ ratio.

Other descriptions and considerations are reported by Groen et al. [87]. These authors postulated that the HZSM-5 of an energetically homogenous surface would yield a pronounced low pressure hysteresis loop, while in the more heterogeneous surfaces (with low

Si/Al ratios), such hysteresis would be more greatly diminished. Triantafillidis et al. [49] argued that a combined effect of larger crystals and lower aluminum content could result in a distinguished vertical hysteresis loop at $P/P_0 < 0.2$.

The plateau after substep B at $P/P_0 > 0.05$ for ZSM5-30 and -80, and at $P/P_0 > 0.25$ for ZSM5-280, can be considered an indication of packing in all intracrystalline pores. Thereafter, the isotherms display a second hysteresis loop of type H4 according to IUPAC classification [86]. This is attributed to filling and emptying the voidages between the particles whereas capillary condensation and evaporation which occurs during the course of the adsorption and desorption process [87].

The hysteresis loop for ZSM5-30 exhibited a short increase at the end of the loop. This was found to be wider than those for ZSM5-80 and -280. Such an observation is possibly attributed to the slightly higher particle sizes of ZSM5-30 (2.85 μm) compared to those of ZSM5-80 and -280 (2.14 and 2.04 μm , respectively). With regard to the hysteresis loops for ZSM5-80 and -280, one can observe that the former is found to be larger. Although both ZSM5-80 and -280 have similar mean particle sizes, the particle size distribution for ZSM5-80 shows a somewhat higher distribution of larger particle sizes between 10 and 30 μm as one can observe in Figure 5.1. The HZSM-5 of larger crystal sizes was reported to produce wider high pressure hysteresis loop irrespective of its aluminum content [56,107].

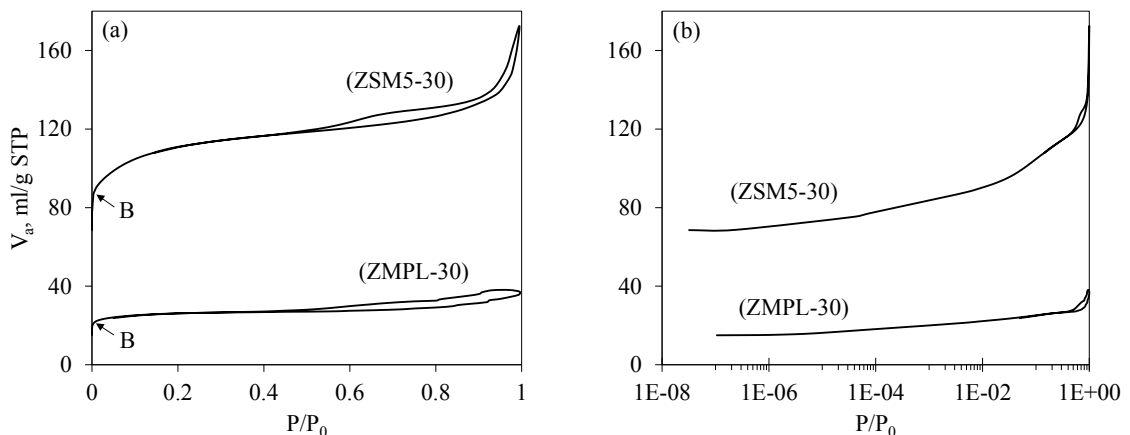


Figure 5.3: N_2 adsorption/desorption isotherm for ZSM5-30 and ZMPL-30: (a) Normal scale, (b) Semi-log scale.

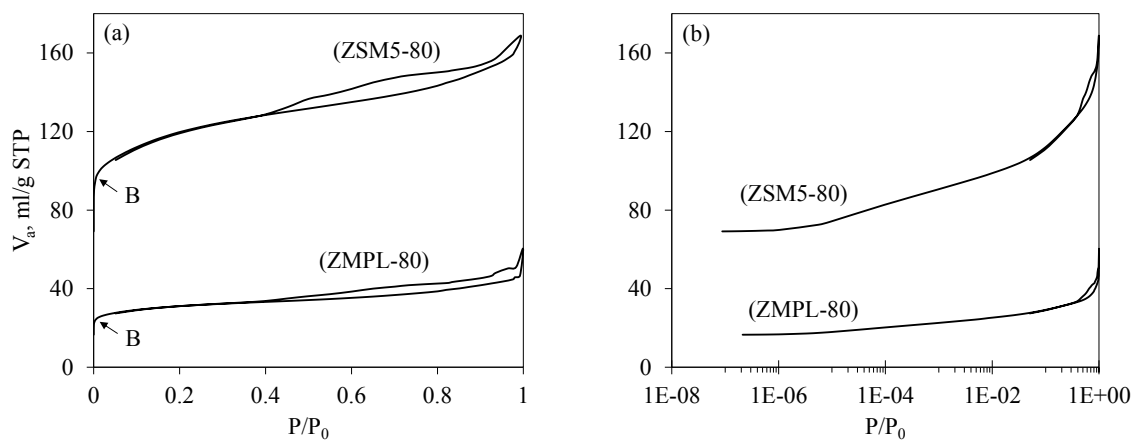


Figure 5.4: N_2 adsorption/desorption isotherm for ZSM5-80 and ZMPL-80: (a) Normal scale, (b) Semi-log scale.

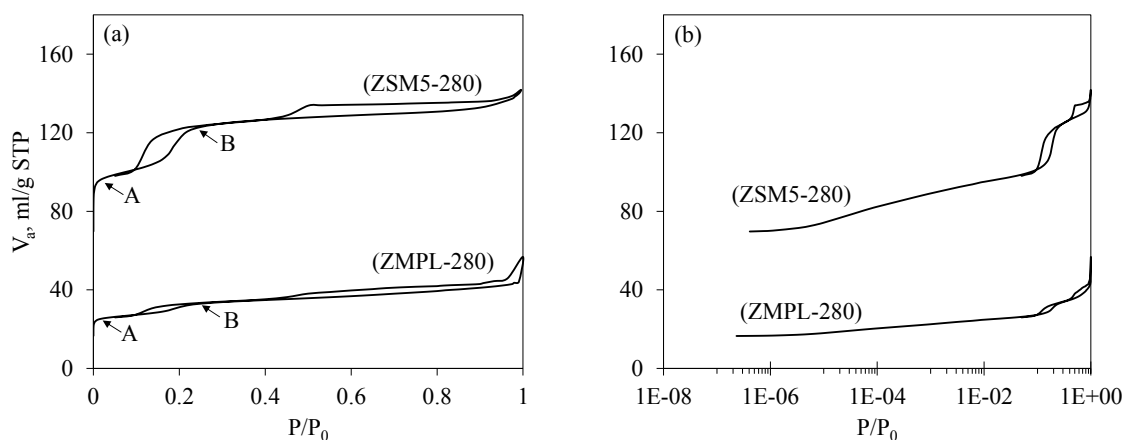


Figure 5.5: N_2 adsorption/desorption isotherm for ZSM5-280 and ZMPL-280: (a) Normal scale, (b) Semi-log scale.

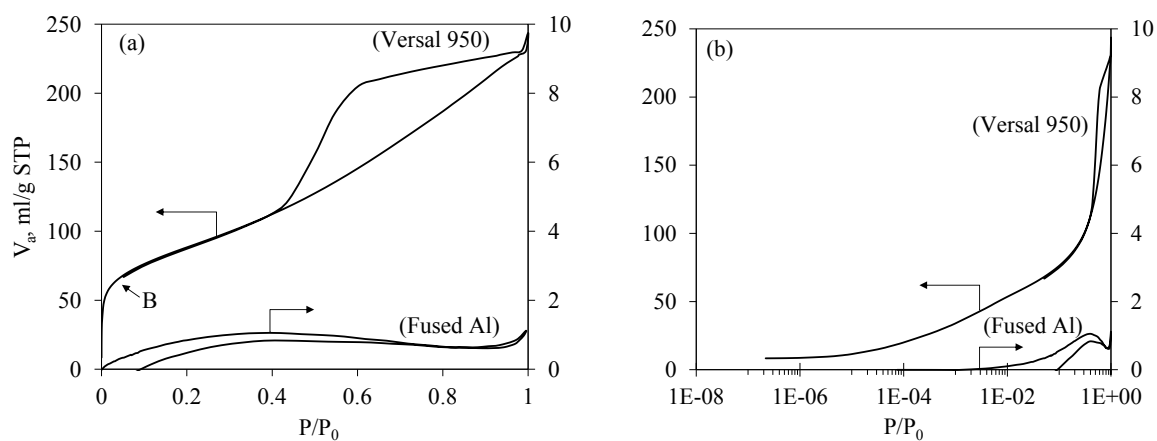


Figure 5.6: N_2 adsorption/desorption isotherm for Versal 950 and Fused Al : (a) Normal scale, (b) Semi-log scale.

5.2.2.2 NLDFT method validity

Specific surface area, specific pore volume, and pore diameter can be calculated from N_2 isotherms. Different methods have been used in the literature to calculate these parameters based on the zeolite pore size. Among them, the density functional theory (DFT) is the state of the art technique that is found to yield a reliable estimation of these parameters [120–123]. Since its introduction by Seaton et al. [124], it has received considerable attention in the studies of sorption and phase behavior of fluids. The original DFT form, a local mean field denoted as LDFT, succeeds in describing the fillings of both macro- and mesopore fillings. It fails however, to model micropores like the ones in HZSM-5 zeolites [125]. On the other hand, the Non-Local Density Functional Theory (NLDFT) was introduced to treat more precisely the fluid adsorption in microporous solids [126]. Since then, NLDFT has been employed to analyze the isotherm data of HZSM-5 materials [122,125]. NLDFT formalism treats the fluid sorption process microscopically on a molecular level based on statistical mechanics. For each relative pressure point and based on the assumed geometry, NLDFT calculates the fluid density profiles across the inner pore surfaces using a complex mathematical modeling of gas-solid and gas-gas interactions. From these density profiles, the adsorbed amount can be derived at each relative pressure, that formulates the isotherm curve [125]. The original form of the NLDFT method was developed for modeling slit-like pores on activated carbons. It was extended later to cylindrical pores by Saito and Foley [89,118] whom demonstrated its usefulness for predicting the true micropore size for the HZSM-5 structure from the N_2 adsorption data. Afterward, multiple studies proved that a cylindrical pore model can be justified for the inner channels of HZSM-5 [87,102,122,127]. The approach in the current study, however, is to examine both geometries for predicting the N_2 adsorption isotherm and calculating the main porosity parameters.

Table 5.2 reports gas adsorbed volume (V_a) and STD of gas adsorbed volumes calculated values using both the cylindrical and slit pore shapes. One can notice that the cylindrical model V_a displays slightly higher error spans than the slit pore model. However, both models show low STD spans within the predicted V_a . One can also observe from Figure 5.7 and Figure 5.8 that both models provide a good prediction of the experimental isotherm values.

On this basis, one can conclude that both pore models are equally suitable for fitting the adsorption isotherm data.

Table 5.2: NLDFT^a standard deviation (STD) of isotherm fit.

		ZSM5-30	ZSM5-80	ZSM5-280
		68.5-172.5 ^b	69.2-168.8 ^b	69.7-141.8 ^b
STD on V_a (ml/g STP)	Cylindrical	2.08	0.89	1.23
	Slit	0.86	0.40	0.51

^a Method: Non-negative regularization; no smoothing. ^b V_a range (ml/g STP)

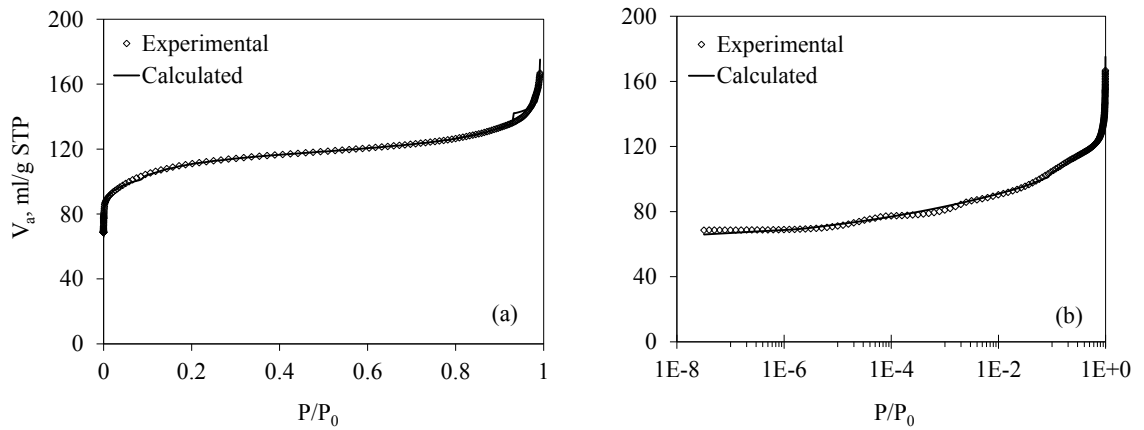


Figure 5.7: NLDFT N₂ isotherm goodness of fit using cylindrical geometry for ZSM5-30 (a) Normal scale, (b) Semi-log scale.

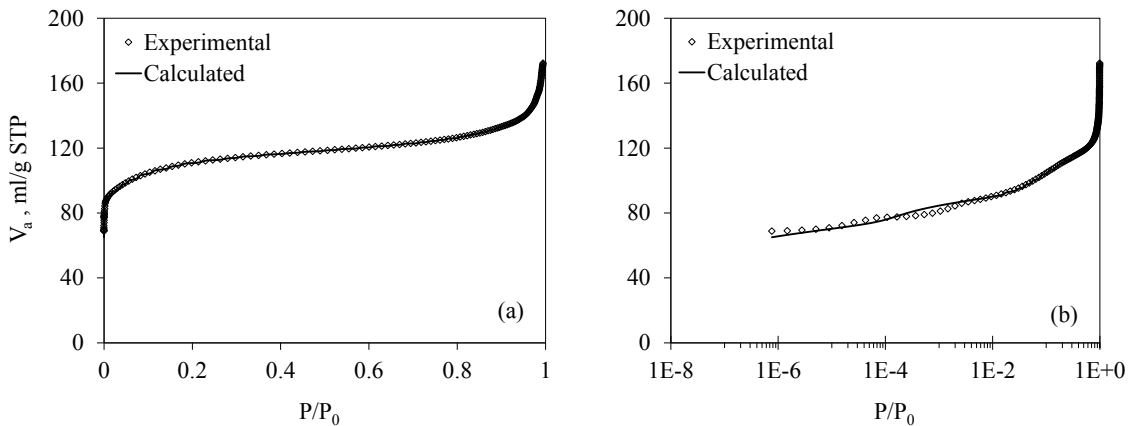


Figure 5.8: NLDFT N₂ isotherm goodness of fit using slit-like geometry for ZSM5-30 (a) Normal scale, (b) Semi-log scale.

5.2.2.3 Porosity characteristics methods

NLDFT method, in addition to its employment as a technique for measuring porosity characteristics, it can be utilized as in present study as a bench mark to validate the other traditional methods. These methods include BET, Langmuir, *t*-plot, D-A, BJH, and HK. These techniques are configured in the same analyzer employed for the isotherm measurements as describe in section 4.3.3. The theoretical background of these methods can be found elsewhere [125].

BET, Langmuir, *t*-plot, and D-A all use linear regression (least squares) to fit their respective transformed isotherm data. The y-axis $\left(\frac{1}{V_a(P/P_0-1)}\right)$ for BET, $\left(\frac{1}{V_a(P/P_0)}\right)$ for Langmuir, and statistical thickness (*t*), all are plotted versus (P/P₀). The D-A formalism, on the other hand, has a $\log(V_a)$ vs $\log(P/P_0)^n$ linear relationship. While performing a D-A calculation, the instrument searches for the best n values that give error at the y-intercept smaller than 10⁻⁴ that results in n = 1 for ZSM5-30 and ZSM5-80, and n = 1.154 for ZSM5-280.

Table 5.3 shows the high degree of applicability of each model with their correlation coefficients being very close to unity. In spite of its importance many studies have reported the BET area for HZSM-5 without mentioning the pressure range [53,54,60,106–109,117,128–130]. Others authors, on the other hand, have used 0.05-0.3 relative pressure for USY zeolites [102]. However the much lower relative pressure range of 0.01 is known to be highly recommended for BET measurements with microporous sorbents [88,125]. In these cases there is also agreement between the BET area and its single point value, as depicted in Table 5.5 .

Table 5.3: Statistical parameters for N₂ isotherm linear methods.

Method	ZSM5-30			ZSM5-80			ZSM5-280		
	P/P ₀	R ² ^a	DOF ^b	P/P ₀	R ² ^a	DOF ^b	P/P ₀	R ² ^a	DOF ^b
BET	0.001 - 0.1	0.9999	34	0.001 - 0.1	0.9999	17	0.001 - 0.1	0.9999	19
Langmuir	0.02 - 0.1	0.9998	27	0.05 - 0.2	0.9998	18	0.001 - 0.1	0.9999	19
<i>t</i> -plot	0.5 - 0.97	0.9991	11	0.64 - 0.98	0.9962	10	0.55 - 0.93	0.9972	9
D-A	0.05 - 0.2	0.9999	48	0.07 - 0.17	0.9991	12	0.00003 - 0.09	0.9991	24

^a Correlation coefficient.

^b Degree of freedom = data points – 2.

The BJH model [131], based on the classical Kelvin equation and the selected thickness formula, is commonly used for estimating the mesoporosity parameters. The Kelvin equation describes the capillary condensation in a cylindrical pore in which the saturation pressure point (i.e. the adsorptive will condense and evaporate) is calculated. Thus, the BJH method applies the Kelvin equation to calculate the pore sizes using the measured pressure and the multilayer thickness [87,88,125]. Among the common equations used to calculate the multilayer thickness, the one proposed by Harkins and Jura [132] is often employed for zeolitic materials [125] and hence it is selected here.

The HK formula [133] describes a semi-empirical method to calculate the effective micropore size distribution from the adsorption isotherm. The model is originally based on the statistical analysis of confined fluid in slit-shape pores and then extended to cylindrical pores for zeolite materials [89]. Cheng and Yang [134] proposed an additional model modification that incorporates a Langmuir isotherm. This was implemented in order to correct the deviation of the isotherm data from Henry's law at higher relative pressures. In the present study, the cylindrical HK model with the Cheng and Yang correction is used to predict the micropore sizes. The covered isotherm data for each NLDFT, BJH, and HK technique is taken according to the relative pressure ranges for the micro- and mesopores filling as specified earlier for each HZSM-5 sample.

D-A formalism calculates the surface area and pore volume based on the micropore filling principle. The volume of monolayer gas adsorbed obtained from the D-A linear relation is converted to pore volume using the density conversion factor:

$$V_{monolayer} = V_m \left(\frac{\text{ml STD}}{\text{g}} \right) \times 0.001547 \left(\frac{\text{ml liq}}{\text{ml STD}} \right) \quad (5.1)$$

The monolayer volume is then used for calculating the internal surface area following an empirical correlation described in [88,125].

In the t -plot method, a multilayer formation of N_2 is modeled mathematically to calculate a layer "thickness, t " as a function of increasing the P/P_0 . The t -plot method is designed to determine the micropore volume and external surface areas by plotting the adsorbed volume

versus the statistical thickness. The thickness formula used in the present study is similar to one for the BJH technique (Harkins and Jura).

Concerning the isotherm data with the hysteresis effect, it was reported that the porosity results obtained from the adsorption data differ greatly from the ones obtained from the desorption data due to the Tensile Strength effect (TSE). This phenomenon happens at the high pressure hysteresis loop when the desorption curve is forcedly lowered at the closure point with the adsorption curve having a relative pressure of about 0.4. This is believed to be due to the spontaneous evaporation of the metastable liquid packed in the pores [125]. Such an effect in the PSD calculation implies that an artificial spike in the PSD curve may produce one that is normally lower than the true size. Such peaks may take place due to the characteristic steps at the desorption isotherm because of the nature of the adsorptive material. However, they certainly do not reflect a real pore size [87,125]. Similar to the TSE phenomena, a phase transition occurs at a low pressure hysteresis loop that may lead to false PSD results. This is the case, since this phase transition is related to HZSM-5 composition and does not show any real porosity. It was reported that a material with combined micro- and mesopores is most probably affected by TSE and phase transition [87]. In order to avoid such effects, the adsorption branch data are applied in the present study in the NLDFT, BJH, and HK calculations.

5.2.2.4 HZSM-5 pore size distribution

As described earlier, the HZSM-5 catalyst features both micro- and mesoporosity. Thus, the selected methods for calculating the pore size distribution (PSD) should be adequate to consider the entire isotherm data. One approach is to select a suitable method in each section, e.g. HK for micropores and BJH for mesopores [105]. A challenge that may arise when using this approach is the inter-influence between the micro- and mesopores which may lead to erroneous PSD estimations. An accurate pore size analysis applied to the entire isotherm data could be attained by applying an advanced microscopic technique based on statistical mechanics such as NLDFT. Therefore, NLDFT is used in the present study to predict the PSD and the mean pore diameter for HZSM-5 and its formulated pellets.

The adsorption isotherms in Figure 5.3 to Figure 5.5 can be used to establish PSD by applying differential plots that include incremental pore volume per incremental pore size ($\Delta V_p/\Delta d_p$, ml/g/Å) as a function of pore size (d_p , Å) in accordance with the ASTM D4641-12 standard [135]. On this basis, the mean mesopore diameter can be calculated according to the following equation:

$$\overline{d_p} = \frac{\int_{d_{pmin}}^{d_{pmax}} f d_p \Delta d_p}{\int_{d_{pmin}}^{d_{pmax}} f \Delta d_p} \quad (5.2)$$

where $f = \Delta V_p/\Delta d_p$.

By IUPAC classification, pores larger than 500 Å are termed macropores, smaller than 20 Å named micropores, and those in between termed mesopores [86]. Figure 5.9 shows the narrow distribution of the micropore sizes derived from the cylindrical model. These pores are centered at 5.22 Å for both of ZSM5-30 and -80, while they are centered at 5.58 Å for ZSM5-280. This observed pore size is in agreement with the expected HZSM-5 channel dimensions [30,51,105]. The slit-like micro-PSD in Figure 5.10, on the other hand, shows a sharp peak at 3.93 Å. This value is lower than the 5.4-5.6 Å pore size expected for HZSM-5 zeolites. Saito and Foley [89] observed similar variations in Y zeolites in comparison to the cylindrical and slit-like models. The HK micropore filling, conversely, overpredicts the micropores (6.8 – 7.6 Å) as one can see from Table 5.4. This could be the effect of the high mesoporosity as one can notice in Table 5.5 as will be discussed in section 5.2.2.5 [87]. Therefore, the NLDFT cylindrical model is the only technique that was found to predict the true dimension of HZSM-5 pore openings.

Concerning the PSD of mesopores, the cylindrical model gives a limited distribution of mesopores of up to 400 Å. The slit-like model, however, shows the sharpest peaks being close to 20 Å with the various HZSM-5 displaying macropores of up to 2300 Å. This could be the reason behind the higher observed mean meso- d_p (140-60 Å) using the slit-like model while compared with that of the cylindrical model (70-50 Å) (refer to Table 5.4). On the other hand, the meso- d_p obtained by BJH and cylindrical NLDFT models show similar predictions. Thus, the PSD results jointly suggest that the cylindrical pore model of the

NLDFT formalism would give a closer representation of the HZSM-5 micro- and mesopores structures.

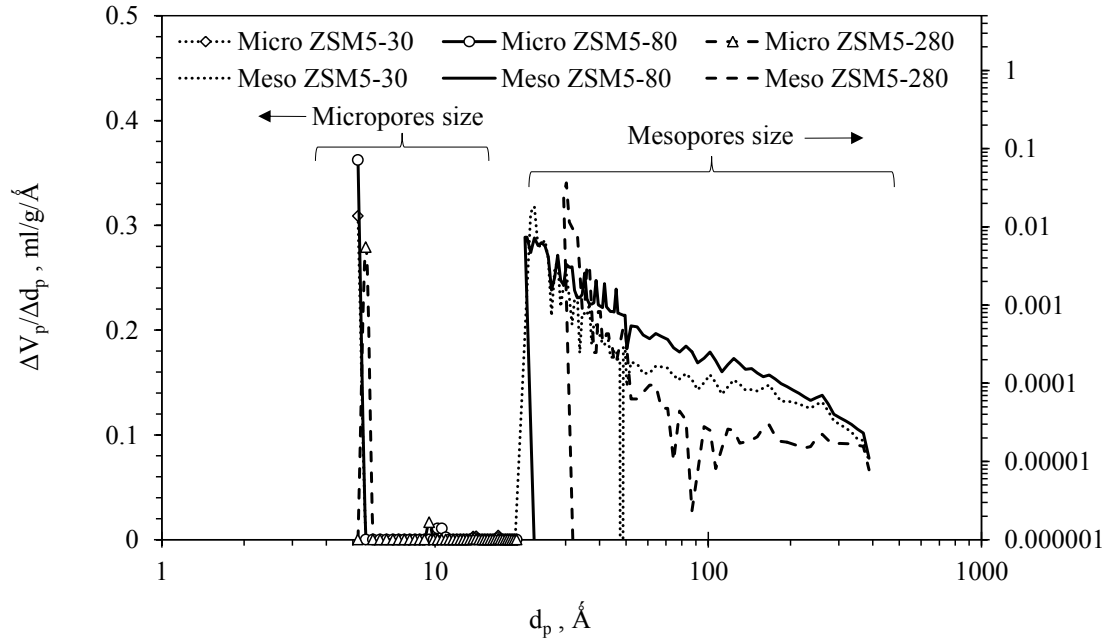


Figure 5.9: NLDFT pore size distribution of HZSM-5 (cylindrical geometry model).

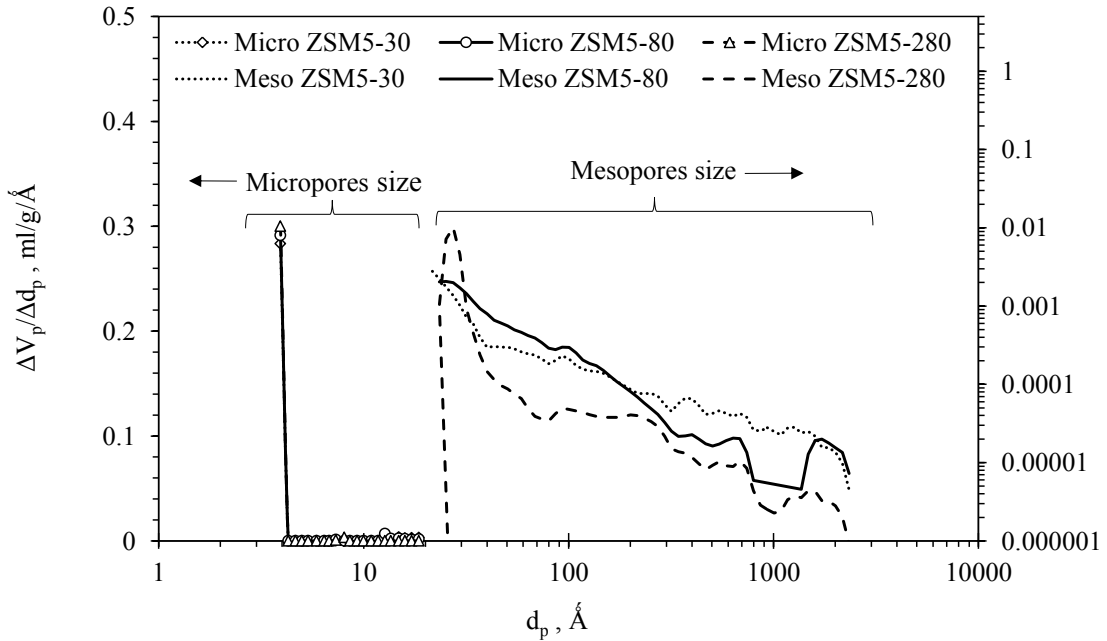


Figure 5.10: NLDFT pore size distribution of HZSM-5 (slit-like geometry model).

Table 5.4: HZSM-5 and pellets pore size (Å).

Method	BJH ^{a,b,c} ($4V_p/A_p$)		HK ^{c,d}		NLDFT cylindrical ^e		NLDFT Slit-like ^f	
Sample	Micro- d_p	Meso- d_p	Micro- d_p	Meso- d_p	Micro- d_p	Meso- d_p	Micro- d_p	Meso- d_p
ZSM5-30	N/A ^g	61	6.8	N/A ^g	5.22	59	3.93	140
ZSM5-80	N/A ^g	49	7.1	N/A ^g	5.22	69	3.93	93
ZSM5-280	N/A ^g	48	7.6	N/A ^g	5.58	50	3.93	60
ZMPL-30	N/A ^g	N/A ^g	N/A ^g	N/A ^g	6.52	68	N/A ^g	N/A ^g
ZMPL-80	N/A ^g	N/A ^g	N/A ^g	N/A ^g	6.54	75	N/A ^g	N/A ^g
ZMPL-280	N/A ^g	N/A ^g	N/A ^g	N/A ^g	7.31	61	N/A ^g	N/A ^g
Fused Al	N/A ^g	N/A ^g	N/A ^g	N/A ^g	N/A	34	N/A ^g	N/A ^g
Versal 950	N/A ^g	N/A ^g	N/A ^g	N/A ^g	14.36	91	N/A ^g	N/A ^g

^a Thickness curve type Harkins and Jura: t -plot = $[13.99/(0.034 - \log(P/P_0))]^{0.5}$.

^b Barrett-Joyner-Halenda method.

^c Mesopores range: $20 < d_p < 500$ Å.

^d Horvath-Kawazoe, micropore pressure range, Method: interaction parameter for zeolite adsorbent = 3.49×10^{-43} ergs/cm⁴, Cheng and Yang correction.

^e Cylindrical pore geometry model (Saito/Foley): Method: Non-negative Regularization; No Smoothing.

^f Slit pore geometry model: Method: Non-negative Regularization; No Smoothing.

^g Not applicable.

The influence of the pellet matrix materials on the HZSM-5 pore size is examined using the NLDFT cylindrical pore model as shown in Figure 5.11. One can observe that the binder material (Versal 950) displays micropores at 5.5, 15.5 and 18.5 Å. The porous structure of the fused Al, however, did not show microporosity as expected. Concerning the mesopores, the cylindrical model gives a wide distribution within 20-400 Å for all samples as shown in Figure 5.11-b with the majority of the mesopores being concentrated in the 20 - 100 Å range. Regarding the observed increase in the pellet mean pore diameter from Table 5.4 (micro- d_p = 6.5-7.3 Å, meso- d_p = 61-75 Å) while compared to the pure zeolite (micro- d_p = 5.2-5.6 Å, mesopores = 50-69 Å), one can attribute this behavior to the Versal 950 addition (micro- d_p = 14.4 Å, mesopores = 91 Å).

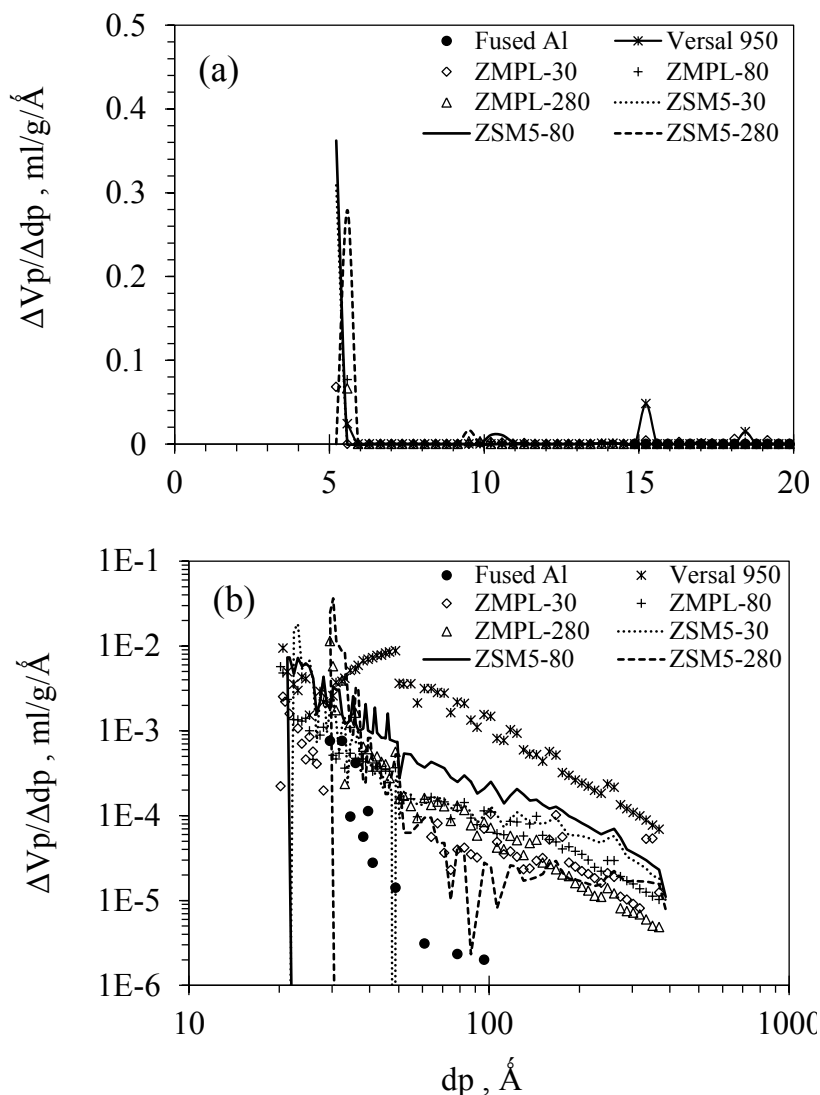


Figure 5.11: Pore Size Distribution (NLDFT cylindrical model): (a) Micropores, (b) Mesopores.

5.2.2.5 Specific surface area and pore volume

Table 5.5 reports the micro-, meso-, and total surface area and pore volume for HZSM-5 using multiple methods. The resulting BET-C values (>1000 for ZSM5-30 and ZSM5-80, <0 for ZSM5-280) are one indication of micropores [88]. BET is the most commonly used method in the literature for HZSM-5 surface area measurements with typical values as those presented in Table 5.5 ($399\text{--}441 \text{ m}^2/\text{g}$) [53,54,60,106–109,117,128–130]. It can be noticed that these values along with the Langmuir method ($442\text{--}544 \text{ m}^2/\text{g}$) and the NLDFT slit-like model ($569\text{--}605 \text{ m}^2/\text{g}$) apparently differ from those of the NLDFT cylindrical model (826--

1142 m²/g). Such inconsistency can be explained by knowing that both BET and Langmuir methods assign the filling of micropore volumes to the free surface coverage. Depending on the known pore sizes of the zeolite tested, Langmuir and BET may underestimate or overestimate the surface area.

According to Table 5.5, the pores with a size smaller than 20 Å have a volume of around 0.12 ml/g. Converting this value by using the area occupied by a single N₂ molecule (1.62×10⁻¹⁹ m²/molecule) times Avogadro's number (6.023×10²³ molecule/mol) times the molar volume of liquid N₂ (0.0288 mol/ml) would yield an internal surface area of 298 m²/g. One can notice that from a simple geometrical analysis; assuming a cylindrical pore size, the pore area (A_p) = 4V_p/d_p and a typical pore size of 5.5 Å, the HZSM-5 area is 872.7 m²/g. This is much higher than the expected 298 m²/g value. On the other hand, if we assume an upper pore size limit of 20 Å for the micropores, then the internal surface area would be 240 m²/g which instead of 298 m²/g. Those specific surface areas can only be equal with pore sizes of 16.1 Å. This analysis shows that BET and Langmuir models would give specific surface areas lower than the true HZSM-5 values.

In addition, the resulting BET-C values for ZSM5-30 and ZSM5-80 (>>100) provide indication of a non-uniform surface coverage with preferential adsorption sites [88].

In their book, Lowell et al. [125] reported that the BET surface area for microporous solids may not reflect true values. These data can be rather considered as a kind of “equivalent BET area” since the micropore filling does not occur completely in the multilayer adsorption region. These authors concluded that the BET equation is not applicable to microporous substances. In the case of HZSM-5 with 5.5 Å micropores, formalism based on molecular scale statistical thermodynamic, like NLDFT, would provide a more realistic micropore surface area.

When comparing the two shape options of the NLDFT model, the cylindrical model estimates a micropore area closer to the true value than those that obtained by the slit-like model for a given micropore volume (Table 5.5). The same holds true for the case of mesopore surface area. In view of the above facts, it can be concluded that the NLDFT cylindrical model is an ideal option for predicting the “true” surface area of HZSM-5. Similar

findings for several microporous materials were reported in the studies on HZSM-5 [127], FCC catalysts (Y zeolites) [102,122,123], and Pillared Interlayered Clay (PILC) [121]. Occelli and coworkers [123] stated that the deviations between NLDFT and traditional methods increase as the micropore size approaches the adsorptive molecular diameter. This is the case in the present study, since N₂ molecular size is 3.1 Å.

By looking at Table 5.5, one can see that the *t*-plots' external surface area (11-36 m²/g) underestimates the true one, based on the NLDFT cylindrical model. Additionally, *t*-plots overpredict the internal pore volume (0.16-0.19 ml/g). Since the external surface area and the internal pore volume are both proportional to the slope of the *t*-plot's linear equation, Sayari et al. [136] reported the decrease of its accuracy as the slope approaches zero. This is the case of the present samples (2.2, 2.3, 0.7 for ZSM5-30, ZSM5-80, and ZSM5-280, respectively).

Like in the case of the *t*-plot method, the D-A technique overestimates the micropore volumes (0.16-0.21 ml/g) and underestimates the internal surface areas (465-518 m²/g). Similarly, the BJH technique underpredicts the external surface area (48-72) compared to the results obtained by the cylindrical model (98-106 m²/g) while the external pore volumes (0.08-0.09 ml/g) were in good proximity with those from NLDFT calculations (0.1-0.11 ml/g) for ZSM5-30 and ZSM5-80.

The predicted micro-, meso-, and total pore volumes from the two models of NLDFT show a negligible influence by the HZSM-5 pore geometry as one can notice in Table 5.5. To confirm the validity of the NLDFT estimation, this estimation was cross-checked with the total pore volume using a single point method. This method assumes that the gas volume adsorbed on the free surface is insignificant compared to the gas volume adsorbed into the pores. One should notice that the true volume of an incompressible fluid occupying the pores can be calculated by converting the gas volume adsorbed near the saturation pressure to the liquid volume. The resulting values in 0.21-0.24 ml/g range are in good agreement with the total pore volume calculated by the NLDFT model (0.19-0.23 ml/g). Even though the pore geometry shows not to have significant effect on pore volume, the slit-like model fails to describe pore diameter and surface area. Thus, it can be concluded that the extension of the NLDFT formalism for cylindrical geometry is more suitable for HZSM-5 exhibiting

cylindrical pores. Given the above reasons, the NLDFT cylindrical model is selected in the present study as a reliable method for evaluating the HZSM-5 porous characteristics of different SiO₂/Al₂O₃.

Table 5.5: Pore surface area (m²/g) and pore volume (ml/g).

Sample		ZSM5 -30	ZSM5 -80	ZSM5 -280	ZMPL -30	ZMPL -80	ZMPL -280	Fused Al	Versal 950
Sample weight (g)		0.101	0.115	0.083	0.165	0.159	0.146	0.113	0.15
Micro -A _p	D-A ^a	465	512	518	N/A ⁱ	N/A ⁱ	N/A ⁱ	N/A ⁱ	N/A ⁱ
	NLDFT cylindrical ^b	861	1036	728	211	207	177	0	120
	NLDFT Slit-like ^c	540	572	556	N/A ⁱ	N/A ⁱ	N/A ⁱ	N/A ⁱ	N/A ⁱ
Meso -A _p	BJH ^{d,e,f}	48	72	48	N/A ⁱ	N/A ⁱ	N/A ⁱ	N/A ⁱ	N/A ⁱ
	<i>t</i> -plot ^d	34	36	11	N/A ⁱ	N/A ⁱ	N/A ⁱ	N/A ⁱ	N/A ⁱ
	NLDFT cylindrical ^b	101	106	98	14	31	31	2	198
	NLDFT Slit-like ^c	29	33	42	N/A ⁱ	N/A ⁱ	N/A ⁱ	N/A ⁱ	N/A ⁱ
Total- A _p	BET C parameter	1441	4414	-1833	N/A ⁱ	N/A ⁱ	N/A ⁱ	N/A ⁱ	N/A ⁱ
	BET A _p	414	441	399	N/A ⁱ	N/A ⁱ	N/A ⁱ	N/A ⁱ	N/A ⁱ
	BET, single point ^g	410	439	397	N/A ⁱ	N/A ⁱ	N/A ⁱ	N/A ⁱ	N/A ⁱ
	Langmuir	474	544	442	N/A ⁱ	N/A ⁱ	N/A ⁱ	N/A ⁱ	N/A ⁱ
	NLDFT cylindrical ^b	962	1142	826	225	238	208	2	318
	NLDFT Slit-like ^c	569	605	598	N/A ⁱ	N/A ⁱ	N/A ⁱ	N/A ⁱ	N/A ⁱ
Micro -V _p	D-A ^a	0.194	0.213	0.161	N/A ⁱ	N/A ⁱ	N/A ⁱ	N/A ⁱ	N/A ⁱ
	<i>t</i> -plot ^d	0.161	0.184	0.191	N/A ⁱ	N/A ⁱ	N/A ⁱ	N/A ⁱ	N/A ⁱ
	NLDFT cylindrical ^b	0.12	0.14	0.104	0.033	0.031	0.026	0	0.032
	NLDFT Slit-like ^c	0.119	0.126	0.111	N/A ⁱ	N/A ⁱ	N/A ⁱ	N/A ⁱ	N/A ⁱ
Meso -V _p	BJH ^{d,e,f}	0.075	0.088	0.033	N/A ⁱ	N/A ⁱ	N/A ⁱ	N/A ⁱ	N/A ⁱ
	NLDFT cylindrical ^b	0.095	0.108	0.085	0.017	0.035	0.033	0.002	0.305
	NLDFT Slit-like ^c	0.114	0.077	0.073	N/A ⁱ	N/A ⁱ	N/A ⁱ	N/A ⁱ	N/A ⁱ
Total- V _p	Single point ^h	0.235	0.249	0.212	N/A ⁱ	N/A ⁱ	N/A ⁱ	N/A ⁱ	N/A ⁱ
	NLDFT cylindrical ^b	0.215	0.248	0.189	0.05	0.066	0.059	0.002	0.337
	NLDFT Slit-like ^c	0.233	0.203	0.184	N/A ⁱ	N/A ⁱ	N/A ⁱ	N/A ⁱ	N/A ⁱ

^a Dubinin–Astakhov method, affinity coefficient for N₂ = 0.33.

^b Cylindrical pore geometry model (Saito/Foley): Method: Non-negative Regularization; No Smoothing.

^c Slit pore geometry model: Method: Non-negative Regularization; No Smoothing.

^d Thickness curve type Harkins and Jura: *t*-plot = [13.99/(0.034–log(*P*/*P*₀))] ^{0.5}.

^e Barrett-Joyner-Halenda method.

^f Mesopores range: 20 < *d*_p < 500 Å.

^g at *P*/*P*₀ = 0.1.

^h liquid N₂ volume adsorbed at saturation pressure (*P*/*P*₀ = 0.98).

ⁱ Not applicable.

The reported 0.2-0.25 ml/g pore volumes, 826-962 m²/g surface areas, 50-69 Å meso-d_p, and 5.22-5.58 micro-d_p in Table 5.4 and Table 5.5 are based on the NLDFT cylindrical model applicable to HZSM-5 zeolites [49,105–107,137]. The examination of these results shows slightly larger surface area, pore volume and mesopore diameters for ZSM5-80 than for ZSM5-30 and ZSM5-280. The reported specific surface areas and pore volumes are consistent with HZSM-5 materials of comparable structural properties.

After pelletization, one can observe a reduction of both the surface area and pore volumes of 75-79% and 69-77%, respectively. By analyzing the properties of fused Al, that occupy 70% of the pellet, one can confirm its negligible porosity (SA = 2 m²/g, V_p = 0.002 ml/g). Thus, fused Al is likely being the main factor responsible for the reduction in the pellet porosity. The binder (Versal 950), on the other hand, shows dominant mesopores that contain 90% of the total pore volume and 62% of the total surface area. Thus, Versal 950 is unlikely to affect the pellets specific surface area or pore volume given that it contributes with 5 wt% of the pellet composition.

5.2.2.6 Summary

This section presents a detailed investigation on the effect of the SiO₂/Al₂O₃ ratio and the pellet materials on HZSM-5 porosity characteristics based on N₂ isotherm data. HZSM-5 with low aluminum content produced a dual hysteresis loop compared to a single one produced by HZSM-5 with a higher SiO₂/Al₂O₃ ratio. With regard to the method used to predict HZSM-5 porosity, an NLDFT cylindrical pore model provides a good description over the entire range of micro and mesopores and shows a channel size in the expected pore diameter of 5.4-5.6Å. The reported porosity results show that the SiO₂/Al₂O₃ ratio is unlikely to have a significant effect on the structural properties of the HZSM-5 and its formulated pellets. There is, however, a reduction in the pellet porosity and this is attributed to the filler addition. The binder, on the other hand, is considered to contribute to the increase in the pellet mean micro- and meso-pore dimensions.

5.3 Surface Acidity Characterization

5.3.1 Total Acidity and Acidity Distribution

Figure 5.12 reports a set of NH₃-TPD curves obtained with $\beta = 15^\circ\text{C}/\text{min}$ temperature ramp. The TPD plots were first baseline-corrected by subtracting the “blank” TPD from the NH₃-TPD. Two distinct temperature peaks were observed at 346-385°C and at 180-193°C for HZSM-5. These two peaks represent two different types of acidity strength: i.e. weak and strong site acidity. Similar findings were obtained for HZSM-5 by others [49,97,98,104,107–109,138–147].

Upon pelletizing HZSM-5, the overlapping between the strong and weak acid sites became even more pronounced as reported in Figure 5.12-b. Additionally, the amount of strong acid sites displayed a reduction in catalyst pellets, with a shift of the peaks towards lower temperatures (249-316°C). One can also notice that the binder material (Versal 950) showed a high adsorption capacity. This is expected given the adhesive property of Versal 950. However, when it was diluted with the fused alumina (i.e. ZMPL-BL), the TPD data showed a limited acidity. On this basis, one can assume a negligible contribution of the matrix materials on HZSM-5 catalytic properties.

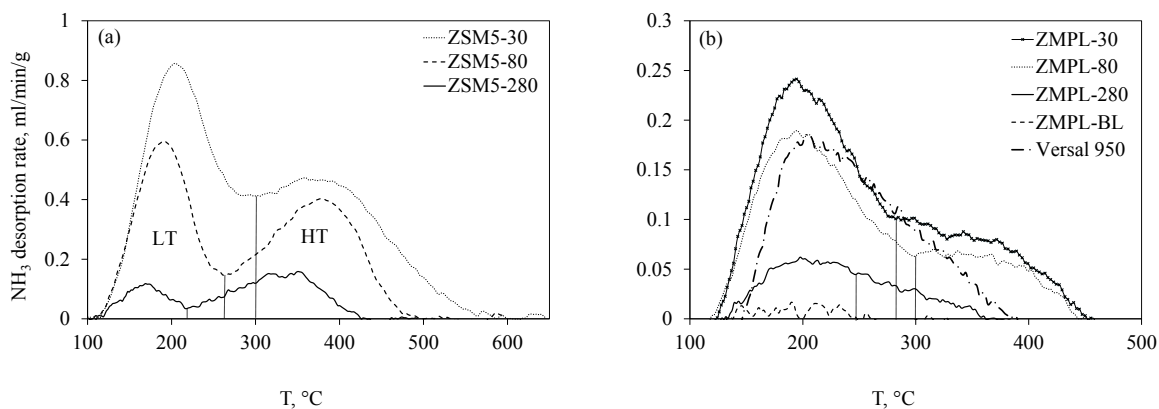


Figure 5.12: NH₃-TPD thermograms at $\beta = 15^\circ\text{C}/\text{min}$ for: (a) pure HZSM-5 (b) HZSM-5 pellets.

To quantify weak and strong acidities, each NH₃-TPD profile was separated into two sections. The “valley” between the two partially overlapped peaks was used as a separation

reference point. A vertical line was drawn between the “valley” and the baseline as presented in Figure 5.12 (a,b). The pellet matrix (ZMPL-BL) displayed indistinctive peaks while the TPD curve for Versal 950 shows showed only one peak. Following this step, the acidity was estimated by integrating the resulting TPD area.

Table 5.6 reports theoretical and measured acidity values. The theoretical acidity is the one obtained via the reaction stoichiometry (Equation 4.1, section 4.2) according to the following formula:

$$\text{Stoichiometric acidity} = \alpha \left(\frac{\text{mole } NH_3}{\text{mole } HZSM-5} \right) \frac{1}{Mw_{HZSM-5}} \left(\frac{\text{mole } HZSM-5}{g \text{ } HZSM-5} \right) \quad (5.3)$$

with α being a stoichiometric coefficient of 1 and Mw being the molecular weight of the HZSM-5. Mw is calculated according to the HZSM-5 chemical formula: $(SiO_2)_x(Al_2O_3)H^+$, where x is the SiO_2/Al_2O_3 ratio.

Data in Table 5.6 confirms that the measured strong site acidity agrees with the theoretical one for ZSM5-280 and ZSM5-80 (1.1 and 0.8 ratio). This parameter is, however, reduced by 60% in the ZSM5-30. This is in line with ZSM5-30 having the highest aluminum content. One should notice that these results are in good agreement with those by Rodríguez-González et al [141]. These authors found that the fraction between the strong acid content and theoretical acidity was close to 1 for the low range of aluminum content (0-0.1 mmol/g). This ratio was, however, reduced by increasing the aluminum content. Miyamoto et al. [104] obtained similar findings using the Ga-MFI zeolite.

Table 5.6 also suggests that the ammonia adsorbs on the strong acid sites as ammonium cations (protonic acidity) whereas its sorption on the weak sites occurs via a hydrogen-coordinated bond. These findings concur with those by Katada et al. [140], Niwa et al. [140,143], Miyamoto et al. [104], Forni et al. [100], and Bangasco et al. [148]. These authors reported a correlation between the measured strong acid sites and the stoichiometric total acidity. Additionally, Katada et al. [140] and Niwa et al. [140,143] showed a decrease of weak acidity with the extent of ion exchange (decreasing Na/Al ratio) while strong acidity, on the contrary, was increased. This should, in principle, imply that there is a formation of acid sites with ion exchange. Furthermore, it was also proven that a 12-16 h evacuation at

100°C after ammonia adsorption on HZSM-5 resulted in the disappearance of weak acidity while the strong acidity remained unchanged [100,140,141,143,146]. Katada et al. [140] and Niwa et al. [140,143] acknowledged that while the adsorption sites in the low temperature peak region could be termed acid sites, they likely do not have significant catalytic value.

Table 5.6: Theoretical and measured acidities for HZSM-5 samples ($\times 10^{-5}$ mol_{NH₃}/g_{HZSM-5}).

Sample	Mw (g/mol)	Measured acidity		Theoretical acidity	Measured Strong acidity Theoretical acidity
		Weak	Strong		
ZSM5-30	1906	42.9	21	52.5	0.4
ZSM5-80	4910	16.5	16.7	20.4	0.8
ZSM5-280	16931	4.3	6.3	5.9	1.1

A more detailed discussion of this matter is given by Woolery et al. [147] and Rodríguez-González et al. [141,146] who assumed that ammonia is adsorbed on weak sites of Lewis nature which is bound via hydrogen-coordination to NH₄⁺ (i.e., (NH₃)_nNH₄⁺/ZSM-5⁻ complex). On the other hand, ammonia adsorption on strong acid sites occurs by specific interactions with framework aluminum sites that lead to the decomposition of the stoichiometric adsorption complexes (i.e. NH₄⁺/ZSM-5⁻ ion-pair complex). These researchers support their hypothesis by demonstrating that the low-temperature-peak disappears when the NH₃-saturated sample is purged with wet He gas. The wet sample then yields one TPD peak profile similar to the high-temperature TPD peak obtained after purging with dry He. Similar findings were obtained also by Katada et al. [140] and Bagnasco et al. [148] when HZSM-5 was exposed to water vapor. Thus, the ability of water to build hydrogen bridges leads to the replacement of ammonia by water in the weak sites while ammonia stays bound on the strong acid sites [141]. Miyamoto et al. [104] got similar results using the Ga-MFI zeolite. They concluded that water replaces ammonia on the weak sites via physisorption hydrogen-bonding. Thus, the present study along with the technical literature confirm that weak sites are non-acidic in nature with ammonia species being either adsorbed (weakly chemisorbed) and/or held in place by means of hydrogen bridging bonds (physisorbed).

Table 5.7 describes the total number of acid sites, the breakdown of strong and weak sites, their ratios, and the corresponded maximum temperatures for HZSM-5 and its formulated

pellets. The NH_3 uptake per gram of HZSM-5 for each of the weak and strong acidities was also estimated by integrating a corrected concentration of desorbed NH_3 . One can see from Table 5.7 a range of 43.7 to 429.4, 62.6 to 210.5, and 106 to 640 $\mu\text{mol/g}$ for weak, strong, and total acidities, respectively. Rodríguez-González et al. [141] obtained comparable total acidities (700, 270, and 100 for ZSM5-30, -80, and -280, respectively). One can also notice a 243 $\mu\text{mol/g}$ acidity displayed by pure Versal 950. However, when it was diluted with 95% Fused Alumina to form the blank pellet (ZMPL-BL), a small acidity was obtained (8.9 $\mu\text{mol/g}$). This very low acidity of both the binder and the fused alumina filler explains the dilution effect of these materials on the HZSM-5 acidity with a 60-75% reduction of total acidity after pelletization (43-158 $\mu\text{mol/g}$).

Table 5.7 also shows a reduction of the weak acidity/strong acidity ratio and a decrease in acid site density with an increasing $\text{SiO}_2/\text{Al}_2\text{O}_3$ ratio. It appears that the HZSM-5 with a higher aluminum content tends to form strong acid centers that weaken the interactions between neighboring sites, raising as a result the weak to strong acidity ratio [97,141]. These data strongly suggest a correlation between the aluminum content and the acidity that can be attributed to the acid center formation by aluminum in the porous HZSM-5 internal framework [62,109].

Regarding the ZSM5-30 pellets, they showed no change in the weak/strong acidity ratio of about 2 after pelletization. On the other hand, ZSM5-80 and ZSM5-280 once pelletized displayed an increase of the weak/strong acidity ratio by a factor of 2. TPD profiles in Figure 5.12 (a,b) confirm these findings, with an apparent reduction in the strong acidity branch of the TPD for ZMPL-80 and ZMPL-280. To describe these findings, one can argue that the binder with its gluing properties influences the NH_3 adsorption in which the binder interacts with strong acid sites both in the internal and external framework of the HZSM-5. These factors may influence the weak/strong acidity ratio to increase from 0.7 to 1.45 in the case of ZMPL-280 and from 0.99 to 1.85 for ZMPL-80. However, ZMPL-30 remains unaffected by the binder addition. This is consistent with ZMPL-30 having the highest density of strong acid sites.

Table 5.7: NH₃-TPD data.

Sample	T _{peak} (°C)		NH ₃ Acidity (μmol/g)			
	LT-peak	HT-peak	Weak	Strong	Total	$\frac{\text{Weak acidity}}{\text{Strong acidity}}$
ZSM5-30	193	385	429	210.5	640	2.04
ZSM5-80	187	372	165.2	166.7	331.9	0.99
ZSM5-280	180	346	43.7	62.6	106	0.70
ZMPL-30	194	299	105.1	52.7	157.8	1.99
ZMPL-80	195	316	74.8	40.5	115.3	1.85
ZMPL-280	198	249	25.6	17.7	43.3	1.45
ZMPL-BL ^a	N/A	N/A	N/A	N/A	8.9	N/A
Fused Al ^b	N/A	N/A	N/A	N/A	N/A	N/A
Versal 950	204 ^c	N/A	N/A	N/A	243	N/A

^a No distinguished peak is produced, ^b No acidity measured, ^c Only one peak produced.

5.3.2 Nature of HZSM-5 Acid Sites

FTIR using pyridine as a probe molecule can be utilized to identify the different types of acid sites (Brønsted, Lewis, and physisorptive hydrogen-bonded sites). This could be achieved by recognizing the adsorption bonds formed between the sites and the probe molecule. These kinds of adsorptive sites are normally observed within the IR band region of 1400-1600 cm⁻¹. Brønsted acid sites, as proton donors, protonate the pyridine to form pyridinium ions. These ions display C–C stretching vibrational frequencies at the 1550 cm⁻¹ band. There is a band at about 1450 cm⁻¹ showing the presence of Lewis sites. It is an electron pair acceptor, and arises from the C–C stretch of molecularly coordinated pyridine via a covalent bond. On the other hand, the band at 1490 cm⁻¹ reflects a mix of the two kinds of acid sites [95,101,102,147,149,150]. Finally, the band at 1600 cm⁻¹ is generally assigned to physisorbed pyridine due to the hydrogen-bonding with surface hydroxyl [102,127].

In the current study, HZSM-5 samples were subjected to pyridine adsorption at 100°C followed by N₂ purges at 100, 150 and 200°C. The Pyridine-FTIR spectra for each case, along with the plain spectra for ZSM5-30, were all used as a base line as displayed in Figure 5.13 within the IR band domain of 1400-1600 cm⁻¹. Identical spectra to the plain ZSM5-30

were recorded for ZSM5-80 and -280 (not shown here). As can be seen in Figure 5.13, the samples that were purged at 100°C display Lewis (1448cm⁻¹), hydrogen-bonded (1602cm⁻¹), and Brönsted sites (1548cm⁻¹). All these intensities are consistently reduced when raising the SiO₂/Al₂O₃ ratio. Elevating the temperature of the N₂ purge to 150°C caused an attenuation of both bands of Lewis and hydrogen-bonded sites while the Brönsted bands remained resistant. According to these results, it can be argued that the nature of the weak sites predicted by NH₃-TPD (section 5.3.1) is a mix of Lewis acids and hydrogen-bonded-physisorption sites while the strong acid sites are predominantly of the Brönsted type. The bands at about 1490 cm⁻¹, which reflect a mix of Brönsted and Lewis acidity, reveal a gradual intensity-decrease by reducing the aluminum content. This agrees with the TPD-data as well.

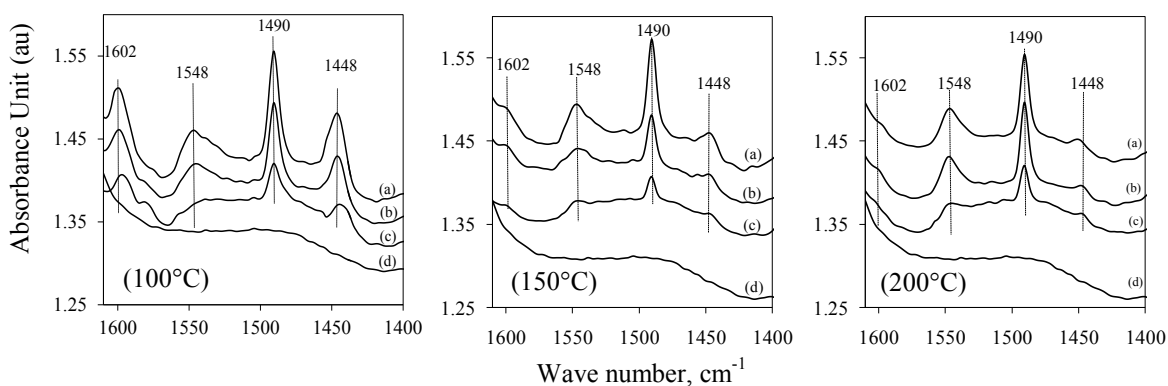


Figure 5.13: Pyridine-FTIR spectra of HZSM-5 measured in the 1400-1600 cm⁻¹ region when using different purge temperatures. (a) ZSM5-30, (b) ZSM5-80, (c) ZSM5-280, and (d) Plain ZSM5-30.

Concerning the effect of the purge temperature, Meng et al. [107] attained equivalent results to the present data. In this case, the Lewis acidity was almost eliminated from 0.47 to 0.1 au while Brönsted acidity was only reduced from 0.42 to 0.29 au when the purge temperature increased from 100 to 300°C. The drop of the Lewis acidity and the gradual decrease of the Brönsted acidity while elevating the purge temperature have also been reported by Jin et al. [95] when using HZSM-5 with a 125 Si/Al ratio. Similar findings were also obtained by others [54,149].

In addition, FTIR can be employed to discriminate between hydroxyl groups in the HZSM-5 adsorbed phase. According to the IR studies, three significant bands can be recognized in the OH stretching regions that are assigned to different vibrations. The band at 3610 cm⁻¹ is

assigned to the vibration of framework bridged OH groups, Al(OH)Si, which is responsible for strong-Brönsted acid sites [59,95,149–154]. The intensity of this band is related to the aluminum content and the amount of proton exchange [128]. With regard to the second band at around 3690 cm^{-1} , various theories were given. One assumption is given by Jin et al. [95] and Borade et al. [153] where the band is associated with the vibration of the extra-lattice AlOH groups formed by dehydroxylation. The other hypothesis is the attribution of this band to SiOH sites predominantly located inside the HZSM-5 framework where it remains virtually unperturbed upon adsorption of large molecules [151,152,154]. The third band at around 3740 cm^{-1} is assigned to the isolated silanol (SiOH) located at the external surface of the HZSM-5 framework [95,128,147,150–153,155]. In the course of examining the HZSM-11 acidity effect by its crystal size, Vedrine et al [156] noticed a decrease in the 3470 cm^{-1} band when increasing the crystal dimensions. Thus, they concluded that the SiOH groups were situated at the external surface of the crystals. There are different views concerning the silanol group on whether it is weakly acidic or non-acidic [128]. However, when using NH_3 -TPD, it was proven that the HZSM-5 with very high $\text{SiO}_2/\text{Al}_2\text{O}_3$ ratios ($>20,000$) showed no acidity. This indicated that these silanols are non-acidic in nature [147] and therefore, they take no part in the weak acidity.

Figure 5.14 reports the FTIR spectra of the OH stretching groups for three HZSM-5 zeolites with different $\text{SiO}_2/\text{Al}_2\text{O}_3$ ratios as a function of the purge temperature. Within the selected range of purge temperatures ($100\text{--}200^\circ\text{C}$), the hydroxyl stretching band (3610 cm^{-1}), assigned to the strong-Brönsted hydroxyl acid sites, almost disappears. This is likely due to the remaining adsorbed pyridine on these strong-Brönsted sites. Similar results were obtained by Jin et al. [95] when the HZSM-5 sample with a Si/Al ratio of 125 was evacuated at 100 and 150°C . However, at higher evacuation temperatures, these authors observed that the 3610 cm^{-1} band could be observed again. The existence of such peaks was reported as well by Borade et al. [153] at 200°C , and by Benito et al. [54] and Gayubo et al. [128] at 150°C evacuation temperatures. It is expected that a further increase in the purge temperature could remove the adsorbed pyridine and eventually restore the strong-Brönsted band.

With regard to the silanol groups in the internal surfaces of the HZSM-5 (3690 cm^{-1}) at a 100°C purge temperature, the bands, even though small, were in-line with the HZSM-5

silicon content. The 3690 cm^{-1} band was also reported by Jin et al. [95], however, at a purge temperature $\geq 200^\circ\text{C}$. On the other hand, the bands around 3745 cm^{-1} were clearly visible and hence, proved that the HZSM-5 may contain some silanol groups on the external surfaces but with no considerable influence by the aluminum content. Gayubo et al. [54,128] studied the pyridine FTIR response using four HZSM-5 samples with a Si/Al range of 24-154. These authors obtained comparable results as the ones reported for a 3745 cm^{-1} band. However, they could not detect the internal silanol group band at 3690 cm^{-1} . These authors concluded that the band at 3745 cm^{-1} does not depend on the Si/Al ratio.

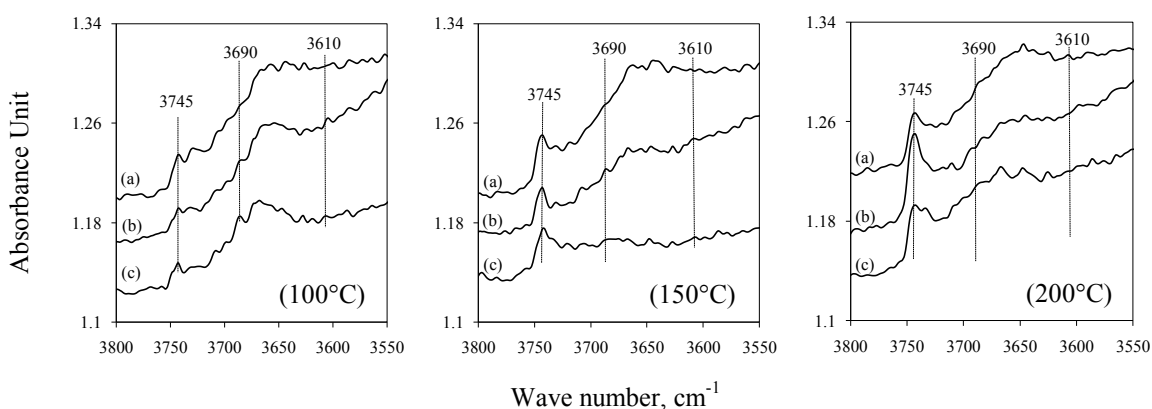


Figure 5.14: Pyridine-FTIR Spectra of HZSM-5 Measured in the Region $3550\text{-}3800\text{ cm}^{-1}$ After Different Purge Temperatures. (a) ZSM5-30, (b) ZSM5-80, (c) and ZSM5-280.

Regarding purge temperatures, purges at 150°C and at 200°C show a reduction of internal-silanol (peak at 3690 cm^{-1}) with an increase of the extra-framework silanol (peak at 3745 cm^{-1}). This can be attributed to the lattice structure changes (structural defects) promoted at higher purge temperatures. Under these conditions, a migration of SiOH species from the internal pores to the external surfaces of the HZSM-5 zeolite is anticipated.

Table 5.8: Relative hydrogen-bonded, Lewis, and Brönsted acid sites concentrations obtained from the areas of the FTIR bands (au/cm^{-1}) using a nitrogen gas purge flow at 100°C .

Sample	Hydrogen-bonded ^a	Lewis ^b	Brönsted ^c	B/L ^d	Total
ZSM5-30	0.61	1.02	1.01	0.99	2.64
ZSM5-80	0.45	0.66	0.73	1.11	1.83
ZSM5-280	0.29	0.25	0.38	1.52	0.92

^a Bands range: $1590\text{-}1614\text{ cm}^{-1}$, ^b Bands range: $1432\text{-}1460\text{ cm}^{-1}$, ^c Bands range: $1510\text{-}1560\text{ cm}^{-1}$, ^d Brönsted /Lewis bands ratio.

From the reported FTIR results, it is shown that FTIR is valuable to identify the nature of the HZSM-5 acid sites. At 100°C, and having a N₂ purge flow, Pyridine-FTIR shows that the weak acid sites encompass two types of sites: i.e. Lewis and hydrogen-bonded sites. The strong acid sites involve, on the other hand, the Brönsted acid sites.

Table 5.8 reports FTIR relative acidity estimated from the areas of the peaks shown in Figure 5.13-a. One can observe that acidities are proportional to the aluminum content. Table 5.8 also reports the increase of Brönsted/Lewis site ratios with the SiO₂/Al₂O₃ fraction. This trend can be attributed to the limited dehydroxylation of Brönsted sites to Lewis sites occurring at high SiO₂/Al₂O₃ fractions [59]. These findings are in general agreement with the results of others [54,128,153].

5.4 NH₃-Desorption Kinetics for HZSM-5

Ammonia desorption kinetic modeling aims to describe NH₃-TPD and how these changes are affected by heating rate and desorption temperatures. The rate of desorption can be related to a kinetic constant of ammonia desorption and to an energy of activation. This approach was first suggested by Amenomiya and Cvetanovic [157]. The parameters considered in this analysis include a desorption activation energy (E_d) and an intrinsic desorption rate constant (k_{d0}).

To consider this model, the following assumptions have to be applicable:

- i. The desorption process can be represented via an Arrhenius equation with this involving a single activation energy of desorption:

$$k_d = k_{d0} \exp\left(-\frac{E_d}{R} \left(\frac{1}{T} - \frac{1}{T_c}\right)\right) \quad (5.4)$$

where T and T_c are desorption variable and centering temperatures, and R is the universal gas constant. The mathematical form, as proposed in Equation (5.4), is adequate considering the use of a “centering” temperature which reduces cross-correlation between parameters, facilitating their adequate computation.

- ii. The activation energy of desorption (E_d) is independent of the surface coverage of the desorbed species:

$$\theta_d = 1 - \frac{V_d}{V_m} \quad (5.5)$$

where V_d and V_m are the variables of desorbed volume and volume of monolayer, respectively. This means that surface adsorption is a uniform process with the same adsorption probability assigned to all active sites. As a result, the probability of adsorption on empty sites is independent of whether the adjacent sites are already occupied or not. Thus, there is no interaction between the adsorbed molecules [30]. This model assumption can be statistically validated once one determines the two kinetic parameters involved in equation (5.4) with the narrow spans for the 95% confidence interval.

- iii. Re-adsorption of the desorbed gas is not significant. This assumption is adequate given the equilibrium interaction between the adsorbate and gaseous ammonia [143,158]:



where (NH_3) and $(*)$ represent the adsorbed ammonia and vacant acid sites, respectively. This interaction takes place under a high He flow (50 ml/min) and at always increasing temperature. Thus, adsorption-desorption equilibrium is consistently shifted towards ammonia desorption. This is confirmed with the data of Figure 5.15 which shows that the cumulative desorbed ammonia amount (V_d) for ZSM5-80 remains unchanged at the end of the desorption experiment with this being independent of the heating rate. Similar consistent cumulative desorption values were obtained for ZSM5-30 and ZSM5-280 (not shown here).

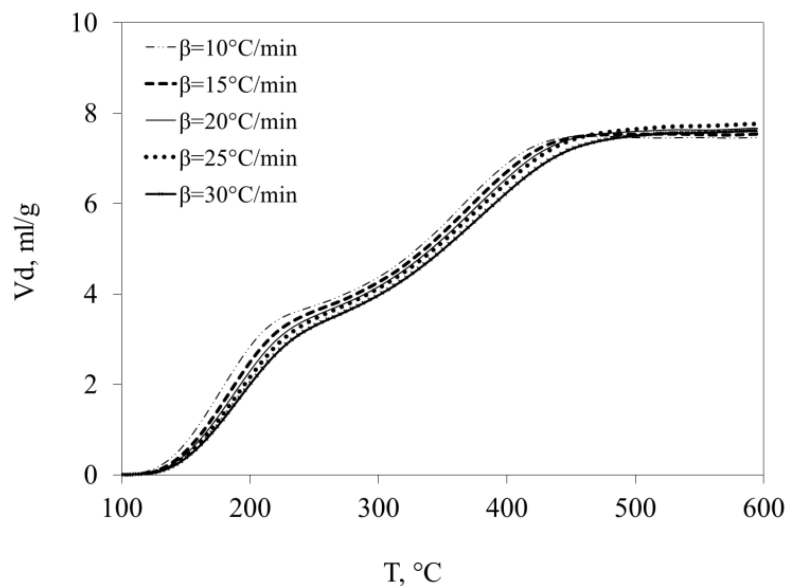


Figure 5.15: Cumulative volume of desorbed ammonia over a ZSM5-80 at different Ramping temperatures.

- iv. The concentration of the adsorbate in the gas phase is uniform throughout the catalyst bed. This is accomplished given the significant difference in the experiments between gas phase contact times (in the range of seconds) and catalyst time-on-stream (in the range of minutes). This is especially true given that the He flow is kept constant throughout the experiment (section 4.4).
- v. The temperature increases linearly with time. This is accomplished through a special design and carefully selected temperature bed control as achieved in the Micromeritics Unit used in the experiments as described in section 4.4.1.
- vi. The kinetic equation is related to a desorption controlled by a first rate order process. This is considered acceptable given that the desorption process can be considered equivalent to an elementary decomposition reaction with only adsorbed and desorbed ammonia as main chemical species involved [62,144,145].
- vii. Resistances to the mass transfer at the external particle surface via convective transport and to the internal diffusion inside the catalyst particles (molecular transport) are negligible. This is considered adequate given the 2-3 μm particle sizes as well as the expected ammonia effective diffusivity in the H-ZSM5 crystallites used in the desorption experiments.

Considering the above mentioned assumptions and by performing a material balance of the ammonia transport across the HZSM-5 bed, the following one dimensional pseudo-homogeneous model can be proposed to describe the ammonia desorption rate:

$$r_d = k_d \theta_d^n \quad (5.7)$$

where n represents the order of the desorption process. Substituting k_d and θ_d from equations (5.4) and (5.5) into (5.7) gives,

$$r_d = k_{d0} \left(1 - \frac{V_d}{V_m}\right)^n \exp\left(-\frac{E_d}{R} \left(\frac{1}{T} - \frac{1}{T_c}\right)\right) \quad (5.8)$$

In each TPD test, the temperature was linearly increased following the $T=T_0+\beta T$ ramp. Therefore,

$$\frac{dT}{dt} = \beta \quad (5.9)$$

where β represent the temperature increasing rate.

Thus, given Equation (5.9), one can consider the following:

$$r_d = \frac{dV_d}{dt} = \left(\frac{dV_d}{dT}\right) \left(\frac{dT}{dt}\right) = \beta \left(\frac{dV_d}{dT}\right) \quad (5.10)$$

From Equations (5.8) and (5.10), the change of the desorbed species volume with the temperature for a first order desorption process ($n = 1$) yields:

$$\frac{dV_d}{dT} = \frac{k_{d0}}{\beta} \left(1 - \frac{V_d}{V_m}\right) \exp\left(-\frac{E_d}{R} \left(\frac{1}{T} - \frac{1}{T_c}\right)\right) \quad (5.11)$$

Amenomiya and Cvetanovic [157] further differentiated Equation (5.11) in their proposed model and set the second derivative at zero in order to find the peak temperature associated with the maximum desorption amount. These authors derived, as a result, the following linear equation:

$$2 \ln\left(\frac{T_p}{\beta}\right) = \ln\left(\frac{V_m E_d}{k_{d0} R}\right) + \frac{E_d}{RT_p} \quad (5.12)$$

where T_p represents the peak temperature.

The linear parameter regression using equation (5.12) yields the energy of desorption (E_d). This E_d value is calculated at T_p or at a temperature associated with the maximum desorption rate. This equation has been extensively used to evaluate the ammonia desorption kinetics over HZSM-5 [52,98,100,138,139,144,145,149,159]. However, the use of the linearized Equation (5.12) is a questionable numerical calculation. One is strongly advised to develop non-linear regression of the desorption parameters using Equation (5.11) directly.

Given the above mentioned issues, Equation (5.11) was solved numerically using least squares method and employing MATLAB[®] software. Two solvers were examined (i.e. ODE23: 2nd order Runge-Kutta, and ODE45: 4th order Runge-Kutta). The later was found to solve Equation (5.11) adequately. The NH₃-TPD data used for the model parameter calculations were at $\beta = 20, 25, 30^\circ\text{C}/\text{min}$ for ZSM5-30, and at $\beta=10, 20, 30^\circ\text{C}/\text{min}$ for both ZSM5-80 and ZSM5-280. Even though different ramping rates are not required for the model calculations, this was done in the present study to obtain kinetic desorption parameters applicable to a wide range of temperature ramping rates. One should also note that weak and strong desorption data were treated separately in this study. This was required given the significant difference in the acidity character between strong and weak acid sites.

To establish the TPD data ranges for weak and strong sites desorption kinetics, “deconvolution” of each TPD peaks was implemented. This helped, as shown in Figure 5.16 with ZSM5-80 at $\beta = 20^\circ\text{C}/\text{min}$, identifying the temperature range (start- T_1) where weak sites were solely contributing and the (T_2 -end) of TPD data where strong acid sites were influencing only. Once T_1 and T_2 were identified, desorption kinetics calculations were applied for weak sites and strong sites. This procedure was adopted for all the other TPD data (not shown here). Thus and on this basis, one can ensure that the overlapping between the acidity data was excluded so that only an E_d and a k_{d0} parameter pair were considered for either the weak or the strong acid sites.

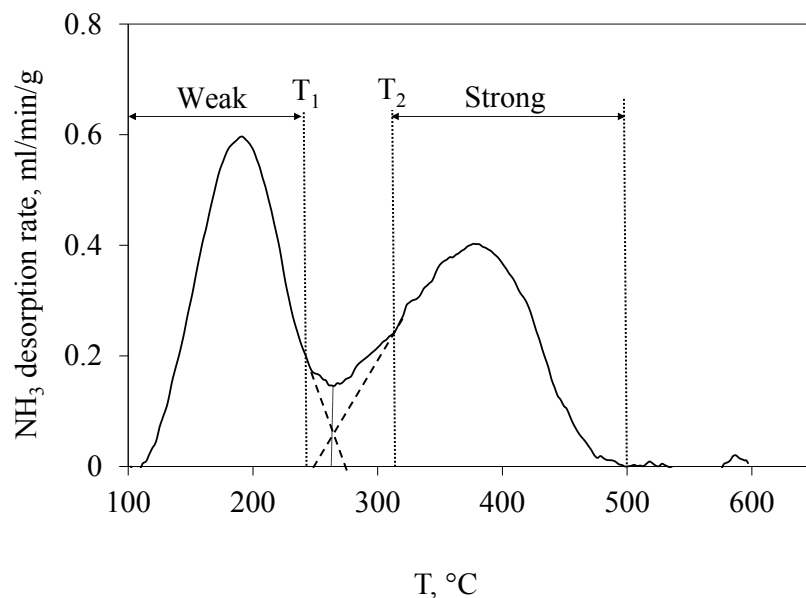


Figure 5.16: Illustration of the deconvolution of the weak and strong acidity data for NH₃ desorption kinetics (ZSM5-80 at $\beta = 20^\circ\text{C}/\text{min}$). T₁ shows the temperature where the sole influence of weak sites ends and T₂ represents the temperature where the sole influence of strong sites begins.

Furthermore, the nonlinear regression adjusted the two kinetic parameters (desorption rate constant and energy of desorption) using a rigorous statistical analysis. Table 5.9 reports the calculated energy of desorption (E_d) and the intrinsic desorption rate constant (k_{d0}) for weak and strong acid sites using ZSM5-30, -80 and -280 zeolites. The regression analysis was considered converged when the change in the summation model-experimental data deviations was less than a set 10^{-6} tolerance. Kinetic desorption parameters are reported with the following statistical indicators: a) small spans for the 95% confidence interval, b) degree of freedom (DOF = data points - 2) in the 150-199 range, c) cross-correlation coefficients between parameters close to zero (refer to Table 5.10), and d) correlation coefficient (R^2) close to one.

Table 5.9: Optimized kinetic constants for NH₃ desorption in HZSM-5

Parameter	Sites	ZSM5-30				ZSM5-80				ZSM5-280			
		Value	95% CI	R ²	DOF	Value	95% CI	R ²	DOF	Value	95% CI	R ²	DOF
$k_{d0} \left(\frac{\text{ml}}{\text{g min}} \right)$	Weak	1.528	±0.026	0.996	151	0.617	±0.011	0.995	166	0.143	±0.003	0.994	150
	Strong	1.042	±0.030	0.987	199	0.664	±0.017	0.991	177	0.213	±0.008	0.985	155
$E_d \left(\frac{\text{kJ}}{\text{mol}} \right)$	Weak	51.7	±1.4	0.996	151	61.4	±1.6	0.995	166	68.3	±2.1	0.994	150
	Strong	57.2	±4.9	0.987	199	85.7	±4.6	0.991	177	93.0	±6.0	0.985	155

Table 5.10: Cross-correlation coefficient matrix for the desorption kinetic constants.

Sites		ZSM5-30		ZSM5-80		ZSM5-280	
		k_{d0}	E_d	k_{d0}	E_d	k_{d0}	E_d
Weak	k_{d0}	1.00		1.00		1.00	
	E_d	-0.005	1.00	0.004	1.00	0.002	1.00
Strong	k_{d0}	1.00		1.00		1.00	
	E_d	0.003	1.00	0.003	1.00	0.004	1.00

Figure 5.17 to Figure 5.19 report the goodness of fit using the proposed desorption model for both strong and weak acid sites. One can observe a good agreement between the measured and predicted ammonia desorbed volumes from weak and strong acid sites. One should also notice that while the original data file includes data points every 10 sec, only points every 50 sec are reported in Figures 5.17-5.19 to facilitate the plotting.

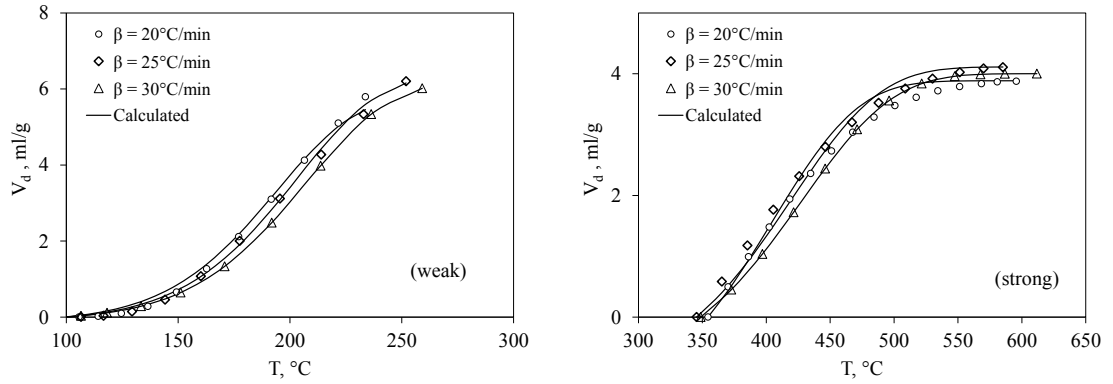


Figure 5.17: Comparison of experimental ammonia volume desorbed versus model ammonia volume desorbed for ZSM5-30 (Equation (5.11)).

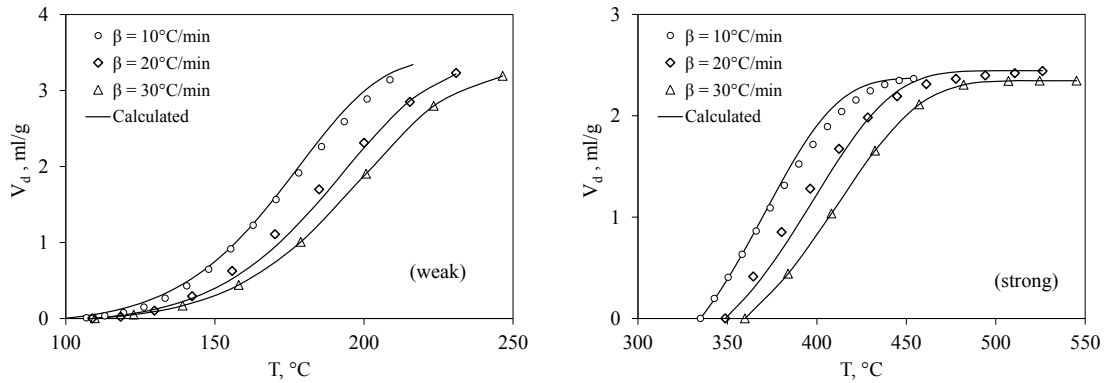


Figure 5.18: Comparison of experimental ammonia volume desorbed versus model ammonia volume desorbed for ZSM5-80 (Equation (5.11)).

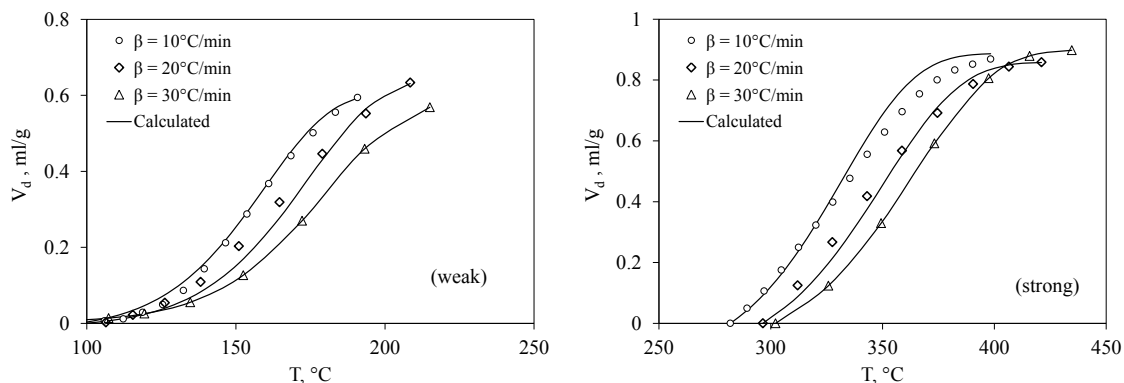


Figure 5.19. Comparison of experimental ammonia volume desorbed versus model ammonia volume desorbed for ZSM5-280 (Equation (5.11)).

Previous ammonia desorption studies [62,141,158] referred to a single energy of ammonia desorption in the 128-155 kJ/mol range for HZSM-5 zeolites. This approach neglected the weak acidity. It is, however, the purpose of this study to elucidate this matter by distinguishing between energies of activation for weak and strong acid sites. Table 5.9 shows, in this respect, the desorption energies in the 57 to 93 kJ/mol range, and in the 51 to 68 kJ/mol range for strong and weak acid sites, respectively. These values are in line with the activation energies (69-92 kJ/mol) for strong sites and the somewhat higher values (44-48 kJ/mol) for weak sites reported by Rodríguez-González et al [146]. One should also observe that there are activation energies in the range of 45-109 kJ/mol for weak sites and 73-169 kJ/mol for strong sites, as reported by other authors [98,138]. This cited data is valuable to illustrate the general consistency of kinetic desorption parameters as shown in Table 5.9 and in the previous reported literature. However, the desorption energies obtained in this study are more reliable and statistically significant, given the care taken both when developing the experimentation and the numerical analysis.

Previous studies also refer to a higher desorption energy for the stronger sites versus the one for weaker sites [98,139,146]. This is probably attributed to the nature of ammonia coordination on each type of acid site. As described in section 5.3.1 of this study, ammonia adsorption on the strong sites likely occurs via chemical bonding as ammonium cations ($\text{NH}_4^+\text{ZSM-5}^-$) creating a covalent bond between NH_4^+ and ZSM-5^- . In the case of weak sites, ammonia is likely held via hydrogen-bonds (5 to 30 kJ/mol). These weak sites provide interactions stronger than the Vander Waals interaction, but weaker than chemical bonds

[160]. These observations are consistent with the NH₃-TPD peak temperatures for strong and weak acid sites.

The intrinsic desorption rate constant (k_{d0}) can be used to establish the fraction of weak to strong acid sites. Table 5.11 reports the (k_{d0W}/k_{d0S}) ratio and compares it to those measured by NH₃-TPD and Pyridine-FTIR. One can notice a similar trend in the three zeolite studied with weak/strong acidity ratios being reduced with SiO₂/Al₂O₃. One can also observe a good consistency when comparing the (k_{d0W}/k_{d0S}) ratio from TPDs for ZSM5-80 and ZSM5-280. The (k_{d0W}/k_{d0S}) ratio is for the ZSM5-30 zeolite, however, somewhat lower than the measured value. This can be attributed to the more uncertain peak deconvolution error due to more overlapping between the weak and strong acid sites of the TPD data for the ZSM5-30 (refer to Figure 5.12-a).

Table 5.11: Measured and estimated ratio of weak to strong acidity.

Catalyst	$\frac{\text{Weak acidity}^a}{\text{Strong acidity}}$	$\frac{\text{Weak acidity}^b}{\text{Strong acidity}}$	$\frac{k_{d0W}}{k_{d0S}}$
ZSM5-30	2.04	1.61	1.466
ZSM5-80	0.99	1.52	0.929
ZSM5-280	0.70	1.42	0.671

^a Data is measured based on NH₃-TPD, ^b Data is measured based on Pyridine-FTIR bands' areas. Weak acidity \equiv Hydrogen-bonded + Lewis sites; Strong acidity \equiv Brønsted sites.

In summary, the various methods considered in the present study, allow quantifying the acidity differences in the HZSM-5 zeolites using both weak and strong acidities and their ratios. These weak/strong ratio parameters are established using both NH₃-TPD desorption areas and Pyridine-FTIR peak areas. In addition, this weak/strong acidity ratio is calculated using a kinetic desorption model. This give a more reliable assessment of weak to strong acid site ratio via an independent evaluation using an intrinsic desorption kinetics. Thus, it is shown in this study that the relative weak/strong acidities, as expressed by the ratio of desorption kinetic constants augment consistently for the HZSM-5 studied, with the reduction of the SiO₂/Al₂O₃ ratio.

5.5 Conclusions

This study is aimed at investigating the influence of the $\text{SiO}_2/\text{Al}_2\text{O}_3$ ratio (30, 80, and 280) and the pelletization process on the HZSM-5 zeolite physicochemical properties. Therefore, the prepared HZSM-5 zeolite and its fabricated extrudates were evaluated with different physical and chemical characterization techniques, in order to estimate their suitability in DTO reaction. Thus, on the basis of the results presented in this chapter the following can be concluded:

1. The XRD patterns show highly crystalline HZSM-5 zeolites with no significant presence of impurities. One can find that crystallinity in HZSM-5, as established with XRD, is comparable irrespective of the zeolite aluminum content. HZSM-5 pellet, on the other hand, shows an effect on the HZSM-5 intensities with new lines at 25.5, 35.1, 37.8, and 43.3° 2θ angles and with an attenuation of (011), (200), (051), (033) and (313) bands. Such an effect could be assigned either to the dilution of the zeolite crystallites by the matrix materials and/or to a particle size increase.
2. The N_2 adsorption/desorption isotherm data show a dual hysteresis loop produced by an HZSM-5 sample with low aluminum content compared to a single hysteresis loop produced by HZSM-5 with a lower $\text{SiO}_2/\text{Al}_2\text{O}_3$.
3. The N_2 adsorption isotherm data were analyzed using the NLDFIT (slit-like and cylindrical models) and other traditional techniques. Among the examined methods, the NLDFIT cylindrical model shows a channel size which is in the expected pore range of 5.4-5.6Å for the HZSM-5 and is thus employed for examining the porosity characteristics.
4. The specific surface area, pore volume, and pore diameter over the micropores and mesopores show comparable results among the HZSM-5 with different aluminum content. On this basis, the $\text{SiO}_2/\text{Al}_2\text{O}_3$ ratio appears not to have an effect on HZSM-5 structural properties. The formulated pellets, however, display a porosity reduction that could be attributed to the filler addition. The binder, on the other hand, is

considered to be the contributor to the slight increase in the pellets micro- and mesopore dimensions.

5. The NH_3 -TPD showed both weak-to-strong acid sites ratio with the total acidity being reduced by increasing the $\text{SiO}_2/\text{Al}_2\text{O}_3$ ratio. The pellet matrix, on the other hand, displays negligible acidity and thus caused 60-75% reduction of HZSM-5 total acidity after pelletization.
6. The Pyridine-FTIR and the NH_3 -TPD results demonstrate that acidity in the HZSM-5 encompasses two types of weak and strong acids sites. Pyridine-FTIR data obtained at a 100°C nitrogen purge allows one to associate the weak sites with hydrogen-bonded ($1590\text{-}1614\text{ cm}^{-1}$) and Lewis acidity ($1432\text{-}1460\text{ cm}^{-1}$) while the strong sites can be related to Brønsted acidity ($1510\text{-}1560\text{ cm}^{-1}$).
7. The NH_3 -desorption kinetics also allows the prediction of desorption activation energies and of the intrinsic rate constants for both strong and weak acid sites. It is found that the HZSM-5 studied displays higher activation energy for the stronger sites (57 to 93 kJ/mol) and lower activation energies for the weaker sites (51 to 68 kJ/mol). It also shows that the activation energies increase with the $\text{SiO}_2/\text{Al}_2\text{O}_3$ ratio of HZSM-5.
8. The changes of NH_3 -desorption kinetic constants with a $\text{SiO}_2/\text{Al}_2\text{O}_3$ ratio follow similar trends to the ones observed for NH_3 -TPD acidity areas and Pyridine-FTIR peaks areas. These findings demonstrate that acidity in HZSM-5 zeolites can be correlated with Al_2O_3 content.

CHAPTER 6 CONVERSION OF DIMETHYL-ETHER TO OLEFINS OVER HZSM-5: REACTIVITY AND REACTION MECHANISM

6.1 Introduction

As outlined in section 2.4.4, it is generally accepted that light olefins are first produced from DME. By taking advantage of HZSM-5 properties and/or reaction conditions, light olefins can continue reacting, forming heavy olefins, normal-/iso-paraffins, naphthenes and aromatics [8,11,14,17,26,48]. Thus, the primary objective during the design of the DTO catalytic process is to select the optimum parameters that lead to enhanced light olefins formation with minimum additional conversion before they have the opportunity of being further transformed.

This chapter reports the effect of the $\text{SiO}_2/\text{Al}_2\text{O}_3$ ratio on the reactivity properties of the HZSM-5 for light olefins production from DME. This is done with the aim of identifying both a selective and durable catalyst for the DTO process. The candidate HZSM-5 catalyst with the adequate properties is then employed to investigate the DTO reaction network based on reactivity runs using neat DME at different temperatures and contact times.

6.2 DME Reactivity Runs

6.2.1 Thermal Conversion of DME

In order to confirm the negligible DME thermal conversion as well as to check the inertness of the Berty Reactor materials, two blank runs (i.e. no catalyst loaded) were performed at 400 and 500°C temperature, 1.36 barg pressure, and 8.3 ml/s pure DME flow. No DME conversion or products formed were observed in any of these blank runs. Thereby, this confirms that the reactor material was inert and the DME was not converted thermally.

6.2.2 Conversion of DME to Olefins (DTO) over HZSM-5 with Different SiO₂/Al₂O₃: Catalyst Screening

As shown in section 5.3.1, the surface acidity changes with the different SiO₂/Al₂O₃ ratios of HZSM-5 zeolites. Therefore, it is expected that altering the HZSM-5 acidity would affect its catalytic properties for DME transformation into light olefins. Furthermore, in order to assess this matter, a series of DTO reactivity runs were performed at different reaction temperatures.

For each experimental run, the C-balance closure was established to gain confidence on the experimental data obtained. On this basis, C-balance closures within 96.4-104.6% were obtained for all runs developed.

Figure 6.1 reports HZSM-5 stability (DME conversion versus time-on-stream (TOS)) for various SiO₂/Al₂O₃ ratios in the 330-450°C range. One should mention that using HZSM-5 at 300 °C, there was no detectable DME conversion and this was the case for various zeolites studied. However, increasing the temperature to 330°C yielded 41% DME conversion for ZSM5-30, 59% for ZSM5-80, and 0.2% for ZSM5-280 at TOS of 60 min.

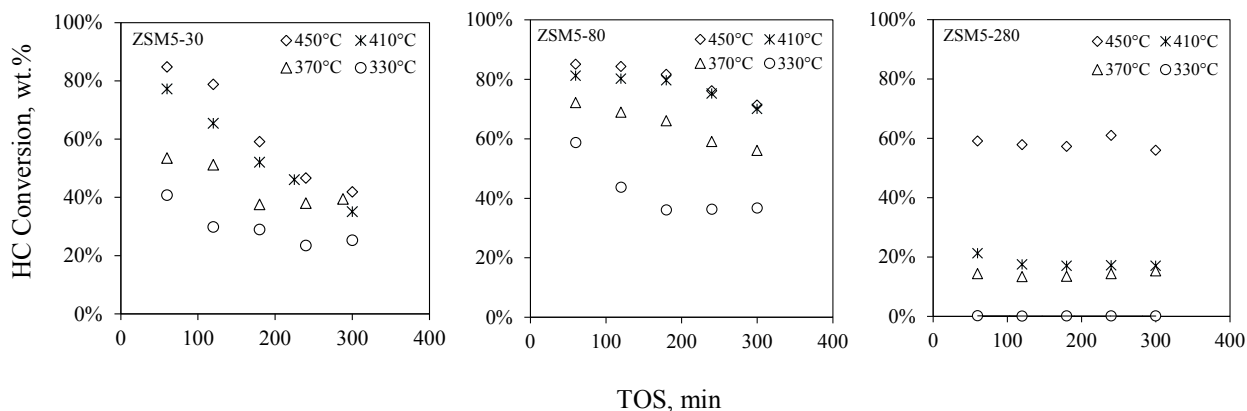


Figure 6.1: Changes of HC Conversion of DME with time on stream (TOS) at different temperatures using different HZSM-5 catalysts.

Furthermore, when the temperature was increased to 370-450 °C, the DME conversions at the same TOS of 60 min were consistently increased. In fact, DME conversions reached 85% for both of ZSM5-30 and ZSM5-80 and 59% for ZSM5-280. This favorable temperature

influence is expected, given the reaction rate constants, thereby, the rate of reaction follows an Arrhenius' type of dependence.

There was, however, a significant difference between DTO conversion with TOS for the different zeolites considered: a) DTO conversion remained essentially unchanged with TOS for ZSM5-280, b) DTO conversion declined steadily with TOS for ZSM5-30 and ZSM5-80.

Figure 6.2 displays the formed coke-on-catalyst and its changes with temperature. This is the case for all the HZSM-5 zeolites studied. For instance, when running at 410 and 450°C, ZSM5-30 and ZSM5-80 yielded 2.5-2.65 and 1.7-2.2 wt% coke, respectively. The ZSM5-280 consistently gave, on the other hand, the lowest coke content at 0.9-1.16 %.

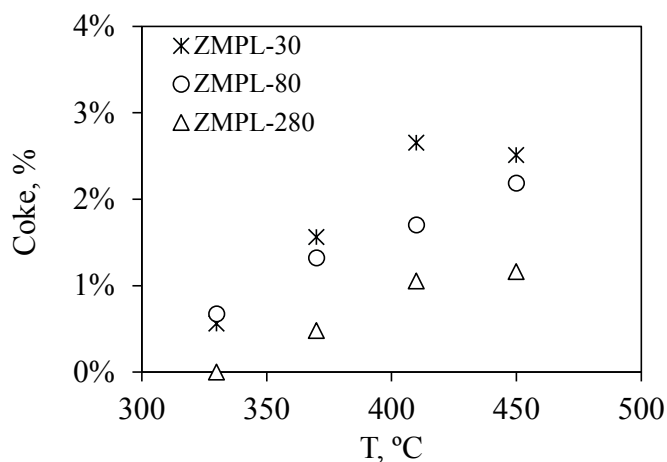


Figure 6.2: Coke Concentration in Different Spent HZSM-5 Catalysts as a Function of Temperature.
TOS=300min.

Coke deposition during DME conversion depends on many factors. The main ones are the HZSM-5 acidity and temperature. In fact, increasing one or both of these parameters, enhances side cracking reactions leading to coke formation on acidic sites. Consistent with this, the ZSM5-280 with a $106 \mu\text{mol}_{\text{NH}_3}/\text{g}$ acidity gave 1.16wt% coke at 5 h TOS. On the other hand, samples of ZSM5-80 and ZSM5-30 with acidity = 332 and $640 \mu\text{mol}_{\text{NH}_3}/\text{g}$ display coke yields of 2.2-2.6 wt%.

Thus, on this basis, the declining DTO conversion with TOS can be justified given coke formation, with this being true for both ZSM5-30 and ZSM5-80. On the other hand, ZSM5-280 with much lower coke content showed a DTO conversion remaining essentially

unchanged. Thus, 1.16% coke yield as found in the ZSM5-280 limits pore blockage, with this securing the steady activity of the ZSM5-280 catalyst.

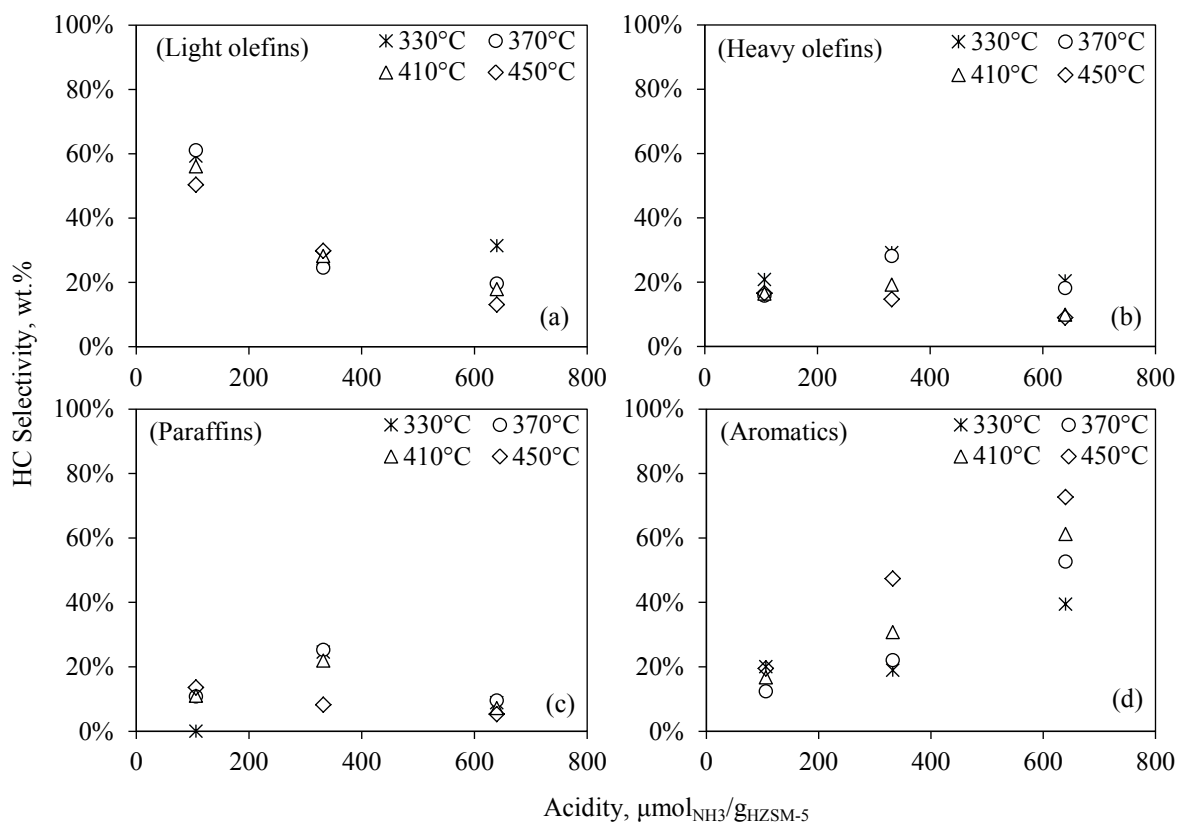


Figure 6.3: Lumped product selectivity versus total acidity of HZSM-5 at different reaction temperatures. (a) Light olefins (ethylene- butene), (b) Heavy olefin lump (pentene-octene), (c) Paraffins (butane-octane), (d) Aromatics (C7-C12 methylbenzene). Note: Acidity at 106 $\mu\text{mol}_{\text{NH}_3}/\text{g}_{\text{HZSM-5}}$ is for ZSM5-280, acidity at 332 $\mu\text{mol}_{\text{NH}_3}/\text{g}_{\text{HZSM-5}}$ is for ZSM5-80, and acidity at 640 $\mu\text{mol}_{\text{NH}_3}/\text{g}_{\text{HZSM-5}}$ is for ZSM5-30.

Figure 6.3 (a-d) reports the lumped hydrocarbon product selectivity as a function of the total acidity of the three zeolites at different reaction temperatures. The products are lumped into the following groups: (a) light-olefins (ethylene, propylene, and butene); (b) heavy-olefins (pentene, hexene, heptene, octene); (c) paraffins (butane, pentane, hexane, heptane, and octene); and (d) aromatics (toluene, xylene, mesitylene, and durene, pentamethylbenzene, and hexamethylbenzene). The formation of CO, CO₂, CH₄, methanol, and benzene are not considered given that their concentrations were found to be negligible. In order to avoid an inaccurate estimation of the selectivity due to the deactivation of ZSM5-30 and ZSM5-80, the results in Figure 6.3 and Figure 6.4 were obtained based on the first measurements at 60 min TOS. For ZSM5-280, averages were considered for the complete spans of TOS.

Figure 6.3-a reports the light-olefin selectivity reduction with increasing temperature in the 330 to 450°C range: (a) from 61% to 50% for ZSM5-280, (b) from 29 to 25% for ZSM5-80, and (c) from 31 to 13% for ZSM5-30. On the other hand, and as shown in Figure 6.3-b, the heavy-olefins show a selectivity remaining in a 10-30 % range for the three catalysts at various thermal levels. In particular, when catalyst acidity is increased from 106 to 640 $\mu\text{mol}_{\text{NH}_3}/\text{g}$, the heavy olefin selectivity is increased first and reduced later.

Figure 6.3 (c, d) displays paraffin and aromatic lump selectivity and their changes with total acidity. One can observe that the paraffin lump displays trends similar to the heavy olefins with maximum values for ZSM5-80 of 20-22% selectivity. Regarding the aromatic lump, it can be noticed that it increases consistently with higher acidity zeolites and temperatures. For instance, ZSM5-30 with 640 $\mu\text{mol}_{\text{NH}_3}/\text{g}$ acidity yields an aromatic selectivity steadily augmenting with temperature from 39 to 73%.

Figure 6.4 (a-c) describes the ethylene, propene and butene selectivities and their changes with HZSM-5 acidity at four temperature levels. Figure 6.4-c reports 59% ethylene selectivity over ZSM5-280 with this being attained at 330°C. This is expected given that the extent of DME conversion at these conditions is very limited: 0.2 % DME conversion only. However, with the further temperature increase in the 370-450 °C range, the ethylene selectivity decreases steadily with propene selectivity staying in a narrow 21-26% range and butene selectivity increasing from 13 to 25%. For the ZSM5-80 catalyst, ethylene, propene and butene selectivities remain in the 3-6%, 10-12%, and 11-15% range, respectively at 330-450°C. Similar results were also obtained for the ZSM5-30, with ethylene, propene, and butene selectivities varying in the 2-8%, 5-10%, and 7-11% ranges respectively. Thus, the influence of the reaction temperature becomes less pronounced when using ethylene, propene and butene and when operating with higher acidity HZSM-5 zeolites. These data shows that for ZSM-280, at higher temperatures, the following occurs: a) there is a significant effect when methyl groups are inserted into formed olefins, b) there is a reduced influence of condensation reactions leading to aromatic species.

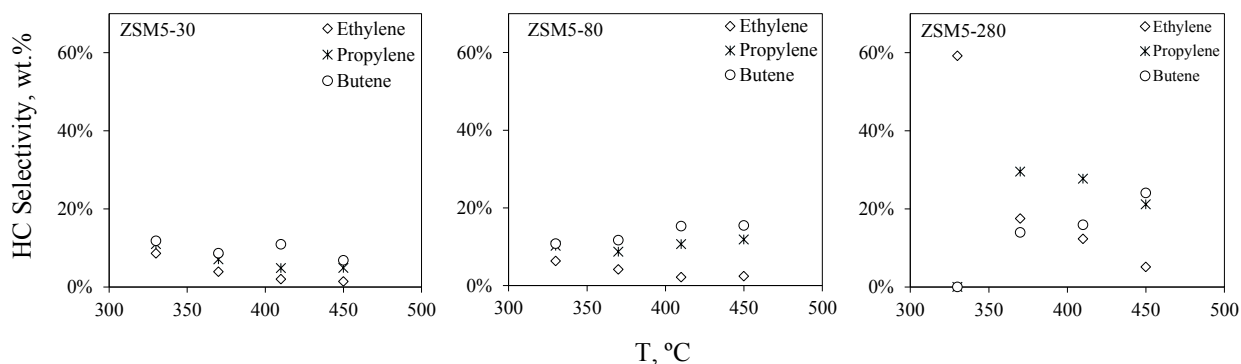


Figure 6.4: Individual light olefin selectivity vs total acidity of HZSM-5 at Different Reaction Temperatures.

Regarding the DTO reaction using the HZSM-5 catalyst, authors agreed that the DME conversion increases with temperature [16,26,35,47]. Zhao and co-workers [14,47] investigated the DTO reaction employing a Zr-P-HZSM-5 catalyst. These authors pointed out that lowering the temperature from 450 to 250°C reduces DME conversion significantly from 100 to 8.6%, while light-olefin selectivity was improved from 64.6 to 75.2 C-mole%. Birykova et al. [35] investigated the influence of changing the temperature from 320 to 360°C in the performance of the thermally treated La-Zr-HZSM-5. Their experimental data agree closely with Zhao's results in which light-olefin selectivity decreases from 75.7 wt% at T = 320°C to 44.1 wt% at T = 360°C, along with a higher alkane fraction being produced. On this basis, these authors concluded that the rate of the secondary reactions increases at higher temperatures.

However, other relevant aspects such as the extent of the secondary reactions (i.e. further olefin conversion) and the influence of both temperature and SiO₂/Al₂O₃ ratio of HZSM-5 still remain to be fully elucidated. Sardesai et al. [8,11,18,45] investigated the influence of varying the SiO₂/Al₂O₃ ratio within a range of 30 to 150. Similar to the results of the present study, these authors showed that the higher the SiO₂/Al₂O₃ ratio, the higher the light olefin selectivity. Comparable behaviors were observed also by Chang with the methanol to olefin (MTO) reaction, where olefin selectivity increased at higher SiO₂/Al₂O₃ ratios. Omata et al. [9] extended the range of the SiO₂/Al₂O₃ ratio to cover 100 to 1600 in their study of the DTO reaction using a Ca-HZSM-5. These authors reported that light-olefin selectivity changed with the SiO₂/Al₂O₃ ratio as follows: a) 54 C% for a 100 SiO₂/Al₂O₃ ratio, b) 63 C% for a 200 SiO₂/Al₂O₃ ratio and c) 53 C% for a 1600 SiO₂/Al₂O₃ ratio.

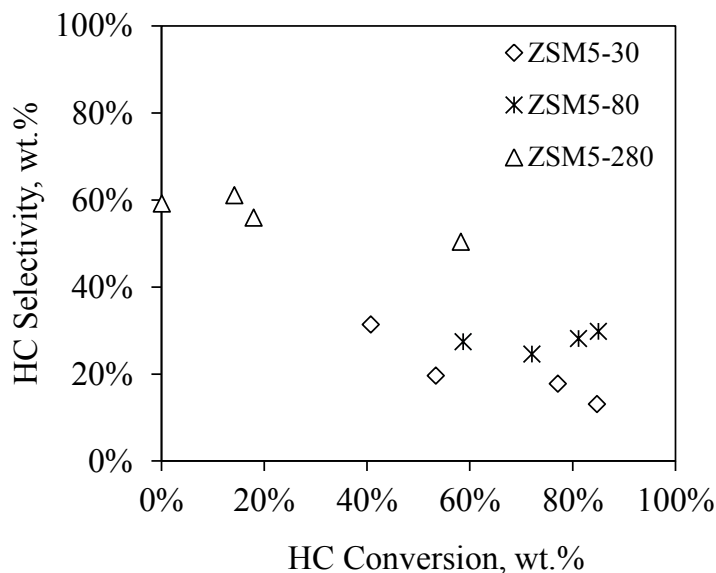


Figure 6.5: Changes of light olefin selectivity with DME conversion for various $\text{SiO}_2/\text{Al}_2\text{O}_3$ ratios. Note: For each catalyst, the increase in the DME conversion is the result of higher reaction temperatures in the 330-450°C range.

In summary, the DTO reactivity tests of the present study, allow correlating the acidity of the HZSM-5 zeolites with their performance in terms of activity, durability and light olefin selectivity. Figure 6.5 summarizes the changes of the light olefin selectivity with respect to the increase of DME conversion when elevating the temperature and modifying the zeolite type used. It is shown that the ZSM5-280 catalyst, displaying the lowest acidity, yields the highest light olefin selectivity in the 50-60%, with this being the case for all the thermal levels considered. It is further demonstrated that the ZSM5-280 is the catalyst able to produce the higher ethylene, propene, and butene selectivities by carefully selecting the reaction temperature. Additionally, the ZSM5-280 displays a stable DME conversion with a maximum level of coke at 1.16wt%. As a result, the ZSM5-280 can be considered as a potential catalyst for the selective and stable production of light olefins from DME.

6.2.3 Conversion of DME to Olefins (DTO) over HZSM-5 with $\text{SiO}_2/\text{Al}_2\text{O}_3 = 280$

DTO Catalytic runs using an HZSM-5 with a $\text{SiO}_2/\text{Al}_2\text{O}_3 = 280$ were performed with the aim of understanding the reaction network and for kinetic modeling. The reactivity experiments were developed using an approximate 10 g amount of the catalyst pellets where the reaction

temperatures points were 350, 375, 400, and 425 °C at 1.36 barg constant pressure. At each reaction temperature, the contact time was systematically varied from 3.5 to 19.5 with an increment of 1.07 $\text{g}_{\text{cat}}\text{h}/\text{mole}_{\text{DME0}}$. The contact time was obtained as the ratio of catalyst weight per molar DME feed flow ($\tau = W/F_{\text{DME0}}$).

Each experimental data are taken after 40 min of time-on-stream at a certain temperature and contact time. Then, a repeat of each experiment was performed to assure the reproducibility of the obtained results. Thus, the presented data points in the upcoming figures are displayed in a form of an error bar that shows the two repeats with the mean value. Finally, the closure for the atomic balance (C, H, and O) was established for each run to attain confidence on the obtained findings and gain a reliable data on DME conversion and product selectivity. On this basis, the obtained C-, H-, and O-balances closures were within 97-103% for all runs.

In section 6.2.2, HZSM-5 catalyst with a $\text{SiO}_2/\text{Al}_2\text{O}_3$ ratio = 280 demonstrated a stable operation up to 1.16% coke yield. Keeping this as a bench mark, the coke content after each experiment was examined at four temperature levels as presented in Figure 6.6. One can observe that the coke was below 1.16% (1.1% maximum) at all the times. Additionally, the surface area measurements after each experiment as reported in Figure 6.7 show comparable values between fresh and coked catalysts. Thus, 1.1% coke content in the ZSM5-280 limits the pore blockage and as a result, the surface area remains unchanged, with this securing the durability of the ZSM5-280. These measures collectively verify the stability of the ZSM5-280 used in the present work and thus exclude the deactivation effect.

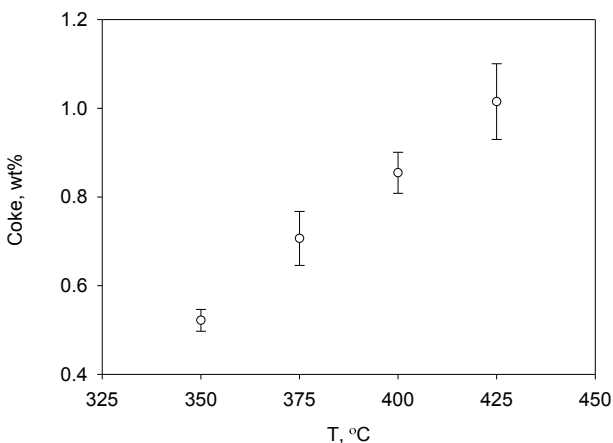


Figure 6.6: Coke concentration in spent ZMPL-280 as a function of temperature. TOS = 10 h.

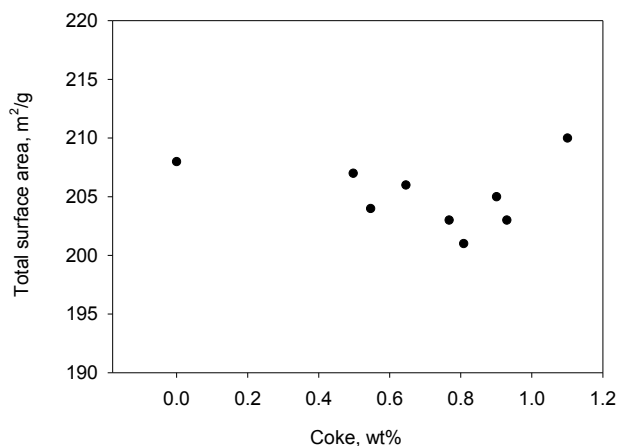


Figure 6.7: ZMPL-280 total surface area at different coke yields. Note: 0% coke content refers to a fresh catalyst.

The DTO reaction trajectory can be assessed by tracking the evolution of the DME conversion and products selectivities over the contact time at different temperature levels. Figure 6.8 reports the influence of the HZSM-5 activity (DME conversion versus contact time) with the reaction temperature in the 350-425 °C range. At a low temperature scale, one can observe a linear increase of the conversion with the contact time from 2 to 10.3% at 350°C, and from 8.7 to 19.8% at 375°C. Further elevating the reaction temperature caused a higher incremental increase of conversion in the range of 21-49% and 35-74% at 400 and 425°C, respectively. This favorable temperature influence is expected given the exothermicity of the DTO reaction in which the rate of reaction follows Arrhenius' relation. On the other hand, the proportional increase of the conversion with the contact time is an expected process given that the more time the DME molecules spend on the active sites, the more chance they have of being transformed. One can also notice that the conversion profiles follow the “Langmuir” model. At lower conversion levels (at 350, 375, and 400°C), the conversion profiles were linearly increased. When running at 425°C, however, the conversion increased until it reached its equilibrium at 74% and at $\tau = 16.3 \text{ g}_{\text{cat}}\text{h}/\text{mol}_{\text{DME}0}$. Thereafter, the conversion became stable when increasing the contact time.

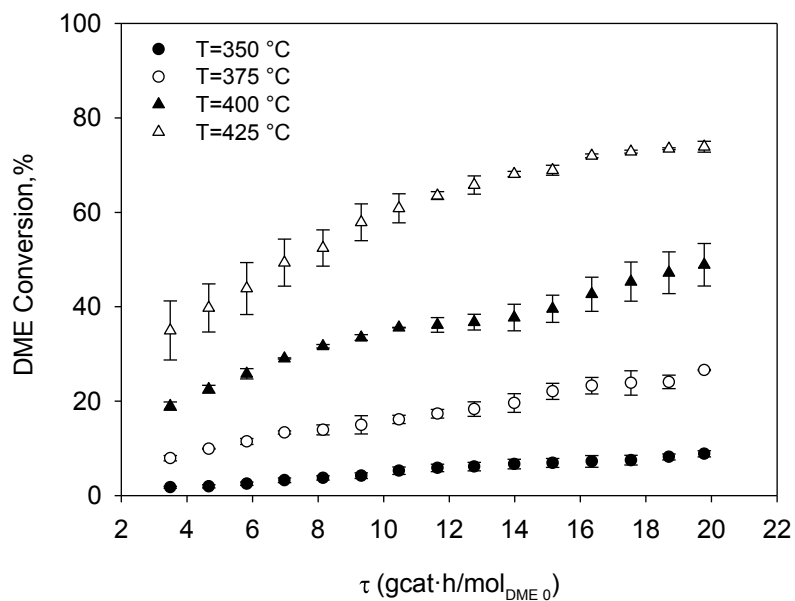


Figure 6.8: DME conversion vs contact time (τ) at different reaction temperatures.

Figure 6.9 displays the lumped hydrocarbon product selectivity as a function of the DME conversion. One should notice that the increase in the DME conversion is a combined result of elevating the reaction temperature along with the contact time as demonstrated earlier from Figure 6.8. Therefore, each curve shown in the upcoming figures contains 60 data points (4 temperatures \times 15 τ 's).

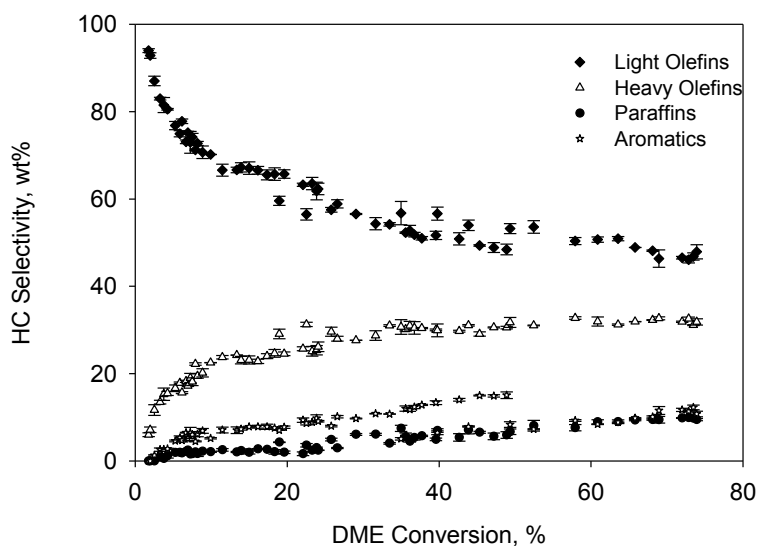


Figure 6.9: Lumped product selectivity vs DME conversion.

The hydrocarbon products are lumped into the following groups: (a) light-olefins (ethylene, propene, and butene); (b) heavy-olefins (pentene, hexene, heptene, octene); (c) paraffins (butane, pentane, and hexane, heptane, and octane); (d) aromatics (toluene, xylene, mesitylene, durene, pentamethylbenzene, and hexamethylbenzene). The formation of methanol, methane, ethane, propane, and benzene are not considered given that their concentrations were found to be insignificantly small and therefore negligible.

Regarding the very low conversions of DME in Figure 6.9 (1.8%), one can observe that the light olefins are the dominant products (94% selectivity) followed by traces of heavy olefins (6% selectivity) with no paraffin or aromatic being produced. Further increasing the conversion resulted in a logarithmic increase of the heavy olefin selectivity at the expense of the light ones. On the other hand, the rise of the paraffins and aromatics selectivities with the conversion is less prevalent. This trend of the heavy olefins, paraffins, and aromatics increasing at the expense of the light olefins continue to slow down till reached about 45% conversion. Thereafter, the change in the product selectivity becomes less pronounced. At the maximum conversion of 74%, the obtained selectivities for light olefins, heavy olefins, paraffins and aromatics were 48%, 32%, 9%, and 11%, respectively.

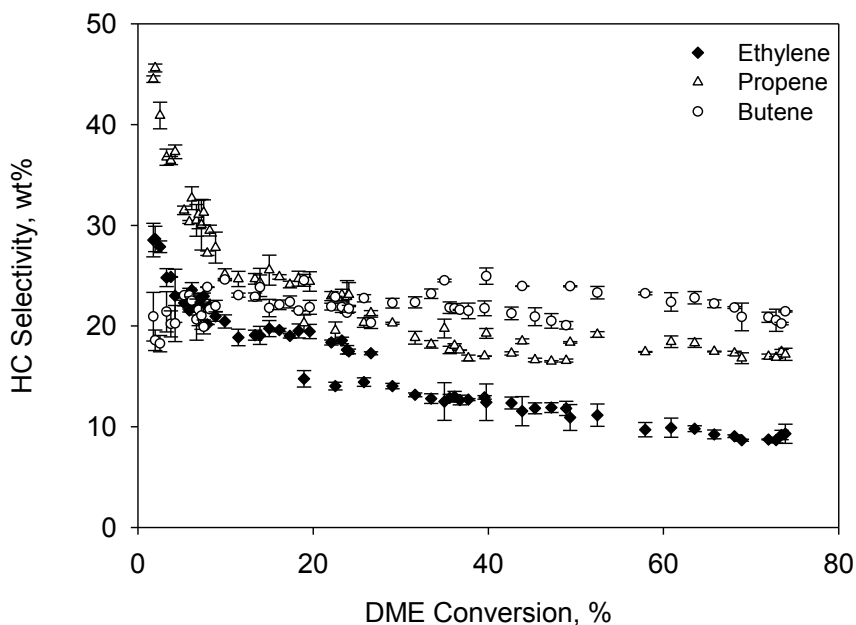


Figure 6.10: Individual light olefin selectivity vs DME conversion.

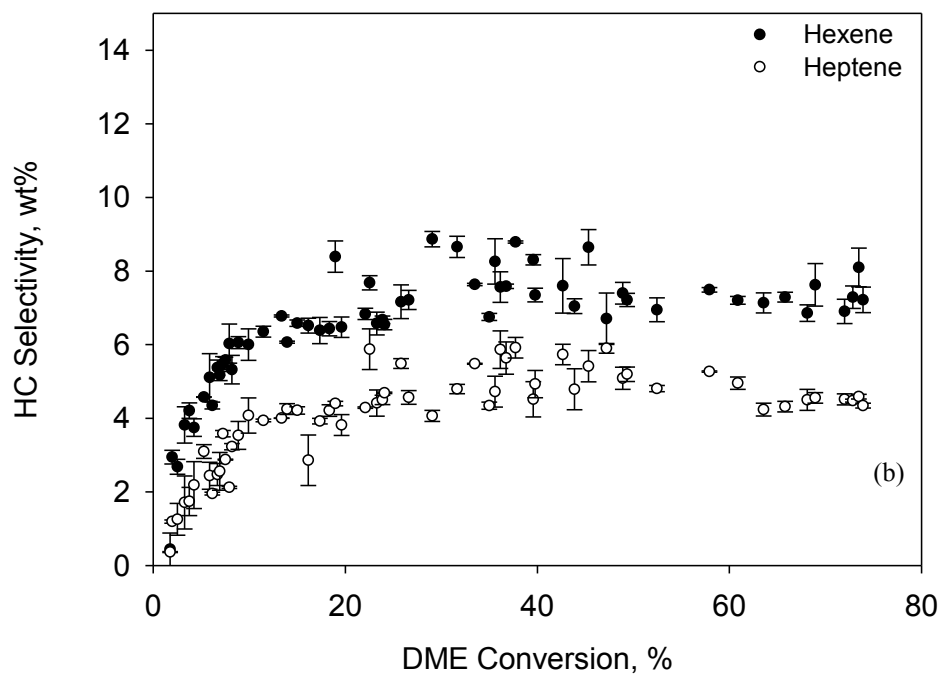
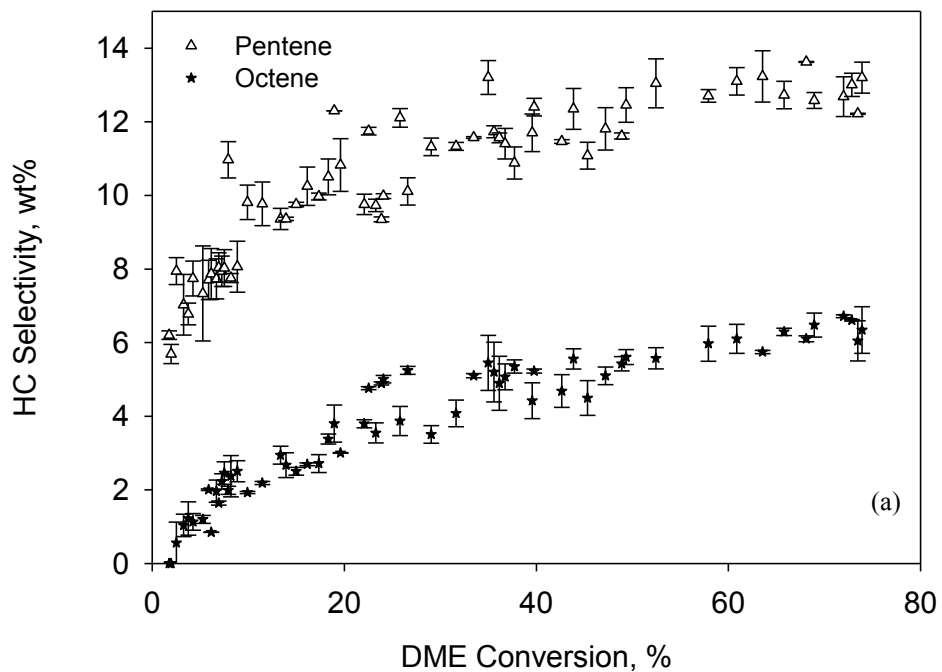


Figure 6.11: Individual heavy olefins selectivity vs DME conversion: (a) Pentene and octene, (b) Hexene and octene.

Figure 6.10 and Figure 6.11 report the individual olefin selectivity changes when increasing the DME conversion. One can notice from Figure 6.10, a logarithmic reduction from 28 to 10% and from 45 to 17% for ethylene and propene, respectively. Given that ethylene and propene are at their maximum selectivities and are the dominant products at the lowest DME conversion (2%), it is likely that these species are produced primarily from the DME. When increasing the conversion, the produced ethylene and propene are consumed to produce butene. Butene keeps increasing slightly from 20% to 25% at 38% conversion then reduced back to 21%. It is expected that butene is produced intermediately from propene through methylation. Following this, in the same way, butene is consumed to form the next higher olefin: pentene.

Similar behavior as for butene selectivity is also observed for heavier olefins. One can notice this from Figure 6.11(a,b) as follows: (a) pentene selectivity progressive increases from 6 to 13% with DME conversion, (b) hexene selectivity augments quickly from 2.5 to 8.5% at 40% DME conversion and slightly decrease to 7.2% later, (c) heptene selectivity at low DME conversions is 2.2 %, reaches a maximum at 5.7 % at 37% conversion and then declined back to 4.3%. The reductions of both hexene and heptene selectivities after reaching their maximum levels are possibly the result of olefin consumption, most likely dehydrogenation/condensation to toluene. The octene selectivity, on the other hand, shows a polynomial increase from 0% to 6.6%. This is presumably due to a continuous methylation of heptene with a slight transformation to octane via hydrogen insertion.

Figure 6.12 (a-d) and Figure 6.13 (a-d) describe the variations in the individual paraffin and aromatic selectivities with the DME conversion. One can observe that at the lowest DME conversion (2%), there are no significant paraffins or aromatics formed. This may confirm that these components are not intermediates but rather final products synthesized from the olefins.

When increasing the DME conversion, one can notice from Figure 6.12(a-d), a linear increase of the paraffin selectivity that reaches up to 4% for butane, 1.8% for pentane, 2% for hexane, 2.4% for heptane, and 1.1% for the octane. Such an observation may suggest that

these paraffinic species are formed individually from their corresponding olefins through hydrogen insertion with no further chemical transformations taking place.

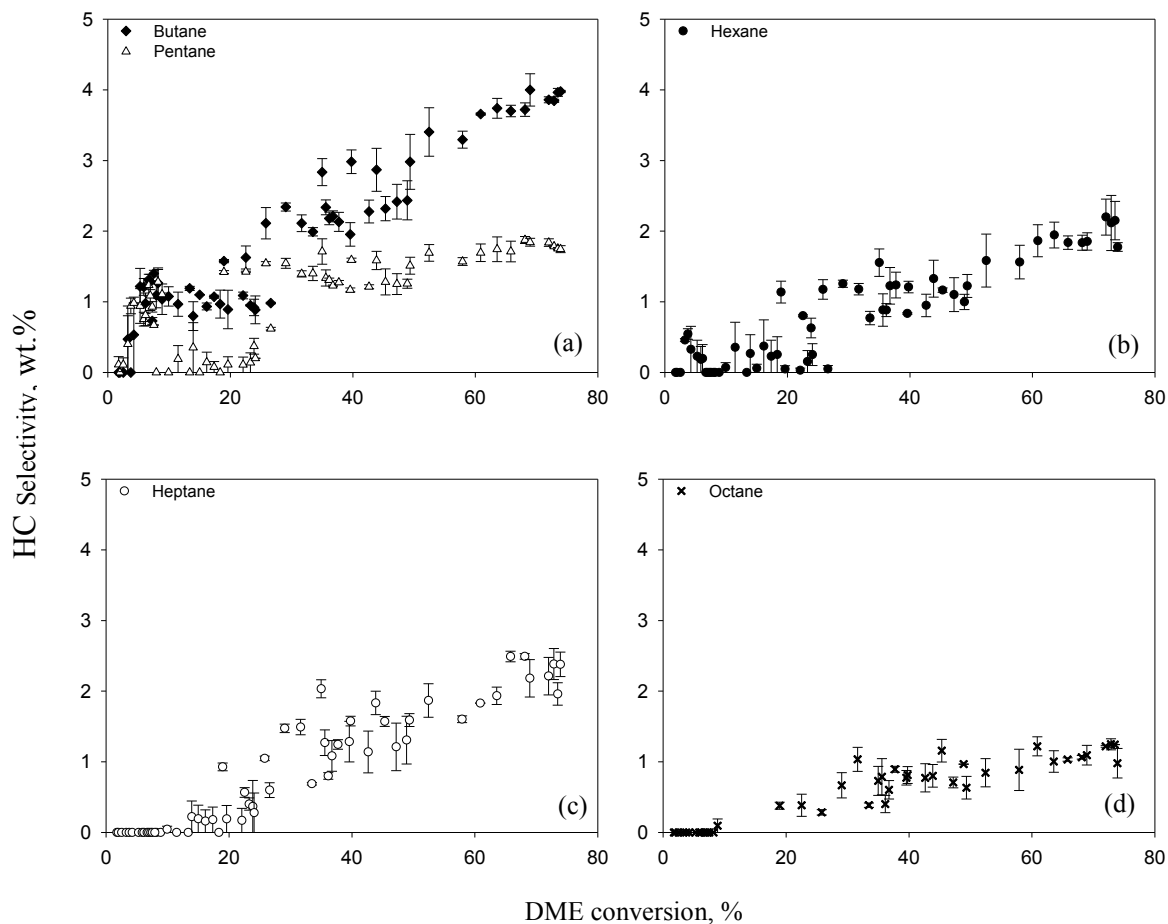


Figure 6.12: Individual paraffin selectivity vs DME conversion: (a) Butane and pentane, (b) Hexane, (c) Heptane, (d) Octane.

While examining the aromatic selectivity curves from Figure 6.13-a, one can observe that the toluene selectivity significantly augmented and peaked at 3.5% at the low DME conversion of 9%. Then decreased until it reached a 1.5% selectivity at a 74% DME conversion. Given these data and considering hexene and heptene selectivity results in Figure 6.11-b, one can argue that toluene was first produced through hexene and heptene dehydrogenation/condensation. Subsequently, toluene was further transformed, producing the heavier methylbenzenes. As for the heavier aromatics, the same olefin reaction pathways are anticipated for the xylene, mesitylene, and durene, pentamethylbenzene (PMB), and

hexamethylbenzene (HMB). In these aromatic reaction pathways, each component was formed first, and then subjected to methyl group insertion.

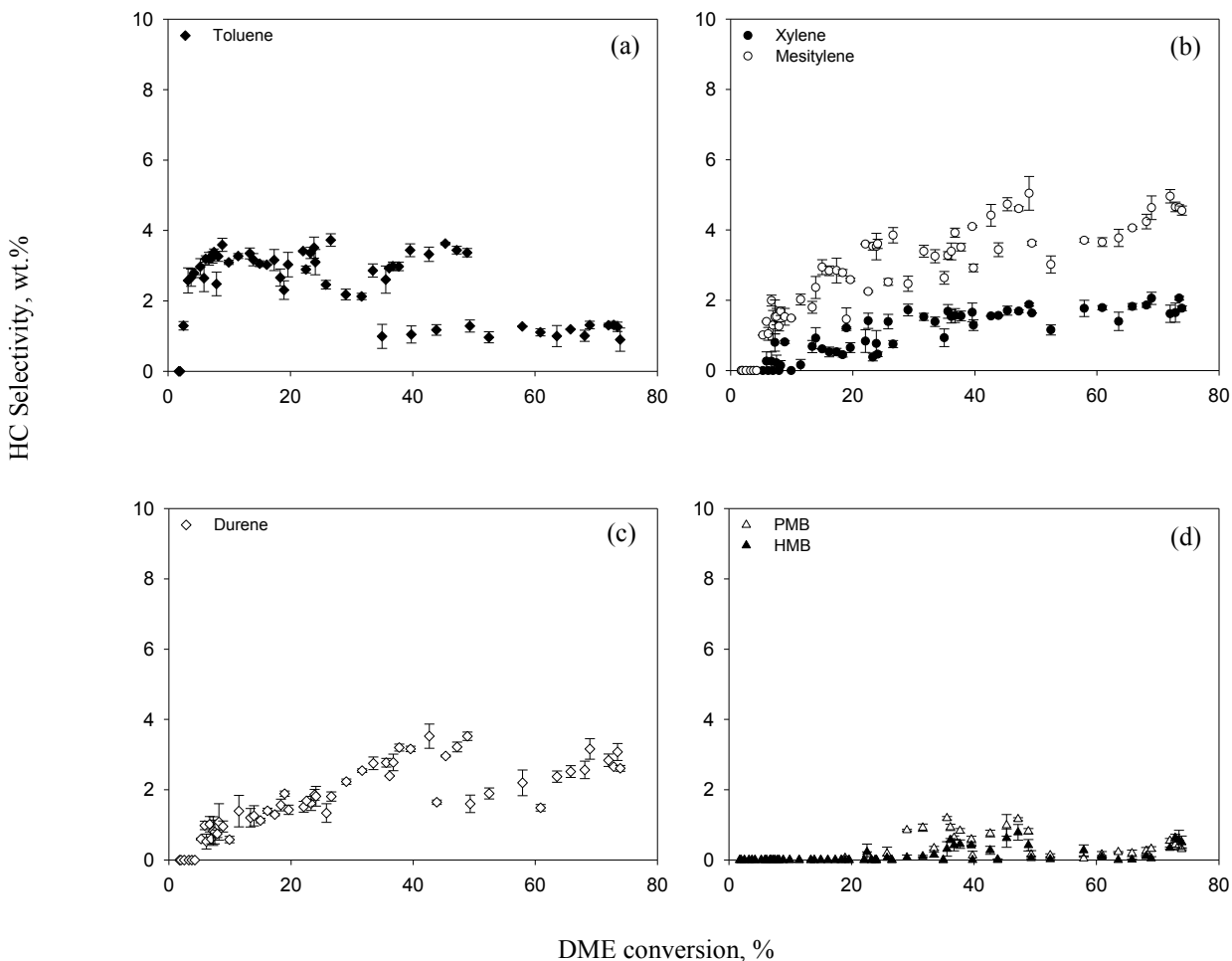


Figure 6.13: Individual aromatic selectivity vs DME conversion: (a) Toluene, (b) Xylene and mesitylene, (c) Durene, (d) Pentamethylbenzene (PMB) and Hexamethylbenzene (HMB).

The selectivity of each of these aromatics increases exponentially with the conversion of DME ending at 1.8% and 4.7% levels for xylene and mesitylene, respectively (Figure 6.13-b), and 2.8% for durene (Figure 6.13-c). Pentamethylbenzene (PMB) and hexamethylbenzene (HMB), however, are produced in all cases in small amounts (0.5 and 0.4% maximum selectivities, Figure 6.13-d). This could be attributed to a weaker methylation process as the number of methyl branches is increased (4 for the durene, and 5 for the pentamethylbenzene). Sevelle et al.[161] obtained comparable results for the durene, pentamethylbenzene, and

hexamethylbenzene in their study of the MTO reaction using an HZSM-5 catalyst. The authors argue that the incorporation of the methoxy species in the methylbenzenes is slower as the number of methyl groups increases in the aromatic species.

In summary, the DTO reactivity tests in the present study allow understanding qualitatively the DTO reaction trajectory employing an HZSM-5 catalyst with a ratio of $\text{SiO}_2/\text{Al}_2\text{O}_3 = 280$. It is shown that ethylene and propene are primary intermediates in the DTO reaction network. Each of these formed olefins undergoes methylation to its next higher parent olefin up to octene. Simultaneously, the hydrogen insertion of C_4^+ olefins leads to producing their corresponding paraffins. In addition, heptenes are partially transformed to toluene, as a precursor for producing the heavier aromatics. Then, each aromatics species undergoes a methyl group addition process. This process becomes slower when increasing the number of the methyl branches in the methylbenzenes.

6.3 DTO Reaction Network

One can consider DTO reaction network studies using HZSM-5 catalyst, in the early stages of development. Most studies are still attempting to optimize the catalytic system. To our knowledge, there is no study in the technical literature addressing this topic. This is the case, in spite of its great significance for DTO reactor scale up. Since DME and methanol in the MTO process are in equilibrium, a good point to start for developing a DTO reaction network is to consider the proposed reaction network for the MTO conversion on HZSM-5 catalysts.

As mentioned in the section 2.4.5, two approaches can be considered for modeling MTO process: lumped or detailed reaction schemes. Given the drawbacks of the lumped models, a detailed model appears as more promising. Concerning the MTO detailed reaction network, there are two main proposed mechanisms: a) the consecutive type, and b) the hydrocarbon pool mechanism. In the consecutive type mechanism, ethylene is first produced via the dehydration of methanol. Then, a further alkylation reaction by methanol with ethylene produces propylene, butenes and heavier olefins. The hydrocarbon-pool mechanism, on the other hand, distinguishes between three major steps: a) the dimethyl-ether formation, b) the establishment of the initial C-C bond, and c) the succeeding conversion of the primary light

hydrocarbons to heavier hydrocarbons, which is hypothesized to proceed via a carbenium ion mechanism [51,162].

Park and Froment [162] have proposed a detailed MTO reaction mechanism for an HZSM-5 catalyst with a Si/Al of 200 ratio based on three major steps using the hydrocarbons-pool mechanism. These authors suggested the DME formation as a result of protonated methanol dehydration. Surface methyl groups react with gas phase methanol yielding an intermediate surface dimethyl-oxonium ion which is deprotonated into DME. Then, a proton transfer from the methyl group to an adjacent Al-O basic site yields a surface-bonded oxonium methylide which reacts with protonated dimethyl ether. These two reacting substances produce a surface-bonded ethyl and/or propyl carbenium ion that are finally deprotonated to form ethylene and propene as primary hydrocarbon products. Ethylene and propene are then further transformed to higher hydrocarbons via elementary steps that include methylation, oligomerization and cracking via β -scission of surface carbenium ions.

Furthermore, regarding a possible DTO reaction network, it is proposed in the present work that dimethyl ether is converted into various species formed as reported in section 6.2.3. Carbenium ion chemistry is considered for the key species in this network. The 19 chemical species observed in DTO were described in Figure 4.3 (section 4.5.4). Components displaying a smaller than 2% selectivity, as shown in section 6.2.3, are considered insignificant in the proposed reaction network. These include pentane, hexane, heptane, octane, pentamethylbenzene, and hexamethylbenzene. The butane, on the other hand, is observed to be formed in minute amounts ($\text{butane}/(\text{butane}+\text{butene}) = 0.16$, Figure 6.14). On this basis, one can assume that the production of butane is kinetically insignificant. As a result, paraffin formation is considered negligible in the proposed reaction scheme.

As a result and for the DTO reaction in the present study, four critical steps are included: a) the formation of surface methoxy species, b) the formation of ethylene and propene as primary hydrocarbon products, c) the further methylation of ethylene and propene into heavier olefins, and d) the transformation of olefins into aromatics. In the following subsections, further discussion about these steps is provided. It should be mentioned that the

olefins and aromatic methylation steps are considered in the proposed network, as analogous to those from methanol [163].

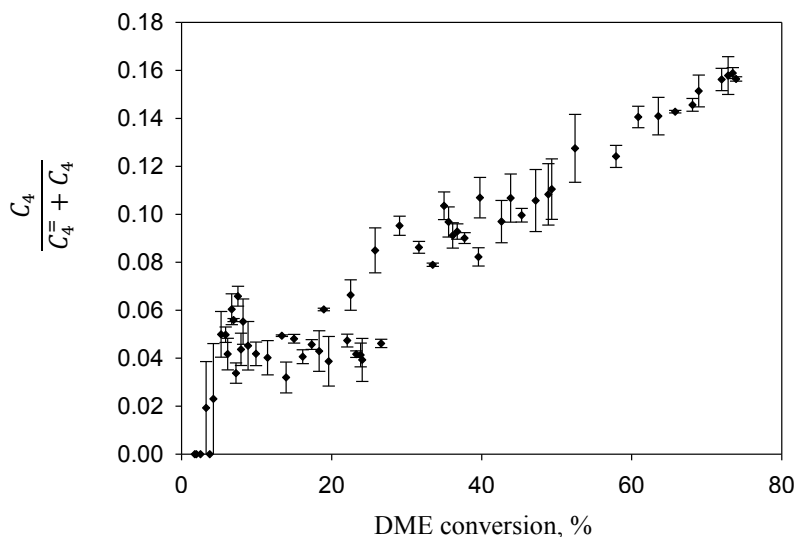


Figure 6.14: Butane/(Butane+Butene) Ratio versus DME conversion.

6.3.1 Surface Methoxy Formation

There is consensus in the technical literature regarding the first C-C carbon bond formation from the DME and the subsequent hydrocarbon methylation [164,165]. In this respect, two mechanistic routes are suggested for the olefinic and aromatic products: a stepwise or direct DME interaction [166,167]. The stepwise mechanism involves the formation of the surface methoxy species bound to the lattice oxygen and formed as an intermediate via dissociation of DME on acidic sites. The direct mechanism involves the co-adsorption of DME and the species to be methylated. It is suggested using quantum chemical calculations, that at temperatures above 170°C, the stepwise route appears to be the preferred pathway [168].

In addition, the presence of the surface-bound methoxy species using HZSM-5 zeolites has received significant support from both the experimental and theoretical studies [165]. In fact, surface methoxy species were found to play an important role as methylating intermediates in most of the proposed MTO hydrocarbon-pool reaction mechanisms [161–163,165,167,169–178].

Regarding the identification of surface methoxy species bound to HZSM-5 acidic sites three methods have been considered:

a) *HZSM-5 Brönsted Acid Site Titration with DME*. This was achieved by introducing pulses of DME into an HZSM-5 sample in a tubular reactor. Using this technique, it was possible to monitor the DME uptake on the HZSM-5 acidic sites. The ratio of DME species adsorbed per Al atom was found to be nearly 0.5(mol/mol). This is consistent with the DME being dissociated on the acidic sites forming two methoxy species [164,167,179].

b) *DME Conversion Studies Using In-Situ FTIR*. In-situ Fourier Transform Infrared Spectroscopy (FTIR) allows detecting methoxy species which are expected to initiate the initial C-C bond formation followed by methylation of olefins and formation of aromatics. Using this approach, Forester et al. [170,171] performed a DME pulse injection into an HZSM-5 sample at $T \geq 200^\circ\text{C}$ using *in-situ* FTIR. The IR spectrums showed a reaction of DME with internal hydroxyl groups which produced new bands in the CH stretching region with vibrational frequencies of 2980 and 2869 cm^{-1} . These bands were found to be reduced when injecting a pulse of substrate to be methylated (e.g. benzene), with a new methylated product (e.g. toluene) being detected. These authors identified these reactive methylating species as surface methoxy groups bound to Brönsted acid sites ($\text{CH}_3\text{-ZSM5}$). Similar findings were also obtained by Campbell et al. [169] when studying DME adsorption in four different HZSM-5 zeolites.

c) *^{13}C MAS NMR spectroscopy*. Surface methoxy species were detected using *in-situ* Solid-state Magic Angle Spinning Carbon-13 Nuclear Magnetic Resonance (^{13}C MAS NMR) signals on HZSM-5 Brönsted acid sites [165,169,172,174–177]. Campbell et al. [169] studied the ^{13}C NMR spectra response to DME adsorption using HZSM-5 at different temperatures. These authors attributed the newly produced band at 60 ppm to methoxy species when operating at $T \geq 200^\circ\text{C}$. From these results, along with the FTIR measurements, the authors concluded that the Brönsted acid sites and the methoxy species bound to them were the key species leading to hydrocarbon formation from DME. Similar observations were done by Irina et al. [172,173] who investigated the alkylation of toluene with DME to produce xylene

employing HZSM-11 at 160°C using ^{13}C MAS NMR. The authors found that methoxy species (49 ppm) were reactive in toluene alkylation.

Given the significant role of methoxy species in a DTO/MTO reaction, the proposed DTO reaction network in this study assumed a stepwise route for the methylation reaction. In this reaction, methoxy species are formed as a reaction intermediates. They then contribute in the hydrocarbon methylation process as elucidated in Figure 6.16. A similar scheme for the surface methoxy formation was also suggested by Cheung et al. [179] and Ivanova et al. [172].

Figure 6.15 reports the surface methoxy species formation by DME dehydration with an HZSM-5 catalyst. At first, di-methyl-ether is adsorbed on the Brönsted acid sites forming dimethyloxonium ions ($\text{CH}_3\text{OCH}_3\text{-HZ}$). ^{13}C MAS NMR studies [172,173] have shown that the adsorption of DME on HZSM-11 Brönsted acid sites produced new peaks at 59.5 and 62.5 ppm. These peaks were assigned to DME adsorbed species. In addition, while investigating FTIR spectroscopy of a DME reaction with HZSM-5 at 100-150°C, Foster et al. [170] and Campbell et al. [169] both reported a negative peak produced at 3610 cm^{-1} that was accompanied by the appearance of newly broad positive peaks at 2300 and 1600 cm^{-1} . The authors attributed these changes to the DME protonation forming dimethyloxonium species. On the other hand, the deprotonation of dimethyloxonium ions yielding DME and HZSM-5 acid sites, has been proven to be an important step for the DME formation from methanol [162,178]. This probably suggests that DME adsorption is a reversible process.

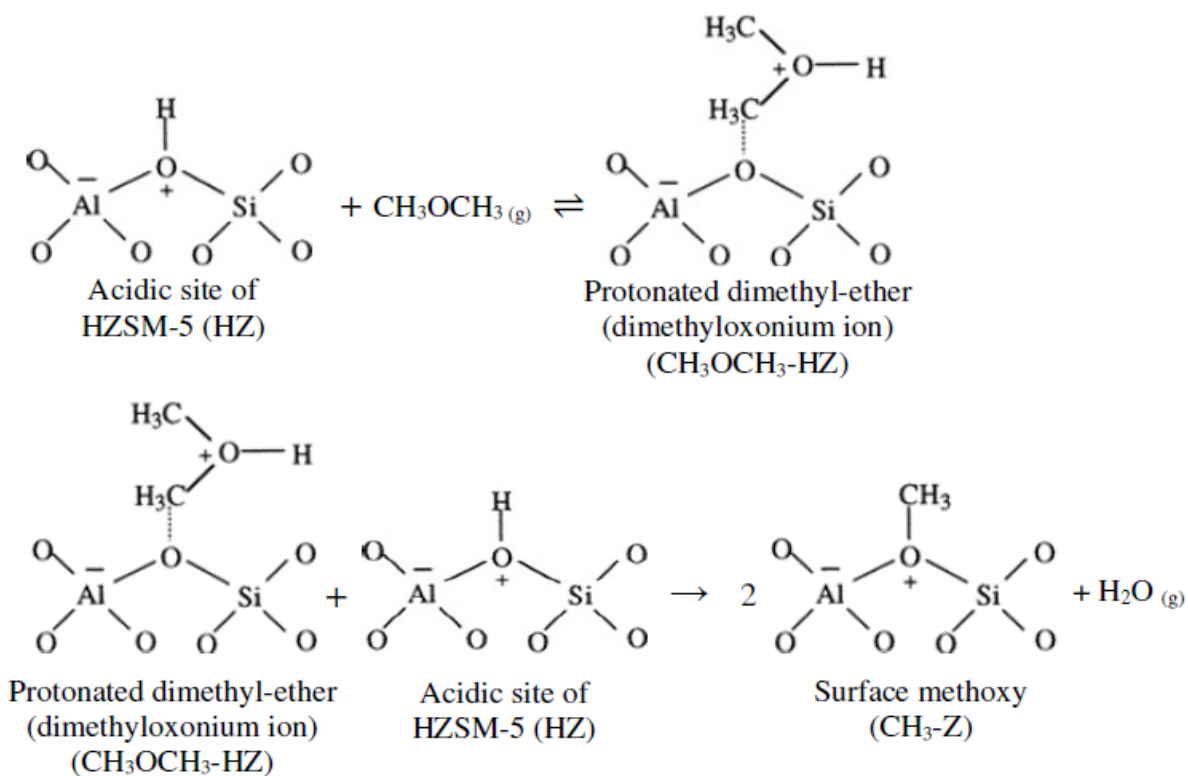


Figure 6.15: Reaction scheme for the surface methoxy species formation by DME dehydration over HZSM-5.

A possible next step in the proposed reaction network is the dehydration of the dimethyloxonium ions ($\text{CH}_3\text{OCH}_3\text{-HZ}$) with an adjacent acid site (HZ) yielding water and dual methoxy species ($\text{CH}_3\text{-Z}$). These species are covalently bound to the lattice oxygen of ZSM-5 (refer to Figure 6.15). A similar proposal for the dual methoxy species formation from DME was suggested by Cheung et al. [179]. These authors reported that two Brønsted acid sites can adsorb one DME molecule based on DME titration experiments as described earlier. Additionally, an FTIR study [170] has shown that at $T \geq 200^\circ\text{C}$, the protonated DME eliminates methanol to form methoxy species.

6.3.2 Formation of Primary Hydrocarbons Products

Knowing that HZSM-5 performs as a dehydration catalyst, many studies have suggested the production of ethylene, as a primary MTO/DTO product, via methanol/DME dehydration [28,41,51,70,85]. Additionally, other studies have suggested ethylene and propene as primary products from DME for the MTO reaction network as well [162,178,180,181]. With

this in mind, the proposed initial hydrocarbons formed from DME are described in Figure 6.16-b.

Following this, the protonated DME ($\text{CH}_3\text{OCH}_3\text{-HZ}$) is dehydrated using the acidic sites of HZSM-5 yielding ethylcarbenium ions ($\text{C}_2\text{H}_4\text{-HZ}$, step-b.1) which reversibly deprotonated and forming ethylene (step-b.2). The propene, on the other hand, is formed via the reaction of methoxy species with gas phase ethylene forming a secondary propylcarbonium ion ($\text{C}_3\text{H}_6\text{-HZ}$) that deprotonates to yield propene (step-c.1).

In this respect, Hill in his study [164] performed a steady-state ethylene methylation experiments with methoxy species formed from DME at very low conversions ($< 0.2\%$, to inhibit propene further reactions). The author showed that the propene formation rate obeys a first-order dependence on the partial pressure of ethylene. The methylation of ethylene by methoxy species to yield propene has been considered as well by several authors [162,167,169,182]. In addition, FTIR results reported by Forester et al. [170,171] showed that the injection of ethylene onto an HZSM-5 sample pretreated with DME, produced propene and caused a reduction in 2980, 2868, and 1460 cm^{-1} bands that were assigned to methoxy species.

a) Surface methoxy formation: $\text{CH}_3\text{OCH}_3(\text{g}) + \text{HZ} \rightleftharpoons \text{CH}_3\text{OCH}_3 - \text{HZ}$ $\text{CH}_3\text{OCH}_3 - \text{HZ} + \text{HZ} \rightarrow 2\text{CH}_3 - \text{Z} + \text{H}_2\text{O}(\text{g})$	a.1 a.2	$\text{C}_5\text{H}_{10}(\text{g}) + \text{CH}_3 - \text{Z} \rightarrow \text{C}_6\text{H}_{12} - \text{HZ} \rightleftharpoons \text{C}_6\text{H}_{12}(\text{g}) + \text{HZ}$ c.4 $\text{C}_6\text{H}_{12}(\text{g}) + \text{CH}_3 - \text{Z} \rightarrow \text{C}_7\text{H}_{14} - \text{HZ} \rightleftharpoons \text{C}_7\text{H}_{14}(\text{g}) + \text{HZ}$ c.5 $\text{C}_7\text{H}_{14}(\text{g}) + \text{CH}_3 - \text{Z} \rightarrow \text{C}_8\text{H}_{16} - \text{HZ} \rightleftharpoons \text{C}_8\text{H}_{16}(\text{g}) + \text{HZ}$ c.6
b) Ethylene formation: $\text{CH}_3\text{OCH}_3 - \text{HZ} \rightarrow \text{C}_2\text{H}_4 - \text{HZ} + \text{H}_2\text{O}(\text{g})$ $\text{C}_2\text{H}_4 - \text{HZ} \rightleftharpoons \text{C}_2\text{H}_4(\text{g}) + \text{HZ}$	b.1 b.2	d) Hexene aromatization: $\text{C}_6\text{H}_{12} - \text{HZ} \rightarrow \text{C}_6\text{H}_{10} - \text{HZ} \xrightarrow{-3\text{H}_2(\text{g})} \text{C}_6\text{H}_6 - \text{HZ} \rightleftharpoons \text{C}_6\text{H}_6(\text{g}) + \text{HZ}$
c) Olefins methylation: $\text{C}_2\text{H}_4(\text{g}) + \text{CH}_3 - \text{Z} \rightarrow \text{C}_3\text{H}_6 - \text{HZ} \rightleftharpoons \text{C}_3\text{H}_6(\text{g}) + \text{HZ}$ $\text{C}_3\text{H}_6(\text{g}) + \text{CH}_3 - \text{Z} \rightarrow \text{C}_4\text{H}_8 - \text{HZ} \rightleftharpoons \text{C}_4\text{H}_8(\text{g}) + \text{HZ}$ $\text{C}_4\text{H}_8(\text{g}) + \text{CH}_3 - \text{Z} \rightarrow \text{C}_5\text{H}_{10} - \text{HZ} \rightleftharpoons \text{C}_5\text{H}_{10}(\text{g}) + \text{HZ}$	c.1 c.2 c.3	e) Aromatics methylation: $\text{C}_6\text{H}_6(\text{g}) + \text{CH}_3 - \text{Z} \rightarrow \text{C}_6\text{H}_7 - \text{HZ} \rightleftharpoons \text{C}_6\text{H}_7(\text{g}) + \text{HZ}$ e.1 $\text{C}_6\text{H}_6(\text{g}) + \text{CH}_3 - \text{Z} \rightarrow \text{C}_6\text{H}_7 - \text{HZ} \rightleftharpoons \text{C}_6\text{H}_7(\text{g}) + \text{HZ}$ e.2 $\text{C}_6\text{H}_6(\text{g}) + \text{CH}_3 - \text{Z} \rightarrow \text{C}_6\text{H}_7 - \text{HZ} \rightleftharpoons \text{C}_6\text{H}_7(\text{g}) + \text{HZ}$ e.3 $\text{C}_6\text{H}_6(\text{g}) + \text{CH}_3 - \text{Z} \rightarrow \text{C}_6\text{H}_7 - \text{HZ} \rightleftharpoons \text{C}_6\text{H}_7(\text{g}) + \text{HZ}$ e.4

Figure 6.16: Proposed DTO elementary reaction network over HZSM-5.

6.3.3 Methylation of C_3^+ Olefins

In the present study, the formation of C_4^+ olefins (butene, pentene, hexene, heptene, and octene) is proposed to proceed via carbenium ions and elementary steps similar to the ones for propene formation (refer to Figure 6.16, steps c.2-c.6): a) Adsorbed olefins are methylated with methyl-carbenium ions (i.e. methoxy species). This yields a larger olefin (with one additional carbon) in a protonated state, b) Larger adsorbed olefins formed can proceed to new methylation steps or be deprotonated and desorbed to the gas phase.

The methylation of olefins by methoxy species to yield the higher carbon number of olefins has been shown to be an important route to higher hydrocarbons in methanol/DME conversion [170,171,175]. Such a methylation process has been demonstrated experimentally [162,169,182] and theoretically using quantum chemical calculations [167,183,184]. In his study, Hill [164] performed an isolated steady-state methylation of propene and butene using an HZSM-5 by methoxy species generated from DME. These authors showed that such reactions produced a higher degree of methoxy substituted olefins (i.e. butene and pentene), displaying a first-order rate dependence with the olefinic species already methylated (i.e. propene and butene). Svelle et al. [163] showed that the rate of propene methylation to form butene with HZSM-5 is about double when using DME instead of methanol. This is expected given that DME can produce the double of methoxy species than methanol, as shown from the HZSM-5 titration experiments [164,167,179].

6.3.4 Hexene Aromatization

In the present study, the formation of benzene, the precursor of aromatics, is considered via hexene aromatization (cyclization). As in the reaction scheme in Figure 6.16-d, the process starts by cyclization of the protonated hexene to a protonated cyclohexane. Dehydrogenation of the protonated cyclohexane yields the protonated benzene that deprotonates to gas phase benzene.

In this respect, the formation of the aromatics through a hydrogen transfer from olefinic species, with an intermediate cyclization step to naphthenes, has been established using a

pure HZSM-5 [74,185–187] , a modified Zn-, Ga-, and Pt-HZSM-5 [188–190], and alkali-treated (NaOH) HZSM-5 [191] at different reaction conditions.

6.3.5 Methylation of C₆₊ Aromatics

Benzene, the precursor for the produced aromatics species, undergoes methyl group insertion to produce toluene as shown in Figure 6.16-e.1. Since benzene it is only detected in minute amounts at the reactor outlet, benzene is considered an intermediate formed and fully converted in the reaction network.

Regarding the toluene reaction pathway, a toluene selectivity curve was shown to display a maximum of 3.5% at 9% DME conversion (Figure 6.13-a, section 6.2.3). Thereafter, the reduction of toluene selectivity was ascribed to its further transformation into poly-methylbenzene species. Thus, the formation of poly-methylbenzene species can be considered via methoxy group alkylation process similar to the one of olefinic species (section 6.3.3) as detailed in Figure 6.16-e.

In this respect, a ¹³C MAS NMR investigation showed that the methylation of the toluene by methoxy species to yield xylene, is an important pathway of the MTO reaction mechanism using HZSM-5 [175], HZSM-11 [172], and Y zeolites [165,176]. In addition, a benzene injection into an HZSM-5 catalyst pretreated with methanol showed an immediate decline in the FTIR intensities of 2980, 2868, and 1460 cm⁻¹ bands (assigned to methoxy species) with a detection of toluene and traces of xylene [171]. Hill et al. [192] performed kinetic analysis of benzene, toluene, and xylene methylation employing HZSM-5 with DME at low conversions (<0.1%) and with high DME aromatic ratios (>30:1). These authors found that the products (toluene, xylene, and mesitylene) showed a first order dependence on the aromatic being methylated. This was consistent with the results of olefin methylation. This was also indicative of a zeolite surface covered by reactive DME-derived methoxy species.

6.4 Conclusions

This chapter examines the reactivity properties of the HZSM-5 for light olefin production from DME with different SiO₂/Al₂O₃ ratios. On the basis of the product species formed and

various trends with temperature and reaction times, a detailed reaction mechanism is proposed. The following are the most significant conclusions:

1. DME conversions augmented with the acidity of the HZSM-5 catalyst. Higher acidity led to higher initial catalyst activity, with however lower catalyst stability with time-on-stream.
2. DME conversion and coke formation increased with temperature. In the case of ZSM5-280, coke yields were limited to 1.16wt% with negligible catalyst deactivation. Additionally, ZSM5-280 proved to be selective towards light olefins, particularly propene and butene. For this reason, it has been selected for investigating the DTO reaction network.
3. Reactivity tests using HZSM-5 with a $\text{SiO}_2/\text{Al}_2\text{O}_3 = 280$ ratio showed an increase of the DME conversion as a result of rising the reaction temperature along with the contact time. At very low conversion (2%), ethylene, propene, and butene were found to be the major products with total selectivity of 94% with the rest being heavy olefins and with no paraffins or aromatics produced. By increasing the conversion, both ethylene and propene selectivities were found to reduce while butene was slightly increased and then reduced later with increasing the DME conversion. On the other hand, a continuous increase of C_5^+ olefins, paraffins, and aromatics with an increasing DME conversion was observed up to 45%. Thereafter, the change of the product selectivities became less pronounced. At the maximum DME conversion of 74%, the attained selectivities for light olefins, heavy olefins, paraffins, and aromatics were 48%, 32%, 9%, and 11%, respectively. These findings show that the production of paraffins from DME using HZSM-5 with a $\text{SiO}_2/\text{Al}_2\text{O}_3$ of 280 is very limited while compared to the corresponding olefins.
4. A DTO reaction network is considered based on the observations from reactivity tests using HZSM-5 catalyst with a $\text{SiO}_2/\text{Al}_2\text{O}_3$ of 280. The elementary steps based on carbenium ion chemistry were found to best describe the DME surface transformation over HZSM-5 acid sites in which methoxy species plays an important role as a methylating agent. The proposed reaction network considers ethylene and propene as

primary intermediates. The formed olefin, then, undergo methylation to its next higher olefin up to octene. In addition, hexene is partially dehydrogenated/condensed forming benzene. Benzene is considered the precursor for producing the heavier aromatics. Benzene is an intermediate species in which its rate of production and transformation are essentially equal. Finally, aromatics species undergo a methyl group addition process. This process becomes slower with increasing number of the methyl groups in the aromatic ring.

CHAPTER 7 KINETIC MODELING OF DIMETHYL ETHER CONVERSION TO OLEFINS OVER HZSM-5

7.1 Introduction

The present chapter reports the kinetic modeling of neat DME conversion to light olefins using an HZSM-5 catalyst with a SiO₂/Al₂O₃ ratio of 280. The proposed reaction mechanism was described in section 6.3. The main assumptions of the proposed heterogeneous kinetic model are justified and discussed in section 7.2. Based on the proposed heterogeneous kinetic model, a non-linear set of equations is established. Following this, the proposed model is simplified and reparameterized. After this, the results of the kinetic modeling, including the various determined kinetic constants and activation energies, are reported and reviewed. Finally, the main conclusions of the kinetic model for DTO are reported.

7.2 Model Assumptions

The proposed model describes a series of 15 sound elementary steps for the DTO reaction network as outlined in Figure 6.16 (section 6.3.3). In order to develop this kinetic model, a number of reaction steps and suitable assumptions are considered:

- i. The intrinsic reaction rate constant is described via an Arrhenius equation, with this involving a single activation energy:

$$k_i = k_i \exp\left(-\frac{E_i}{R}\left(\frac{1}{T} - \frac{1}{T_C}\right)\right) \quad (7.1)$$

where T and T_C are operating and centering reaction temperatures (K), respectively, and R is the universal gas constant (8.314 J/mol/K). The mathematical form, as proposed in Equation 7.1, is adequate, considering the use of a centering temperature which reduces cross-correlation between parameters, facilitating their adequate computation.

- ii. All surface chemical reactions are first order with respect to the reactants. One can observe in section 2.4.5 that all the proposed kinetics model for the MTO (methanol to olefins) reaction system are 1st order dependence on the reactants.
- iii. The activation energy (E_i) is independent of the surface coverage of the surface species. This means that surface reaction involves a uniform process with the same adsorption probability assigned to all active sites. As a result, the probability of adsorption on vacant sites is independent of whether the adjacent sites are already occupied or not. Thus, there is no interaction between the adsorbed species molecules [30]. This model assumption can be statistically validated, once one determines the kinetic parameters involved in the elementary reaction rates (to be described later) with narrow spans for the 95% confidence interval.
- iv. Transport resistances to the external mass transfer at the surface (convection and interface transports) are negligible. Mahay et al. [93] evaluated the external particle mass transfer resistances in the Berty Reactor for N₂, using naphthalene pellets. These pellets had similar dimensions to those of the catalytic bed used for DTO experiments. These authors measured the external particle mass transfer coefficient at different impeller speeds and found that when running the reactor at ≥ 1500 rpm, the external mass transfer limitation was not significant.
- v. The gradientless Berty Reactor operates in the back mixing mode as described in section 4.5.1. Thus, reaction data can be modeled using the CSTR model. Hence, the concentration of the reagent in the gas phase, whether DME or product, and the reaction temperature are both uniform throughout the catalyst bed. Additionally, the temperature and concentration differences between the fluid and HZSM-5 external surface (i.e. interfacial gradients) are insignificant at all times-on-stream. Therefore, the influence of axial and radial dispersions can be neglected.
- vi. The internal diffusion inside the catalyst particles (molecular transport) is insignificant. This is considered adequate given the small size of pellet particles (14 μm) as well as the expected DME effective diffusivity in the H-ZSM5 crystallites used in the kinetic experiments. Additionally, the Berty reactor is an isothermal well

mixed unit with a high fluid gas circulation. As a result, the temperature and concentration gradients inside the HZSM-5 pores (i.e. intraparticle gradients) are expected to be negligibly small. In other word, the effectiveness factor (η) = 1.

- vii. The HZSM-5 with a $\text{SiO}_2/\text{Al}_2\text{O}_3 = 280$ ratio shows to accommodate the coke load up to 1.16% with no influence on the catalyst activity. Therefore, the catalyst deactivation effect is excluded.

7.3 Kinetic Model Development

As described in section 2.4.5, modeling the MTO process can be accomplished using either a lumped or a detailed reaction scheme. The approach considered in this study, however, is to model the DTO reaction based on the observable individual chemical species, as described in section 6.2.3. This allows formulating a detailed reaction scheme as reported in section 6.3. In the specific case of the HZSM-5 acid catalyst for DTO, it is proposed, in the present dissertation, to use a reactant-product based reaction network.

In terms of surface reactions there are three possible mechanisms to be considered: Langmuir-Hinshelwood, Rideal-Eley, and precursor kinetics. Any surface reaction can be described as following one of these mechanisms, or some combination of them. It is generally accepted that Langmuir-Hinshelwood kinetics is ideal for modeling a heterogeneous zeolitic system in which the species adsorption/desorption is an essential step [193–195]. In this respect, it is envisioned to follow the conversion of DME using Langmuir-Hinshelwood formulations.

Table 7.1 reports the DTO elementary reaction steps with their relevant reaction rates. Dehydration and alkylation reactions are considered irreversible while protonation-deprotonation are considered reversible. One should note that the proposed steps are consistent with the mechanism proposed and with the assumptions detailed in section 7.2. In addition, one can notice that the overall heterogeneous catalytic reactions proceed involving: a) surface adsorption (protonation) of DME onto the acidic sites of HZSM-5, b) surface reaction of DME with product formation on the acidic sites of HZSM-5, c) product desorption from the HZSM-5 acidic sites. It is assumed that each surface chemical reaction

follows a first order power low model, with the surface chemical reaction being the rate limiting step.

As described in section 6.3.4, benzene is considered as an intermediate autocatalytic species. On this basis, the formation of toluene (Table 7.1-j.1) is proposed to be a result of three combined steps: a) the formation of the protonated hexene from the reversible hexene adsorption ($C_6H_{12}-HZ$, Figure 6.16-c.4), b) hexene dehydrogenation to form benzene (Figure 6.16-d), and c) benzene methylation to form toluene Figure 6.16-e.1).

For the reaction network shown in Table 7.1, the HZSM-5 acidic site balance gives:

$$1 = \theta_{HZ} + \theta_{DME-HZ} + \sum_{ol=2}^8 \theta_{C_{ol}-HZ} + \sum_{ar=T,X,M,D} \theta_{ar-HZ} \quad (7.2)$$

where *ol* and *ar* refer to olefinic and aromatics species.

At adsorption equilibrium, the net rate of DME adsorption equals zero. When solving for the DME surface coverage (θ_{DME-HZ}) from the DME adsorption Step a-1 (Table 7.1), the following is obtained:

$$\theta_{DME-HZ} = K_{DME-HZ} p_{DME} \theta_{HZ} \quad (7.3)$$

Similarly, the surface coverage of each product species can be obtained based on the product desorption steps set at equilibrium:

$$\theta_{i-HZ} = K_{i-HZ} p_i \theta_{HZ}$$

where K_i is the equilibrium adsorption constant (1/barg) of species “*i*” and p_i is the partial pressure (barg) of species “*i*”.

Substituting θ_{DME-HZ} and θ_{i-HZ} in the site balance (Equation 7.2) the vacant acid sites coverage can be expressed as:

$$1 = \theta_{HZ} + K_{DME-HZ} p_{DME} \theta_{HZ} + \theta_{HZ} \sum_{ol=2}^8 K_{C_{ol}-HZ} p_{C_{ol}} + \theta_{HZ} \sum_{ar=T,X,M,D} K_{ar-HZ} p_{ar}$$

$$\Rightarrow \theta_{HZ} = \frac{1}{1 + K_{DME-HZ} p_{DME} + \sum_{ol=2}^8 K_{C_{ol}^- - HZ} p_{C_{ol}^-} + \sum_{ar=T,X,M,D} K_{ar-HZ} p_{ar}} \quad (7.4)$$

Table 7.1: Elementary steps of the DTO reaction network with the related reaction rates and equilibrium parameters.

a) Surface Methoxy formation:		
$CH_3OCH_3(g) + HZ \rightleftharpoons CH_3OCH_3 - HZ$	$K_{DME-HZ} = \frac{\theta_{DME-HZ}}{p_{DME} \theta_{HZ}}$	a.1
$CH_3OCH_3 - HZ + HZ \xrightarrow{k_1'} 2CH_3 - Z + H_2O(g)$	$r_{1'} = k_1' \theta_{DME-HZ} \theta_{HZ}$	a.2
b) Ethylene formation:		
$CH_3OCH_3 - HZ \xrightarrow{k_1} C_2H_4 - HZ + H_2O$	$r_1 = k_1 \theta_{DME-HZ}$	b.1
$C_2H_4 - HZ \rightleftharpoons C_2H_4(g) + HZ$	$K_{C_2^- - HZ} = \frac{\theta_{C_2^- - HZ}}{p_{C_2^-} \theta_{HZ}}$	b.2
c) Propene formation:		
$C_2H_4(g) + CH_3 - Z \xrightarrow{k_2} C_3H_6 - HZ$	$r_2 = k_2 p_{C_2^-} \theta_{CH_3-Z}$	c.1
$C_3H_6 - HZ \rightleftharpoons C_3H_6(g) + HZ$	$K_{C_3^- - HZ} = \frac{\theta_{C_3^- - HZ}}{p_{C_3^-} \theta_{HZ}}$	c.2
d) Butene formation:		
$C_3H_6(g) + CH_3 - Z \xrightarrow{k_3} C_4H_8 - HZ$	$r_3 = k_3 p_{C_3^-} \theta_{CH_3-Z}$	d.1
$C_4H_8 - HZ \rightleftharpoons C_4H_8(g) + HZ$	$K_{C_4^- - HZ} = \frac{\theta_{C_4^- - HZ}}{p_{C_4^-} \theta_{HZ}}$	d.2
e) Pentene formation:		
$C_4H_8(g) + CH_3 - Z \xrightarrow{k_4} C_5H_{10} - HZ$	$r_4 = k_4 p_{C_4^-} \theta_{CH_3-Z}$	e.1
$C_5H_{10} - HZ \rightleftharpoons C_5H_{10}(g) + HZ$	$K_{C_5^- - HZ} = \frac{\theta_{C_5^- - HZ}}{p_{C_5^-} \theta_{HZ}}$	e.2
f) Hexene formation:		
$C_5H_{10}(g) + CH_3 - Z \xrightarrow{k_5} C_6H_{12} - HZ$	$r_5 = k_5 p_{C_5^-} \theta_{CH_3-Z}$	f.1
$C_6H_{12} - HZ \rightleftharpoons C_6H_{12}(g) + HZ$	$K_{C_6^- - HZ} = \frac{\theta_{C_6^- - HZ}}{p_{C_6^-} \theta_{HZ}}$	f.2

Table 7.1 (continue): Elementary steps of the DTO reaction network with the related reaction rates and equilibrium parameters.

g) Heptene formation:		
$C_6H_{12(g)} + CH_3 - Z \xrightarrow{k_6} C_7H_{14} - HZ$	$r_6 = k_6 p_{C_6} \theta_{CH_3-Z}$	g.1
$C_7H_{14} - HZ \rightleftharpoons C_7H_{14(g)} + HZ$	$K_{C_7-HZ} = \frac{\theta_{C_7-HZ}}{p_{C_7} \theta_{HZ}}$	g.2
h) Octene formation:		
$C_7H_{14(g)} + CH_3 - Z \xrightarrow{k_7} C_8H_{16} - HZ$	$r_7 = k_7 p_{C_7} \theta_{CH_3-Z}$	h.1
$C_8H_{16} - HZ \rightleftharpoons C_8H_{16(g)} + HZ$	$K_{C_8-HZ} = \frac{\theta_{C_8-HZ}}{p_{C_8} \theta_{HZ}}$	h.2
i) Toluene formation:		
$C_6H_{12(g)} + CH_3 - Z \xrightarrow{k_8} \text{C}_6\text{H}_5 - HZ + 3H_2$	$r_8 = k_8 p_{C_6} \theta_{CH_3-Z}$	i.1
$\text{C}_6\text{H}_5 - HZ \rightleftharpoons \text{C}_6\text{H}_5(g) + HZ$	$K_{T-HZ} = \frac{\theta_{T-HZ}}{p_T \theta_{HZ}}$	i.2
g) Xylene formation:		
$\text{C}_6\text{H}_4(g) + CH_3 - Z \xrightarrow{k_9} \text{C}_6\text{H}_3 - HZ$	$r_9 = k_9 p_T \theta_{CH_3-Z}$	j.1
$\text{C}_6\text{H}_3 - HZ \rightleftharpoons \text{C}_6\text{H}_3(g) + HZ$	$K_{X-HZ} = \frac{\theta_{X-HZ}}{p_X \theta_{HZ}}$	j.2
k) Mesitylene formation:		
$\text{C}_6\text{H}_3(g) + CH_3 - Z \xrightarrow{k_{10}} \text{C}_6\text{H}_2 - HZ$	$r_{10} = k_{10} p_X \theta_{CH_3-Z}$	k.1
$\text{C}_6\text{H}_2 - HZ \rightleftharpoons \text{C}_6\text{H}_2(g) + HZ$	$K_{M-HZ} = \frac{\theta_{M-HZ}}{p_M \theta_{HZ}}$	k.2
l) Durene formation:		
$\text{C}_6\text{H}_2(g) + CH_3 - Z \xrightarrow{k_{11}} \text{C}_6\text{H}_1 - HZ$	$r_{11} = k_{11} p_M \theta_{CH_3-Z}$	l.1
$\text{C}_6\text{H}_1 - HZ \rightleftharpoons \text{C}_6\text{H}_1(g) + HZ$	$K_{D-HZ} = \frac{\theta_{D-HZ}}{p_D \theta_{HZ}}$	l.2

Furthermore, considering that the methoxy species formation is at a steady state, one can get the coverage of the surface methoxy species bound to the lattice oxygen of ZSM-5 ($CH_3 - Z$) as follows:

$$\begin{aligned}
r_{\theta_{CH_3-Z}} &= 2r_{1'} - \sum_{j=2}^{12} r_j \\
&= 2k_{1'}\theta_{DME-HZ}\theta_{HZ} - \theta_{CH_3-Z} \left(\sum_{j=2}^7 k_j p_{C_j^-} + k_8 p_{C_6^-} + k_9 p_T + k_{10} p_X + k_{11} p_M \right) = 0 \\
\Rightarrow \theta_{CH_3-Z} &= \frac{2k_{1'} K_{DME-HZ} p_{DME} \theta_{HZ}^2}{\sum_{j=2}^7 k_j p_{C_j^-} + k_8 p_{C_6^-} + k_9 p_T + k_{10} p_X + k_{11} p_M} \quad (7.5)
\end{aligned}$$

where k_j is the rate constant of reaction step “ j ”.

7.4 Species Mole Balance in Berty Reactor

Kinetic modeling in the Berty reactor requires the consideration of the species balances. Such species balance equations can be established on the basis of the various assumptions described in section 7.2. In addition, reactions rates can be considered as functions of species surface coverage as defined in section 7.3. Since the reactor used for getting the data is a CSTR, each one of the chemical species mole balances across the reactor can be written as:

$$Wr_i = F_T y_i - F_{T0} y_{i0} = F_{T0} (\alpha y_i - y_{i0})$$

$$\text{so, } \frac{\alpha y_j - y_{j0}}{\tau} = r_j \quad (7.6)$$

where $\alpha = F_T/F_{T0}$, $\tau = W/F_{T0}$, F_{T0} and F_T are the total inlet (DME) and outlet molar DME flow rates (mol/hr).

By substituting the rate equations from Table 7.1 with the species surface coverage from Equations 7.3, 7.4, 7.5 and 7.6, the product species balances can be expressed using a set of nonlinear algebraic equations as follows:

For DME:

$$\frac{1 - \alpha y_{DME}}{\tau} = -r_{DME} = r_{1'} + r_1 = k_{1'} \theta_{DME-HZ} \theta_{HZ} + k_1 \theta_{DME-HZ}$$

$$\Rightarrow -r_{DME} = k_{1'} K_{DME-HZ} p_{DME} \theta_{HZ}^2 + k_1 K_{DME-HZ} p_{DME} \theta_{HZ} \quad (7.7)$$

For Ethylene:

$$\frac{\alpha y_{C_2^-}}{\tau} = r_{C_2^-} = r_1 - r_2 = k_1 \theta_{DME-HZ} - k_2 p_{C_2^-} \theta_{CH_3-Z}$$

$$\Rightarrow r_{C_2^-} = k_1 K_{DME-HZ} p_{DME} \theta_{HZ} - \frac{2k_{1'} k_2 K_{DME-HZ} p_{C_2^-} p_{DME} \theta_{HZ}^2}{\sum_{j=2}^7 k_j p_{C_j^-} + k_8 p_{C_6^-} + k_9 p_T + k_{10} p_X + k_{11} p_M} \quad (7.8)$$

For Propene:

$$\frac{\alpha y_{C_3^-}}{\tau} = r_{C_3^-} = r_2 - r_3 = (k_2 p_{C_2^-} - k_3 p_{C_3^-}) \theta_{CH_3-Z}$$

$$\Rightarrow r_{C_3^-} = \frac{2k_{1'} K_{DME-HZ} p_{DME} (k_2 p_{C_2^-} - k_3 p_{C_3^-}) \theta_{HZ}^2}{\sum_{j=2}^7 k_j p_{C_j^-} + k_8 p_{C_6^-} + k_9 p_T + k_{10} p_X + k_{11} p_M} \quad (7.9)$$

For Butene:

$$\frac{\alpha y_{C_4^-}}{\tau} = r_{C_4^-} = r_3 - r_4 = (k_3 p_{C_3^-} - k_4 p_{C_4^-}) \theta_{CH_3-Z}$$

$$\Rightarrow r_{C_4^-} = \frac{2k_{1'} K_{DME-HZ} p_{DME} (k_3 p_{C_3^-} - k_4 p_{C_4^-}) \theta_{HZ}^2}{\sum_{j=2}^7 k_j p_{C_j^-} + k_8 p_{C_6^-} + k_9 p_T + k_{10} p_X + k_{11} p_M} \quad (7.10)$$

For Pentene:

$$\frac{\alpha y_{C_5^-}}{\tau} = r_{C_5^-} = r_4 - r_5 = (k_4 p_{C_4^-} - k_5 p_{C_5^-}) \theta_{CH_3-Z}$$

$$\Rightarrow r_{C_5^-} = \frac{2k_1'K_{DME-HZ}p_{DME}(k_4p_{C_4^-}-k_5p_{C_5^-})\theta_{HZ}^2}{\sum_{j=2}^7 k_j p_{C_j^-} + k_8 p_{C_6^-} + k_9 p_T + k_{10} p_X + k_{11} p_M} \quad (7.11)$$

For Hexene:

$$\frac{\alpha y_{C_6^-}}{\tau} = r_{C_6^-} = r_5 - r_6 - r_8 = (k_5 p_{C_5^-} - (k_6 + k_8) p_{C_6^-}) \theta_{CH_3-Z}$$

$$\Rightarrow r_{C_6^-} = \frac{2k_1'K_{DME-HZ}p_{DME}(k_5p_{C_5^-}-(k_6+k_8)p_{C_6^-})\theta_{HZ}^2}{\sum_{j=2}^7 k_j p_{C_j^-} + k_8 p_{C_6^-} + k_9 p_T + k_{10} p_X + k_{11} p_M} \quad (7.12)$$

For Heptene:

$$\frac{\alpha y_{C_7^-}}{\tau} = r_{C_7^-} = r_6 - r_7 = (k_6 p_{C_6^-} - k_7 p_{C_7^-}) \theta_{CH_3-Z}$$

$$\Rightarrow r_{C_7^-} = \frac{2k_1'K_{DME-HZ}p_{DME}(k_6p_{C_6^-}-k_7p_{C_7^-})\theta_{HZ}^2}{\sum_{j=2}^7 k_j p_{C_j^-} + k_8 p_{C_6^-} + k_9 p_T + k_{10} p_X + k_{11} p_M} \quad (7.13)$$

For Octene:

$$\frac{\alpha y_{C_8^-}}{\tau} = r_{C_8^-} = r_7 = k_7 p_{C_7^-} \theta_{CH_3-Z}$$

$$\Rightarrow r_{C_8^-} = \frac{2k_1'K_{DME-HZ}p_{DME}(k_7p_{C_7^-})\theta_{HZ}^2}{\sum_{j=2}^7 k_j p_{C_j^-} + k_8 p_{C_6^-} + k_9 p_T + k_{10} p_X + k_{11} p_M} \quad (7.14)$$

For Toluene:

$$\frac{\alpha y_T}{\tau} = r_T = r_8 - r_9 = (k_8 p_{C_6^-} - k_9 p_T) \theta_{CH_3-Z}$$

$$\Rightarrow r_T = \frac{2k_1'K_{DME-HZ}p_{DME}(k_8p_{C_6^-}-k_9p_T)\theta_{HZ}^2}{\sum_{j=2}^7 k_j p_{C_j^-} + k_8 p_{C_6^-} + k_9 p_T + k_{10} p_X + k_{11} p_M} \quad (7.15)$$

For Xylene:

$$\frac{\alpha y_X}{\tau} = r_X = r_9 - r_{10} = (k_9 p_T - k_{10} p_X) \theta_{CH_3-Z}$$

$$\Rightarrow r_X = \frac{2k_1' K_{DME-HZ} p_{DME} (k_9 p_T - k_{10} p_X) \theta_{HZ}^2}{\sum_{j=2}^7 k_j p_{C_j} + k_8 p_{C_6} + k_9 p_T + k_{10} p_X + k_{11} p_M} \quad (7.16)$$

For Mesitylene:

$$\frac{\alpha y_M}{\tau} = r_M = r_{10} - r_{11} = (k_{10} p_X - k_{11} p_M) \theta_{CH_3-Z}$$

$$\Rightarrow r_M = \frac{2k_1' K_{DME-HZ} p_{DME} (k_{10} p_X - k_{11} p_M) \theta_{HZ}^2}{\sum_{j=2}^7 k_j p_{C_j} + k_8 p_{C_6} + k_9 p_T + k_{10} p_X + k_{11} p_M} \quad (7.17)$$

For Durene:

$$\frac{\alpha y_D}{\tau} = r_D = r_{11} = (k_{11} p_M) \theta_{CH_3-Z}$$

$$\Rightarrow r_D = \frac{2k_1' K_{DME-HZ} p_{DME} (k_{11} p_M) \theta_{HZ}^2}{\sum_{j=2}^7 k_j p_{C_j} + k_8 p_{C_6} + k_9 p_T + k_{10} p_X + k_{11} p_M} \quad (7.18)$$

7.5 Model Simplification and Reparameterization

The proposed DTO kinetic model includes 12 rate constants and 12 equilibrium constants. Each of these constants has pre-exponential factor and activation energy. Therefore, the total number of parameters to be estimated is 48. It is a challenging task to fit such a large number of parameters with limited number of data points. Thus, the number of parameters present in the rate expressions given in Equations 7.7 to 7.18 needs to be reduced.

In this respect, one can notice that the vacant acid sites coverage in Equation 7.4 includes the contribution of each adsorbed species. If one assumes that surface adsorption of DME onto

the acidic sites of the HZSM-5 is the dominant process compared to the desorption of the products, equation 7.4 can be rewritten as:

$$\Rightarrow \theta_{HZ} = \frac{1}{1 + K_{DME} p_{DME}} \quad (7.19)$$

The coverage of the surface methoxy species (θ_{CH_3-Z} , Equation 7.5), on the other hand, encompasses, in the denominator, the product formation and the further methylation reaction rates.

Figure 7.1 compares the experimental reaction rates of the C₂-C₅ olefins with the total reaction rates contributing in the denominator of θ_{CH_3-Z} formula (Equation 7.5). One can observe that the summation of the C₂-C₅ olefins reaction rates accounts for 85-100% of total reaction rates defined in the denominator of θ_{CH_3-Z} formula. On this basis, one can safely assume that the contribution of the C₅⁺ products on the surface methoxy coverage is very small. Therefore, Equation 7.5 can be revised as:

$$\Rightarrow \theta_{CH_3-Z} = \frac{2k_1 K_{DME-HZ} p_{DME} \theta_{HZ}^2}{\sum_{j=2}^5 k_j p_{C_j}} \quad (7.20)$$

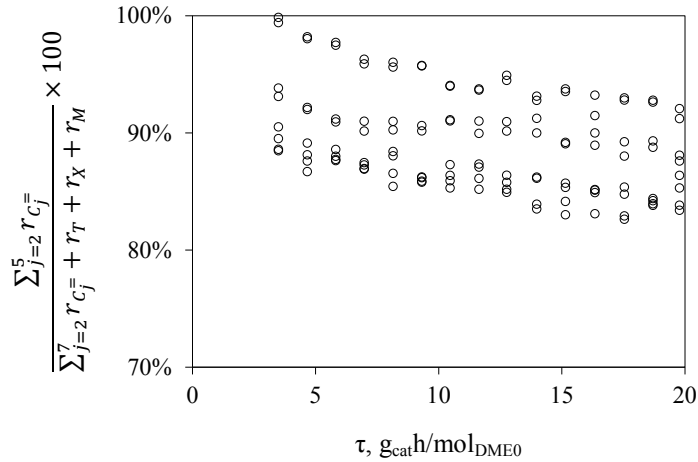


Figure 7.1: Ratio of C₂-C₅ olefins to the total hydrocarbon products reaction rates.

As for the species reaction rates, the rate constants in the nominator of Equations 7.7 to 7.18 can be lumped as shown in Table 7.2. The resulting model reaction rates after simplification and reparameterization along with the experimental reaction rates are summarized in Table

7.3. Therefore, the total number of independent parameters to be estimated is reduced to 25 (12 lumped rate pre-exponential factors, 12 activation energies, and one DME adsorption enthalpy).

Table 7.2: Lumped reaction rate and equilibrium constants.

Reaction rate	Rate and equilibrium constants	Lumped constant
$r_{1'}$	$k_{1'}K_{DME-HZ}$	$k_{1'}$
r_1	k_1K_{DME-HZ}	k_1
r_2	$2k_{1'}K_{DME-HZ}k_2$	k_2
r_3	$2k_{1'}K_{DME-HZ}k_3$	k_3
r_4	$2k_{1'}K_{DME-HZ}k_4$	k_4
r_5	$2k_{1'}K_{DME-HZ}k_5$	k_5
r_6	$2k_{1'}K_{DME-HZ}k_6$	k_6
r_7	$2k_{1'}K_{DME-HZ}k_7$	k_7
r_8	$2k_{1'}K_{DME-HZ}k_8$	k_8
r_9	$2k_{1'}K_{DME-HZ}k_9$	k_9
r_{10}	$2k_{1'}K_{DME-HZ}k_{10}$	k_{10}
r_{11}	$2k_{1'}K_{DME-HZ}k_{11}$	k_{11}

Table 7.3: Experimental and model components reaction rates after simplification and reparameterization.

Component	Experimental Reaction rate	Model Reaction rate	No.
DME	$\frac{1-\alpha y_{DME}}{\tau}$	$\frac{k_1 p_{DME}}{(1+K_{DME} p_{DME})^2} + \frac{k_1 p_{DME}}{1+K_{DME} p_{DME}}$	a
Ethylene	$\frac{\alpha y_{C_2}}{\tau}$	$\frac{k_1 p_{DME}}{1+K_{DME} p_{DME}} - \frac{k_2 p_{C_2} p_{DME}}{(1+K_{DME} p_{DME})^2 \sum_{j=2}^5 k_j p_{C_j}}$	b
Propene	$\frac{\alpha y_{C_3}}{\tau}$	$\frac{(k_2 p_{C_2} - k_3 p_{C_3}) p_{DME}}{(1+K_{DME} p_{DME})^2 \sum_{j=2}^5 k_j p_{C_j}}$	c
Butene	$\frac{\alpha y_{C_4}}{\tau}$	$\frac{(k_3 p_{C_3} - k_4 p_{C_4}) p_{DME}}{(1+K_{DME} p_{DME})^2 \sum_{j=2}^5 k_j p_{C_j}}$	d
Pentene	$\frac{\alpha y_{C_5}}{\tau}$	$\frac{(k_4 p_{C_4} - k_5 p_{C_5}) p_{DME}}{(1+K_{DME} p_{DME})^2 \sum_{j=2}^5 k_j p_{C_j}}$	e
Hexene	$\frac{\alpha y_{C_6}}{\tau}$	$\frac{(k_5 p_{C_5} - (k_6 + k_8) p_{C_6}) p_{DME}}{(1+K_{DME} p_{DME})^2 \sum_{j=2}^5 k_j p_{C_j}}$	f
Heptene	$\frac{\alpha y_{C_7}}{\tau}$	$\frac{(k_6 p_{C_6} - k_7 p_{C_7}) p_{DME}}{(1+K_{DME} p_{DME})^2 \sum_{j=2}^5 k_j p_{C_j}}$	g
Octene	$\frac{\alpha y_{C_8}}{\tau}$	$\frac{k_7 p_{C_7} p_{DME}}{(1+K_{DME} p_{DME})^2 \sum_{j=2}^5 k_j p_{C_j}}$	h
Toluene	$\frac{\alpha y_{C_T}}{\tau}$	$\frac{(k_8 p_{C_6} - k_9 p_T) p_{DME}}{(1+K_{DME} p_{DME})^2 \sum_{j=2}^5 k_j p_{C_j}}$	i
Xylene	$\frac{\alpha y_{C_X}}{\tau}$	$\frac{(k_9 p_T - k_{10} p_X) p_{DME}}{(1+K_{DME} p_{DME})^2 \sum_{j=2}^5 k_j p_{C_j}}$	j
Mesitylene	$\frac{\alpha y_{C_M}}{\tau}$	$\frac{(k_{10} p_X - k_{11} p_M) p_{DME}}{(1+K_{DME} p_{DME})^2 \sum_{j=2}^5 k_j p_{C_j}}$	k
Durene	$\frac{\alpha y_{C_D}}{\tau}$	$\frac{k_{11} p_M p_{DME}}{(1+K_{DME} p_{DME})^2 \sum_{j=2}^5 k_j p_{C_j}}$	l

The DME adsorption equilibrium constant in Equation 7.21, can be obtained by applying the following thermodynamic formula:

$$K_{DME} = \exp\left(-\frac{\Delta G_{ads,DME}^0}{RT}\right) \quad (7.21)$$

where $\Delta G_{ads,DME}^0$ is the Gibbs free energy for DME adsorption at standard conditions (298 K and 1 atm) which is related to the change of enthalpy ($\Delta H_{ads,DME}^0$) and the change of entropy of adsorption ($\Delta S_{ads,DME}^0$) by,

$$\Delta G_{ads,DME}^0 = \Delta H_{ads,DME}^0 - T\Delta S_{ads,DME}^0 \quad (7.22)$$

where T and T_C are the system and the centering reaction temperatures (K), respectively.

Combining Equations 7.21 and 7.22 yields:

$$K_{DME} = \exp\left(\frac{\Delta S_{ads,DME}^0}{R} - \frac{\Delta H_{ads,DME}^0}{RT}\right)$$

When introducing the centering temperature for reducing cross-correlation between parameters, K_{DME} becomes:

$$K_{DME} = \exp\left(\frac{\Delta S_{ads,DME}^0}{R} - \frac{\Delta H_{ads,DME}^0}{RT_C}\right) \exp\left(-\frac{\Delta H_{ads,DME}^0}{R}\left(\frac{1}{T} - \frac{1}{T_C}\right)\right) \quad (7.23)$$

The DME adsorption entropy change can be calculated with neglecting mixing effects on gas phase entropy at standard conditions using the following relation [196]:

$$\Delta S_{ads,DME}^0 = -S_{tr} - \frac{2}{3}S_{rot} \quad (7.24)$$

where S_{tr} and S_{rot} are the translational and rotational entropy contributions to the overall gas phase entropy of a DME molecule.

According to quantum mechanical theory, the translational entropy contribution to the overall gas phase entropy of a molecule can be estimated using the following formula [197]:

$$S_{tr} = \left[\ln\left(\frac{M^{1.5}T^{2.5}}{P}\right) - 1.165 \right] R \quad (7.25)$$

where M is the DME molecular weight (46 g/mol), T is the absolute temperature (298 K), P is the total pressure (1.34 atm) and R is the ideal gas constant (8.314 J/mol/K). As a result, the calculated $S_{tr,DME} = 156.5$ J/mol/K.

On the other hand, the vibrational entropy can be calculated using the total gas phase entropy (S_g) that accounts for the translational (S_{tr}), rotational (S_{rot}), and vibration (S_{vib}) entropies:

$$S_g = S_{tr} + S_{rot} + S_{vib} \quad (7.26)$$

Knowing that $S_{g,DME}$ is 266.7 J/mol/K [198] and assuming vibrational gas entropy as negligible given DME low molecular weight [196], the calculated $S_{rot,DME}$ from Equation 7.26 is 110.2 J/mol/K. Therefore, the resulting $\Delta S_{ads,DME}^0 = -230$ J/mol/K. Applying the $\Delta S_{ads,DME}^0$ value to Equation 7.23, the DME adsorption equilibrium formula becomes:

$$K_{DME} = \exp\left(-\frac{230}{R} - \frac{\Delta H_{ads,DME}^0}{RT_C}\right) \exp\left(-\frac{\Delta H_{ads,DME}^0}{R} \left(\frac{1}{T} - \frac{1}{T_C}\right)\right) \quad (7.27)$$

One can notice here, that fitting this form of equation to the experimental data requires the DME adsorption enthalpy (ΔH_{ads}^0) to be an adjustable parameter only.

7.6 Regression Analysis and Parameter Estimation

The proposed rate expressions in Table 7.3 are nonlinear with respect to their parameters. Therefore, the estimation of the intrinsic kinetic constants was developed using nonlinear least square regression using measured rates and model predicted rates as defined in Table 7.3. The MATLAB[®] solver “lsqcurvefit” was employed to the model solution and regression analysis. Each rate constant was modeled using a pre-exponential factor and an activation energy in line with the Arrhenius’ equation (Equation 7.1).

The regression analysis was considered converged when the following objective function display tolerance below 10^{-6} :

$$OF = \sum_{k=1}^P (r_{i,model} - r_{i,exp})^2 \quad (7.28)$$

where r_i is the component reaction rate, and P is the number of data points at different experimental conditions.

One should notice that all kinetic parameters were calculated with the following statistical indicators: a) small spans for the 95% confidence interval, b) 117 degree of freedom for each component (DOF =data points-2), c) low cross-correlation coefficients between parameters, and d) correlation coefficient (R^2) close to one. Additionally, the following constraints for calculating the model parameters were considered: a) positive rate constants and activation energies, b) a negative DME adsorption enthalpy(ΔH_{ads}^0).

7.6.1 DME Reaction Rate

The significance of the adsorption term ($1 + K_{DME}p_{DME}$) for the rate expressions in Table 7.3 was examined by solving the DME rate equation (Table 7.3-a) with k_1' and k_1 considered as lumped constants.

Table 7.4 reports the calculated pre-exponential factor (k_1), the activation energy (E_1) and the DME adsorption enthalpy (ΔH_{ads}^0). One can observe that both of k_1 and E_1 values display the desirable statistical indicators (low confidence intervals and low cross correlation coefficients). The predicted ΔH_{ads}^0 (-127 kJ/mol), however, shows a large confidence interval (± 50.1 kJ/mol) and a high cross correlation coefficient for E_1 (0.85). However, when plotting the resulting $(1/(1 + K_{DME}p_{DME}))$ and $(1/(1 + K_{DME}p_{DME})^2)$ groups at different reaction temperatures, as can be seen in Figure 7.2, one can notice that both terms were close to unity (0.93-1). Given these results, one can conclude that the adsorption term can be neglected. Thus, the resulting DME rate expression becomes:

$$r_{DME} = (k_1 + k_1')p_{DME} \quad (7.29)$$

Table 7.5 reports the kinetic constants according to Equations 7.1 and 7.29. One can see that separating k_1' and k_1 , leads to predicted constants complying with the statistical indicators for adequacy as discussed in section 7.6. However, when comparing the experimental reaction rates for DME versus the calculated ones as shown in Figure 7.3, one can observe a good agreement between the measured and model values.

Table 7.4: Optimized intrinsic kinetic constants for DME reaction rate (Table 7.3-a).

Parameter	Estimated	95% CI	Cross-Correlation Coefficient Matrix		
			$k_{0,1}$	E_1	ΔH_{ads}
$k_{0,1}^a$	0.1507	± 0.004	1.00		
E_1^b	170.9	± 11.8	0.26	1.00	
$\Delta H_{ads}^0{}^b$	-127	± 50.1	-0.06	0.85	1.00

^a ($\text{mol g}^{-1} \text{h}^{-1} \text{bar g}^{-1}$), ^b (kJ/mol). $R^2 = 0.96$, $T_C = 690.8 \text{ K}$.

Table 7.5: Optimized intrinsic kinetic constants for DME reaction rate (Equation 7.29).

Parameter	Estimated	95% CI	Cross-Correlation Coefficient Matrix			
			$k_{0,1}$	E_1	$k'_{0,1}$	E'_1
$k_{0,1}^a$	0.0420	± 0.002	1.00			
E_1^b	156.7	± 6.1	0.11	1.00		
$k'_{0,1}^a$	0.0451	± 0.0005	0.89	0.18	1.00	
$E'_1{}^b$	184.8	± 2.8	0.13	0.90	0.21	1.00

^a ($\text{mol g}^{-1} \text{h}^{-1} \text{bar g}^{-1}$), ^{b,c} (kJ/mol). $R^2 = 0.96$, $T_C = 690.8 \text{ K}$.

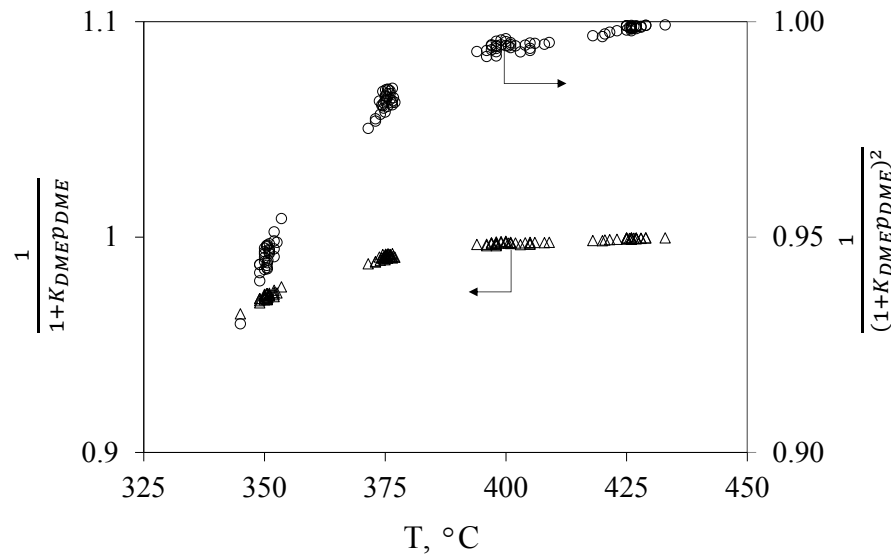


Figure 7.2: Variation of DME rate equation (Table 7.3-a) adsorption term with reaction temperature.

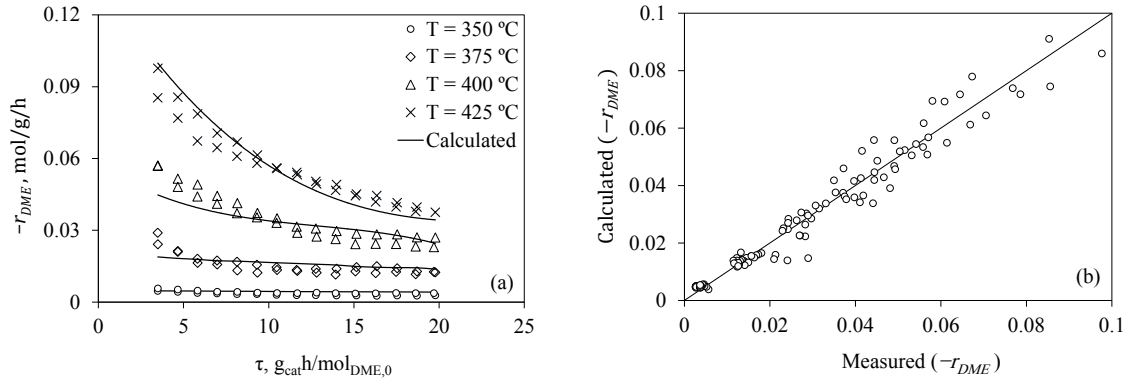


Figure 7.3: Comparison of experimental DME reaction rates versus model calculations: a) individual conditions (Note: Full lines represent calculated values using estimated rate parameters), b) overall parity plot.

7.6.2 Light Olefins Methylation Reactions

Following the kinetic model equation simplification, and neglecting the DME adsorption term, ethylene to pentene reaction rates can be written as:

$$r_{C_2^=} = k_1 p_{DME} - \frac{k_2 p_{C_2^=} p_{DME}}{\sum_{j=2}^5 k_j p_{C_j^=}} \quad (7.30)$$

$$r_{C_3^=} = \frac{(k_2 p_{C_2^=} - k_3 p_{C_3^=}) p_{DME}}{\sum_{j=2}^5 k_j p_{C_j^=}} \quad (7.31)$$

$$r_{C_4^=} = \frac{(k_3 p_{C_3^=} - k_4 p_{C_4^=}) p_{DME}}{\sum_{j=2}^5 k_j p_{C_j^=}} \quad (7.32)$$

$$r_{C_5^=} = \frac{(k_4 p_{C_4^=} - k_5 p_{C_5^=}) p_{DME}}{\sum_{j=2}^5 k_j p_{C_j^=}} \quad (7.33)$$

Given the estimated k_1 parameters as reported in Table 7.5 and after fitting the data to the reaction rates in Equations 7.30 to 7.33, the cross correlation were found to be relatively high and the 95% confidence interval quite large (i.e. ranged from negative to positive values). So, the estimated parameters were not statistically meaningful.

When reviewing Equations 7.30 to 7.33, one should notice the importance of assigned “a priori” values to “ k_j ” parameters. One possible consideration is to make all of the k_j equal. On

the other hand, the measured partial pressure ratio $\left(p_i / \sum_{j=2}^5 p_{C_j^=}\right)$ was found to be comparable for all products as shown in Figure 7.4. Under these conditions, the term $\left((k_i p_i) / \sum_{j=2}^5 k_j p_{C_j^=}\right)$ is estimated as a constant at a fixed temperature and can be lumped as k_i , or a single constant. This approach can be followed as well for Equations (7.30) to (7.33). Therefore, the following equations can be derived for light olefins:

$$r_{C_2^=} = (k_1 - k_2) p_{DME} \quad (7.34)$$

$$r_{C_3^=} = (k_2 - k_3) p_{DME} \quad (7.35)$$

$$r_{C_4^=} = (k_3 - k_4) p_{DME} \quad (7.36)$$

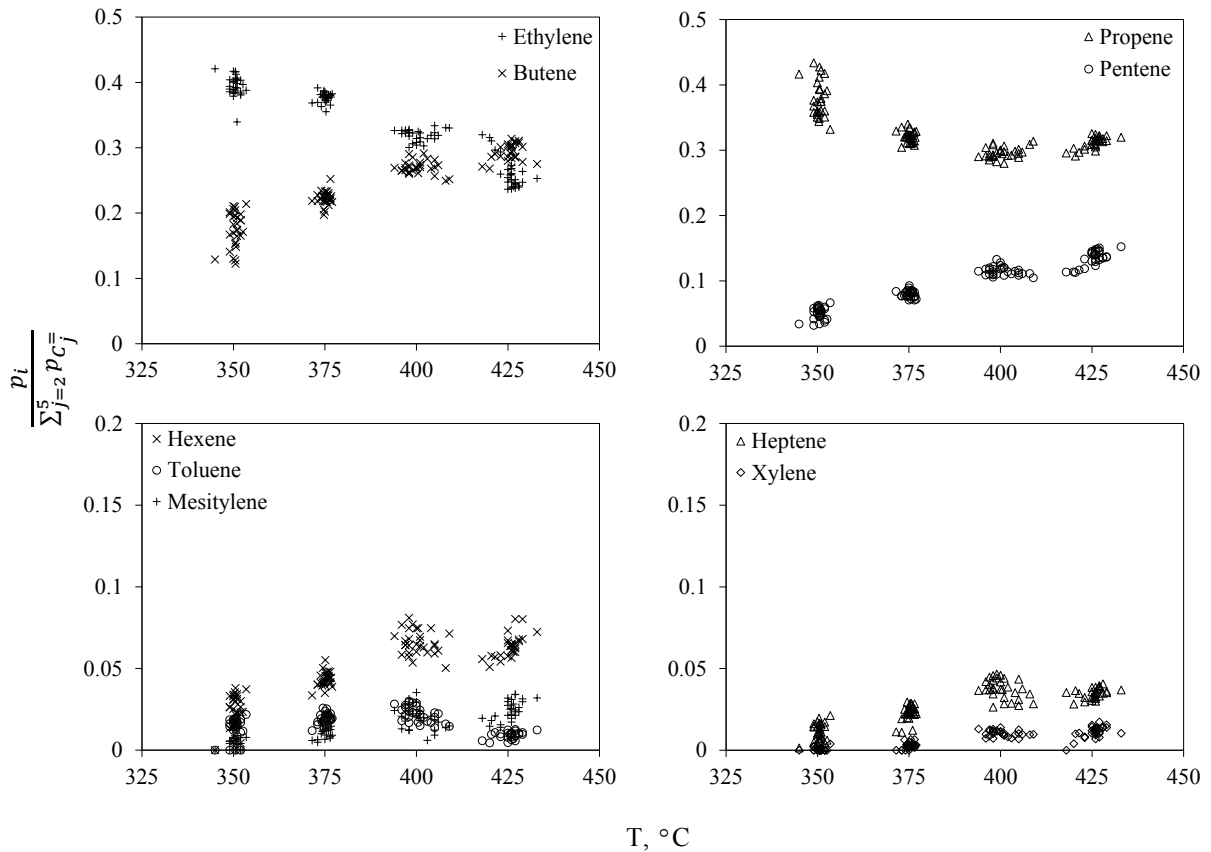


Figure 7.4: Hydrocarbon product pressure ratio versus reaction temperature.

Table 7.6 reports the results of fitting C_2 - C_4 olefins reaction rates (Equations 7.34 to 7.36) to their experimental data. One can observe that the 95% confidence interval for E_4 ($199.6 \pm$

22.5 kJ/mol) is limited, being, however, large enough to overlap with E_3 (183.4 ± 7.1 kJ/mol). Therefore, E_3 and E_4 can be considered, for all practical purposes, as being the same. This assumption also leads to the same finding for E_2 . It allows one to reach the conclusion that the activation energy for the insertion of methoxy species is comparable for components ranging from C_2 to C_4 olefins. As a result, single activation energy (E_{2-4}) is estimated for C_2 to C_4 olefin methylation as one can see in Table 7.7. Figure 7.5 to Figure 7.7 report the goodness of fit using the proposed model for C_2 to C_4 olefin reaction rates. One can observe good agreement between the measured and model values.

Table 7.6: Optimized intrinsic kinetic constants for C_2 to C_4 olefins reactions.

Parameter	Estimated	95% CI	Cross-Correlation Coefficient Matrix					
			$k_{0,2}$	E_2	$k_{0,3}$	E_3	$k_{0,4}$	E_4
$k_{0,2}^a$	0.0310	± 0.0003	1.00					
E_2^b	170.5	± 2.8	0.12	1.00				
$k_{0,3}^a$	0.0191	± 0.0005	0.71	0.06	1.00			
E_3^b	183.4	± 7.1	0.05	0.70	0.03	1.00		
$k_{0,4}^a$	0.0081	± 0.0006	0.57	0.01	0.82	-0.02	1.00	
E_4^b	199.6	± 22.5	0.01	0.57	-0.02	0.81	-0.08	1.00

^a ($\text{mol g}^{-1} \text{h}^{-1} \text{barg}^{-1}$), ^b (kJ/mol). $R^2 = 0.93$, $T_C = 690.8$ K.

Table 7.7: Optimized intrinsic kinetic constants for C_2 to C_4 olefin methylation reactions with single activation energy.

Parameter	Estimated	95% CI	Cross-Correlation Coefficient Matrix			
			$k_{0,2}$	E_{2-4}	$k_{0,3}$	$k_{0,4}$
$k_{0,2}^a$	0.0309	± 0.0004	1.00			
E_{2-4}^b	168.8	± 2.6	0.11	1.00		
$k_{0,3}^a$	0.0189	± 0.0005	0.71	0.05	1.00	
$k_{0,4}^a$	0.0081	± 0.0006	0.58	0.02	0.82	1.00

^a ($\text{mol g}^{-1} \text{h}^{-1} \text{barg}^{-1}$), ^b (kJ/mol). $R^2 = 0.92$, $T_C = 690.8$ K.

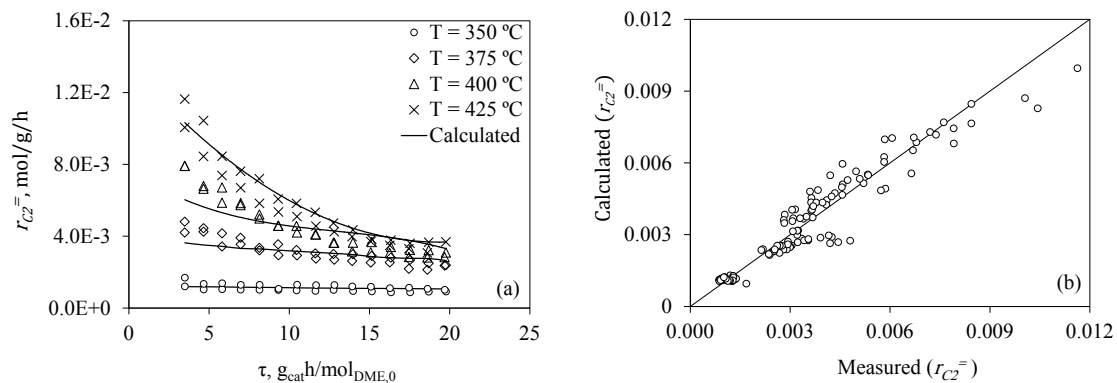


Figure 7.5: Comparison of experimental ethylene reaction rates versus model calculations: a) individual conditions (Note: Full lines represent calculated values using estimated rate parameters), b) overall parity plot.

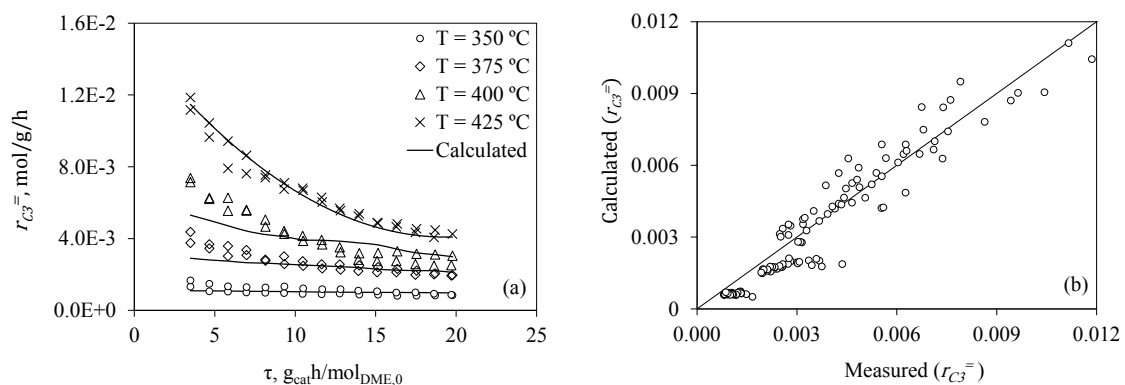


Figure 7.6: Comparison of experimental propene reaction rates versus model calculations: a) individual conditions (Note: Full lines represent calculated values using estimated rate parameters), b) overall parity plot.

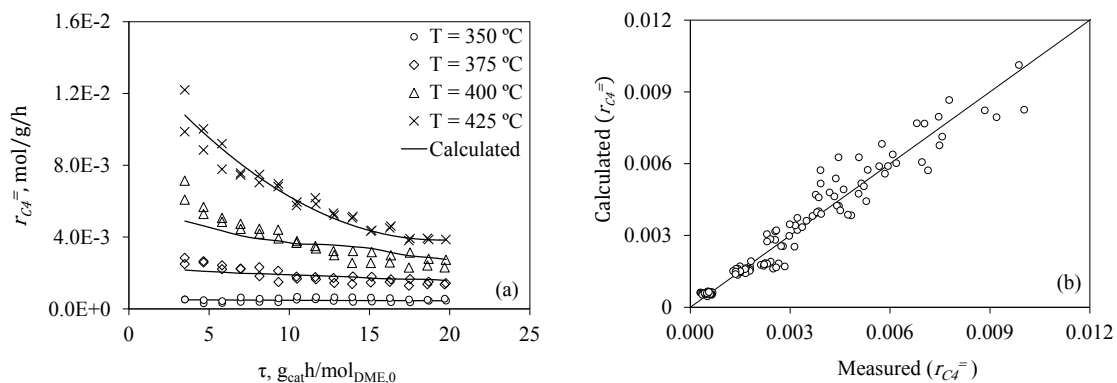


Figure 7.7: Comparison of experimental butene reaction rates versus model calculations: a) individual conditions (Note: Full lines represent calculated values using estimated rate parameters), b) overall parity plot.

7.6.3 Heavy Olefins Methylation Reactions

Following the same approach discussed in the sections 7.6.1 and 7.6.2, pentene, heptene, and octene reactions rates in Table 7.3 (equations e-g) can be written as:

$$r_{C_5} = (k_4 - k_5)p_{DME} \quad (7.37)$$

$$r_{C_6} = (k_6 - k_7)p_{DME} \quad (7.38)$$

$$r_{C_8} = k_7 p_{DME} \quad (7.39)$$

Similar to what was found for light olefin methylation activation energy, E_5 to E_7 95% confidence spans were found to overlap each other, so that a single activation energy for the methylation of C_5 to C_7 olefins (E_{5-7}) was considered. As a result, the estimated kinetic parameters from fitting Equations 7.37 to 7.39 are reported in Table 7.8.

While examining the goodness of fitting the heavy olefins reaction rate (Equations 7.37 to 7.39), one was able to observe good agreement between the measured and model values as displayed in Figure 7.8 to Figure 7.10. Therefore, the proposed reaction rate formulas were found to be adequate for the fitting of the heavy olefin methylation reaction.

Table 7.8: Optimized intrinsic kinetic constants for C_5 to C_7 olefin methylation reactions with a single activation energy.

Parameter	Estimated	95% CI	Cross-Correlation Coefficient Matrix			
			$k_{0,5}$	E_{5-7}	$k_{0,6}$	$k_{0,7}$
$k_{0,5}^a$	0.0032	± 0.0001	1.00			
E_{5-7}^b	155.6	± 6.8	0.19	1.00		
$k_{0,6}^a$	0.0026	± 0.0001	0.02	0.11	1.00	
$k_{0,7}^a$	0.0013	± 0.0001	0.01	0.08	0.71	1.00

^a ($\text{mol g}^{-1} \text{h}^{-1} \text{barg}^{-1}$), ^b (kJ/mol). $R^2 = 0.95$, $T_C = 690.8 \text{ K}$.

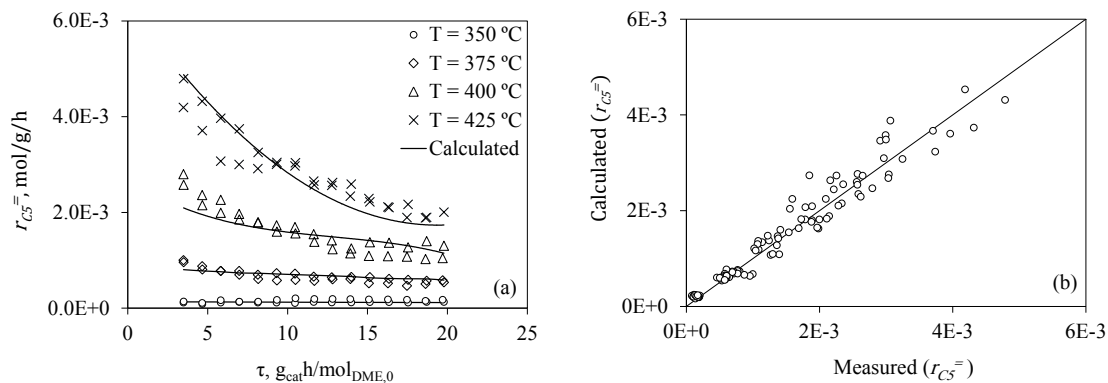


Figure 7.8: Comparison of experimental pentene reaction rates versus model calculations: a) individual conditions (Note: Full lines represent calculated values using estimated rate parameters), b) overall parity plot.

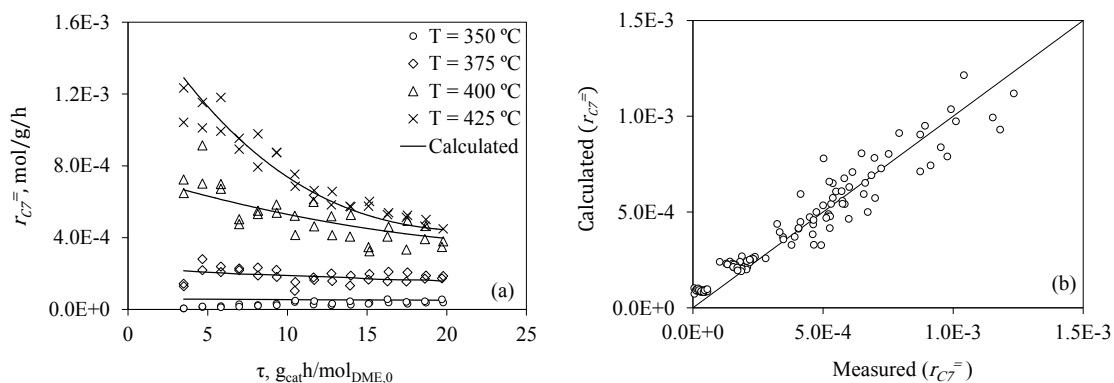


Figure 7.9: Comparison of experimental heptene reaction rates versus model calculations: a) individual conditions (Note: Full lines represent calculated values using estimated rate parameters), b) overall parity plot.

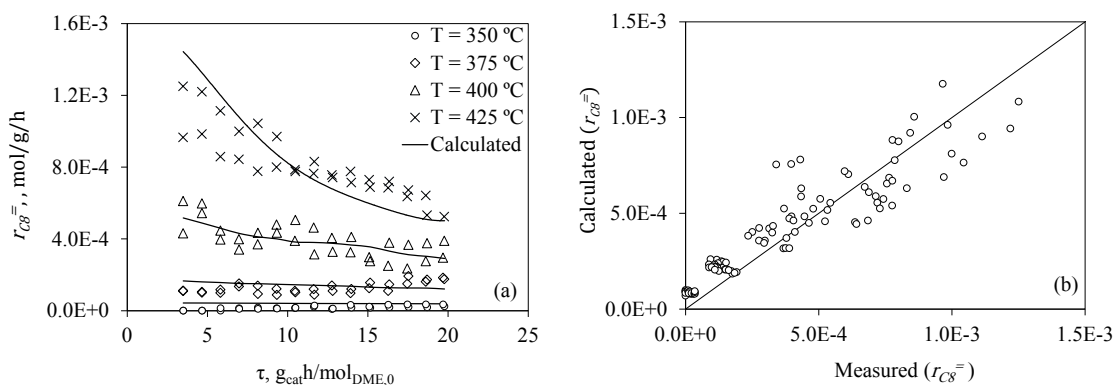


Figure 7.10: Comparison of experimental octene reaction rates versus model calculations: a) individual conditions (Note: Full lines represent calculated values using estimated rate parameters), b) overall parity plot.

7.6.4 Hexene Aromatization to Toluene

Regarding toluene, it is speculated that its formation is the result of a separate process where benzene is formed through hexene dehydrogenation/condensation and is immediately followed by benzene alkylation. Thus, all aromatics formed have toluene as the key intermediate species. A toluene formation reaction rate (r_8) can be calculated by adding up the contributions of all aromatics reaction rates (Table 7.3 e-l). Furthermore, by neglecting the DME adsorption term and considering a constant partial pressure species ratio term at a given temperature (refer to section 7.6.2), one can write r_8 as:

$$\sum(r_T + r_X + r_M + r_D) = r_8 = k_8 p_{DME} \quad (7.40)$$

On this basis, Table 7.9 reports the k_8 constants while Figure 7.11 displays a close estimation of the toluene formation reaction to the measured one.

Table 7.9: Optimized intrinsic kinetic constants for toluene formation (r_8 , Equation 7.40)

Parameter	Estimated	95% CI	Cross-Correlation Coefficient Matrix	
			$k_{0,8}$	E_8
$k_{0,8}$ ^a	0.1627	± 0.0045	1.00	
E_8 ^b	83.9	± 7	0.22	1.00

^a (molg⁻¹h⁻¹bar⁻¹), ^b (kJ/mol). R² = 0.94, T_C = 690.8 K.

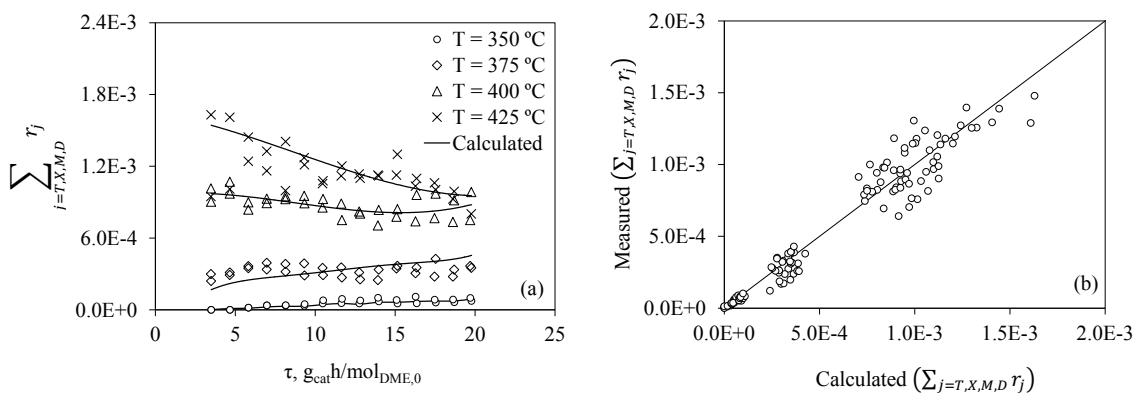


Figure 7.11: Comparison of experimental toluene formation rates (r_8) versus model calculations: a) individual conditions (Note: Full lines represent calculated values using estimated rate parameters), b) overall parity plot.

7.6.5 Aromatics Methylation Reactions

Following a similar approach as the one discussed in the sections 7.6.1 and 7.6.2, the xylene, mesitylene, and durene reactions rates reported in Table 7.3 (equations j-l) can be revised as shown below:

$$r_X = (k_9 - k_{10})p_{DME} \quad (7.41)$$

$$r_M = (k_{10} - k_{11})p_{DME} \quad (7.42)$$

$$r_D = k_{11}p_{DME} \quad (7.43)$$

Table 7.10 reports the estimated kinetic constants for the aromatic methylation reactions. One can notice that in this case, the activation energy displays a significant increase with respect to olefin methylation as shown in sections 7.6.2 and 7.6.3. In this respect, the toluene methylation activation energy is 103.8 kJ/mole which becomes 191.3 kJ/mole in the methylation of xylene and mesitylene. On the other hand, the activation energies for methylating xylene and mesitylene were found to have overlapping confidence intervals. Thus, a single activation energy could be considered for the methylation of these species.

Table 7.10: Optimized intrinsic kinetic constants for aromatics methylation reactions.

Parameter	Estimated	95% CI	Cross-Correlation Coefficient Matrix				
			$k_{0,9}$	E_9	$k_{0,10}$	E_{10-11}	$k_{0,11}$
$k_{0,9}^a$	0.18084	± 0.0062	1.00				
E_9^b	103.8	± 11.1	-0.11	1.00			
$k_{0,10}^a$	0.0012	± 0.000048	0.71	-0.01	1.00		
E_{10-11}^b	191.3	± 11.2	-0.02	0.71	-0.02	1.00	
$k_{0,11}^a$	0.0005	± 0.000034	0.71	-0.01	0.71	-0.01	1.00

^a (molg⁻¹h⁻¹barg⁻¹), ^b (kJ/mol). R² = 0.95, T_C = 690.8 K.

While examining the goodness of fit in Figure 7.13, one can observe a good agreement between the measured and predicted xylene and mesitylene reaction rates (Equations 7.41 and 7.42). The parity plot for durene reaction rates (Equation 7.43), on the other hand, show slight variations especially at higher reaction rates, as one can notice from Figure 7.14-b. This is likely due to the lower measured reaction rate for durene (maximum 3×10⁻⁴ mole/g/h) while compared to the same for xylene and mesitylene (maximum 4-7×10⁻⁴ mole/g/h). In

spite of this, it was considered that the proposed kinetic models were found to be adequate for fitting the aromatics methylation reactions.

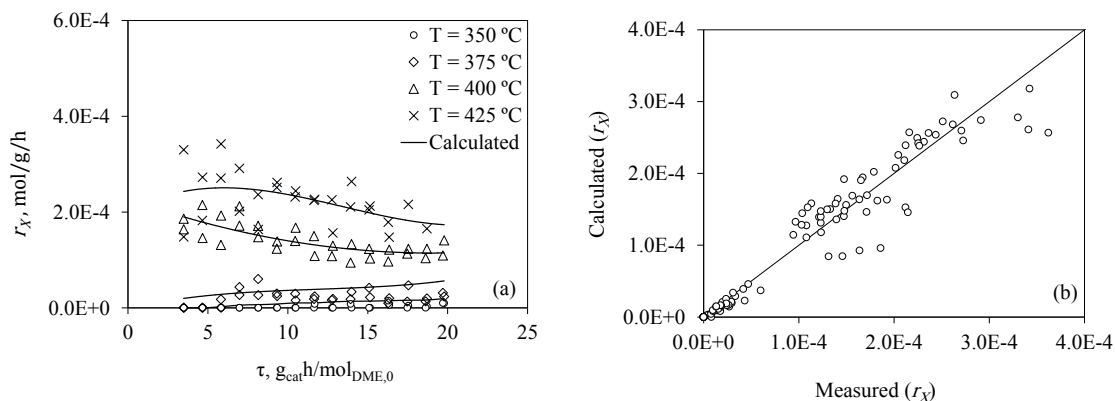


Figure 7.12: Comparison of experimental xylene reaction rates versus model calculations: a) individual conditions (Note: Full lines represent calculated values using estimated rate parameters), b) overall parity plot.

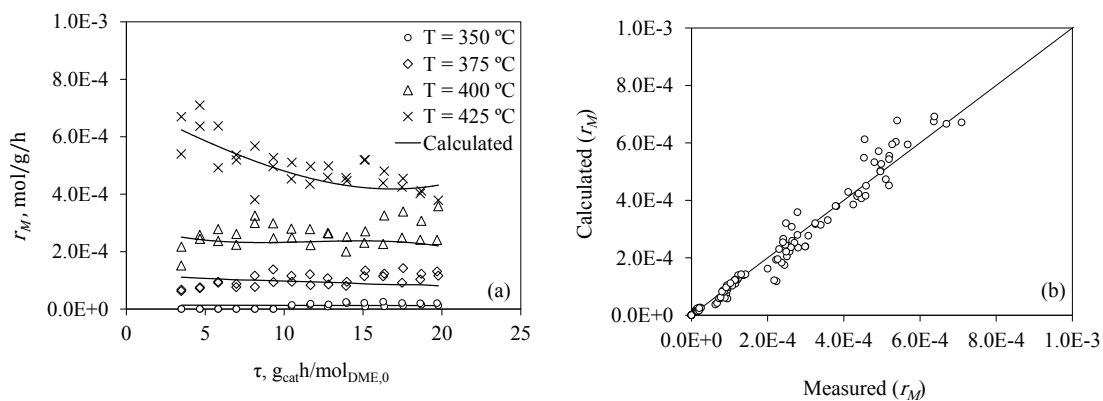


Figure 7.13: Comparison of experimental mesitylene reaction rates versus model calculations: a) individual conditions (Note: Full lines represent calculated values using estimated rate parameters), b) overall parity plot.

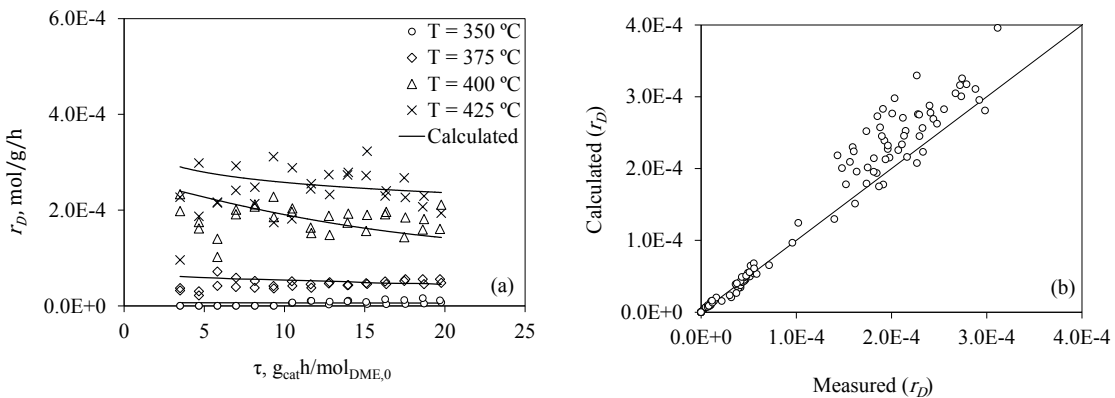


Figure 7.14: Comparison of experimental durene reaction rates versus model calculations: a) individual conditions (Note: Full lines represent calculated values using estimated rate parameters), b) overall parity plot.

7.6.6 Discussions

In sections 7.6.1 to 7.6.5, the kinetic constants of the proposed DME reaction network formulas after simplification and reparameterization (Equations 7.29 and 7.34-7.43) were estimated. One should notice that all the obtained kinetic parameters obey the statistical indicators described at the beginning of section 7.6. This confirms that the parameters are highly reliable in predicting the experimental reaction rates. This is clearly evident from the goodness of fit and parity plots (Figure 7.3 and Figure 7.5 to Figure 7.14), where the model data calculated using these estimated parameters lie within the close proximity of experimental data points.

Table 7.11 summarizes the calculated kinetic parameters (a total of 24) for modeling the proposed DTO reaction network. The R^2 values were found to be within a 0.92-0.96 span.

Table 7.11: Intrinsic kinetic and statistical parameters for the proposed DTO kinetic model.

Reaction type	Rate constant	$k_{0,i}(\text{mole g}^{-1}\text{h}^{-1}\text{barg}^{-1})$		$E_i(\text{kJ/mole})$		R^2
		Estimated	95% CI	Estimated	95% CI	
DME dehydration to methoxy species	k'_1	0.0451	± 0.0005	184.8	± 2.8	0.96
DME dehydration to ethylene	k_1	0.0420	± 0.002	156.7	± 6.1	0.96
Ethylene methylation to propene	k_2	0.0309	± 0.0004	168.8	± 2.6	0.92
Propene methylation to butene	k_3	0.0189	± 0.0005	168.8	± 2.6	0.92
Butene methylation to pentene	k_4	0.0081	± 0.0006	168.8	± 2.6	0.92
Pentene methylation to hexene	k_5	0.0032	± 0.0001	155.6	± 6.8	0.95
Hexene methylation to heptene	k_6	0.0026	± 0.0001	155.6	± 6.8	0.95
Heptene methylation to octene	k_7	0.0013	± 0.0001	155.6	± 6.8	0.95
Hexene aromatization to toluene	k_8	0.1627	± 0.0045	83.9	± 7	0.94
Toluene methylation to xylene	k_9	0.18084	± 0.0062	103.8	± 11.1	0.95
Xylene methylation to mesitylene	k_{10}	0.0012	± 0.000048	191.3	± 11.2	0.95
Mesitylene methylation to durene	k_{11}	0.0005	± 0.000034	191.3	± 11.2	0.95

$$*k_i = k_i \exp\left(-\frac{E_i}{R}\left(\frac{1}{T} - \frac{1}{T_C}\right)\right), T_C = 690.8 \text{ K.}$$

Concerning the DME dehydration reactions, both pre-exponential factors ($0.042, 0.045 \text{ mole g}^{-1}\text{h}^{-1}\text{barg}^{-1}$) and the activation energies (157, 185 kJ/mole) were found to be close for both of methoxy species and ethylene formations, respectively. With regard to the olefin methylation reactions, on the other hand, one can observe a consistent reduction of the pre-exponential factors from 0.030 to 0.0013. This is expected, given that the measured rate of the olefin methylation is reduced with increasing carbon numbers. Similar outcome is obtained as well for the aromatic methylation reaction in which the calculated pre-exponential factors are reduced from 0.18 to 0.0005.

It is important to review the values of the activation energies for the methylation reaction of the present study and to compare them with values already reported in the technical literature. species were getting heavier.

Table 7.12, in this respect, reports the activation energies (E_i) for the C_2 - C_4 olefins, toluene and xylene methylation reactions using HZSM-5 with various $\text{SiO}_2/\text{Al}_2\text{O}_3$ ratios. One should notice that the reported activation energies in the literature were estimated either experimentally or theoretically using quantum chemical calculations. The reported E_i for the light olefin methylation shows lower values (109-37 kJ/mole) when compared with the ones of the present study (169 kJ/mole). Furthermore, one can notice, a steady reduction in the reported E_i with increasing olefin carbon numbers (94-109 kJ/mole for ethylene, 62-77 kJ/mole for propene, and 37-56 kJ/mole for butene) while E_i is found to be constant for light olefins in the current study. The present study shows an E_i reduction when methylating C_5^+ olefins (156 kJ/mole) only (refer to Table 7.11). Similarly, previous studies reported lower values of E_i for the toluene and xylene methylation reaction (52-100 kJ/mole for toluene, and 25-62 kJ/mole for xylene) while compared to ones of the present study (104 kJ/mole for toluene and 191 kJ/mole for xylene and durene). The increase of the E_i of the present study as well as the increase of the weight of the aromatic species are in general agreement with ones reported by Hill et al. [192] who attested that $E_i = 52$ and 62 kJ/mole for methylation of toluene and xylene, respectively. However, the difference between the toluene and the xylene-durene methylation E_i (104-191 kJ/mole) in the present study is much higher compared to the values reported by Hill et al. [192].

Regarding the increase in the methylation E_i for the heavier aromatics species, this could be attributed to a higher activation energy barrier as the number of methyl branches is increased (1 for the toluene, 2 for the xylene, and 3 for mesitylene). It appears that the methylation process requires higher energy with the increasing number of methyl groups in the aromatic ring. Furthermore, the reactivity results in section 6.2.3 support this finding at which the C_7^+ aromatic selectivity was observed to be reduced as the aromatics species were getting heavier.

Table 7.12: Reported activation energies for the methylation reactions of light olefins and aromatics using HZSM-5 catalyst.

Methylated components	Methylating agent	HZSM-5 SiO ₂ /Al ₂ O ₃	E_i (kJ/mole)	Ref
Ethylene	methanol	45	103 ^e	[163]
	methanol	N/A	94 ^t	[182]
	DME	43	94±3 ^e	[199]
	methanol	45	109 ^e	[167]
	methanol	N/A	104 ^t	[200]
Propene	methanol	45	69 ^e	[163]
	methanol	N/A	62 ^t	[182]
	DME	43	63±3 ^e	[199]
	methanol	45	69 ^e	[167]
	methanol	N/A	77 ^t	[200]
Butene	methanol	45	45 ^e	[163]
	methanol	N/A	37 ^t	[182]
	DME	43	44±2 – 56±3 ^e	[164]
	methanol	45	45 ^e	[167]
	methanol	N/A	48 ^t	[200]
Toluene	DME	42.6	52±4 ^e	[192]
	methanol	HZSM-11 with SiO ₂ /Al ₂ O ₃ = 117	61±5 ^e	[201]
	methanol	N/A	100 ^t	[202]
Xylene	methanol	30	57±5 – 79±6 ^e	[194]
	DME	42.6	62±4 ^e	[192]
	methanol	HZSM-11 with SiO ₂ /Al ₂ O ₃ = 117	30±2 – 33±3 ^e	[201]
	methanol	30	25±5 ^e	[194]

^e Experimental value, ^t Theoretical estimation using quantum chemical modeling.

The discrepancy between the reported activation energies compared to those reported in the literature can be attributed to different reasons:

- a) The proposed DTO kinetic model is the first of its kind in which the presented rate constants for each of the methylation reactions is a combination of the lumped methoxy formation rate constant ($k_{1'}$), the DME equilibrium constant (K_{DME-HZ}), and the product rates ratio $\left(k_i p_i / \sum_{j=2}^5 k_j p_{C_j^-}\right)$.
- b) The components being methylated in the present study are products that undergo further conversion while those reported in the technical literature are feedstocks already being mixed with a methylated agent (e.g. methanol).
- c) The methylated agents used in the technical literature are diluted ones while neat DME is used in the present study.
- d) The HZSM-5 catalyst used in the present study has a $\text{SiO}_2/\text{Al}_2\text{O}_3$ ratio of 280. This is a stable and selective catalyst towards light olefins. This is in contrast with the highly acidic catalysts reported in the literature with a $\text{SiO}_2/\text{Al}_2\text{O}_3$ ratio in the 30 – 45 range.

Thus, these cited kinetic parameters are valuable as a reference, in a general comparison of methylation reactions. The activation energies obtained in this study are also valuable for developing a possible reliable simulation of a scaled DTO process. This is particularly true, given the care taken while collecting experimental data and while applying the statistical methods used for the parameter regression analysis.

7.7 Conclusions

Kinetic modelling of a DTO reaction was investigated using a reaction scheme as proposed in CHAPTER 6. The applicability of the kinetic models was established on the basis of statistical significance of the fitted parameters. The findings of this chapter could be summarized as follows:

1. A heterogeneous kinetic model based on surface bound methoxy species formation was proposed. The proposed kinetic model accounted for DME and 11 significant

products (C₂-C₈ olefins, toluene, xylene, mesitylene and durene). On this basis, rate equations were developed considering both reactant adsorption and catalytic reactions on the catalyst surface.

2. Based on sound model assumptions, simplifications, and reparameterizations, the proposed intrinsic phenomenological based kinetic model for a DTO reaction network was found to be adequate in the estimation of the DTO species reaction rates under various experimental conditions of this study.
3. The intrinsic kinetic parameters were estimated using non-linear least square fit and employing the experimental data obtained at different reaction temperatures and contact times.
4. DME equilibrium constant (K_{DME}) was formulated to be function of DME adsorption enthalpy (ΔH_{ads}^0) as an adjustable parameter.
5. The determined kinetic parameters included the pre-exponential factor ($k_{0,i}$), the activation energy (E_i), and DME adsorption enthalpy (ΔH_{ads}^0).
6. The DME adsorption term ($1/(1 + K_{DME}p_{DME})$) was found to be insignificant (close to unity). On this basis, Langmuir–Hinshelwood formulation was found irrelevant for modeling the DTO reaction.
7. The pre-exponential factors and the activation energies for the DME dehydration reactions were found to be close for both of methoxy species and ethylene formations.
8. The pressure ratio term in the product methylation reactions and toluene formation rates ($k_i p_i / \sum_{j=2}^5 k_j p_{C_j}$) were estimated to be constant at a given temperature. Therefore, the product reaction rates were found to be of first order dependence on DME partial pressure. On this basis, the calculated kinetic parameters were able to predict the observed reaction rates of all carbon containing products.

9. The pre-exponential factors for the olefinic species ($k_2 - k_7$) and aromatic species ($k_9 - k_{11}$) were consistently reduced with the increase of the carbon number of the compounds being methylated.
10. The methylation activation energies were found to be similar for each olefinic lump (i.e. light olefins, heavy olefins). On the other hand, the activation energies for methylating light olefins was slightly higher ($E_{2-4} = 169$ kJ/mole) compared to that for the heavy olefins ($E_{5-7} = 156$ kJ/mole).
11. The methylation reaction displayed a weaker process as the number of methyl groups increased in the aromatic species. This could be attributed to a higher activation energy barrier as the number of methyl branches are increased ($E_i = 104 - 191$ kJ/mole).

CHAPTER 8 CONCLUSIONS AND RECOMMENDATIONS

8.1 Conclusions

The present study aims at finding a feasible way of producing light olefins from neat DME. It was envisioned, at the initiation of this research, that this could be achieved by selecting a DTO catalyst and operating conditions that would be selective towards light olefins. It was anticipated, that this could be accomplished using an HZSM-5 catalyst with $\text{SiO}_2/\text{Al}_2\text{O}_3$ ratios in the 30-280 range. In order to reach these goals, additional issues involved having a pelletized catalyst available as required for large scale fixed bed reactors. In this respect, it was necessary to be able to characterize the catalyst using XRD, PSD, N_2 -isotherm, NH_3 -TPD, and pyridine-FTIR and to test it utilizing a Berty reactor unit. In addition, it was of paramount importance to be able to establish a heterogeneous kinetic model for a DTO reaction that could be used as a tool for the DTO process scale-up.

On the basis of the results obtained and reported in this PhD dissertation, the following are the most significant conclusions:

1. The XRD crystallinity of the HZSM-5 was found to be comparable irrespective of the aluminum content. XRD results showed that the HZSM-5 used was comprised of highly crystalline zeolites with no significant presence of impurities.
2. The HZSM-5 pellets, on the other hand, showed new XRD bands at 25.5, 35.1, 37.8, and $43.3^\circ 2\theta$ angles. These extra bands were assigned to the diluting effect and/or to a particle size increase of matrix materials.
3. The N_2 adsorption isotherm using the NLDFT cylindrical model predicted that pore sizes for the HZSM-5 would be in the expected range of 5.4-5.6 Å.
4. The specific surface area, pore volume, and pore diameter (micropores and mesopores) were found to be comparable among the various HZSM-5 with different aluminum content. The formulated pellets, however, displayed a porosity reduction

that could be attributed to the filler addition. The slight increase in the pellet pore sizes, on the other hand, was considered as the influence of the binder.

5. The NH_3 -TPD analysis showed a reduction in both weak-to-strong acid site ratio and the total acidity with increasing the $\text{SiO}_2/\text{Al}_2\text{O}_3$ ratio. The pellet matrix, on the other hand, showed negligible acidity and thus, caused 60-75% reduction of the HZSM-5 total acidity after pelletization.
6. The pyridine-FTIR and NH_3 -TPD results demonstrated that acidity in the HSMZ-5 encompasses two types of weak and strong acids sites. Based on Pyridine-FTIR data, one can associate the weak sites with hydrogen-bonded and Lewis acidity, while the strong sites can be related to Brönsted acidity.
7. The NH_3 -desorption kinetics also allowed the prediction of desorption activation energies and of the intrinsic rate constants for both strong and weak acid sites. It was found that the HZSM-5 studied exhibited higher activation energies for the stronger sites versus the weaker sites (57-93 and 51-68 kJ/mol, respectively). It was also shown that the activation energies augmented with increasing the $\text{SiO}_2/\text{Al}_2\text{O}_3$ ratio of the HZSM-5.
8. The NH_3 -desorption rate constants were found to reduce with the increase of $\text{SiO}_2/\text{Al}_2\text{O}_3$ ratio. These findings demonstrated that acidity in the HZSM-5 zeolites can be correlated with Al_2O_3 content.
9. The DME conversions and coke formation augmented with the acidity of HZSM-5 and temperature. Higher acidity led to higher initial catalyst activity, with however lower catalyst durability with time-on-stream. In the case of ZSM5-280, a lower coke content (max 1.16wt %) and a stable operation with higher light olefins selectivity, particularly propene and butene, were established. For that reason, ZSM5-280 has been chosen for investigating the DTO reaction network.
10. The reactivity tests using HZSM-5 with $\text{SiO}_2/\text{Al}_2\text{O}_3 = 280$, showed an increase of the DME conversion, as a result of the rising reaction temperature along with the contact time. Light olefins (ethylene, propene and butene) were found to be the major

products (94% selectivity) at very low conversion (2%), with the rest being heavy olefins and with no paraffins or aromatics produced. It was also observed that with DME increasing conversion, there was a progressive enhancement of C_5^+ olefins, paraffins, and aromatics selectivities. It was noticed that this was at the expense of both of ethylene and propene, while butene slightly increased first and was reduced later. These trends were consistently observed up to 45% DME conversion. Thereafter, the product selectivity changes became less pronounced.

11. A DTO reaction network was proposed, based on the reactivity tests with HZSM-5 having a $SiO_2/Al_2O_3 = 280$ ratio. This reaction network considers the methoxy species as key methylating agents. The proposed reaction network accounts for ethylene and propene as primary intermediates. The formed olefins, then, undergo methylation to its next higher olefin up to octene. In addition, hexene is partially dehydrogenated to benzene, as a precursor for producing the heavier aromatics. Benzene was considered as a key intermediate species. Finally, aromatic species undergo a methyl group addition process.
12. A heterogeneous kinetic model was formulated based on the established DTO reaction network. The proposed kinetic model accounts for DME and 11 significant products (C_2 - C_8 olefins, toluene, xylene, mesitylene and durene). Individual rate equations were developed considering a Langmuir–Hinshelwood formulation.
13. The DME equilibrium constant (K_{DME}) was considered to be a function of DME adsorption enthalpy (ΔH_{ads}^0) with one adjustable parameter only.
14. The intrinsic kinetic parameters were estimated using non-linear least square fitting at different reaction temperatures and contact times. The determined kinetic parameters included the pre-exponential factor ($k_{0,i}$), the activation energy (E_i), and DME adsorption enthalpy (ΔH_{ads}^0).
15. The DME adsorption term ($1/(1 + K_{DME}p_{DME})$) was found to be insignificant (close to unity). On this basis, a Langmuir–Hinshelwood formulation was found to be irrelevant for modeling the DTO reaction.

16. The pressure ratio term in the product methylation reaction and the toluene formation rate $\left(k_i p_i / \sum_{j=2}^5 k_j p_{C_j}\right)$ were estimated as a constant value at every given temperature. Therefore, the product reaction rates were found to be of first order dependence on the DME partial pressure.
17. The pre-exponential factors and the activation energies for the DME dehydration reactions were found to be close for both the methoxy species and ethylene formations. The methylation activation energy was found to be similar for each of the olefinic lumps (i.e. light olefins and heavy olefins). The activation energy for methylating light olefins was, however, slightly higher (169 kJ/mole) while compared to that for the heavy olefins (156 kJ/mole). The aromatics methylation reaction, on the other hand, displayed a more demanding energy process as the number of methyl groups increases ($E_i = 104 - 191$ kJ/mole).

8.2 Recommendations

As DTO reaction studies are in their early stages of development, the present contribution exposes potential recommended areas for future research as follows:

1. To test milder operating conditions (higher temperatures and lower contact times) in order to examine if 100% DME conversion can be achieved with no negative impact on the catalyst performance. The current study with an HZSM-5 catalyst having a $\text{SiO}_2/\text{Al}_2\text{O}_3$ ratio of 280 was limited to DME conversions in the 45-74% range.
2. To consider investigating the DTO reaction using neat DME with new HZSM-5 doped promoters like La, Zr, Ca, or Rh. It is expected that such promoters could provide additional gains in terms of light olefin selectivity.
3. To use the kinetic model developed in the present study to simulate a large fixed multi-tubular reactor.

4. To consider the effect of the $\text{SiO}_2/\text{Al}_2\text{O}_3$ ratio for modeling a DTO reaction over HZSM-5. This may allow accounting for the deactivation effect on the hydrocarbon species rate equations of the proposed kinetic model.

REFERENCES

- [1] ChemSystems. Report Abstract-Gas to Ethylene. 2009.
- [2] ChemSystems. Report Abstract-Ethylene. 2009.
- [3] KBR. KBR's Olefins Technology n.d.
- [4] ChemSystems. Report Abstract-Olefins via Enhanced FCC. 2009.
- [5] Plotkin JS. The changing dynamics of olefin supply/demand. *Catal Today* 2005;106:10–4.
- [6] Xieqing W, Chaogang X, Zaiting L, Genquan Z. Catalytic Processes for Light Olefin Production. *Pract. Adv. Pet. Process. Vol. 1*, New York: Springer; 2006, p. 149–68.
- [7] Chenier P. Survey of Industrial Chemistry. Third. New York: Kluwer Academic / Plenum; 2002.
- [8] Sardesai A, Lee S. HYDROCARBON SYNTHESIS FROM DIMETHYL ETHER OVER ZSM-5 CATALYST. *ACS Div Fuel Chem* 1998;43:722–6.
- [9] Omata K, Yamazaki Y, Watanabe Y, Kodama K, Yamada M. Artificial Neural Network (ANN) -Aided Optimization of ZSM-5 Catalyst for the Dimethyl Ether to Olefin (DTO) Reaction from Neat Dimethyl Ether (DME). *Ind Eng Chem Res* 2009;48:6256–61.
- [10] Zhu W, Li X, Kaneko H, Fujimoto K. Selective Transformation of Dimethyl Ether into Small Molecular Hydrocarbons Over Large-pore Beta Zeolite. *Catal Letters* 2007;120:95–9.
- [11] Sardesai A, Lee S. Alternative Source of Propylene. *Energy Sources* 2005;27:489–500.

- [12] Ito H, Ooyama K, Yamada S, Kume M, Chikamatsu N. Catalyst, process for preparing the catalyst and process for producing lower hydrocarbon with the catalyst. 20070032379, 2007.
- [13] Kolesnichenko N V., Yashina O V., Markova N a., Biryukova EN, Goryainova TI, Kulumbegov R V., et al. Conversion of dimethyl ether into C2-C4 olefins on zeolite catalysts. *Pet Chem* 2009;49:42–6.
- [14] Zhao T-S, Takemoto T, Tsubaki N. Direct synthesis of propylene and light olefins from dimethyl ether catalyzed by modified H-ZSM-5. *Catal Commun* 2006;7:647–50.
- [15] Jian-ming M, Zhang Q, Xie H, Pan J, Tan Y, Han Y. Effects of reaction atmosphere on dimethyl ether conversion to propylene process over Ca/ZSM-5. *J Fuel Chem Technol* 2011;39:42–6.
- [16] Kolesnichenko N V., Goryainova TI, Biryukova EN, Yashina O V., Khadzhiev SN. Synthesis of lower olefins from dimethyl ether in the presence of zeolite catalysts modified with rhodium compounds. *Pet Chem* 2011;51:55–60.
- [17] Abramova A V. Development of catalysts based on pentasil-type zeolites for selective synthesis of lower olefins from methanol and dimethyl ether. *Catal Ind* 2009;1:267–77.
- [18] Sardesai A. Catalytic Conversion of Dimethyl Ether to Lower Olefins: Process and Catalyst Deactivation Studies. The University of Akron, 1997.
- [19] Sardesai A, Tartamellaa T, Lee S. Synthesis of hydrocarbons from dimethyl ether: Selectivities towards light hydrocarbons. *Fuel Sci Technol* 1996;14:703–12.
- [20] ChemSystems. Olefins Outlook Positive Until 2009 2007.
- [21] ChemSystems. Report Abstract-Alternative Routes to Propylene. 2010.
- [22] AlWahabi S. Conversion of Methanol to Light Olefins on SAPO-34 Kinetic Modeling and Reactor Design. Texas A&M University, 2003.

- [23] ChemSystems. Report Abstract-Ethylene via Catalytic Ethane Partial Oxidation. 2004.
- [24] Mulla S, Buyevskaya O, Baerns M. A comparative study on non-catalytic and catalytic oxidative dehydrogenation of ethane to ethylene. *Appl Catal* 2002;226:73–8.
- [25] Park Y-K, Lee CW, Kang NY, Choi WC, Choi S, Oh SH, et al. Catalytic Cracking of Lower-Valued Hydrocarbons for Producing Light Olefins. *Catal Surv from Asia* 2010;14:75–84.
- [26] Abramova a. V., Kulumbegov R V., Goryainova TI, Khadzhiev SN. Production of lower unsaturated hydrocarbons via catalytic conversion of dimethyl ether. *Pet Chem* 2008;48:15–21.
- [27] Keil FJ. Methanol-to-hydrocarbons: process technology. *Microporous Mesoporous Mater* 1999;29:49–66.
- [28] Stöcker M. Methanol-to-hydrocarbons: catalytic materials and their behavior. *Microporous Mesoporous Mater* 1999;29:3–48.
- [29] Pisarenko E V., Pisarenko VN. Kinetics of the reaction of olefin synthesis from methanol and dimethyl ether. *Theor Found Chem Eng* 2008;42:822–31.
- [30] Saterfield C. Heterogeneous catalysis in industrial practice. repr. 2nd. Florida, USA: Krieger; 1996.
- [31] Koempel H, Liebner W. Lurgi's Methanol To Propylene (MTP®) Report on a successful commercialisation. 8th Int. Nat. Gas Convers. Symp., vol. 167, *Studies in Surface Science and Catalysis*; 2007, p. 261–7.
- [32] ChemSystems. Report Abstract-Methanol to Olefins. 2002.
- [33] Chen JQ, Bozzano A, Glover B, Fuglerud T, Kvisle S. Recent advancements in ethylene and propylene production using the UOP/Hydro MTO process. *Catal Today* 2005;106:103–7.
- [34] UOP. UOP / HYDRO MTO Process Methanol to Olefins Conversion. 2007.

- [35] Biryukova EN, Goryainova TI, Kulumbegov R V., Kolesnichenko N V., Khadzhiev SN. Conversion of dimethyl ether into lower olefins on a La-Zr-HZSM-5/Al₂O₃ zeolite catalyst. *Pet Chem* 2011;51:49–54.
- [36] Cai G, Liu Z, Shi R, Changqing H, Yang L, Sun C, et al. Light alkenes from syngas via dimethyl ether. *Appl Catal A Gen* 1995;125:29–38.
- [37] Liu ZM, Cai GY, Sun CL, He CQ, Chang YJ, Yang LX, et al. Research progress and pilot plant test on SDTO process. 5th Int. Nat. Gas Convers. Symp., vol. 119, 1998, p. 895–900.
- [38] ChemSystems. Report abstract – Coal to Olefins. 2007.
- [39] Li Y, Zhang M, Wang D, Wei F, Wang Y. Differences in the methanol-to-olefins reaction catalyzed by SAPO-34 with dimethyl ether as reactant. *J Catal* 2014;311:281–7.
- [40] Chen W-H, Lin B-J, Lee H-M, Huang M-H. One-step synthesis of dimethyl ether from the gas mixture containing CO₂ with high space velocity. *Appl Energy* 2012;98:92–101.
- [41] Inomata M, Higashi A, Makino Y, Mashiko Y. Process for the preparation of lower olefins. US 6,852,897 B2, 2005.
- [42] JGC. DTP® (Dominant Technology for Propylene Production) Process n.d.
- [43] Ito H, Yoshida J, Funatsu S, Ooyama K, Chikamatsu N. Process and apparatus for producing propylene. 20100179366, 2010.
- [44] Zhou H, Wang Y, Wei F, Wang D, Wang Z. In situ synthesis of SAPO-34 crystals grown onto α -Al₂O₃ sphere supports as the catalyst for the fluidized bed conversion of dimethyl ether to olefins. *Appl Catal A Gen* 2008;341:112–8.
- [45] Sardesai A, Tartamella T, Lee S. Performance of Zsm-5 Catalyst in the Dimethyl Ether To Olefins Process. *Pet Sci Technol* 1999;17:273–89.

- [46] Iida A, Nakamura R, Komura K, Sugi Y. Remarkable Improvement of Catalytic Performance in Dimethyl Ether to Olefin Reaction over CeO₂-modified Calcium-containing MFI Type Zeolite. *Chem Lett* 2008;37:494–5.
- [47] Zhao T-S, Takemoto T, Yoneyama Y, Tsubaki N. Selective Conversion of Dimethyl Ether to Propylene and Light Olefins over Modified H-ZSM-5. *Chem Lett* 2005;34:970–1.
- [48] Chen Y, Zhou H, Zhu J, Zhang Q, Wang Y, Wang D, et al. Direct Synthesis of a Fluidizable SAPO-34 Catalyst for a Fluidized Dimethyl Ether-to-Olefins Process. *Catal Letters* 2008;124:297–303.
- [49] Triantafillidis CS, Vlessidis AG, Nalbandian L, Evmiridis NP. Effect of the degree and type of the dealumination method on the structural, compositional and acidic characteristics of H-ZSM-5 zeolites. *Microporous Mesoporous Mater* 2001;47:369–88.
- [50] Muller U, Reichert H, Robens E, Unger KK, Grillet Y, Rouquerol F, et al. High-resolution sorption studies of argon and nitrogen on large crystals of microporous zeolite ZSM-5. *Fresenius' Zeitschrift Fur Anal Chemie* 1989;333:433–6.
- [51] Froment GF, Dehertog WJH, Marchi AJ. Zeolite Catalysis in the Conversion of Methanol into Olefins. *Catalysis* 1992;9:1–64.
- [52] Weber RW, Fletcher JCQ, Möller KP, O'Connor CT. The characterization and elimination of the external acidity of ZSM-5. *Microporous Mater* 1996;7:15–25.
- [53] Armaroli T, Simon LJ, Digne M, Montanari T, Bevilacqua M, Valtchev V, et al. Effects of crystal size and Si/Al ratio on the surface properties of H-ZSM-5 zeolites. *Appl Catal A Gen* 2006;306:78–84.
- [54] Benito PL, Gayubo AG, Aguayo AT, Olazar M, Bilbao J. Effect of Si/Al Ratio and of Acidity of H-ZSM5 Zeolites on the Primary Products of Methanol to Gasoline Conversion. *J Chem Technoloby Biotechnol* 1996;66:183–91.

- [55] Llewellyn P, Coulomb J, Grillet Y, Patarin J, Andre G, Rouquerolt J. Adsorption by MFI-Type Zeolites Examined by Isothermal Microcalorimetry and Neutron Diffraction. 2. Nitrogen and Carbon Monoxide. *Langmuir* 1993;9:1852–6.
- [56] Llewellyn P, Reichert H, Patarin J, Grillet Y, Rouquerol J, Chemie FIRA, et al. A Microcalorimetric Study of the Different States of Argon And Nitrogen Adsorbed at 77 K on Silicalite-I and ZSM-5. *J Therm Anal* 1992;38:683–92.
- [57] Shan XL, Guan NJ, Zeng X, Xiang S. In-situ Synthesis of ZSM-5 with Different Si/Al Ratios on Honeycomb-shaped Cordierite and their Behavior on NO Decomposition. *Chinese Chem Lett* 1999;10:885–8.
- [58] Shirazi L, Jamshidi E, Ghasemi MR. The effect of Si/Al ratio of ZSM-5 zeolite on its morphology, acidity and crystal size. *Cryst Res Technol* 2008;43:1300–6.
- [59] Datka J, Tuznik E. Infrared Spectroscopic Studies of Acid Properties of NaHZSM-5 Zeolites. *J Catal* 1986;102:43–51.
- [60] Reitmeier SJ, Gobin OC, Jentys A, Lercher J a. Enhancement of sorption processes in the zeolite H-ZSM5 by postsynthetic surface modification. *Angew Chem Int Ed Engl* 2009;48:533–8.
- [61] Reitmeier SJ, Mukti RR, Jentys a., Lercher J a. Surface Transport Processes and Sticking Probability of Aromatic Molecules in HZSM-5. *J Phys Chem C* 2008;112:2538–44.
- [62] Kouva S, Kanervo J, Schüßler F, Olindo R, Lercher J a., Krause O. Sorption and diffusion parameters from vacuum-TPD of ammonia on H-ZSM-5. *Chem Eng Sci* 2013;89:40–8.
- [63] AUERBACH SM, CARRADO KA, DUTTA PK. *Handbook of Zeolite and Technology*. 1st ed. New York: Marcel Dekker; 2003.

- [64] Lok BM, Messina CA, Patton RL, Gajek RT, Cannan TR, Flanigen EM. Silicoaluminophosphate molecular sieves: another new class of microporous crystalline inorganic solids. *J Am Chem Soc* 1984;106:6092–3.
- [65] Haw JF, Song W. Ship-in-a-bottle catalysts. 7078364, 2006.
- [66] Cui Y, Zhang Q, He J, Wang Y, Wei F. Pore-structure-mediated hierarchical SAPO-34: Facile synthesis, tunable nanostructure, and catalysis applications for the conversion of dimethyl ether into olefins. *Particuology* 2013;11:468–74.
- [67] Lee S-G, Kim H-S, Kim Y-H, Kang E-J, Lee D-H, Park C-S. Dimethyl ether conversion to light olefins over the SAPO-34/ZrO₂ composite catalysts with high lifetime. *J Ind Eng Chem* 2014;20:61–7.
- [68] Chen D, Rebo HP, Moljord K, Holmen A. Dimethyl ether conversion to light olefins over SAPO-34: Deactivation due to coke deposition. 5th Int. Nat. Gas Convers. Symp., *Studies in Surface Science and Catalysis*; 1998, p. 521–6.
- [69] Chang CD, Silvestri AJ. The Conversion of Methanol and Other O-Compounds to Hydrocarbons over Zeolite Catalysts. *J Catal* 1977;47:249–59.
- [70] Chang CD. Methanol Conversion to Light Olefins. *Catal Rev* 1984;26:323–45.
- [71] Kaarsholm M. Methanol-To-Olefins in a Fluidized Bed: Experimental and Modelling Study. University of Montreal, 2009.
- [72] Hagey HL. Kinetic modelling of synthesis gas into hydrocarbons. The University of Western Ontario, 2001.
- [73] Gayubo AG, Aguayo AT, Olazar M, Vivanco R, Bilbao J. Kinetics of the irreversible deactivation of the HZSM-5 catalyst in the MTO process. *Chem Eng Sci* 2003;58:5239–49.

- [74] Fougerit JM, Gnep NS, Guisnet M. Selective transformation of methanol into light olefins over a mordenite catalyst: reaction scheme and mechanism. *Microporous Mesoporous Mater* 1999;29:79–89.
- [75] Chen N, Reagan W. Evidence of autocatalysis in methanol to hydrocarbon reactions over zeolite catalysts. *J Catal* 1979;59:123–9.
- [76] Chang CD. A kinetic model for methanol conversion to hydrocarbons. *Chem Eng Sci* 1980;35:619–22.
- [77] Anthony R. A kinetic model for methanol conversion to hydrocarbons. *Chem Eng Sci* 1981;36:789.
- [78] Sedran U, Mahay A, de Lasa HI. Modelling Methanol Conversion to Hydrocarbons: Revision and Testing of a Simple Kinetic Model. *Chem Eng Sci* 1990;45:1161–5.
- [79] Schipper P, Krambeck F. A reactor design simulation with reversible and irreversible catalyst deactivation. *Chem Eng Sci* 1986;41:1013–9.
- [80] Sedran U, Mahay A, de Lasa HI. Modelling methanol conversion to hydrocarbons: Alternative kinetic models. *Chem Eng J* 1990;45:33–42.
- [81] GAYUBO AG, BENITO PL, AGUAYO AT, CASTILLA M, BILBAO J. Kinetic model of the MTG process taking into account the catalyst deactivation. Reactor simulation. *Chem Eng Sci* 1996;51:3001–6.
- [82] Gayubo AG, Aguayo AT, Castilla M, Olazar M, Bilbao J. Catalyst reactivation kinetics for methanol transformation into hydrocarbons. Expressions for designing reaction–regeneration cycles in isothermal and adiabatic fixed bed reactor. *Chem Eng Sci* 2001;56:5059–71.
- [83] Gayubo AG, Benito PL, Aguayo AT, Aguirre I, Bilbao J. Analysis of kinetic models of the methanol-to-gasoline (MTG) process in an integral reactor. *Chem Eng J* 1996;63:45–51.

- [84] Benito PL, Gayubo AG, Aguayo AT, Castilla M, Bilbao J. Concentration-Dependent Kinetic Model for Catalyst Deactivation in the MTG Process. *Ind Eng Chem Res* 1996;35:81–9.
- [85] Schoenfelder H, Hinderer J, Werther J, Keil FJ. Methanol to olefins—prediction of the performance of a circulating fluidized-bed reactor on the basis of kinetic experiments in a fixed-bed reactor. *Chem Eng Sci* 1994;49:5377–90.
- [86] Sing KSW, Everett DH, Haul r. AW, Moscou L, Pierotti RA, Rouquerol J, et al. Reporting Physisorption Data for Gas/Solid Systems with Special Reference to the Determination of Surface Area and Porosity. *Pure Appl Chem* 1985;57:603–19.
- [87] Groen JC, Peffer L a. ., Pérez-Ramírez J. Pore size determination in modified micro- and mesoporous materials. Pitfalls and limitations in gas adsorption data analysis. *Microporous Mesoporous Mater* 2003;60:1–17.
- [88] Webb PA, Orr C. *Analytical methods in fine particle technology*. 1st ed. Norcross, GA, USA: Micromeritics Instrument Corporation; 1997.
- [89] Saito A, Foley HC. Curvature and parametric sensitivity in models for adsorption in micropores. *AIChE J* 1991;37:429–36.
- [90] *Diffuse Reflectance – Theory and Applications*. PIKE Technologies, Madison, WI, USA: n.d.
- [91] Berty JM. Testing Commercial Catalysts in Recycle Reactors. *Catal Rev* 1979;20:75–96.
- [92] Berty JM. Reactor for vapour-phase catalytic studies. *Chem Eng Prog* 1974;70:78–84.
- [93] Mahay A, de Lasa HI, Ravella A. Kinetic modeling of the catalytic conversion of methanol into hydrocarbons. 37th CSChE Conf., Montreal: 1987.
- [94] Autoclave Engineers. Berty Stationary Basket Catalyst Reactor n.d.

- [95] Jin F, Li Y. A FTIR and TPD examination of the distributive properties of acid sites on ZSM-5 zeolite with pyridine as a probe molecule. *Catal Today* 2009;145:101–7.
- [96] ASTM International. ASTM D5758 - 01: Standard Test Method for Determination of Relative Crystallinity of Zeolite ZSM-5 by X-Ray Diffraction. West Conshohocken, PA. United States: 2011.
- [97] Costa C, Dzikh IP, Lopes JM, Lemos F, Ribeiro FR. Activity–acidity relationship in zeolite ZSM-5. Application of Brønsted-type equations. *J Mol Catal A Chem* 2000;154:193–201.
- [98] Hidalgo C v., Itoh H, Hattori T, Niwa M, Murakami Y. Measurement of the Acidity of Various Zeolites by Desorption of Ammonia. *J Catal* 1984;85:362–9.
- [99] Al-Ghamdi S, Volpe M, Hossain MM, de Lasa H. VO_x/c-Al₂O₃ Catalyst for Oxidative Dehydrogenation of Ethane to Ethylene: Desorption Kinetics and Catalytic Activity. *Appl Catal A Gen* 2013;450:120–30.
- [100] Forni L, Vatti FP, Ortoleva E. Temperature-programmed desorption-diffusion of ammonia in molecular sieves V. ZSM-5 zeolite. *Microporous Mater* 1995;3:367–75.
- [101] Topaloglu Yazıcı D, Bilgiç C. Determining the surface acidic properties of solid catalysts by amine titration using Hammett indicators and FTIR-pyridine adsorption methods. *Surf Interface Anal* 2010;42:959–62.
- [102] Tonetto G, Atias J, de Lasa H. FCC catalysts with different zeolite crystallite sizes: acidity, structural properties and reactivity. *Appl Catal A Gen* 2004;270:9–25.
- [103] Hardenberg T, Mertens L, Mesman P, Muller HC, Nicolaidis CP. A catalytic method for the quantitative evaluation of crystallinities of ZSM-5 zeolite preparations. *Zeolites* 1992;12:685–9.
- [104] Miyamoto T, Katada N, Kim J, Niwa M. Acidic Property of MFI-Type Gallosilicate Determined by Temperature-Programmed Desorption of Ammonia. *J Phys Chem B* 1998;102:6738–45.

- [105] Cooper CA, Lin YS. Synthesis and characterization of silicalite powders and membranes with micro–meso bimodal pores. *J Mater Sci* 2007;42:320–7.
- [106] Singh M, Kamble R, Viswanadham N. Effect of Crystal Size on Physico-Chemical Properties of ZSM-5. *Catal Letters* 2008;120:288–93.
- [107] Meng T, Mao D, Guo Q, Lu G. The effect of crystal sizes of HZSM-5 zeolites in ethanol conversion to propylene. *Catal Commun* 2012;21:52–7.
- [108] Konno H, Okamura T, Kawahara T, Nakasaka Y, Tago T, Masuda T. Kinetics of n-hexane cracking over ZSM-5 zeolites – Effect of crystal size on effectiveness factor and catalyst lifetime. *Chem Eng J* 2012;207-208:490–6.
- [109] Kim WJ, Lee MC, Hayhurst DT. Synthesis of ZSM-5 at low temperature and atmospheric pressure in a pilot-scale batch reactor. *Microporous Mesoporous Mater* 1998;26:133–41.
- [110] Pollack SS, Adkins JW, Wetzel EL, Newbury D. SiO₂/Al₂O₃ ratios of ZSM-5 crystals measured by electron microprobe and X-ray diffraction. *Zeolites* 1984;4:181–7.
- [111] Treacy MMJ, Higgins JB. *Collection of Simulated XRD Powder Patterns for Zeolites*. 5th ed. Amsterdam: ELSEVIER; 2007.
- [112] Cullity BD, Stock SR. *Elements of X-Ray Diffraction*. 3rd ed. Upper Saddle River, New Jersey, USA: Prentice Hall; 2001.
- [113] Awate S V., Joshi PN, Shiralkar VP, Kotasthane AN. Synthesis and Characterization of Gallosilicate Pentasil (MFI) Framework Zeolites. *J Incl Phenom Mol Recognit Chem* 1992;13:207–18.
- [114] Nicolaidis CP. A novel family of solid acid catalysts: substantially amorphous or partially crystalline zeolitic materials. *Appl Catal A Gen* 1999;185:211–7.
- [115] Özvatan S, Yürüm Y. Synthesis of Crystalline ZSM-5 Type Zeolites Utilizing Primary Monoalkylamines 1 . Characterization. *Energy Sources* 2001;23:475–85.

- [116] Reichert H, Müller U, Unger KK, Grillet Y, Rouquerol F, Rouquerol J, et al. Sorption of argon and nitrogen on network types of zeolites and aluminophosphates. *Charact. Porous Solids II*, Amsterdam: Elsevier B.V.; 1991, p. 535–42.
- [117] Sulikowski B, Klinowski J. Preparation and characterization of titanosilicates with ZSM-5 structure. *Appl Catal A Gen* 1992;84:141–53.
- [118] Saito A, Foley HC. High-resolution nitrogen and argon adsorption on ZSM-5 zeolites: effects of cation exchange and Si/Al ratio. *Microporous Mesoporous Mater* 1995;3:543–56.
- [119] Peterson BK, Gubbins KE, Heffelfinger GS, Marini Bettolo Marconi U, van Swol F. Lennard-Jones fluids in cylindrical pores: Nonlocal theory and computer simulation. *J Chem Phys* 1988;88:6487.
- [120] Occelli ML, Olivier JP, Perligon-Melon A, Auroux A. Surface Area, Pore Volume Distribution, and Acidity in Mesoporous Expanded Clay Catalysts from Hybrid Density Functional Theory (DFT) and Adsorption Microcalorimetry Methods. *Langmuir* 2002;18:9816–23.
- [121] Olivier JP, Occelli ML. Surface Area and Microporosity of a Pillared Interlayered Clay (PILC) from a Hybrid Density Functional Theory (DFT) Method. *J Phys Chem B* 2001;105:623–9.
- [122] Occelli ML, Olivier JP, Petre A, Auroux A. Determination of Pore Size Distribution, Surface Area, and Acidity in Fluid Cracking Catalysts (FCCs) from Nonlocal Density Functional Theoretical Models of Adsorption and from Microcalorimetry Methods. *J Phys Chem B* 2003;107:4128–36.
- [123] Occelli ML, F. Baldiraghi, Olivier JP, Auroux A. Dual function fluid cracking catalyst (DFCC) containing a microporous additive for olefin selectivity. *Prepr - Am Chem Soc Div Pet Chem* 2003;48:231–4.

- [124] Seaton N a., Walton JPRB, Quirke N. A new analysis method for the determination of the pore size distribution of porous carbons from nitrogen adsorption measurements. *Carbon N Y* 1989;27:853–61.
- [125] Lowell S, Shields JE, Thomas MA, Thommes M. *Characterization of Porous Solids and Powders: Surface Area, Pore Size and Density*. Dordrecht, The Netherlands: Kluwer Academic Publishers; 2004.
- [126] Lastoskie C, Gubbins KE, Quirk N. Pore Size Distribution Analysis of Microporous Carbons: A Density Functional Theory Approach. *J Phys Chem* 1993;97:4786–96.
- [127] Al-Bogami S a., de Lasa HI. Catalytic conversion of benzothiophene over a H-ZSM5 based catalyst. *Fuel* 2013;108:490–501.
- [128] Gayubo AG, Benito PL, Aguayo AT, Olazar M. Relationship between Surface Acidity and Activity of catalysts in the Transformation of Methanol into Hydrocarbons. *J Chem Technol Biotechnol* 1996;65:186–92.
- [129] Serrano DP, Calleja G, Botas J a., Gutierrez FJ. Characterization of adsorptive and hydrophobic properties of silicalite-1, ZSM-5, TS-1 and Beta zeolites by TPD techniques. *Sep Purif Technol* 2007;54:1–9.
- [130] Song W, Justice RE, Jones C a, Grassian VH, Larsen SC. Synthesis, characterization, and adsorption properties of nanocrystalline ZSM-5. *Langmuir* 2004;20:8301–6.
- [131] Barrett EP, Joyner LG, Paul P. Halenda. The Determination of Pore Volume and Area Distributions in Porous Substances. I. Computations from Nitrogen Isotherms. *J Am Chem Soc* 1951;73:373–80.
- [132] Harkins WD, Jura G. *Surfaces of Solids*. XIII. A Vapor Adsorption Method for the Determination of the Area of a Solid without the Assumption of a Molecular Area, and the Areas Occupied by Nitrogen and Other Molecules on the Surface of a Solid. *J Am Chem Soc* 1944;66:1366–73.

- [133] Horváth G, Kawazoe K. Method for the Calculation of Effective Pore Size Distribution in Molecular Sieve Carbon. *J Chem Eng Japan* 1983;16:470–5.
- [134] Cheng S, Yang T. Improved Horvath-Kawazoe equations including spherical pore models for calculating micropore size distribution. *Chem Eng Sci* 1994;49:2599–609.
- [135] ASTM International. D4641-12: Standard Practice for Calculation of Pore Size Distributions of Catalysts and Catalyst Carriers from Nitrogen Desorption Isotherms. West Conshohocken, PA. United States: 2012.
- [136] Sayari A, Crusson E, Kaliaguine S, Brown JR. External Surface Areas of H-ZSM-5 Zeolites. *Langmuir* 1991;7:314–7.
- [137] Du X, Wu E. Porosity of microporous zeolites A, X and ZSM-5 studied by small angle X-ray scattering and nitrogen adsorption. *J Phys Chem Solids* 2007;68:1692–9.
- [138] Post JG, Hooff JHC Van. Acidity and activity of H-ZSM-5 measured with NH₃-t.p.d. and n-hexane cracking. *Zeolites* 1984;4:9–14.
- [139] Kapustin GI, Brueva TR, Klyachko AL, Beran S, Wichterlova B. Determination of the Number and Acid Strength of Acid Sites in Zeolites by Ammonia Adsorption. Comparison of Calorimetry and Temperature- Programmed Desorption of Ammonia. *Appl Catal* 1988;42:239–46.
- [140] Katada N, Niwa M. Analysis of acidic properties of zeolitic and non-zeolitic solid acid catalysts using temperature-programmed desorption of ammonia. *Catal Surv from Asia* 2004;8:161–70.
- [141] Rodríguez-González L, Hermes F, Bertmer M, Rodríguez-Castellón E, Jiménez-López A, Simon U. The acid properties of H-ZSM-5 as studied by NH₃-TPD and ²⁷Al-MAS-NMR spectroscopy. *Appl Catal A Gen* 2007;328:174–82.
- [142] Lasa H De, Enriquez RH, Tonetto G. Catalytic Desulfurization of Gasoline via Dehydrosulfidation. *Ind Eng Chem Res* 2006;45:1291–9.

- [143] Katada N, Igi H, Kim J-H, Niwa M. Determination of the Acidic Properties of Zeolite by Theoretical Analysis of Temperature-Programmed Desorption of Ammonia Based on Adsorption Equilibrium. *J Phys Chem B* 1997;5647:5969–77.
- [144] Hunger B, Hoffmann J, Heitzsch O, Hunger M. Temperature-Programmed Desorption (TPD) of Ammonia from HZSM-5 Zeolites. *J Therm Anal* 1990;36:1379–91.
- [145] Hunger B, Hoffmann J. Kinetic analysis of NH₃ temperature programmed desorption (TPD) on a HZSM-5 zeolite. *Thermochim Acta* 1986;106:133–40.
- [146] Rodriguez-Gonzalez L, Rodriguezcastellon E, Jimenezlopez A, Simon U. Correlation of TPD and impedance measurements on the desorption of NH₃ from zeolite H-ZSM-5. *Solid State Ionics* 2008;179:1968–73.
- [147] Woolery GL, Kuehl GH, Timken HC, Chester AW, Vartuli JC. On the nature of framework Brønsted and Lewis acid sites in ZSM-5. *Zeolites* 1997;19:288–96.
- [148] Bagnasco G. NOTE Improving the Selectivity of NH₃ TPD Measurements. *J Catal* 1996;159:249–52.
- [149] Topsøe N-Y, Pedersen K, Eric Derouane. Infrared and temperature-programmed desorption study of the acidic properties of ZSM-5-type zeolites. *J Catal* 1981;70:41–52.
- [150] Matsuura H, Katada N, Niwa M. Additional acid site on HZSM-5 treated with basic and acidic solutions as detected by temperature-programmed desorption of ammonia. *Microporous Mesoporous Mater* 2003;66:283–96.
- [151] Holm MS, Svelle S, Joensen F, Beato P, Christensen CH, Bordiga S, et al. Assessing the acid properties of desilicated ZSM-5 by FTIR using CO and 2,4,6-trimethylpyridine (collidine) as molecular probes. *Appl Catal A Gen* 2009;356:23–30.
- [152] Bjørgen M, Joensen F, Spangsborg Holm M, Olsbye U, Lillerud K-P, Svelle S. Methanol to gasoline over zeolite H-ZSM-5: Improved catalyst performance by treatment with NaOH. *Appl Catal A Gen* 2008;345:43–50.

- [153] Borade R, Sayari A, Adnot A, Kaliaguine S. Characterization of Acidity in ZSM-5 Zeolites: An X-ray Photoelectron and IR Spectroscopy Study. *J Phys Chem* 1990;94:5989–94.
- [154] Datka J, Piwowarska Z. Acid properties of NaHZSM-5 zeolites of various Si/Al ratios and of NaHZSM-11 zeolite studied by i.r. spectroscopy. *Zeolites* 1988;8:30–4.
- [155] Requejo FG, Ramallo-López JM, Lede EJ, Miró EE, Pierella LB, Anunziata OA. In-containing H-ZSM5 zeolites with various Si/Al ratios for the NO SCR in the presence of CH₄ and O₂. PAC, TPAD and FTIR studies. *Catal Today* 1999;54:553–8.
- [156] Vedrine JC, Auroux A, Coudurier G. Combined Physical Techniques in the Characterization of Zeolite ZSM-5 and ZSM-11 Acidity and Basicity. *ACS Symp Ser* 1984;248:253–73.
- [157] Cvetanović RJ, Amenomiya Y. Application of a Temperature-Programmed Desorption Technique to Catalyst Studies. *Adv Catal* 1967;17:103–49.
- [158] Suzuki K, Noda T, Katada N, Niwa M. IRMS-TPD of ammonia Direct and individual measurement of Brønsted acidity in zeolites and its relationship with the catalytic cracking activity. *J Catal* 2007;250:151–60.
- [159] Amenomiya Y, Cvetanovic RJ. Application of flash-desorption method to catalyst studies. I. Ethylene-Alumina system. *J Phys Chem* 1963;67:144–7.
- [160] Wikipedia. Hydrogen bond n.d.
- [161] Svelle S, Joensen F, Nerlov J, Olsbye U, Lillerud K-P, Kolboe S, et al. Conversion of methanol into hydrocarbons over zeolite H-ZSM-5: ethene formation is mechanistically separated from the formation of higher alkenes. *J Am Chem Soc* 2006;128:14770–1.
- [162] Park T-Y, Froment GF. Kinetic Modeling of the Methanol to Olefins Process. 1. Model Formulation. *Ind Eng Chem Res* 2001;40:4172–86.

- [163] Svelle S, Kolboe S, Swang O, Olsbye U. Methylation of alkenes and methylbenzenes by dimethyl ether or methanol on acidic zeolites. *J Phys Chem B* 2005;109:12874–8.
- [164] Hill IM. Kinetics and mechanisms of methanol to hydrocarbons conversion over zeolite catalysts. University of Minnesota, 2013.
- [165] Wang W, Jiang Y, Hunger M. Mechanistic investigations of the methanol-to-olefin (MTO) process on acidic zeolite catalysts by in situ solid-state NMR spectroscopy. *Catal Today* 2006;113:102–14.
- [166] Maihom T, Boekfa B, Sirijaraensre J, Nanok T, Probst M, Limtrakul J. Reaction Mechanisms of the Methylation of Ethene with Methanol and Dimethyl Ether over H-ZSM-5: An ONIOM Study. *J Phys Chem C* 2009;113:6654–62.
- [167] Svelle S, Visur M, Olsbye U, Bjørgen M. Mechanistic Aspects of the Zeolite Catalyzed Methylation of Alkenes and Aromatics with Methanol: A Review. *Top Catal* 2011;54:897–906.
- [168] Vos a M, Rozanska X, Schoonheydt R a, van Santen R a, Hutschka F, Hafner J. A theoretical study of the alkylation reaction of toluene with methanol catalyzed by acidic mordenite. *J Am Chem Soc* 2001;123:2799–809.
- [169] Campbell SM, Jiang X-Z, Howe RF. Methanol to hydrocarbons: spectroscopic studies and the significance of extra-framework aluminium. *Microporous Mesoporous Mater* 1999;29:91–108.
- [170] Forester TR, Howe RF. In situ FTIR studies of methanol and dimethyl ether in ZSM-5. *J Am Chem Soc* 1987;109:5076–82.
- [171] Forester TR, Wong S, Howe RF. In situ Fourier transform i.r. observation of methylating species in ZSM-5. *J Chem Soc, Chem Commun* 1986:1611–3.
- [172] Ivanova II, Corma A. Surface Species Formed and Their Reactivity during the Alkylation of Toluene by Methanol and Dimethyl Ether on Zeolites As Determined by in Situ ¹³C MAS NMR. *J Phys Chem B* 1997;101:547–51.

- [173] Ivanova II, Kolyagin YG. Impact of in situ MAS NMR techniques to the understanding of the mechanisms of zeolite catalyzed reactions. *Chem Soc Rev* 2010;39:5018–50.
- [174] Seiler M, Schenk U, Hunger M. Conversion of methanol to hydrocarbons on zeolite HZSM- 5 investigated by in situ MAS NMR spectroscopy under flow conditions and on- line gas chromatography. *Catal Letters* 1999;62:139–45.
- [175] Seiler M, Wang W, Buchholz A, Å MH. Direct evidence for a catalytically active role of the hydrocarbon pool formed on zeolite H-ZSM-5 during the methanol-to-olefin conversion. *Catal Letters* 2003;88:187–91.
- [176] Wang W, Buchholz A, Seiler M, Hunger M. Evidence for an initiation of the methanol-to-olefin process by reactive surface methoxy groups on acidic zeolite catalysts. *J Am Chem Soc* 2003;125:15260–7.
- [177] Wang W, Seiler M, Hunger M. Role of Surface Methoxy Species in the Conversion of Methanol to Dimethyl Ether on Acidic Zeolites Investigated by in Situ Stopped-Flow MAS NMR Spectroscopy. *J Phys Chem B* 2001;105:12553–8.
- [178] Alwahabi SM, Froment GF. Single Event Kinetic Modeling of the Methanol-to-Olefins Process on SAPO-34. *Ind Eng Chem Res* 2004;43:5098–111.
- [179] Cheung P, Bhan A, Sunley GJ, Iglesia E. Selective carbonylation of dimethyl ether to methyl acetate catalyzed by acidic zeolites. *Angew Chem Int Ed Engl* 2006;45:1617–20.
- [180] Perot G, Cormerais FX, Guisnet M. The role of ethers in the methanol-hydrocarbon conversion of silica-alumina and ZSM-5 zeolite. *J Mol Catal* 1982;17:255–60.
- [181] Hutchings GJ, Gottschalk F, Hall MVM, Hunter R. Hydrocarbon formation from methylating agents over the zeolite catalyst ZSM-5. Comments on the mechanism of carbon–carbon bond and methane formation. *J Chem Soc Faraday Trans 1 Phys Chem Condens Phases* 1987;83:571–83.

- [182] Van Speybroeck V, Van der Mynsbrugge J, Vandichel M, Hemelsoet K, Lesthaeghe D, Ghysels A, et al. First principle kinetic studies of zeolite-catalyzed methylation reactions. *J Am Chem Soc* 2011;133:888–99.
- [183] Svelle S, Arstad B, Kolboe S, Swang O. A Theoretical Investigation of the Methylation of Alkenes with Methanol over Acidic Zeolites. *J Phys Chem B* 2003;107:9281–9.
- [184] Van der Mynsbrugge J, Visur M, Olsbye U, Beato P, Bjørgen M, Van Speybroeck V, et al. Methylation of benzene by methanol: Single-site kinetics over H-ZSM-5 and H-beta zeolite catalysts. *J Catal* 2012;292:201–12.
- [185] Liu C, Deng Y, Pan Y, Gu Y, Qiao B, Gao X. Effect of ZSM-5 on the aromatization performance in cracking catalyst. *J Mol Catal A Chem* 2004;215:195–9.
- [186] Song Y, Zhu X, Xie S, Wang Q, Xu L. The effect of acidity on olefin aromatization over potassium modified ZSM-5 catalysts. *Catal Letters* 2004;97:31–6.
- [187] Song Y, Zhu X, Xu L. Study on the process of transformation of olefin into aromatics over HZSM-5. *Catal Commun* 2006;7:218–23.
- [188] Viswanadham N, Pradhan a. R, Ray N, Vishnoi SC, Shanker U, Prasada Rao TSR. Reaction pathways for the aromatization of paraffins in the presence of H-ZSM-5 and Zn/H-ZSM-5. *Appl Catal A Gen* 1996;137:225–33.
- [189] Nash RJ, Dry ME, O'Connor CT. Aromatization of 1-hexene and 1-octene by gallium/H-ZSM-5 catalysts. *Appl Catal A Gen* 1996;134:285–97.
- [190] Guisnet M, Gnep NS, Alario F. Aromatization of short chain alkanes on zeolite catalysts. *Appl Catal A Gen* 1992;89:1–30.
- [191] Li Y, Liu S, Zhang Z, Xie S, Zhu X, Xu L. Aromatization and isomerization of 1-hexene over alkali-treated HZSM-5 zeolites: Improved reaction stability. *Appl Catal A Gen* 2008;338:100–13.

- [192] Hill I, Malek A, Bhan A. Kinetics and Mechanism of Benzene, Toluene, and Xylene Methylation over H-MFI. *ACS Catal* 2013;3:1992–2001.
- [193] Alabi W, Atanda L, Jermy R, Al-Khattaf S. Kinetics of toluene alkylation with methanol catalyzed by pure and hybridized HZSM-5 catalysts. *Chem Eng J* 2012;195-196:276–88.
- [194] Rabiou S, Al-Khattaf S. Kinetics of Toluene Methylation over ZSM-5 Catalyst in a Riser Simulator. *Ind Eng Chem Res* 2008;47:39–47.
- [195] Krishna R, Baur R. On the Langmuir–Hinshelwood formulation for zeolite catalysed reactions. *Chem Eng Sci* 2005;60:1155–66.
- [196] Creaser DC. The role of oxygen in the oxidative dehydrogenation of propane. Waterloo, 1997.
- [197] Senkan SM. Detailed chemical kinetic modeling: chemical reaction engineering of the future. *Adv Chem Eng* 1992;18:95.
- [198] Kennedy RM, Sagenkahn M, Aston JG. The Heat Capacity and Entropy, Heats of Fusion and Vaporization, and the Vapor Pressure of Dimethyl Ether. The Density of Gaseous Dimethyl Ether. *J Am Chem Soc* 1941;63:2267–72.
- [199] Hill IM, Hashimi S Al, Bhan A. Kinetics and mechanism of olefin methylation reactions on zeolites. *J Catal* 2012;285:115–23.
- [200] Svelle S, Tuma C, Rozanska X, Kerber T, Sauer J. Quantum chemical modeling of zeolite-catalyzed methylation reactions: toward chemical accuracy for barriers. *J Am Chem Soc* 2009;131:816–25.
- [201] Bhat YS, Halgeri a. B, Rao TSRP. Kinetics of toluene alkylation with methanol on HZSM-8 zeolite catalyst. *Ind Eng Chem Res* 1989;28:890–4.

[202] Vos AM, Nulens KHL, De Proft F, Schoonheydt R a., Geerlings P. Reactivity Descriptors and Rate Constants for Electrophilic Aromatic Substitution: Acid Zeolite Catalyzed Methylation of Benzene and Toluene. *J Phys Chem B* 2002;106:2026–34.

APPENDICES

Appendix A. Typical Reactivity Tests Data Collection Sheet

Catalyst	SiO ₂ /Al ₂ O ₃				DTO Run #		Date:			
	Weight before, after the run				DME	Cylinder/Regulator Pr (psig)				
	Acidity before, after the run, after calcinations (mmol/g)					MFC reading	τ (gcat·s/mol c feed)			
	TOC after (%)					BFM before/ after the run (per 90 ml)				
				Start , Stop time						
Reactor	Line Heat tracing? / Line /sample box Temp. (°C)				He	Cylinder/Regulator Pr (psig)				
	Reactor Heater / Body Temp. (°C)/ Pressure (psig)					Flushing time (min), flow (per 90 ml) before the run				
	Mixer running? / Speed (RPM)/ Cooling water?					Flushing time (min), flow (per 90 ml) after the run				
					Unit S/D	GC H ₂ /air/He cyls. closed?			DME/ He cyl. closed?	
						Shimadzu on cleaning?			Agilant on cleaning?	

Sample #	Bubble meter reading		GC-Shimadzu		Sample Box		Reactor Temp (C)	τ (g cat·s /mol c feed)	MFC reading	Comment
	Reading	Time	File #	Time	File #	Time				
1			DTO-		DTO-					
2			DTO-		DTO-					
3			DTO-		DTO-					
4			DTO-		DTO-					
5			DTO-		DTO-					
6			DTO-		DTO-					

Appendix B. Atomic Balance Calculation

Atoms In:

$$mol_{Atom,in}/s = \frac{v_{in}(ml/s)}{1000(ml/l) \times 24.465(l/mol)} \times \left(\frac{\varepsilon mol_C}{1 mol_{DME}} \right) \quad (B.1)$$

where Atom \equiv C, O, H, with $\varepsilon = 2, 1, 6$, respectively.

Atoms out:

$$mol_{Atom,out}/s = \sum_i mol_{Atom,i}/s, \quad \text{where } i = \text{outlet species} + H_2O \quad (B.2)$$

$$mol_{Atom,i}/s = \#Atom \times mol_i/s \quad (B.3)$$

$$mol_i/s = y_i \times mol_{out}/s \quad (B.4)$$

$$mol_{out}/s = \frac{v_{out}(ml/s)}{1000(ml/l) \times 24.465(l/mol)} \quad (B.5)$$

$$y_i = x_i \sum_i \frac{Mw}{Mw_i} \quad (B.6)$$

Where y_i and x_i are mole and mass fractions, Mw and \overline{Mw} are competent and average molecular weight.

$$\overline{Mw} = \frac{1}{\sum_i \frac{x_i}{Mw_i}} \quad (B.7)$$

$$x_i = \frac{x_{HCi}}{\sum_i x_{HCi} + x_{H_2O}} \quad (B.8)$$

where $x_{HCi} \equiv$ outlet hydrocarbons component mass fraction ($g_{HCi}/g_{HCtotal}$), $x_{H_2O} \equiv$ outlet water to hydrocarbons component mass ratio ($g_{H_2O}/g_{HCtotal}$).

$$x_{HCi} \left(\frac{g \text{ gas } HCi}{g \text{ total } HC \text{ gas out}} \right) = \frac{FID \text{ area component } i}{FID \text{ total areas}} \quad (B.9)$$

If we assume a stoichiometric conversion of DME to hydrocarbons, it can be represented as $(\text{CH}_3\text{OCH}_3 = [\text{CH}_2.\text{CH}_2] + \text{H}_2\text{O})$ where 28 g-atoms of hydrocarbons and 18 g-atoms of water are formed. Then,

$$x_{\text{H}_2\text{O}} = \left(\frac{18}{28}\right) \sum_i x_{\text{Hci},\text{prouct}} = \left(\frac{18}{28}\right) (1 - x_{\text{Hc,DMEout}}) \quad (\text{B.10})$$

Thus, the atoms closure expressed on a percent basis is as follows

$$\text{Atom Closure } \% = \frac{\text{mol}_{\text{Atom,out}}/\text{s}}{\text{mol}_{\text{Atom,in}}/\text{s}} \times 100 \quad (\text{B.11})$$

CURRICULUM VITAE

Name: **Abdullah Saad Al-Dughauther**

**Post-secondary
Education and
Degrees:** King Saud University
Riyadh, Saudi Arabia
1997-2001 B.A.

King Saud University
Riyadh, Saudi Arabia
2001-2006 M.A.

Western University
London, Ontario, Canada
2009-2014 Ph.D.

**Honours and
Awards:**

Appreciation letter in recognition of my contribution in the 6th SABIC Technical Meeting (STM6) by STM6 Chairman, Jubail Industrial City, Saudi Arabia, 2004

Appreciation letter in recognition of my contribution in the Acetic Acid technology commercialization, by SABIC R&T management, Riyadh, Saudi Arabia, 2005

Quality award and 1st Prize Winner granted to the team involved in successful Demonstration of Acetic Acid technology by Quality Management systems, SABIC R&T, Riyadh, Saudi Arabia, 2006.

Certificate of Appreciation for active participation in Linear Alpha Olefins Startup Workshop by Jubail United Petrochemical Company, Jubail Industrial City, Saudi Arabia, 2006

Certificate of Appreciation by SABIC on the Occasion of completing five years of service, Riyadh, Saudi Arabia, 2006

Appreciation letter from Jubail United Petrochemical Company in the occasion of saving Linear Alpha Olefin Plant from having a complete shutdown, Jubail Industrial City, Saudi Arabia, 2008

Saudi Basic Industries Corporations (SABIC) Graduate Scholarship
2009-2014

Related Work Experience

Process Engineer
(07/2006-08/2009), α -SABLIN Technology Program-Process Optimization Phase, SABIC R&T, Riyadh, Saudi Arabia
SABIC Research and Technology (R&T) delegated me as a process engineer to LAO Plant, Jubail United Petrochemical Company (JUPC) at Jubail Industrial city, Saudi Arabia (SA).

Process Engineer
(07/2005-06/2006), LAO Pilot Plant - Revamping Phase
SABIC R&T, Riyadh, Saudi Arabia

Process Engineer
(10/2003-06/2005), Demonstration of Acetic Acid technology, SABIC R&T, Riyadh, Saudi Arabia
SABIC R&T delegate to Acetic Acid Plant, Saudi Petrochemical Company for Industrial Fibers (IBN RUSHD), Yanbu, Saudi Arabia

Process Engineer
(07/2001-09/2003), α -SABLIN Program - piloting Phase
SABIC Research and Technology, Riyadh, Saudi Arabia

Publications:

W. Al-Masry, A. Al-Dughaiter, and T. Al-samari, "Relationship between Riser and Downcomer Gas Holdups in Semi-batch Circulating Bubble Columns", The Canadian Journal of Chemical Engineering, Volume 82, June 2004, 607- 612

Abdullah S. Al-Dughaiter, Ahmed A. Ibrahim, Waheed A. Al-Masry "Investigating droplet separation efficiency in wire-mesh mist eliminators in bubble column", Journal of Saudi Chemical Society (2010) 14, 331–339

Abdullah S. Al-Dughaiter, Ahmed A. Ibrahim, Waheed A. Al-Masry "Investigating pressure drop across wire mesh mist eliminators in bubble column", Journal of Saudi Chemical Society (2011) 15,1–9

Abdullah S. Al-Dughaiter and Hugo de Lasa. "HZSM-5 Zeolites with Different $\text{SiO}_2/\text{Al}_2\text{O}_3$ Ratios. Characterization and NH_3 Desorption Kinetics", Article ASAP, Ind Eng Chem Res (Publication Date (Web): January 24, 2014). DOI: 10.1021/ie4039532

Abdullah S. Al-Dughaiter and Hugo de Lasa. "Neat Dimethyl Ether Conversion to Olefins (DTO) over HZSM-5: Effect of $\text{SiO}_2/\text{Al}_2\text{O}_3$ on Porosity, Surface Chemistry, and Reactivity", In press, Corrected Proof, Fuel (Publication Date (Web): January 24, 2014). DOI: 10.1016/j.fuel.2014.07.026

Patents:

Peter Fritz, Heinz Bolt, Fuad Mosa, Talal Ali, A. Al-Dughaither, "Method for cleaning a reactor", International Patent, Application number: PCT/EP2006/005644, Publication date: 15-02-2007

12 inventors from Linde, 1 from Rostock and 8 from SABIC (Mosa, Hazmi, Aliyev, Palakal, A. Al-Dugathier, Ayed, Otaibi and Zahoor.), "Method for Preparing Linear alpha Olefins (Amine addition)", Europe Patent, Application No. 08001677.7,

Fritz, Peter M., Heinz Bölt, Andreas Meiswinkel, Carsten Taube, Florian Winkler, Volker Göke, Wolfgang Müller, A Al-Dugaither et al. "Method for preparing linear alpha-olefins." U.S. Patent 20120184692 A1, Publication date July 19, 2012.

Al Dugaither, Abdullah, Talal Ali, Heinz Bölt, Peter Fritz, and Fuad Mosa. "Method for cleaning a reactor." U.S. Patent 20100206334 A1, Publication date Aug 19, 2010.

Fritz, Peter M., Heinz Bölt, Andreas Meiswinkel, Carsten Taube, Florian Winkler, Volker Göke, Wolfgang Müller, A Al-Dugaither et al. "Method for preparing linear alpha-olefins." U.S. Patent 8809613 B2, Publication date Aug 19, 2014.